GPO PRICE $ _____

OTS PRICE(S) $ _____

Hard copy (HC) $5.00

Microfiche (MF) $1.25

HYPERVELOCITY HEAT TRANSFER STUDIES IN SIMULATED PLANETARY ATMOSPHERES

By

J. S. Gruszczynski

W. R. Warren

General Electric Space Sciences Laboratory

FINAL REPORT

JPL Purchase Order 950297

March 1964

Prepared for

Jet Propulsion Laboratories
Pasadena, California

HYPERVELOCITY HEAT TRANSFER STUDIES IN SIMULATED PLANETARY ATMOSPHERES

By

J. S. Gruszczynski

W. R. Warren

General Electric Space Sciences Laboratory

FINAL REPORT

JPL Purchase Order 950297

March 1964

[Work performed Under NASA Contract NAS 7-100]

Prepared for

Jet Propulsion Laboratories
Pasadena, California

CONTENTS

CONTENTS

LIST OF FIGURES

LIST OF FIGURES

LIST OF FIGURES

LIST OF FIGURES

LIST OF FIGURES

LIST OF FIGURES

LIST OF FIGURES

LIST OF FIGURES

ACKNOWLEDGMENTS

The authors gratefully acknowledge the many helpful discussions with Mr. M. J. Spiegel from JPL. They acknowledge also the assistance given by Mr. D. A. Rogers, Miss B. Maguire, Messrs. R. Ensley, M. Stelman and E. Strybuc in performing the experiments, Dr. R. Breene and Mrs. M. Kaegi in the calculation of theoretical radiative properties, Messrs. H. Sadjian and B. Bellinger in the spectroscopic work, and Miss E. Miller in the analytical calculations.

1. INTRODUCTION

1.1 Statement of Problem

A vehicle entering a planetary atmosphere will be subject to severe aerothermodynamic conditions similar to those encountered during re-entry into the Earth's atmosphere. A great deal has been learned about Earth re-entry during the past decade so that much of the background knowledge required for the investigation of the near planet entry problem now exists. However, certain characteristics of planetary entry are new. The general purpose of this study was to explore these characteristics.

The current interest is in the flight into the atmosphere of Venus by a zero lift ballistic vehicle experiencing a relatively "soft" entry trajectory; that is, the vehicle will decelerate to subsonic velocities at fairly high altitudes and traverse a large portion of the atmosphere at terminal velocities (with or without the aid of additional retardation systems). Such a flight path would be attractive for the conduction of atmospheric property experiments - with transmission of data directly to the Earth or relayed to the Earth through a parent vehicle in the planet's near space, and for soft landings to allow the conduction of surface experiments. The primary concern, however, is not with the terminal function of such a vehicle but rather with the early entry phase in which the surface heat transfer establishes perhaps the most important design requirement - the weight of the

heat protection system. For example, if the heat protection system - probably a large percentage of the mass of the vehicle - is overdesigned, unnecessary and perhaps impractical restrictions will be placed on the size of the payload. Within the context of soft entry, which suggests a high drag or blunt vehicle shape, the study of a hemispherical stagnation region is reasonable, although future studies should investigate flows away from the stagnation region as well as three-dimensional flows.

Two interesting characteristics of flight into the atmospheres of the near planets from the point of view of surface heat transfer are the initial entry velocity and the composition of the atmosphere. The escape velocities for Mars and Venus are approximately 16,400 ft/sec and 34,200 ft/sec., respectively. A vehicle approaching either directly from space (no planetary orbit phase) will enter the atmosphere at least at its escape velocity; however, for various mission considerations - time of flight, relative position of the planets at entry, signal transmission capability, etc. - it will probably be desirable to enter the Martian atmosphere in the 20,000 to 25,000 ft/sec range and the Cytherean atmosphere in the 35,000 to 45,000 ft/sec range.

In terms of our Earth reference, this is well into the super-orbital or hypervelocity regime (the Earth orbital velocity being about 26,000 ft/sec), a field in which aerothermodynamic research studies have been initiated only in the past few years. A key aspect of this

flight regime is the generally increased importance of radiative heat transfer to the surface from the gas in the heated shock layer surrounding the body compared to its importance in suborbital flight. Perhaps the clearest distinction between flight in the atmosphere of the Earth and flight in the atmospheres of Mars and Venus is the uncertainty of the composition of the near planets' atmospheres. It might be expected that this could lead to a large uncertainty in the surface heat transfer, particularly that due to radiation. In this study it was assumed that the atmospheres of interest are composed largely of a mixture of molecular nitrogen and carbon dioxide with trace amounts of water vapor and other contaminants.

Fig. 1 is an illustration of the problems studied. The stagnation region heat transfer is composed of boundary layer, or convective heating and radiative heating from the shock layer gases. The radiative heat transfer may be broken into two parts - equilibrium and non-equilibrium radiation from the parts of the shock wave and shock layer in which the gas has not had time to distribute its kinetic energy among the various degrees of freedom. At high altitude where the density is low the non-equilibrium radiation will dominate the radiative heat transfer. At lower altitudes however the equilibrium radiation will be the major source of radiant flux.

1.2 Scope of Investigations

The present study was restricted to the investigations of

radiative and convective heat transfer. The problem of how heat protection system responds to entry environment was not considered here.

Measurements were made in a blunt model stagnation region of convective heat transfer and gas radiance using an electrically driven shock tube for generation of the required thermodynamic conditions. These measurements are compared with appropriate theoretical predictions. Also equilibrium and non-equilibrium radiation from the incident shock is measured using both the total radiation cavity gage and a multichannel spectrophotometer. The velocity simulation extended up to 45,000 ft/sec which encloses the envelope of possible entry velocities presently contemplated. This is shown in Fig. 2 which also illustrates the magnitude of the entry problem for the assumed model atmosphere and vehicle given trajectories (1). A large portion of the current study was conducted through simulation of this atmosphere. Stagnation point radiation data were however also obtained in 3% CO_2 - 97% N_2 and 25% CO_2 - 75% N_2 gas mixtures. The spectrometric study was confined to the 25% CO_2 - 75% N_2 gas mixture exclusively.

2. EXPERIMENTAL FACILITY

Shock tubes have been used for many years in experiments for the generation of aerodynamic data in flows of high energy and high stagnation pressure (4) (5) (6). The demand for an experimental facility in the areas of simulation of orbital and superorbital enthalpies and pressures forced further development of its performance. It became obvious that these requirements were beyond the capability of the conventional combustion driven shock tubes. The arc-heated shock tube used for the present experiments was specifically developed for this purpose. Its basic design followed closely the features of the smaller prototype tube (2) in which several investigations were carried and which produced the necessary data used for the prediction of performance of the present facility.

2.1 Design Features

The electrically driven shock tube used in this present study is illustrated in Fig. 2.1. The ability of this tube to provide strong shock waves at relatively high initial pressures is obtained from the high temperature, high pressure, low molecular weight driver gas produced by the rapid discharge of capacitor stored energy axially through a tube of helium. The driver section is shown in Fig. 2.2. The internal dimensions of the driver are 3.5 in. diameter and 4.5 ft. long. In practice, the driver is shortened by the insertion of solid plastic cylinders to the dimensions necessary for obtaining required energy

density. An insulating cylindrical sleeve with 1/4 in. wall thickness fits inside the driver tube. It is used to provide electrical insulation along the arc path, that is, to insure that the arc discharge is contained within the driver gas and that the energy is uniformed distributed axially along the driver. A thin wire is used to initiate the arc discharge. This is located on the axis so that the wall losses remain uniform in the axial direction reducing thereby non-homogenity in the properties of the driver gas.

The electrical circuit for the driver heating system is shown in Fig. 2.3a. The energy for the arc discharge is stored in capacitors, each rated at 5 microfarads and 20,000 volts. Total available stored energy was 304,000 joules.

Fig. 2.3b shows a typical current wave form. It indicates that the circuit is critically damped and that the energy is completely dissipated in about 50 microseconds, and before the diaphragm opens which occurs about 150 microseconds later.

Helium is used as the gas heated in the driver. The diaphragm separating the driver and the driven section of the shock tube is made of stainless steel. It is scribed to a controlled depth (generally 20% - 40% of the thickness) along two diametrical cross lines. The required conditions of a given test run dictate the proper selection of the diaphragm. The diaphragm is found to open cleanly with a negligible loss of material. The driven tube is made of stainless steel. Its

internal diameter is 6 in. and the overall length is 31.5 ft. The model stagnation point is located 2 ft. upstream of the end flange at L/D 59. As indicated in Ref. 2, an extensive research program was necessary before a satisfactory operation of this facility was achieved.

A photograph of the complete test facility including the instrumentation, vacuum pumps, etc., is shown in Fig. 2.4. For safety reasons the driver and the capacitive power supply are located in a room separate from the driven tube.

2.2 Performance

The performance of the tube in air is shown in Fig. 2.5 where the attainable shock velocity is plotted as a function of initial pressure and energy input and driver length. The experimental data indicate that shock velocity up to 32,000 ft/sec can be obtained with 1 mm Hg driven tube initial pressure, 18 in. long driver and full energy in the capacitors. With a lower initial pressure, shock velocity up to 36,000 ft/sec can be reached. Superimposed is a curve depicting the performance of a combustion driver facility. The limitation of the latter is self-evident.

Outside the capability of the shock tube to produce high stagnation enthalpy flows another important parameter is the test time which is defined as the time difference between the arrivals of the incident shock wave and the driven gas - driver gas contact zone. In Fig. 2.6 the test times produced in this facility are shown as a function of shock velocity and the initial driven tube pressures. It indicates that ample test time was available during the present study.

3. SHOCK TUBE FLOW PARAMETERS

One of the tools required for a study of this type is a complete set of thermochemical equilibrium calculation for gas mixture to be studied. Such calculation has been previously reported (7) for the 9% CO_2 - 90% N_2 - 1% A and 25% - 74% N_2 - 1% A gas mixtures. However, since the present study called for enthalpy simulation equivalent to flight velocity in excess of 40,000 ft/sec these calculations were extended up to temperatures of 17,000°K. Also a complete set of equilibrium thermodynamic properties for 3% CO_2 - 97% N_2 gas was generated. A Mollier chart for the 9% CO_2 - 91% N_2 is shown in Fig. 3.1. Using these state properties, various gas dynamic properties associated with traveling and stationary shock fronts were calculated and charted as functions of shock velocity and the driven tube initial pressures.

For convenience of subsequent computations the tabulated values of the equilibrium thermodynamic properties were plotted in a form giving non-dimensional enthalpy $\frac{hM_o}{RT_o}$ where $\frac{RT_o}{M_o}$ = 18.74 cal/g as a function of pressure p in atmospheres. Included in these plots are lines of constant temperature T in °K and constant density ratio ρ/ρ_c, where $\rho_c = 1.293 \times 10^{-3}$ g/cm^3. In Figs. 3.2, 3.4 and 3.6 the keys to the thermodynamic charts are shown. The equilibrium thermodynamic properties of the three gas mixtures considered here appear as follows:

3% CO_2 - 97% N_2	Fig. 3.3
9% CO_2 - 90% N_2 - 1% A	Fig. 3.5
25% CO_2 - 74% N_2 - 1% A	Fig. 3.7

The solution of the Rankine-Hugoniot shock relations was performed employing semi-graphical methods. All calculations were made for four initial driven tube pressures of P_1 = 0.1, 1, 5 and 25 mm of Hg. The initial driven tube temperature, T_1, was taken to be 294°K. The range of shock velocities, U_s, between 10,000 ft/sec and 40,000 ft/sec was covered.

3.1 Incident Shock

The state of the gas on both sides of a normal shock is related by three basic equations corresponding to the physical principles of the conservation of mass, momentum and energy. These are:

$$u_2 = u_s \left(1 - \frac{\rho_1}{\rho_2}\right)$$

$$P_2 - P_1 = \rho_1 u_s^2 \left(1 - \frac{\rho_1}{\rho_2}\right)$$

$$h_2 - h_1 = \frac{1}{2} u_s^2 \left[1 - \left(\frac{\rho_1}{\rho_2}\right)^2\right]$$

where h = enthalpy
p = pressure
u = velocity
ρ = density

and subscripts 1 and 2 refer to regions ahead and behind the incident shock respectively. The simultaneous solution of these equations

together with the help of the equilibrium state charts produces results which are plotted in Figures 3.8, 3.11, 3.14, 3.17 and 3.20 for the 3% CO_2 mixture, Figures 3.21, 3.24, 3.27, 3.29 and 3.32 for the 9% CO_2 mixture and in Figures 3.33, 3.36, 3.39, 3.42 and 3.45 for the 25% CO_2 mixture.

3.2 Stationary Normal Shock (Laboratory Coordinates)

After the passing of the incident shock the model finds itself in a supersonic quasi-steady flow with the properties of region 2 ahead of the model bow shock wave. The flow close to the axis of symmetry is decelerated to subsonic velocity. The state of the gas along the stagnation streamline on both sides of the bow shock is governed by the same three conservation laws.

$$\rho_2 u_2 = \rho_3 u_3$$

$$P_3 - P_2 = \rho_2 u_2^2 \left(1 - \frac{\rho_2}{\rho_3}\right)$$

$$h_3 - h_2 = \frac{1}{2} u_s^2 \left[1 - \left(\frac{\rho_2}{\rho_3}\right)^2\right]$$

where subscript 3 refers to the region behind the bow shock. The calculation produced the results which are presented in Figures 3.9, 3.12, 3.15 and 3.18 for the 3% CO_2 gas mixture. Figures 3.22, 3.25 and 3.35 for the 9% CO_2 mixture and in Figures 3.34, 3.37, 3.40 and 3.43 for the 25% CO_2 mixture.

3.3 Stagnation Region

The flow along the stagnation streamline in region 3 is decelerated to a stop at the body. The stagnation conditions are found as follows: The enthalpy is given directly by $h_s = h_3 + 1/2\ U_3^2$. The stagnation pressure is computed approximately by assuming incompressible flow $P_s = P_3 + 1/2\ \rho_3\ U_3^2$. Both the stagnation temperature and the corresponding density are read off directly from the thermodynamic state charts and plotted in Figures 3.10, 3.13, 3.16 and 3.19 for 3% CO_2 mixture, in Figures 3.23, 3.26, 3.28 and 3.31 for the 9% CO_2 gas and in Figures 3.35, 3.38, 3.41 and 3.44 for the 25% CO_2 gas mixture.

3.4 Gas Composition Behind Incident Shock

Using the equilibrium temperature and density obtained in Section 3.1, the composition of the gas was calculated for the initial shock tube pressure of 1 mm as a function of shock velocity. The results for 9% CO_2 and 25% CO_2 gas mixtures are shown in Figures 3.46 and 3.47 respectively.

3.5 Composition of Stagnation Region Gas

The equilibrium concentration of the various species appearing in the dissociated and ionized gas when heated to the enthalpy level corresponding to the stagnation point had also been obtained and plotted as a function of shock velocity. The 9% CO_2 gas mixture at shock tube initial pressure P_1 = 1.0 mm was only considered and shown in Fig.

3.48. Compositions for 9% CO_2 - 90% N_2 - 1% A and 25% CO_2 - 74% N_2 - 1% A and at initial shock tube pressure of 1 mm and 5 mm Hg were reported in reference 8.

4. EXPERIMENTAL PROCEDURE AND INSTRUMENTATION

During the present experimental study special precautions were taken to ensure that the contamination of the test gas was at the minimum. A thorough cleaning of the tube with acetone and dry, clean rags preceded 2-3 hrs. pumping period prior to each test. The tube was normally evacuated down to approximately 8 μ and kept at that pressure to promote outgassing of the walls. A leak check taken at that pressure indicated normally a rate of 0-0.8 μ per minute. The tube was then filled with the test gas to the pressure level required for the experiment. Premixed gas mixtures were purchased from the Matheson Co. The analysis of the gas provided by the supplier indicated nominal composition variation of $\pm$0.2 percentage point of CO_2 with the balance being N_2. Colman grade CO_2 and prepurified grade N_2 with 99.99% and 99.996 minimum purity respectively (as advertised by Matheson) were used to obtain the mixtures. In order to further reduce the contaminants due to outgassing of the shock tube walls a through-flow system was provided. This allowed a continuous scavanging of the tube at test pressure level for approximately 30 minutes prior to the actual run. The test gas was introduced through a cold trap of dry ice and acetone at the diaphragm end of the tube while a mechanical vacuum pump at the model end produced the through flow. With the cold trap temperature of -78°C the moisture present in the test gas was reduced down to 0.005%. Several samples were withdrawn from the tube and analyzed on mass spectrometer. The results agreed closely within

the specified tolerance with the mixture nominal composition. Oxygen was found to be the major contaminant. Measurements of the water vapor content could not be obtained because of the tendency of water to be absorbed on walls of the sampling device and the spectrometer itself. An estimate however was made by analyzing the intensity of H_β line in the stagnation region time resolved spectrum. Assuming that all hydrogen came from the dissociation of water present in the test gas one calculates the concentrations of water vapor to be approximately 0.001%.

4.1 Shock Tube Performance

A schematic diagram showing the standard shock tube instrumentation which is used during all experimental runs is presented in Fig. 4.1. The shock speed is obtained by observing the luminous profile of the shock wave with collimated photomultipliers as it passes five stations ahead of the test section at which the model is located. The signals from each photosensor are differentiated and displayed on a raster trace. The arrival of the shock front at each station can be read with an accuracy of about ± 0.5 μsec which, for example, at 30,000 ft/sec gives shock speed with an accuracy of better than 2%. Pressure gages located at two stations were also used as a check of shock speed obtained from the passage of the luminous shock front. Typical shock speed data is shown in Fig. 4.2

In order to insure that the reflected expansion wave from the driver does not interfere with the test gas flow when using the shortened

length driver, pressure history behind the incident shock is monitored. The pressure data is also useful for verification of equilibrium thermodynamic state behind the incident shock wave.

In addition to the data necessary for the evaluation of shock speed and pressure, photometric and photographic methods are employed to obtain further information about the quality of the incident shock wave generated flow. The emitted light from the shock heated gas behind the incident wave is observed. Fig. 4.3 shows oscilloscope traces obtained with a multichannel monochromator. Note the fairly narrow bandpass of each channel. From that the quality and duration of the steady flow at a given station is determined. Also using a two-color photometer with its entrance slit focused on the shock layer ahead of the stagnation point of the hemispherical model it is possible to determine; 1) when the flow around the model is fully established and how steady the test flow is. 2) when the mixing zone between the test gas and the driver gas arrives at the model. Oscilloscope traces of the signal from the two-color photometer are shown in Fig. 4.4a. The upper trace corresponds to the blue channel. The bottom trace is from the red channel. It is interesting to note the blue signal shows in general an increase of intensity upon arrival of the mixed gas while the red channel always indicates a drop in radiation at its response wavelengths. An image converter camera was also used to assess the quality of flow by showing the shape of the incident shock wave and the symmetry of the model flow. This is

illustrated in Fig. 4.4b where a photograph obtained with .050 μ sec exposure and containing three frames, each taken 10 μ sec apart, is shown.

Traces of the discharge current and voltage in the driver are taken during each run in order to evaluate the operation of the driver. It is felt that in order to assure reliability of the data a thorough diagnostic investigation of the test flow quality must be carried simultaneously with the performance of the experiment.

4.2 Convective Heat Transfer

The determination of convective heat transfer rates in the hypervelocity flight regime has been a controversial subject because of a disagreement between data obtained in the Space Sciences Laboratory and those of several other investigators. For this reason, some care was given to the investigation of measurement techniques for convective heat transfer in the blunt model test configuration. Two different types of heat transfer gages were used. One was the calorimeter or thick film gage and the other the thin film gage. Since we have found that material properties appreciably affect the apparent heat transfer response of the calorimeter gage, several materials were investigated. The thin film gage was also used, since as a basically different means for the measurement of surface heat transfer, it offered a capability for discrimination between the results of the different materials obtained with the calorimeter gage.

Photographs of the types of convective heat transfer gages used in the present study are shown in Fig. 4.5. The two-calorimeter-gage model was used to obtain simultaneous data with gages of different materials or of different geometries. All models had 0.5 in. nose radius. Because of the high heating rates and short test times associated with hypervelocity flight simulation in the shock tube, the use of gage response in which the heat is assumed to be distributed uniformly through the gage will be in error. Time dependent temperature distributions

and corrections for this effect have been calculated for two types of gage materials - platinum and Hytemco (a nickel-iron alloy)- with different gage element thicknesses. The correction curves are shown in Fig. 4.6. Note that the thick Hytemco material has a relatively large correction; this is caused by the fact that the heat is conducted slowly into this material in comparison with the platinum material as shown in Fig. 4.7. Thus, the temperature gradients are relatively steep. Corrections for thinner gages are small; however, a thin gage will lose heat to its backing material early in the test time. Therefore, we have concluded that for the types of tests described in here a 0.002 in. thickness is most appropriate for a platinum gage. In an attempt to check the scaling law of the convective heat transfer several runs were made with a 3 in. model having 2 in. nose radius as shown in Fig. 4.8. Difficulty was experienced however with establishing steady flow around it and no readable data could be obtained.

The heat transfer gages were mounted at the stagnation point of the hemispherical model. The design dimensions of the gages were 1/16 in. wide by 1/4 in. long as illustrated in Fig. 4.9a, also the mounting in the epoxy base is indicated in the same figure. Metal and phenolic nylon models were used in order to determine whether any electrical effects due to conductance of the model could be affecting the gage response. No difference was observed. In the initial stages of the present study signal from the gages was found to have several undesirable characteristics.

A strong negative potential with respect to ground was observed prior to the arrival of the incident shock wave at the model. Also a fair amount of noise was superimposed on the thermal signal once the flow around the model was established. Several schemes were tried. As the first step, each side of the gage was connected through a 10 Ω resistance to ground as shown in Fig. 4.9b. This succeeded to eliminate the strong negative going precursor which affected the gage prior to the shock arrival. However, as soon as the flow was established, quite a strong current, approximately 1A, was observed to flow from the plasma in the shock layer to ground. Presence of such current could produce additional potential drop across the gage which could not be distinguished from the thermal signal. Therefore, this scheme was abandoned and it was decided that the gage must be left floating. In this case the potential of the gage rapidly changes polarity at the moment of shock arrival as shown in Fig. 4.10a. The associated potential jump of several volts was observed. No current between the gage and the ground flows with the gage connected through 1 M Ω resistance to ground, but a very careful balancing of the differential preamplifier is necessary to minimize the effects of the transient potential change on the thermal signal of the gage as shown in Fig. 4.10b. In addition proper shielding of the leads and a perfect circuit symmetry are required for protection against disturbances caused by electromagnetic coupling. With all these precautions applied, a completely clean signal from the

calorimeter gage was obtained.

The output of the heat transfer gage was displayed and photographed in parallel on at least three oscilloscopes which were set at different sweep rates. Cross checks of the signals were made frequently. The signal from the 5 μsec/cm sweep scope was used for the determination of the heat transfer rate.

The data reduction involved reading off the slope of the voltage vs. time signal and applying the simple expression relating the change of voltage across the gage with time.

$$\dot{q} = K \frac{1}{E_o} \frac{dE}{dt}$$

where

$$K = \frac{\rho C L}{\alpha}$$

ρ - density of gage material
C - specific heat of gage material
L - gage thickness
α - temperature coefficient of resistivity
E_o - initial voltage across gage

Since the bulk properties of the gage material are well known, the coefficient K can be easily calculated and the gage response established without an extensive calibration procedure. The temperature coefficient of resistivity, α, has been checked experimentally for the particular batch of material used in fabrication of the gages.

The Hytemco material was used to obtain the measurements reported in Ref. 2. Since other investigators (9) (10) have reported measurements taken with platinum gages that are in significant disagree-

ment with those of Ref. 2, the validity of the measuring techniques employed was investigated. Fig. 4.11 shows traces taken during a high velocity run using both the platinum and Hytemco gages in the two gage model described earlier with gage currents equal to zero. It has been reported by Rose and Stankevics (9) that a spurious zero gage current signal was observed when gages of thicknesses corresponding to the present Hytemco gage thicknesses were used. Fig. 4.11 indicates that this effect is absent from the data presented here. However, there is significantly more signal noise generated during the establishment of the test flow for the Hytemco gage. The second gage evaluation test was the measurement of convective heat transfer (finite gage current), again using the two gage model. Results of this type are shown in Fig. 4.12. Again one sees the more pronounced signal noise associated with the Hytemco material. However, a significant period of test time exists during which accurate slope measurements of the Hytemco signal can be made. The platinum signal is quite clean throughout a large portion of the test time.

The reduced heat transfer data for the two gage materials just discussed were found to be in significant disagreement, the Hytemco material usually indicating apparent heat transfer rates considerably higher than that obtained with platinum (see Fig. 4.14). Also, more data scatter is found with the Hytemco gages. Since it was not apparent which material gave the correct signal, or indeed, if either material

did so, we investigated other approaches to the measurement of stagnation point heating. First, to determine if the alloying process in the Hytemco was causing a discrepancy, nickel thick film gages were constructed and run. These data tended to agree with the Hytemco results, thus suggesting that the properties of nickel itself were causing the difference between the gage responses. Second, the thin film technique was used to provide an essentially different means for measuring the stagnation point heat transfer. A photograph of a sputtered platinum thin film gage and model is shown in Fig. 4.5b and the response of such a gage is shown in Fig. 4.13. The reduced heat transfer rates, corrected for surface material temperature change are shown in Fig. 4.14 along with the observed platinum, Hytemco, nickel and gold calorimeter gage data. Data for air as well as for the 9% CO_2 - 91% N_2 and 25% CO_2 - 75% N_2 mixtures are shown. From this figure, it is seen that the platinum thin film results are at the general level of the platinum calorimeter heat transfer data. It is interesting to note that both types of gages have the same surface material. Seiff (11) has presented a few convective air data at a flight velocity simulation level of about 56,000 ft/sec taken from the observation of the time required to initiate melting of free flying aluminum models. Since this is another method for measuring stagnation point convective heat transfer rates, Seiff's reported results are plotted in Fig. 4.14. They appear to follow the level of the platinum calorimeter gage

measurements. Measurements of other investigators using calorimeter gages in a shock tube are not given since they generally agree with the present data using the same technique. Additional data obtained with gold gages were found to indicate much higher heating rates than those obtained with platinum gages and generally in agreement with nickel gage values. Also, we have conducted a few tests with silicon oxide coated nickel gages. While there is not yet sufficient information to construct a complete story, we have found that the apparent heat transfer rate for these tests has a tendency to agree with the low level of our platinum data. It is clear that some effect other than internal electric phenomena, of which we originally suspected the nickel and Hytemco, produces the difference in heat transfer readings. Therefore, we have tentatively concluded that the other investigators of hypervelocity convective heat transfer have used measurement techniques in which the surfaces can now be suspected of having low effective catalytic activity. For example, concerning the melting aluminum model results (11), Hartunian (12) has stated that aluminum is one of the best non-catalytic materials of which he is aware. Also, Hartunian (13), on the basis of measurements in a discharge tube with oxygen and nitrogen atoms, and Myerson (14), using qualitative arguments, have both stated that platinum is largely non-catalytic to atom recombination unless exceptionally clean.

The uncertainty range of convective heat transfer results has been estimated to be ± 12%.

4.3 Total Radiation Study

In the course of the present shock tube investigations of the total radiative properties of high temperature gas mixtures two experimental configurations of the cavity gage(15), whose principle of operation is described in section 5, were employed. In the first configuration the measurements were made of radiation emitted from the gas flow behind the incident shock wave. The schematic arrangement of the gage is shown in Fig. 4.15. Only the equilibrium radiation was measured. The gage was located at a distance from the collimating slit and therefore was viewing a narrow layer of the gas across the shock tube. Fig. 4.16 shows the gage holder and the gage. A fused silica quartz window was separating the gage from the flow. In reducing the data 90% transmission was assumed over the whole wavelength range. Also the effect of off-axis radiation and variable distance from the gage was accounted for by integrating the solid angle over the whole contributing volume and finding an average value corresponding to the volume extended by the entrance slit area.

The temperatures and densities of the test gas in the region behind the incident shock are limited by the strength of the shock which can be generated at a given initial pressure with the available energy in the shock tube driver. In order to obtain experimental radiation data from gas at temperatures in the range of 12,000 to 16,000°K and at a relatively high density the investigations were customarily carried out

in the reflected shock region of the shock tube. This method, however, holds several disadvantages which can be avoided if the gas in the stagnation region of a hemispherical model located in the flow generated by the incident shock wave is used as the source of the radiating gas. It was therefore decided to employ this test configuration as shown in Fig. 4.17 for the present study of the high temperature gas emission.

From previous investigations of stagnation point convective heat transfer and studies of shock tube flows it is known that the flow establishes itself rather quickly after the passage of the incident shock wave and remains relatively steady for a sufficiently long time to permit the measurement of the radiant emission from the shock layer gas. Since the flow is steady in the laboratory coordinates the requirements on time response of the instrumentation employed in the measurements is less severe. This configuration is restricted to configurations of equilibrium radiative properties only. This is so because the free stream flow entering the bow shock, which forms ahead of the model, is already in a state of high thermochemical excitation being earlier processed by the passage of the incident shock wave, as compared to the free stream conditions a vehicle will experience in a flight through an atmosphere.

A phenolic nylon hemispherical model with a nose radius R_n = 1.0 in. shown in Fig. 4.17 was used for most of the model experiments. Since the magnitude of the signal from the gage is directly proportional

to stand-off distance of the bow shock a larger model with R_n = 2 in. and 3 in. diameter cylindrical after body was tried for several runs. No satisfactory data were obtained mainly due to the difficulty with the establishing of uniform flow around the model as indicated by large fluctuations of the red and blue channel photometer signals. The R_n = 1.0 in. model did not experience this unsteadiness, and the test flow was found to be considerably uniform. The arrangement of the cavity gage itself inside the model is shown in Fig. 4.18. A rectangular shape sapphire window 0.1 in. by 0.5 in. was used at the stagnation point of the model. The gage itself was located away from the window with the entrance slits parallel to the window aperture. Thus, the gage senses only radiation from a region of the shock layer close to the axis of the model. For the test condition range of interest here, the stagnation region has almost uniform temperature and is essentially transparent. For instance, at U_s = 28,000 ft/sec and P_1 = 1.0 mm the temperature in the 9% CO_2 - 91% N_2 gas mixture behind the bow shock is T_3 = 13800°K while the stagnation temperature is T_s = 13920°K. Also the theoretically predicted radiative flux at the same conditions is approximately 1.2×10^{-4} $\frac{\text{watts}}{\text{cm}^2}$ which is about 5% of the black body total radiance. Before the reading obtained from the cavity gage can be interpreted in terms of radiative power emitted by the stagnation region gas one must know the radiating volume and steradiancy of the emitters. The radiating volume is defined by the field of view of the gage entrance slit and the model

window aperture on one side of the normal distance between the model surface and the bow shock wave. The stand-off distance was measured by two techniques. Entrance slits of two two-color photometers were focused on the axis of the model ahead of the stagnation point at a distance encompassing the expected location of the bow shock. The character of the signal from these instruments indicated whether the predicted location was correct. A more accurate measurement was made using STL image converter camera. A photograph obtained by this means is shown in Fig. 4.19. The instants at which the three frames were obtained are indicated on the monitor trace. The upper frame is taken just prior to the incident shock arrival. The center frame corresponds to the test gas flows while the bottom one shows the flow of the mixing zone between the test gas and driver gas.

In the reduction of our cavity gage data the theoretical predictions were used for establishing the radiating volume depth. An effective solid angle corresponding to a parallelpiped defined by the window aperture area and the stand-off distance was computed by performing integration over the total volume seen by the gage entrance slit.

The uncertainty of the gas radiance obtained by means of the total radiation cavity gage has been estimated by considering the uncertainties which enter into the primary measurements of the gage output and also ones which appear in the reduction of the gage signal. The range of uncertainty was found to lie between +17% and -22%.

4.4 Incident Shock Spectrometric Study

The measurement of spectral intensity of equilibrium and non-equilibrium radiation was made behind the incident shock with the use of a calibrated JACo f/6.3 spectrograph specially modified to accept an array of photo detectors in its exit focal plane. The investigation extended from ultraviolet to near infrared regions of the spectrum and covered wavelength interval between 2400 Å - 7000 Å. The experiments were carried out in the electrically-driven shock tube described in an earlier section of this report. The test gas preparation in the driven tube followed the same procedure as in the case of total radiation cavity gage studies. All runs were made in the simulated planetary atmosphere with a nominal composition of 25% O_2 - 75% N_2. The energy supplied to the shock tube driver was selected to give a shock velocity of 28,400 ft/sec in the driven tube gas at a pressure of 0.5 mm Hg. No attempts were made to identify individual radiating species contributing to the total radiation as sensed by the photo detectors and to analyze the thermo-chemical processes which take place behind the incident shock wave as the gas relaxes to the equilibrium state.

Experimental Equipment

Fig. 4.20 shows the general arrangement of the shock tube, the spectrophotometer and the optical system associated with the incident shock radiation study. The entrance slit of the spectrophotometer was imaged at the center of the shock tube by means of a 10 cm focal length

quartz achromatic lens with the entrance slit of the instrument perpendicular to the axis of the tube. Using a suitable stop and a 0.050μ wide and 3 mm high entrance slit an optical resolution of 0.2μsec was achieved. The measurements were made at a station located at a distance of L/D = 51.5 from the diaphragm end of the tube through a flat, fused quartz window, 1.78 cm thick, mounted in the sidewall of the tube. A light trap in the form of a blackened cylindrical cavity was placed directly opposite the observation window in order to eliminate the effects of internal reflections inside the shock tube. The dimensions of the light trap were chosen so that the solid angle substended by the spectrophotometer was lying fully within the bound of the cavity opening.

To measure spectral radiance Jarrell-Ash Co. f/6.3 plane grating spectrograph with a dispersion of approximately 40 Å/mm was equipped with six photomultipliers mounted in the exit slit plane. Because of the size of the individual detectors an arrangement as shown in Fig. 4.20 was necessary in order that the radiation in adjacent spectral intervals could be measured simultaneously. A fibre optics package, with each bundle entrance aperture of 5 mm high and 5 mm wide, giving 200 Å of spectral coverage or a total of 1000 Å for the five channels, was used at wavelengths above 4000 Å. Five 1P28 photomultipliers were located at the other end of the fibre bundles. For the ultraviolet region of the spectrum a quartz lens reimaged a 255 Å wide section of the spectrum from the focal plane of the spectrophotometer

directly on the photocathode of a 1P28 photomultiplier. All six photomultipliers were operated at -700V with 220Ω load resistors. Proper capacitance was inserted across the last 4 dynods in the voltage divider circuit of each photomultiplier. The output from the photomultipliers was fed into the Type L plug-in preamplifiers and the signal was recorded as a function of time by means of Tektronix Type 535 oscilloscopes and Polaroid film cameras. In certain ranges of operation additional amplification of the photomultiplier signal was necessary. Tektronix Type 127 unit, with a gain of 20 was employed to amplify the signal before it was fed into the Type L preamplifier. The time constant of the complete electrical circuit used in the read-out was estimated to be less than 0.075 μsec.

Calibration

The calibration of the complete optical system was made for each run. As a source of radiant energy both the standard tungsten ribbon lamp and a carbon arc were employed.

A G.E. tungsten ribbon lamp was calibrated by the Bureau of Standards and its brightness temperature was given for two current settings, 28 amps and 30 amps. An optical pyrometer manufactured by Leeds and Northrop and calibrated against a black body was used to obtain the tungsten ribbon brightness temperatures at other current settings. Frequent checks were made of the brightness temperature corresponding to 28 and 30 amperes current against the calibration data

supplied by the NBS for this lamp. The temperature deviation was found not to be larger than 6^{o} which corresponds to a maximum uncertainty in the value of absolute intensity measurements of approximately 3%. The true temperature of the ribbon was obtained using radiant properties of tungsten tabulated in the American Institute of Physics Handbook (16). The spectral distribution of emissivity of tungsten was taken from the data given by DeVos (17)in calculations of lamp intensity. During the calibration a 20 c/s light chopper was placed in front of the entrance slit of the spectrophotometer in order to permit the use of a.c. mode of amplifiers.

The calibration of the spectrophotometer at wavelengths below 3200 $\mathring{A}$ was made with the use of a pyrometric carbon arc. The arc was operated with 90^{o} electrode orientation. The positive electrode was formed by a 1/4" diameter National Carbon AGKSP grade graphite rod. The center of the positive crater was imaged on the entrance slit of the spectrophotometer and the current carefully adjusted in order for it to be just below the overload value when the calibration was made. Care was taken to assure that the entrance slit was filled fully by the center section of the positive crater. The arc was assumed to emit as a grey body at a true temperature of 3800°K with an emissivity of 0.97 (18). A check of calibration at a wavelength at which the ribbon filament tungsten lamp could also be used showed good agreement between the two methods.

Data Reduction

The calibration of the optical system was accomplished as described above by means of a localized radiation source placed at a distance from entrance slit of the spectrophotometer equal to the distance between the center of the shock tube and the entrance slit. The spectral radiance of such a radiation source is given in watts per cm^2 - steradian-micron of spectrum length. However the gas radiation which reaches the photomultipliers comes from points located along the depth of the radiating gas equal to the diameter of the shock tube. It is therefore necessary to evaluate the relation between the calibration signal and the total energy measured by the photodetectors from the radiating volume of the gas. An assumption is made that the gas in the shock tube has uniform radiative properties. Three limiting cases will be illustrated. In the first case we consider the distribution of radiators in the plane lying along the axis of the shock tube and normal to the optical axis of the system. Since this plane is focused directly onto the plane containing the entrance slit of the spectrophotometer radiation from point radiators lying outside the image area of the slit will not contribute to the signal observed by the photodetectors. As shown schematically in Fig. 4.21a the point radiator located at 0 will have its image in plane A'. Solid angle extended by point 0 is

$$\Omega_A = \frac{\pi D^2}{4a^2}$$

Points located off-axis in plane A will have their images in plane A' at a distance

$$z' = z \frac{a'}{a}$$

from the optical axis. The limiting point K has its image at K' which coincides with the edge of the entrance slit of the spectrophotometer. Any point with $z > \overline{OK}$ will lie outside the entrance slit and therefore will not contribute to the measured radiation. The solid angle extended by the limit point K is

$$\Omega = \frac{\pi D^2}{4a^2} \cos\varphi$$

Now in the present geometrical arrangement with the slit dimensions .005 cm wide and 0.3 cm high, $\tan\varphi < 10^{-2}$ and therefore the change of solid angle for points off-axis is negligible. We take

$$\Omega = 4.255 \times 10^{-4} \text{ str.}$$

as the solid angle extended for all point radiators lying in plane A and whose radiation is intercepted by the entrance slit. The radiating volume of thickness Δx located in plane A contributing the measured radiation is

$$V_A = sh \left(\frac{a}{a'}\right)^2 \Delta\lambda$$

Where h is the height of the slit and s is its width. Hence the total energy entering the slit from this volume is

$$E_\lambda = \bar{I} V_A \Omega_\lambda$$

$$E_A = I \frac{\pi D^2}{4} \frac{hs}{a'^2} \Delta x$$

Where I is the intensity in watts per cm^3-str-micron.

The second case will consider point radiators located at x between the center plane A and the far wall of the shock tube, plane B. The image of all such points will be formed ahead of the entrance slit at a distance x' determined from the lens formula. As shown in Fig. 4.21b the entrance slit acts as an exit pupil for the optical system limiting the solid angle within which the individual radiating points contribute to the measured radiation. All points lying between L and M subtend a solid angle

$$\Omega_x = \frac{x'}{a'-x'} \frac{s\bar{h}}{x^2}$$

where $\bar{h}$ is an effective height given by

$$\bar{h} = \frac{\pi D}{4}$$

The location of point L is found by following simple geometrical relations

$$Z_L = \left(\frac{a'-x'}{a'} \frac{D}{2} - \frac{x'}{a'} \frac{S}{2} \right) \frac{x}{x'}$$

at $Z > Z_L$ the solid angle decreases rapidly and becomes zero at the limit point, beyond which no radiation enters the slit. This point is located at

$$Z_{max} = \left(\frac{a'-x'}{a'} \frac{D}{2} + \frac{x'}{a'} \frac{S}{2} \right) \frac{x}{x'}$$

The effective width of the radiating volume is therefore

$$W = Z_L + Z_{max}$$
$$= \frac{x(a-x)}{xa} D$$

Similarly the height H is found

$$H = h \frac{x}{a'}$$

Hence the contributing volume is

$$V_x = \frac{x^2}{a'^2} \frac{(a'-x')}{x'} D h \Delta x$$

The energy entering the slit is therefore

$$E_x = I \frac{\pi D^2}{4} \frac{hs}{a'^2} \Delta x \qquad x_A < x < x_B$$

which is exactly the same as that radiant energy contributed by the layer along the shock tube axis. As the third case we consider contributions from gas layers between the center of tube A and the near wall C. The geometry of light rays is shown in Fig. 4.21c. Here again we observe that the entrance slit limits the solid angle extended by the gas radiators. Following similar derivation as in the previous case we arrive at the same expression for the contributing energy

$$E_x = I \frac{\pi D^2}{4} \frac{hs}{a'^2} \Delta x \qquad x_A < x < x_C$$

which again indicates that the action of the exit pupil is compensated by the increased cross-section of the volume of the radiating gas seen by the entrance slit.

The measured radiant energy in the course of this experiment was reduced to intensity by dividing it by the depth of radiating gas equal to the diameter of the tube. Typical data obtained from the spectrophotometer is shown in Fig. 1.22. The beginning of sweeps of the two beams has been shifted in order to prevent an overlap of the radiation overshoots. The traces were enlarged and the time for the overshoot to reach the maximum value was measured. Also the total length of the non-equilibrium region was determined. In integrating the area under the overshoot it was assumed that the radiation grows linearly up to the peak and then follows an exponential decay to the equilibrium level.

The overall uncertainty in the final results of the intensity measured by means of the spectrophotometer was estimated to be ± 15%. The wavelength scale was calibrated with a mercury lamp and the accuracy of setting was estimated to be ± 10Å.

5. TOTAL RADIATION CAVITY GAGE

The measurement of total radiative heat transfer from a high temperature gas volume to the enclosing envelope has always been a difficult problem especially when the duration of the emitting sample is of the order of microseconds. One logical choice of a measuring device would be a resistance thermometer type gage. Such gages have been widely used for convective heat transfer determination in shock tubes and tunnels (19, 20). A thin film resistance gage (preferred due to its fast response) in its normal form will absorb one part of the incident radiation while the other part will be reflected. In most cases the reflectivity is a function of both the surface conditions, the wavelength of the incident radiation, and the incident angle. In practical applications the surface conditions of the gage cannot be closely controlled and even if suitable calibration of the surface characteristics could be carried out, their variation during the test time cannot be predicted. Since the gage will be in contact with the hot gas, convective heat transfer will be present which is very difficult to separate from the total heating sensed by the gage.

From the theoretical studies of the wavelength region which will contribute to the total emission we find that in the experimental studies described above a spectral region from several hundred Angstrom to several microns must be considered. Due to the high temperatures of the gas the bulk of the emitted radiation will lie in the

UV. An additional effect on the gage response is caused by the highly energetic photons eminating from the test gas and incident on the resistance gage. They will produce photoelectric emission of electrons from the gage surface causing an apparent reduction of its resistance and introducing an error not easily accountable into the interpretation of the gage output signal.

Because of all these difficulties the cavity or black body type geometric shape was chosen for the radiation gage. The present form of this gage is shown schematically in Fig. 5.1a. The gage is made in the form of a cylindrical body with a suitably located entrance slit. This form rather than that of a hollow sphere was chosen due to ease of fabrication. The gage does not enclose the radiating gas but the radiative energy enters the cavity through the slit where it is absorbed by the platinum film in the interior of the gage as it undergoes multiple reflection indicated in Fig. 5.1b. This thin film of platinum also serves as an extremely fast response resistance thermometer. The variations of reflectivity with wavelength of electrodeposited opaque platinum film is shown in Fig. 5.2. Data for this plot are taken from reference (21). A complete gage is shown in Fig. 5.3. Energy loss as a fraction of the incident energy for the geometry of the cavity gage described in this paper was computed and is plotted in Fig. 5.4 as a function of the film reflectivity. Parallel beam and specular reflection were assumed for the calculations. It is notable that not more than 5% of the incident

radiation will escape through the opening without being absorbed if the film reflectivity remains below 70%.

Fast thermal response of the gage is dependent on the film thickness, which should be made small relative to the characteristic thermal diffusion depth of the film material. At the same time the film must be opaque to the incident radiation since its function is to absorb the energy. The transmission of thin sputtered platinum film was therefore investigated. The results indicated that a film of about 0.1 micron thickness transmits less than 2% of the incident light in the wavelength range between 0.4 and 0.6 microns. Its transmission becomes even less for shorter wavelengths.

The total cavity radiation gage used in the present study was separated from the flow by a sapphire window in the stagnation model configuration and by a quartz window when measuring radiant emission from the hot gas behind the incident shock. To prevent the photoelectric effects from obscuring the time gage signal it was found necessary to fill the gage with pure nitrogen and to keep it at 1 atm pressure during the test.

The presence of the nitrogen gas reduced the mean free path of the electrons building up a space charge within a fraction of a microsecond close to the surface of the gage thereby inhibiting further electron emission. Nitrogen gas was chosen because of the high energies required for photo dissociation and photo attachment.

During runs when the gage was evacuated to approximately 5 microns the photoelectric effect was strong enough to make the potential of the gage become negative. Few runs were obtained with a glass window with no evidence of the photoelectric effect indicating the photons with energy corresponding to a wavelength smaller than 3500 $\mathring{A}$ are required to cause the photo emission.

5.1 Theoretical Considerations

The operation of the gage is based on the resistance thermometer principle. The radiant energy which enters the cavity through the entrance slit is incident on the internal surface which is covered with thin platinum film deposited in a sputtering process. The energy is absorbed by the film and dissipated into the quartz backing material. The film therefore does not function directly as a gage for measuring the heat transfer rate but is used to indicate surface temperature of the insulator. Applying the theory for heat conduction in a composite (non-homogenous) body the history of the surface temperature can be related to the heat transfer to the gage (22).

The gage will be approximated by a semi-infinite slab composed of two materials with dissimilar thermal and physical properties as shown in Fig. 5.5. Material 1 extends from $x = 0$ to $x = \ell$ while material 2 extends from $x = \ell$ to $x = \infty$. Let k_1, ρ_1, and C_1 be the thermal conductivity, density and specific heat of material 1 while similar quantities with subscript 2 will describe the properties of

material 2. Now it is assumed that the thickness of the region 1 is extremely small (on the order of 0. 1 micron) as compared with other dimensions. Therefore lateral flow of heat will be correspondingly small and the assumption of one-dimensional heat flow in the direction x is justified. At the same time the insulating material 2 is taken to extend to infinity since basically in the time interval of interest the heat flow q (t) can only affect the temperature in the quartz a small distance away from the interface between regions 1 and 2.

The heat conduction into such a model can be described by the following equations.

In region 1

$$0 \leq x \leq L$$

$$\frac{\partial T}{\partial t} = \frac{k_1}{\rho_1 C_1} \frac{\partial^2 T}{\partial x^2}$$

together with boundary conditions

$$t \leq 0 \qquad T(x) = 0$$

$$t > 0 \qquad k_1 \left(\frac{\partial T_1}{\partial x}\right)_{x=0} = -\dot{q}(t)$$

Similarly in region 2

$$L \leq x \leq \infty$$

$$\frac{\partial T_2}{\partial t} = \frac{k_2}{\rho_2 C_2} \frac{\partial^2 T_2}{\partial x^2}$$

while the boundary conditions are

$$t \leq 0 \qquad T_2(x) = 0$$

$$t > 0 \qquad k_2 \left(\frac{\partial T_2}{\partial x}\right)_{x=L} = k_1 \frac{\partial T_1}{\partial x} \quad x = L$$

$$T_2(x \to \infty) = 0$$

where q (t) is arbitrary heat flux applied to the surface region 1 at x = 0. The solution of this boundary value problem gives expressions for $T_1(x,t)$ and $T_2(x,t)$. These relations were simplified by assuming that the thermal conductivity k_1 of material 1 is much larger than the thermal conductivity k_2 of material 2 and that the time interval of interest is large compared to characteristic time l^2/K_1 where thermal diffusivity $K_1 = k_1/\rho_1 C_1$. This allows us to assume that the measured temperature of the film is its surface temperature (x = 0). We recall here that the thickness of material 1 was taken to be small. If this thickness is sufficiently small the expanded expression for the surface temperature can be truncated obtaining the first order solution where the terms containing higher powers of the thickness have been neglected. The resulting expression for temperature is:

$$T(t) = \frac{1}{\sqrt{\pi k_2 \rho_2 C_2}} \int_0^t \frac{q(\lambda)}{\sqrt{t-\lambda}}\, d\lambda - q(t)\frac{l}{k_1}\left(\frac{k_2\rho_2 C_2}{k_1\rho_1 C_1} - 1\right)$$

In our experiments the temperature history T (t) is measured and the unknown heat transfer rate q (t) is required. The problem is therefore to invert in a close form the expression for T (t) given above and to solve for q (t). The final equation is given:

$$q(t) = \sqrt{\pi k_2 \rho_2 C_2}\left\{\frac{T(t)}{2\sqrt{t}} - \frac{1}{2\pi\sqrt{t}}\int_0^t \frac{\sqrt{\lambda}\,T(t) - \sqrt{t}\,T(\lambda)}{(t-\lambda)^{3/2}}\, d\lambda \right.$$
$$\left. + \frac{l}{2\pi K_1}\left(\frac{k_1\rho_1 C_1}{k_2\rho_2 C_2} - 1\right)\left[\frac{q(t)}{\sqrt{t}} + \frac{1}{2}\int_0^t \frac{q(t) - q(\lambda)}{(t-\lambda)^{3/2}}\, d\lambda\right]\right\}$$

The solution for q (t) depends on the heat transfer rate and therefore an iterative approach is necessary. In the use of this equation the temperature change T (t) is replaced by the film voltage change with a proper coefficient reflecting the dependence of the film resistance on temperature.

The solution of the above stated equation has been programed on the IBM 7090 digital computer. Typical oscilloscope traces of the stagnation point cavity gage signal is shown in Fig. 5.6. The approximately parabolic signal of the cavity gage (upper trace) is typical of the response of a thin film thermometer gage to an approximately constant heating rate. The steadiness and duration of the radiating shock layer, as indicated by the stagnation region vicinity phototube trace (lower trace) is also shown in Fig. 5.6. The corresponding history of the stagnation gas radiance, as obtained by the reduction of the cavity gage voltage signal from the previous Figure is shown in Fig. 5.7.

5.2 Gage Construction

The total radiation gage described here was made by depositing a thin platinum film on the internal surfaces of a hollow cylinder which formed the cavity of the gage. The cylindrical part of the gage, Fig. 5.3, was made up of several (two to four) 0.125 in. high slotted quartz rings whose internal surfaces were fire-polished to a surface finish necessary to obtain a uniform and durable film. The ends of the cylinder were formed by two discs onto which a thin film of platinum was deposited forming a grid and hence the ends were included

into the active surface of the gage. In the assembly the rings and the end sections were electrically insulated from each other except at the terminal points.

The film was deposited by the widely used sputtering technique (23). This process involves gas ions, accelerated by high voltage, which bombard a platinum cathode thus energizing certain of its atoms. The atoms leave the surface of the cathode in the form of a vapor and condense on nearby surfaces.

If the current is maintained at a predetermined level, the thickness of the film, and the film consistency can be controlled by the duration of sputtering. To establish exactly the thickness of the film (in this case 0.1 micron) test plugs made of polished quartz were exposed to the coating process in parallel with the cavity gage sections. The film thickness was then measured by means of an interference microscope.

The film strips deposited on the rings and the end discs were connected into a series electrical circuit. The contact between the sections were formed using platinum coloidal solution and curing it at appropriate temperatures. The external leads were soft soldered to the terminal points of the circuit.

The thin film gage is operated in an essentially constant current type circuit as shown in Fig. 5.8. Each gage lead is connected through a 1500 ohm resistor to the power supply output which is

approximately plus and minus 150 volts (300 volts total) either side of ground. The voltages are adjusted to give approximately 500 milliamperes of gage current while leaving the average gage voltage at nearly ground potential. The gage leads are connected to the inputs of a differential amplifier in order to reject as completely as possible any noise and hum pickup in the gage circuit. A Tektronix Type "D" plug-in preamplifier is normally used in a Type 127 power supply ahead of the oscilloscope in order to achieve sufficient trace deflection while preserving microsecond or better rise time. With reasonable care in balancing the preamp, the residual noise on the scope trace can be reduced to less than 20 microvolts over about a megacycle bandwidth. The cleanness of the signal is evident in traces shown in Fig. 5.6.

6. DISCUSSION OF RESULTS

6.1 Convective Heat Transfer

The experimental convective heat transfer data obtained with platinum calorimeter and thin film gages are presented in Fig. 6.1. The results are normalized by the square root of the ratio of the nose radius to the stagnation pressure and plotted against the enthalpy difference between the edge of the stagnation point boundary layer and the wall. The composition in which most of the present data were attained was 9% CO_2 and 91% N_2. A few data were obtained in a mixture containing 87% CO_2 and 13% N_2. The calorimeter gages used in the experiment were 0.002 in. thick and were mounted at the stagnation point of a 0.5 in. nose radius hemispherical model. A new gage was used for each experiment. As described earlier a correction factor was applied, Fig. 4.6, to the observed calorimeter gage signal to account for the non-linear temperature distribution across the thickness of the gage element. The thin film gage results were adjusted for the variation of the heating material properties due to the change of its temperature during the test time.

In analyzing the data the possible contribution of radiative heating to the measured heat transfer rates was considered. For enthalpy levels corresponding to flight velocities below 37,000 ft/sec and stagnation point densities of the present experiments, the radiative flux to the gage, on the basis of Fig. 6.2, was less than 10% of the measured heat transfer

rate. However, for higher flight velocity simulations the radiation becomes appreciably larger and may add considerably to the measured rates. The amount of the incident radiation which the gage will absorb depends on the surface reflectivity, which itself is a function of the wavelength and the surface conditions. Since these factors are difficult to evaluate for each gage used it was assumed that the gage will absorb 50% of the incident radiant energy. Appropriate corrections were made and the data plotted showing the range of uncertainty (25% to 75% absorption) of the radiant heat contribution to the gage reading.

The present data are compared with the theoretical solutions of the stagnation point laminar boundary layer heat transfer in CO_2 and air (24). At enthalpies equivalent to flight velocities below 37,000 ft/sec the data lie between the CO_2 and air predictions, at higher speeds the data lie closer to the CO_2 theory.

In an effort to investigate the scaling low with regard to pressure, several runs were made at approximately the same shock velocity but at widely different stagnation pressures varying between 3.25 and 54.6 atmosphere. At stagnation pressures of 9 atm and above the scaling is precise. However, data obtained at the low pressure gave results which definitely deviate from the main trend of other data. A question arises whether the shock layer is in equilibrium. Using the prediction of reference 9 for the relaxation distance behind a normal shock one concludes that with $P_\infty = 0.25$ mm Hg and $U_s = 23,500$ ft/sec

the gas at the outer edge of the boundary layer can be out of equilibrium. The effect of this on boundary layer flow and the heat transfer has not been treated analytically with a sufficient rigor to provide the answer, whether the heat transfer should be either higher or lower than for the equilibrium shock layer case.

Further consideration must be given to the state of the boundary layer itself which even with its outer edge in equilibrium can be in non-equilibrium due to the finite recombination rates. Fay and Riddell (25) studied the non-equilibrium stagnation point dissociated boundary layer and formulated a parameter which can be used as a measure of the effects of finite recombination rates in the boundary layer. Applying this parameter to the conditions of the present experiments one would conclude that the boundary layer is in equilibrium for heat transfer purposes. However, no electron recombination in the boundary layer was considered in reference 25. This may be quite important since the energy invested in ionization is a large portion of the shock layer flow energy for shock velocities in the present study. Also the electron temperature will probably be higher than ion temperature at any given point of the boundary layer and may approach the stagnation region gas temperature. Thus, if the boundary layer is not in equilibrium with respect to electrons and ions, the energy delivered to its inner surface may be significantly higher than for the equilibrium or one temperature non-equilibrium cases. Such effects in combination with gage surface catalytic effects could explain

the results obtained in the present study (Fig. 4. 14).

A summary of all experimental data available on the convective heat transfer in N_2, CO_2 and CO_2 - N_2 mixtures is shown in Fig. 6. 3 together with the theoretical predictions of Hoshizaki. The data in CO_2 include free flight measurements of Yee, et al (26) and the results of shock tube experiments by Rutowski and Chan (27). Both sets of data correspond to relatively low stagnation enthalpies and thus, provide results at velocity levels lower than that of the present investigations.

In the simulated flight velocity range between 30, 000 and 38, 000 ft/sec it can be seen that the heat transfer results in 9% CO_2 - 91% N_2 gas mixture tend to lie below the CO_2 shock tube data of Nerem (28) and in general agreement with the N_2 results of Rose and Stankevics (9). The few data points from 87% CO_2 - 13% N_2 appear to agree with the 100% CO_2 results of Nerem, which further supports the existence of a somewhat higher level of heat transfer in the CO_2 rich mixtures over that in the N_2 rich mixtures.

6.2 Stagnation Point Equilibrium Total Radiation

The theoretical total radiance of a 9% CO_2 - 91% N_2 gas mixture for wide temperature and density ranges is shown in Fig. 6.4. Also shown are calculations for air (30). Several interesting properties are noted. First, there is a significant increase in radiation at temperatures above 7,000°K and towards the lower density levels when the spectral region between .05 and .2μ is included. This difference is caused primarily by the importance of the de-ionization of N^+ and O^+ in this region. Second, the total radiances of air and of the CO_2 - N_2 mixture are almost identical at the high temperature limits of the curve. This is due to the decreased importance of molecular radiation in these regions and the general similarity of the ionization level of the two gases. Third, at temperatures below about 10,000°K air and the CO_2 N_2 mixture deviate markedly in their radiant intensity. This increase in radiation for the assumed planetary gas mixture is due primarily to the importance of radiation from the CN and CO band systems. Shown in Fig. 6.5 are the contributions to the radiation from the various de-excitation mechanisms in the stagnation region gas of a model in the shock tube for a particular P_1 value. This curve presents the radiant intensities for each mechanism based upon the equilibrium concentrations for the same range of shock tube properties as shown in Fig. 3.48. Note the dominance of the continuum producing radiation mechanisms above a shock velocity value of 24,000 ft/sec. Fig. 6.6 shows the theoretical stand-off distance of a

shock layer on a hemispherical model as a function of shock velocity and initial shock pressure. Experimentally measured values are also shown. It can be seen that the measured distance agrees reasonably well with the calculated values obtained using the formula developed by Serbin (31).

Cavity gage measurements of the total radiative intensity of the stagnation region gas are presented in Fig. 6.7. Results have been obtained for shock velocity values between 22,000 and 34,000 ft/sec. Also shown on Fig. 6.7 are the theoretical curves (.2 to 10 μ spectral region) for the shock tube property ranges covered by the experimental conditions. The radiance has been normalized by the stagnation region density ratio to the 1.55 power which brings the theoretical curves into reasonably good agreement for the property range of interest. In general, the experimental points scatter near the theoretical predictions. There is a tendency for the experimental results to be slightly higher than the theory at shock velocities below about 28,000 ft/sec. Above this value the points generally group somewhat below the predicted level. Note the few points corresponding to P_1 values of .1 mm Hg. These lie significantly above the levels predicted by the equilibrium theory and the general levels obtained experimentally at higher pressures. We associated this behavior with the initiation of non-equilibrium effects in the shock layer. Radiation from a non-equilibrium air shock layer has been investigated experimentally by Page (32). Since the non-equilibrium process in the model test configuration will be different from that investigated by Page because of

the high temperature and dissociation level of the gas entering the shock layer in the shock tube, a direct comparison with Page's results is not necessarily valid. However, it is noted that the magnitudes of the few low pressure points are compatible with those presented by Page.

Several points from different test gas mixtures are also shown in Fig. 6.7. While more data are required for the study of the importance of gas composition, there appears to be a reasonable agreement between these points at flight velocities above 35,000 ft/sec and the other data. However, at lower velocities this is not so. The 25% CO_2 data lie considerably above the predicted values as discussed in connection with incident shock radiation measurements.

A time resolved spectrum of the stagnation region flow observed through a slit in the sidewall of the shock tube is shown in Fig. 6.8. This figure is interesting since it shows that the test gas is largely contaminant free; that is, the strong line radiation seen following the available test time does not extend into the test gas in general. While there is the possibility of small quantities of easily ionized contaminants existing in the test gas, the high stagnation region ionization levels associated with the hypervelocity regime are such that the number of electrons contributed by the contaminants should be negligible. Note that a prominent H_β line exists during the test time.

The small quantity of hydrogen (order of 10 parts per million) has a negligible effect on the thermochemical properties of the gas in

the stagnation region but its presence in the spectrum allows the calculation of electron concentration by the application of Griem's analysis of the Stark broadening effect (32). Calculations have been made for several test spectra by Sadjian (34); they indicate that the ion concentration of the test gas agrees within a factor of two with the concentrations predicted by the thermochemical equilibrium calculations (to temperature levels of 14,500°K).

6.3 Incident Shock Equilibrium Total Radiation

Using a total radiation cavity gage measurements were made of the equilibrium radiation behind the incident shock in 25% CO_2 - 75% N_2 gas mixture at shock velocities up to 30,000 ft/sec. The results are shown in Fig. 6.9. Also stagnation point radiation data obtained with the model cavity gages are shown in the range of the simulated flight velocity overlap. Both sets of data are normalized by the density ratio raised to 1.55 power. Curves representing theoretical calculations obtained with the use of Fig. 6.10 are also shown. Note that at simulated flight velocity above 32,000 ft/sec the theoretical curves collapse on each other indicating that the density effect was correlated correctly, at lower flight speeds the theoretical curves diverge. To make therefore a proper comparison of experimental data with the theoretical predictions the stagnation point data should be compared with a theoretical curve calculated for approximately P_1 = 70 mm Hg since only then the density of the radiating gas will be in proper relation between the experiment and the theory. Data from the incident shock measurements can be compared directly with the appropriate theoretical curve at a corresponding P_1. It should be noted that both sets of experimental results are equally higher than the theoretical predictions. A further comparison is made with the free flight range data of C. James (35). James' interpolated results for 25% CO_2 - 75% N_2 are shown in Fig. 6.9. It is interesting to note that at flight velocity of approximately 26,000 ft/sec free flight data indicate even higher radiance

than present shock tube measurements. To explain the differences between the theory and the results of the present experiment we refer to Fig. 6.11 where species radiation has been plotted. It is found that major contributors to the total radiation are CN and CO bands. Since the theoretical equilibrium composition calculations enter into the computation of the species radiation, any uncertainty of thermodynamic constants entering into the equilibrium calculations which affect the particle density of CO and CN will also affect the final results of total radiation calculations. The dissociation energy of CN radical used in present calculations was taken as D_o = 7.52 ev on the basis of the report by Knight and Rink (36). This value is considered to be true in the light of later experimental results by Berkowitz (37). Fairbairn (38) recently measured the f numbers for CN violet and red band systems. He reports f = 0.0318 for CN violet and f = .0034 for the red band system. In arriving at the theoretical prediction in Fig. 6.9, f = 0.027 and f = 0.020 were used for the violet and red systems respectively. The new values will compensate each other to some extent when used in present calculations. It is therefore unlikely that CN is the source of the higher radiation. The formation energy of CO is very well established however some of the f numbers are not absolutely known. Since higher than theoretically predicted radiation has now been reported from two independent experiments it must be assumed that it represents a true level. Spectrographic studies of the radiation are necessary to explain

fully the reason for the difference between the theory and experiment.

6.4 Equilibrium & Non-equilibrium Spectral Radiance Behind Incident Shock

The results of spectral measurements made with the modified JACo spectrograph described in section 4.4 are shown in Figs. 6.12, 6.13 and 6.14. The measurements were made at one condition of shock velocity U_s = 28,400 ft/sec and initial pressure P_1 = 0.5 mm Hg. The corresponding equilibrium temperature and density ratio of the radiating gas are T = 7400°K and $\rho/\rho_0 = 1.26 \times 10^{-2}$. The wavelength coverage extended from 2500 Å to 7000 Å.

The equilibrium radiation data are plotted in Fig. 6.12 where they are compared with theoretically predicted radiance distribution. There is a reasonable agreement between the experiment and the theory for the violet system of CN except at 2150 Å where the measured intensity is higher than the calculated value (f = 0.027). Another area of higher radiance indicated by the experiment lies between 4300 Å and 6000 Å. It is impossible to identify absolutely the source contributing to the disagreement between the experiment and the theory without a spectrographic investigation of the gas radiation. Both CO and C_2 radiate in this spectral region and therefore both can be suspected to be the contributors.

The peak of the non-equilibrium radiation is shown in Fig. 6.13 as a function of wavelength. Comparison of these data and the equilibrium radiation shown in the previous figure indicates that the non-equilibrium radiation exceeds the equilibrium level depending on the wavelength by a factor varying between three and six. Strong non-equilibrium overshoots

appear in the spectral region between 3400 Å and 4000 Å. The N_2^+(1-) and CN violet systems radiate in this wavelength region. According to Allen (39) the contribution of the N_2^+ (1-) to the non-equilibrium radiation of air is relatively low. It is possible therefore to assume that the N_2^+ (1-) is also a minor contributor and that the strong non-equilibrium overshoot comes from the CN violet system.

The integrated non-equilibrium radiation is shown in Fig. 6.14. The method used in integrating the intensity across the non-equilibrium shock wave front was described in section 4.4. In order to obtain the magnitude of the total non-equilibrium radiation the area under the dashed curve was integrated. The average intensity was found to be 5.95 watts/ cm^2-str-μ. Assuming that this average value extends down to 100 Å and allowing for the atomic line radiation (39) one calculates the total non-equilibrium radiation in the spectral region between 100 Å and 10,000 Å to be 73 watts/cm^2. Allen reported a total non-equilibrium radiation for air to be 40 watts/cm^2 at shock velocity of 33,000 ft/sec. This value was extrapolated down to 28,400 ft/sec using the velocity dependence given by Page (52) with the result of 20 watts/cm^2.

It can be concluded therefore that the non-equilibrium radiation in the planetary atmosphere containing 25% CO_2 and 75% N_2 can be about four times higher than in the Earth's atmosphere.

7. SUMMARY AND RECOMMENDATIONS

7.1 Summary

During the present investigations stagnation point convective heat transfer was measured by means of platinum calorimeter and thin film gages in a simulated planetary atmosphere composed of 9% CO_2 - 91% N_2 over a range of flight velocities up to 45,000 ft/sec. These results and some additional data obtained at different mixture ratios indicate that the composition of the CO_2 - N_2 mixture does not have a large effect on experimental convective heat transfer rates.

Convective heat transfer data were also obtained with gages of different materials. They indicate that the state of the stagnation point boundary layer can be such that the gage surface affects the observed heat transfer rates.

Stagnation point equilibrium total radiation measurements in 9% CO_2 - 91% N_2 for shock velocities between 22,000 and 34,000 ft/sec show a generally good agreement with the theoretical predictions of Breene, et al, above 28,000 ft/sec. At lower speeds the experiments indicate higher radiance. Total radiation measurements behind the incident shock for shock velocities between 20,000 and 30,000 ft/sec in 25% CO_2 - 75% N_2 give results which are more than two times higher than the theoretical predictions but slightly lower than the free flight experimental data of James.

Spectral distributions of equilibrium and non-equilibrium radiation were measured in a 25% CO_2 - 75% N_2 gas mixture. The equilibrium

radiation in the wavelength region between 4300 Å and 6000 Å was higher than the theory but not sufficiently high to explain the total radiation measurements. The integrated non-equilibrium radiation of 25% CO_2 - 75% N_2 was found to be about 70 watts/cm^2 at 28,400 ft/sec which is between three and four times higher than that expected for air.

7.2 Recommendations

As a result of the current investigations certain problems associated with the convective and radiative heat transfer became apparent and they should be considered in future studies.

The most urgent problem is to explain both experimentally and theoretically the phenomena indicated by the present measurements of convective heat transfer with different material gages. The experimental program would involve a series of test runs with various gage materials and surface coatings of known catalytic activities over a range of stagnation point pressures and enthalpies.

At velocities above 36,000 ft/sec it appears that the intensity of the equilibrium radiative flux to the stagnation point of the vehicle is not greatly affected by the composition of the atmosphere, since most of the gas in the shock layer will be completely dissociated and partially ionized. The strong molecular radiators such as CN, CO and N_2 will not be present. The main contributors therefore will be free-free and free-bound modes of radiation. Models for theoretical calculations of such a radiation have been developed by Breene in this Laboratory and others. There exists, however, a certain amount of disagreement among the investigators regarding the validity of some of the assumptions included in the theoretical treatment of the dominant modes of radiant emission. The existing results are found to vary by factors of 2, 3 or even more depending on the methods used in their computation.

Assuming that our theoretical model gives the correct value for the emitted radiation per unit particle, the next step is to compute the total contribution from the given species corresponding to the particle density as given by the equilibrium composition at enthalpy and pressure levels of interest. This equilibrium concentration is obtained by minimizing the Gibbs free energy and by treating the fluid as a perfect gas. In the process of solving this problem thermal functions of molecules, atoms and charged particles are used which in turn are subject to several approximations, especially at high temperature. Also, the assumption of a perfect gas becomes less valid as the charged particle density becomes appreciable. In either case, the computed values of species concentrations can contain an uncertainty factor of up to 2. It appears that direct measurement of radiation from the shock layer which is raised to the energy level equal to enthalpy change due to flight velocity will produce results which have more accuracy than comparable theoretical calculations. This is best achieved by the experimental configuration used in our present studies where the radiation measuring probe is located at the stagnation point of the model. Theoretical predictions of radiation indicate that at temperatures above 7000°K and moderate densities there is a significant contribution from the freebound transitions in the wavelength region below 2000 Å. Because of difficulties with the optical systems and lack of detectors at those wavelengths no information exists to confirm the theory. It can be shown that magnitude of the contribution

below 2000 Å can exceed severalfold all other radiation. A cavity gage, with the window removed and provided with a proper differential pumping system will be able to measure the total radiation far into the vacuum UV region, thereby providing data for the determination of validity of the theoretical predictions.

At lower flight velocities such as these corresponding to Martian entry the contribution from free-free and free-bound transitions is not so important while the molecular radiation produces the bulk of the radiative transfer. In this moderate temperature range the commonly used techniques for calculating species concentrations in a gas mixture are satisfactory. The only question that remains is whether the f numbers of the radiating species are known with sufficient accuracy. Since some of the systems have not been explored under conditions similar to that encountered by an entry vehicle, direct measurements of the radiation by means of the technique used in the present study is the only assurance of being able to determine the radiative heat flux with good enough accuracy necessary for a successful design.

In view of the latest estimates of the Martian atmosphere composition, the radiation to the entering vehicle becomes critical. The presence of a large concentration of Argon will have a tendency to increase the temperature of the shock layer at a given flight velocity mainly due to the absence of chemical changes of Argon which would absorb the energy. In addition Argon itself can contribute to radiation. This, combined with the large cross-sectional dimensions of the entry vehicle necessary for

retardation creates an even heavier demand on the precision with which we must predict the total radiative flux. Experiments should be conducted at several mixtures spanning the anticipated composition of the Martian atmospheres.

The experimental investigation of non-equilibrium radiation should include a study at higher velocities and different compositions than investigated in the current program. Also by applying time resolved spectrography the contributions from various species should also be identified and the non-equilibrium chemical process studied.

The total radiation cavity gage developed at the Space Sciences Laboratory is suitable to the direct measurement of surface heat transfer rates through its modification for location at the model surface. A study using the surface gage would be of value in determining the validity of analytical methods developed for the calculation of surface heat transfer from known gas radiance data and known flow field geometry. Heating rates could be measured at and away from the stagnation point, on symmetric and asymmetric bodies, and on bodies at zero and finite angles of attack.

NOMENCLATURE

A	area
C_D	drag coefficient
C	specific heat
D	diameter, dissociation energy
E	voltage, energy
H	enthalpy
I	intensity
K	thermal diffusivity
L	length
M	molecular weight
N	number density
P	pressure
R	gas constant, radius
Q	energy
S	entropy
T	temperature
U	velocity
V	volume, voltage
X	radial distance
Y	normal distance
a	distance
f	oscillator strength
h	enthalpy, height
i	current
k	thermal conductivity
l	length, thickness
m	mass
q	heat transfer rate
s	slit width
t	time
w	width
x	coordinate
z	coordinate
α	temperature coefficient of resistivity
γ	entry angle
δ	shock layer thickness
λ	variable of integration, wavelength
ρ	density
ϕ	angle for off-axis points
Ω	solid angle

Subscripts

1	initial driven tube
2	behind incident shock, behind bow shock
3	behind bow shock
4	final driver
e	entry conditions, equilibrium
f	flight conditions
i	incident shock
m	model
o	initial, standard conditions, air
t	test
A	in plane A
D	driver
N	nose
R	radiative
S	shock, stagnation
T	total
W	wall
∞	free stream condition
*	of 28.966g

Superscripts

'	in image field
-	effective

REFERENCES

1. G. E. - MSD; Venus-Mars Capsule Study, JPL Contract 950250 (two volumes); July 30, 1962.

2. Warren, W.R., Rogers, D.A., and Harris, C.J.; The Development of an Electrically Heated Shock Driven Test Facility; 2nd Symp. on Hypervelocity Techniques, Univ. of Denver, Denver, Colo.; March, 1962.

3. Camm, J.; Escape Velocity Shock Tube With Arc Heated Driver; Avco-Everett Res. Lab., Res. Rpt., pres. at 2nd Hypervelocity Symp., Denver, Colo.; March, 1962.

4. Resler, E.L., and Kantrowitz, A.; The Production of High Temperature Gases in Shock Tubes; JAP 23, No. 12 (1952).

5. Rose, P.H., and Stark, W.I.; Stagnation Point Heat Transfer Measurements in Dissociated Air; JAS 25, No. 2 (1958) February.

6. Hollyer, R.N., Hunting, A.C., Laporte, O., and Turner, E.B.; Luminosity Generated by Shock Waves; Nature 171, 395 (1953).

7. Browne, W.G.; Thermodynamic Properties of the Venusian Atmosphere; Advanced Aerospace Physics Tech. Memo No. 13, (Three Parts), June 11, 1962.

8. Gruszczynski, J.S., Warren, W.R.; Measurements of Hyper-velocity Stagnation Point Heat Transfer in Simulated Planetary Atmospheres; G.E. - MSD Doc. No. R63SD29; March, 1963.

9. Rose, P.H., and Stankevics, J.O.; Stagnation Point Heat Transfer Measurements in Partially Ionized Air; IAS Paper No. 63-61, January, 1963.

10. Hoshizaki, H.; Heat Transfer in Planetary Atmospheres at Super-Satellite Speeds; ARS Journal; October, 1962.

11. Seiff, A.; A Progress Report on the Ames Hypervelocity Free-Flight Facilities and Some of the Current Research Problems Being Studied in Them; AIAA Paper No. 63-162; June, 1963.

12. Hartunian, R.A.; Private Communication; September, 1963.

13. Hartunian, R.A., and Thompson, W.P.; Non-equilibrium Stagnation Point Heat Transfer Including Surface Catalysis; AIAA Paper No. 63-464, August, 1963.

14. Meyerson, A.L.; Private Communication; August, 1963.

15. Gruszczynski, J.S., Harris, C.J., Rogers, D.A., and Warren, W.R.; Fast Response Total Radiation Gage for Measurement of Radiant Emission from High Temperature Gas; IEEE Paper No. CP 63-438, January, 1963.

16. American Institute of Physics Handbook; McGraw-Hill Co., New York; 1957.

17. DeVos, J.C.; Physics 20, 690, 1954

18. Null, M.R. and Lozier, W.W.; The Carbon Arc as Radiation Standard. Temperature Its Measurement and Control in Science and Industry; Reinhold Publishing Co., New York, 1962.

19. Hall, J.G., and Hertzberg, A.; Recent Advances in Transient Temperature Thermometry; Jet Propulsion Lab., November, 1958.

20. Warren, W.R., et al; Shock Tunnel Studies of the Aerodynamics of Atmospheric Entry; G.E., MSD R62SD56, May, 1962.

21. Hodgman, C.D.; Reflectivity of Platinum; Ed. in Chief, Handbook of Chemistry and Physics, 1952.

22. Vidal, R.J.; Model Instrumentation Techniques for Heat Transfer and Force Measurements in a Hypersonic Shock Tunnel, Cornell Aero. Lab. Rept. No. AD-917-A-1, February, 1956.

23. Peucker, M.P.; Improved Methods and Techniques for the Manufacturing of Heat Transfer Gages and Thin Film Thermocouples; General Electric Co., Aerodynamic Tech. Memo. No. 13, April, 1958.

24. Hoshizaki, H.; Heat Transfer in Planetary Atmospheres at Super-Satellite Speeds; ARS Journal 32, No. 10; October, 1962.

25. Fay, J.A. and Riddell, F.R.; Theory of Stagnation Point Heat Transfer in Dissociated Air; J. Aeron. Sci., Vol. 25, No. 2, February 1958.

26. Yee, L., Bailey, H.E., and Woodward, H.T.; Ballistic Range Measurements of Stagnation-Point Heat Transfer in Air and in Carbon Dioxide at Velocities up to 18,000 Feet per Second; NASA TN D-777, 1961.

27. Rutowski, R.W., and Chan, K.K.; Shock Tube Experiments Simulating Entry into Planetary Atmospheres; LMSD-288139, Lockheed Missiles and Space Co.; January, 1960.

28. Nerem, R.M., Morgan, C.J., and Graber, B.C.; Hypervelocity Stagnation Point Heat Transfer in a Carbon Dioxide Atmosphere; AIAA Journal, Vol. I, Part 9; September 1963.

29. Breene, R.G., Jr., and Nardone, M.C.; Radiant Emission in the Atmospheres of the Terrestrial Planets; Symp. on Dynamics of Manned Lifting Planetary Entry; John Wiley & Sons, 1963. Also, private communication.

30. Nardone, M.C., Breene, R.G., Zeldin, S.S., and Riethof, T.R.; Radiance of Species in High Temperature Air; GE-MSD Doc. No. R63SD3; June, 1963.

31. Serbin, H.; Supersonic Flow Around Blunt Bodies; JAS 25, No. 1; January, 1958.

32. Page, W.A.; Shock Layer Radiation of Blunt Bodies Traveling at Lunar Return Entry Velocities; IAS Paper No. 63-41; January, 1963.

33. Griem, H.R.; Measurement Techniques in High Temperature Plasmas; Temperature - Its Measurement and Control in Science and Industry; Reinhold Publishing Co., 1962.

34. Sadjian, H.; Space Sciences Laboratory, GE Co.; private communication.

35. James, C. S.; Experimental Study of Radiative Transport From Hot Gases Simulating in Composition the Atmospheres of Mars and Venus; AIAA Paper No. 63-455; August, 1963.

36. Knight, H. T., and Rink, J. P.; Dissociation Energy of Cyanogen and Related Quantities by X-Ray Densitometry of Shock Waves; J. Chem. Phys., Vol. 35, No. 1; July, 1961.

37. Berkowitz, J.; Heat of Formation of the CN Radical; J. Chem. Phys., Vol. 36, No. 10; May, 1962.

38. Fairbairn, A.; The Spectrum of Shock-Heated Gases Simulating The Venus Atmosphere; AIAA Paper No. 63-454; August, 1963.

39. Allen, R. A., Rose, P. H., and Camm, J. C.; Non-Equilibrium and Equilibrium Radiation at Super-Satellite Re-Entry Velocities; IAS Paper No. 63-77; January, 1963.

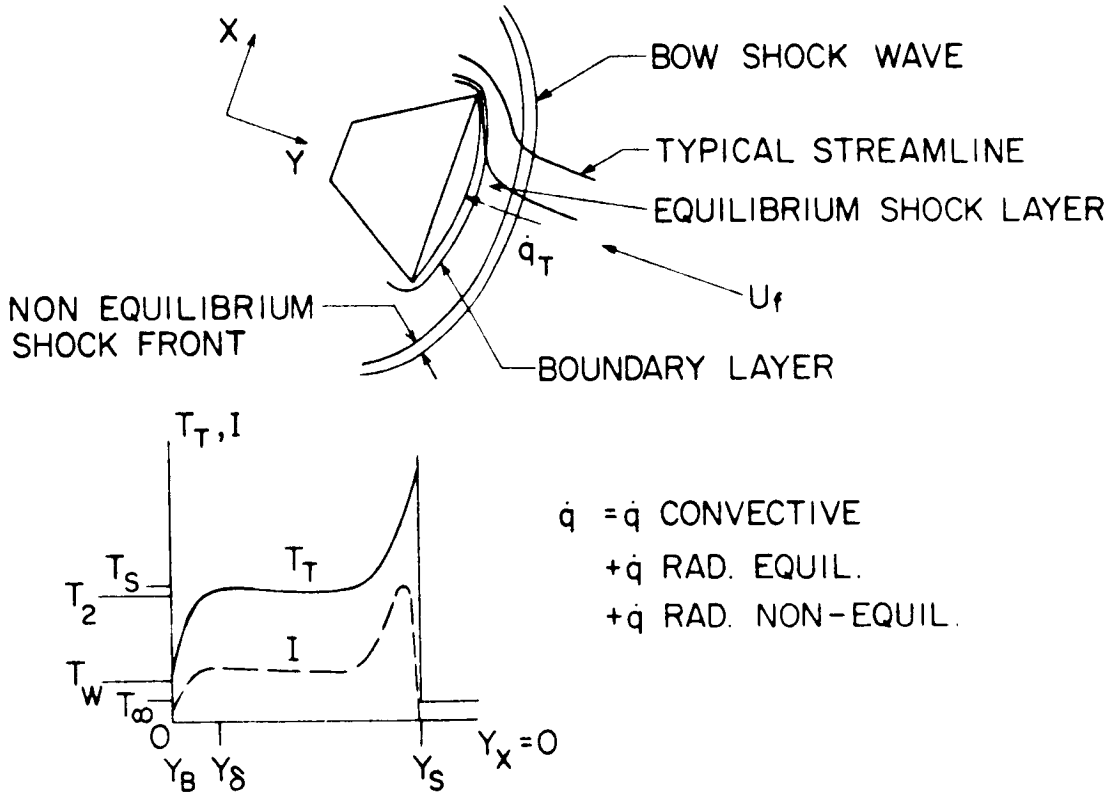

Figure I.1 Description of Hypervelocity Stagnation Region Heat Transfer Problem During Planetary Entry

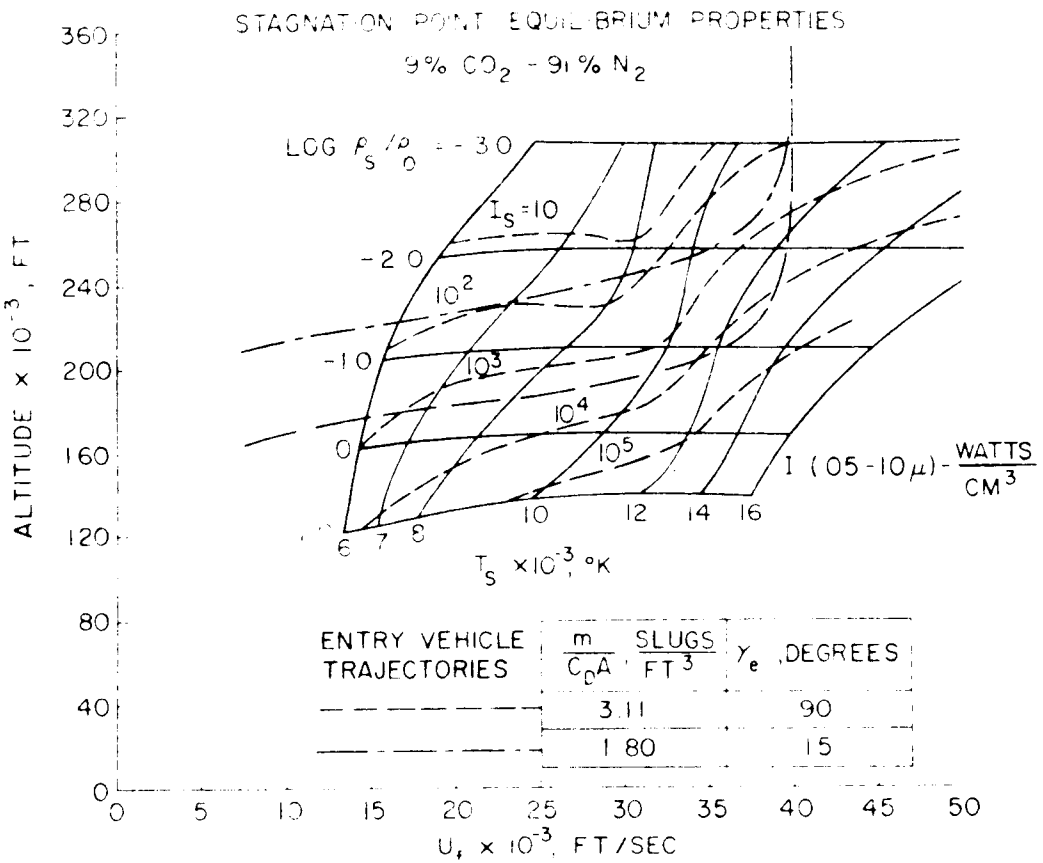

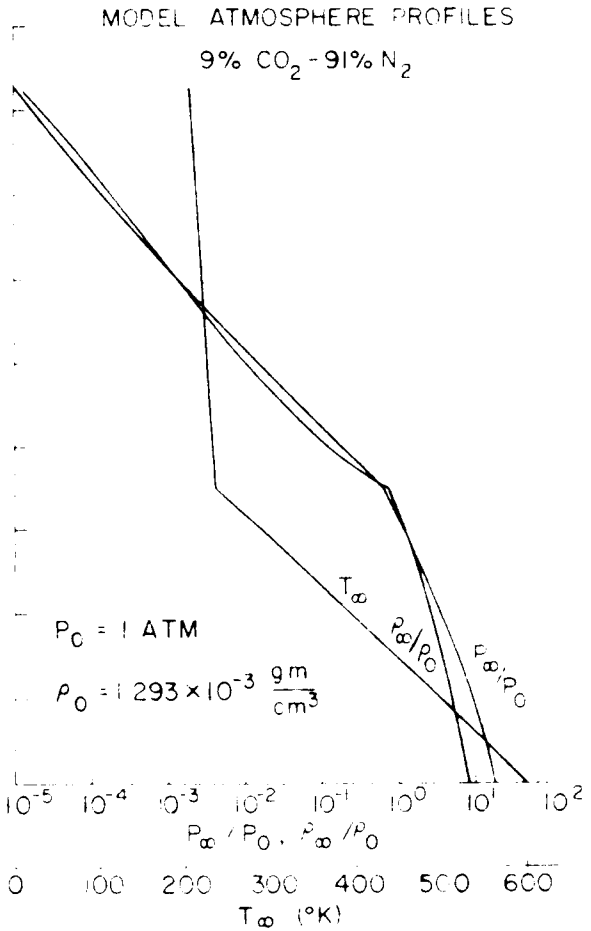

Figure 1.2 Blunt Body Stagnation Point Equilibrium Gas Properties and Assumed Model Atmosphere

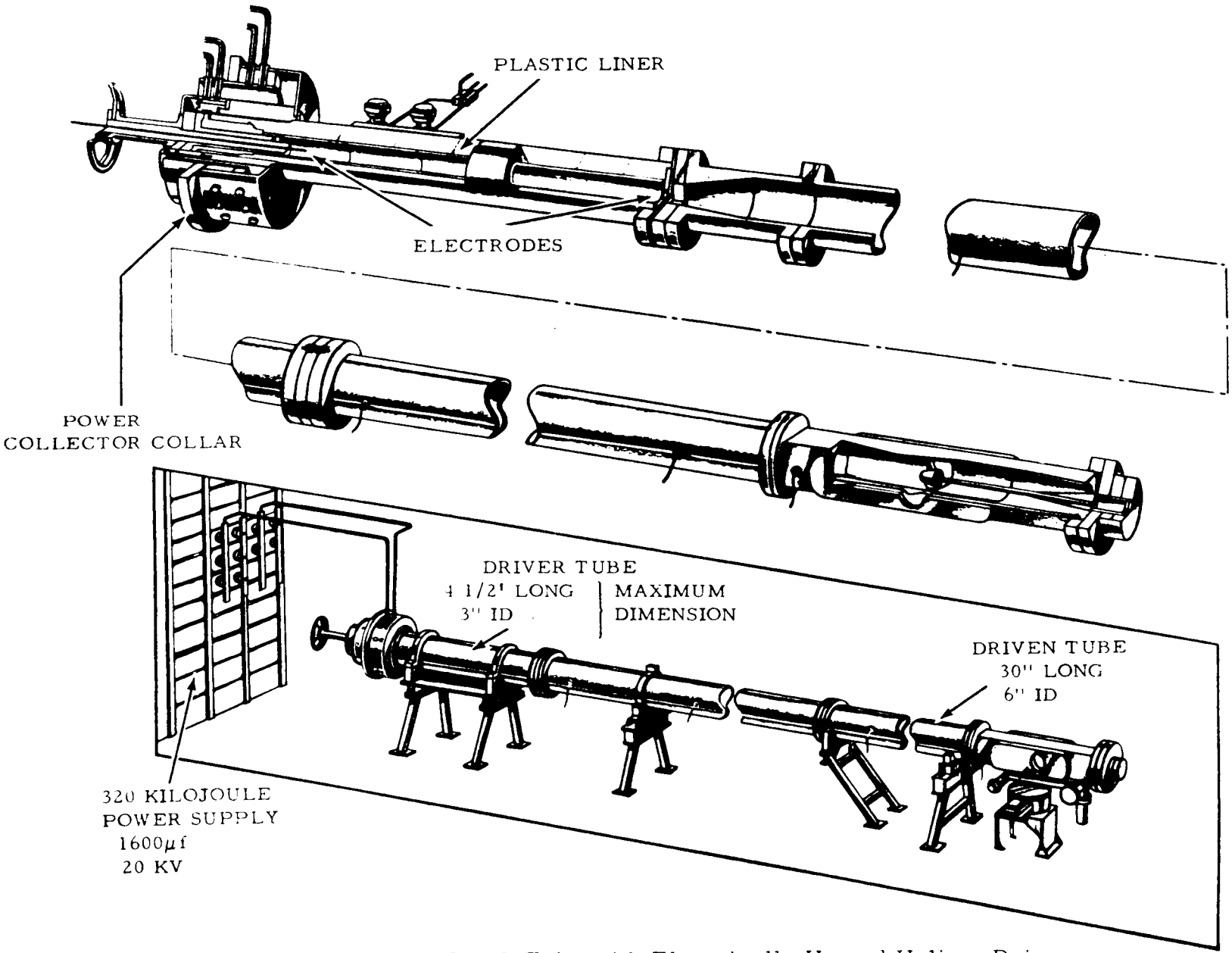

Figure 2.1 Hypervelocity Shock Tube with Electrically Heated Helium Driver

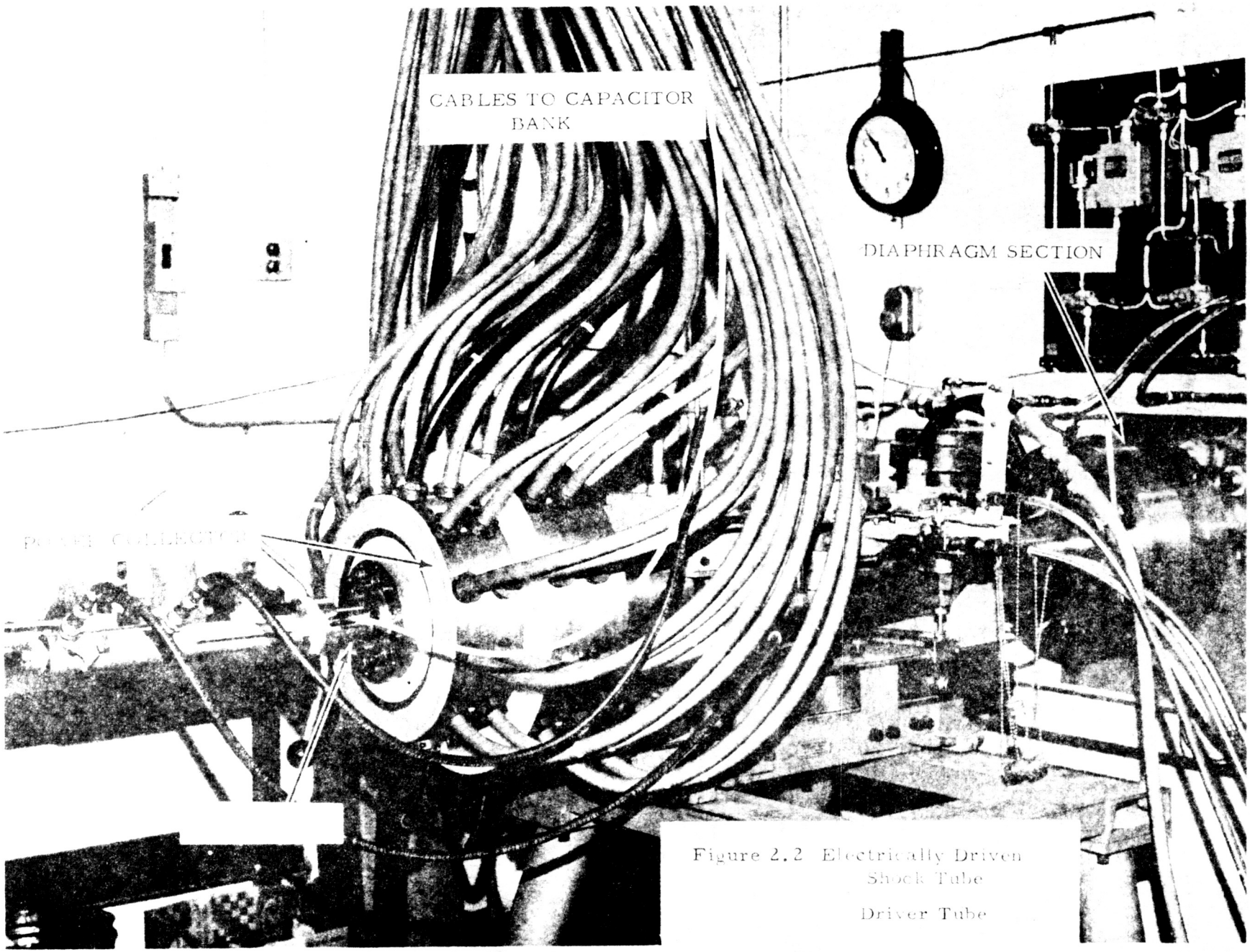

Figure 2.2 Electrically Driven Shock Tube

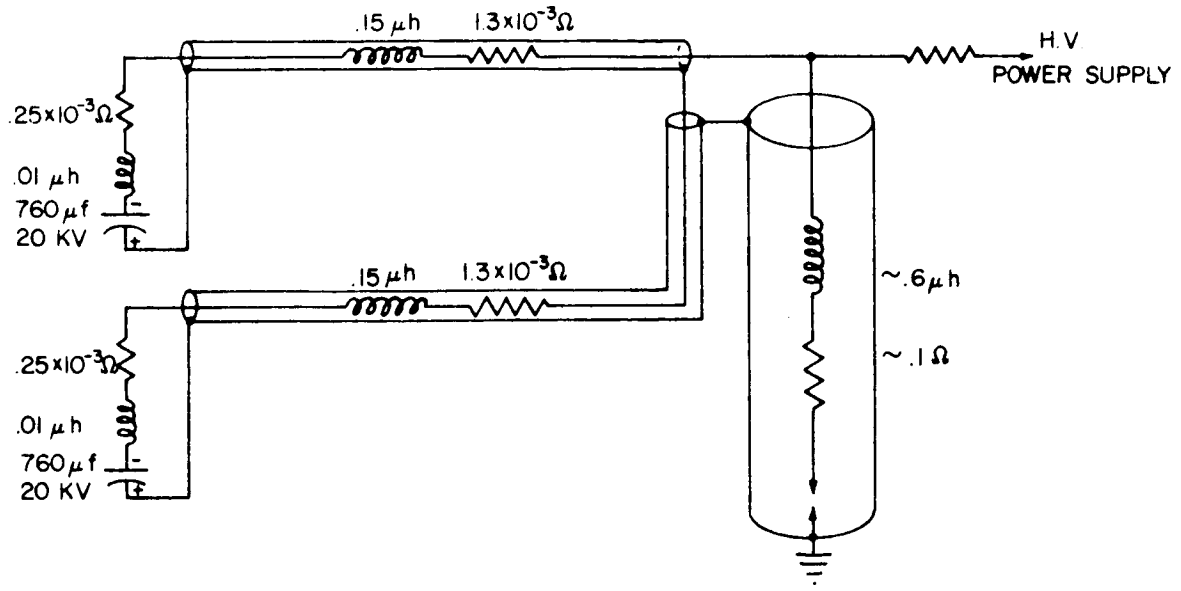

Figure 2.3a Circuit Diagram of the Driver

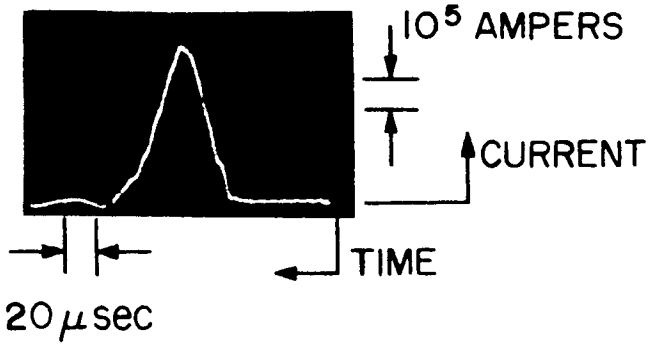

E = 40 KV

P_1 = 17 atm

Figure 2.3b Oscilloscope Trace of Driver Discharge Current

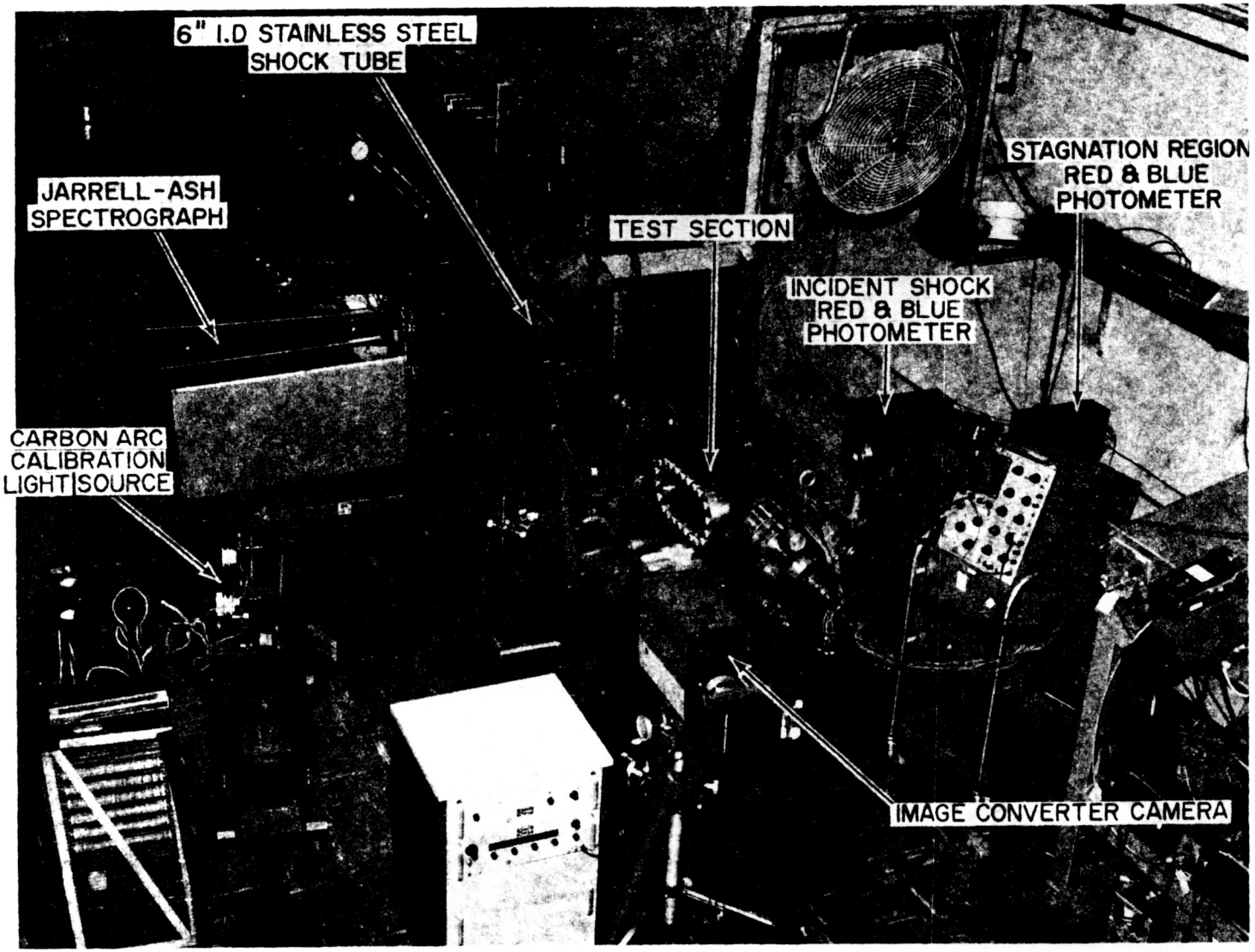

Figure 2.4 Electrically Driven Shock Tube - Driven Tube Including Test Section and Instrumentation

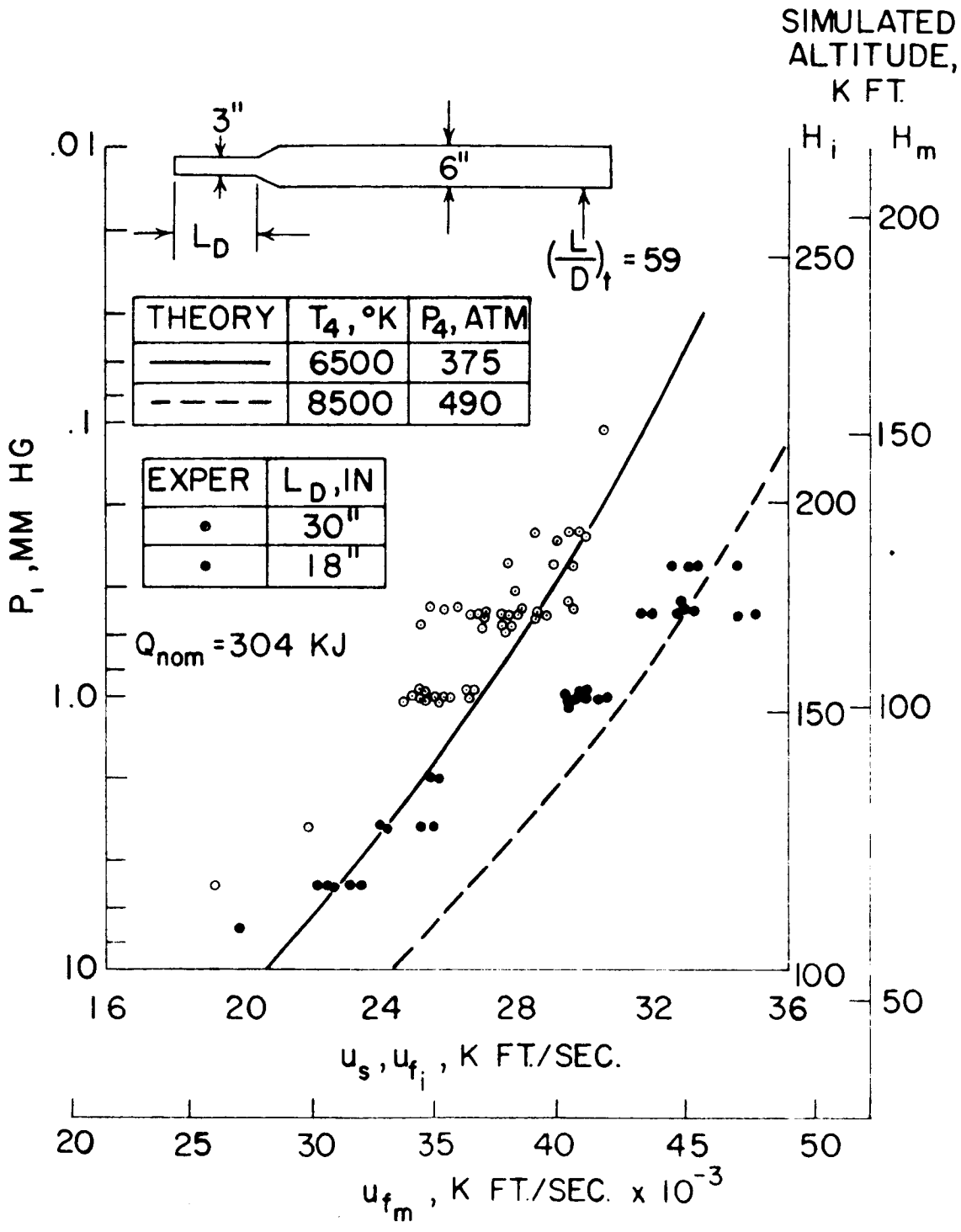

Figure 2.5 Electrically Driven Shock Tube. Shock Velocity Attainable at Different Driven Tube Pressures. Data Shown for 18 and 30 in. Long Driver.

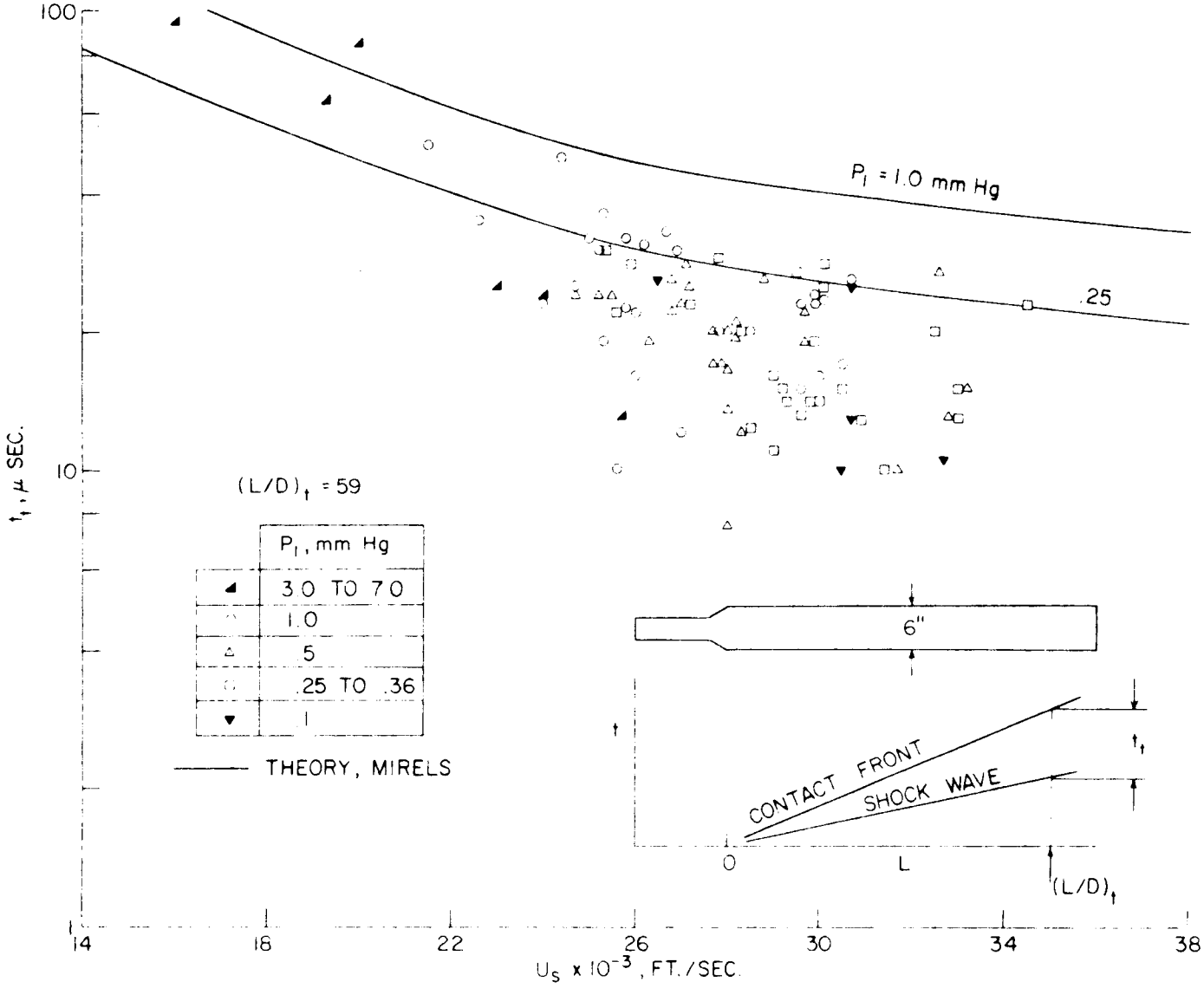

Figure 2.6 Test Time as Function of Shock Velocity. Experimental Data Compared with Theory

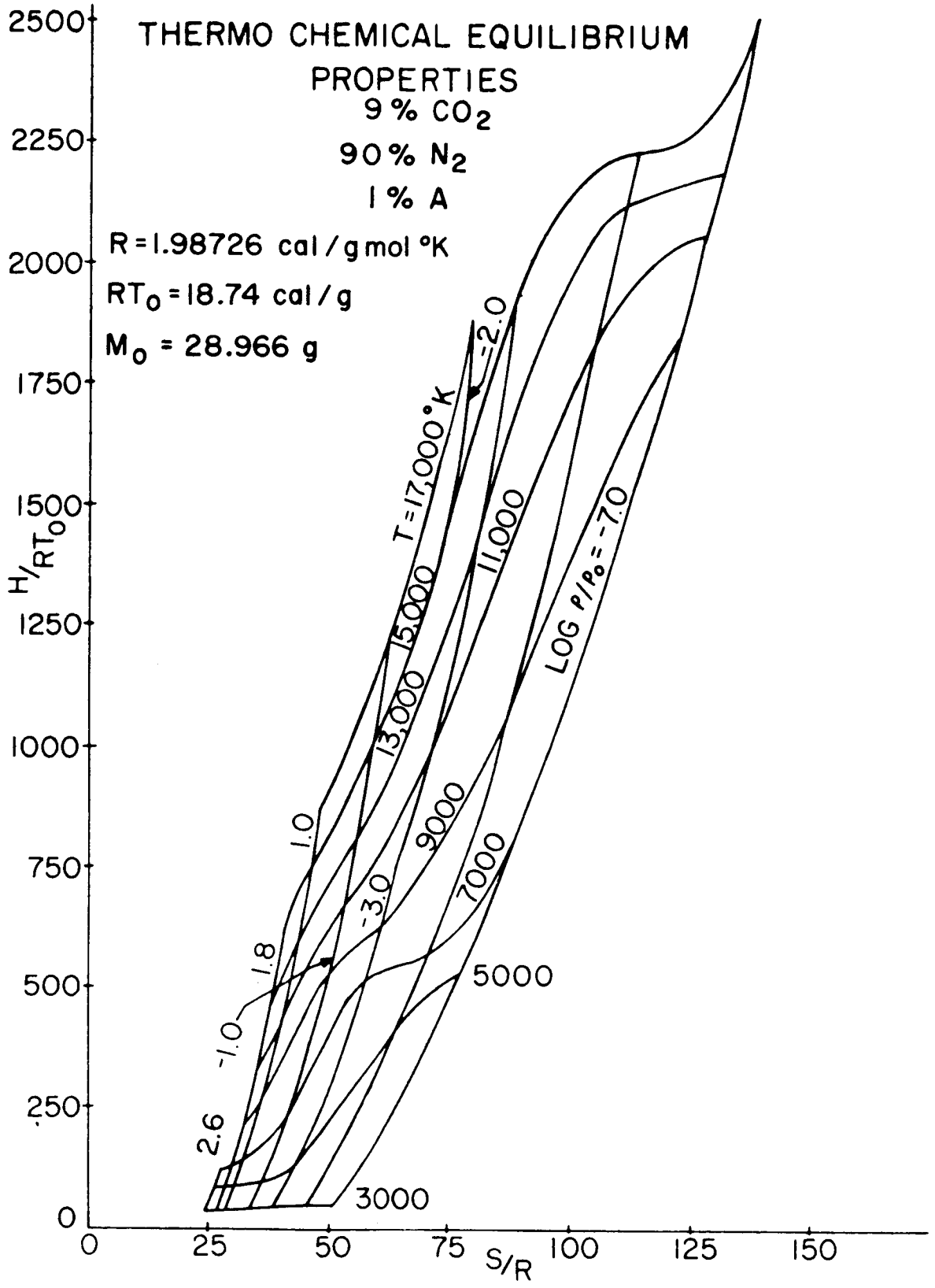

Figure 3.1 Mollier Chart for Initial 9% CO_2 - 90% N_2 - 1% A Molar Mixture

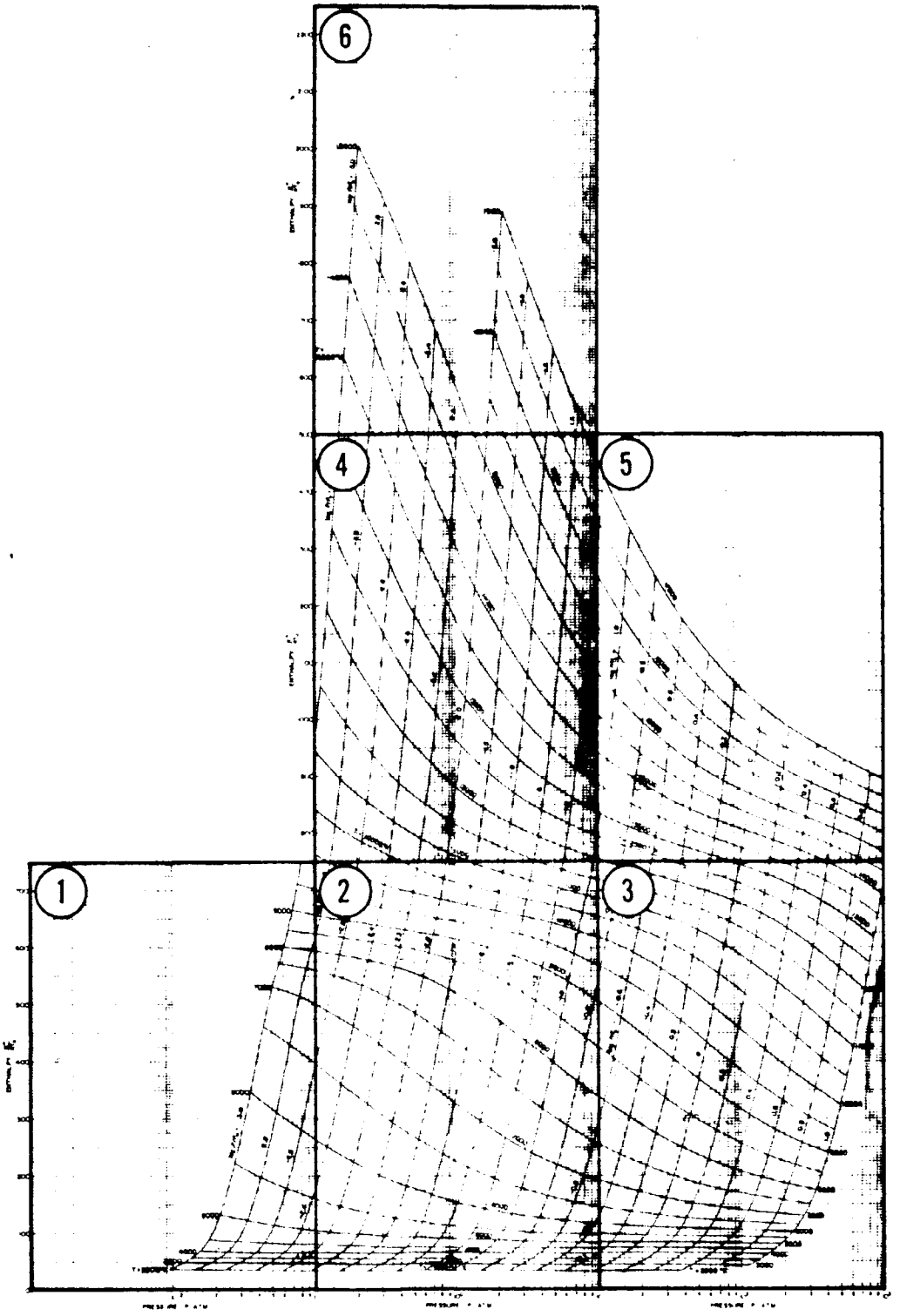

Figure 3.2 Key to Thermodynamics Charts for 3% CO_2 - 97% N_2

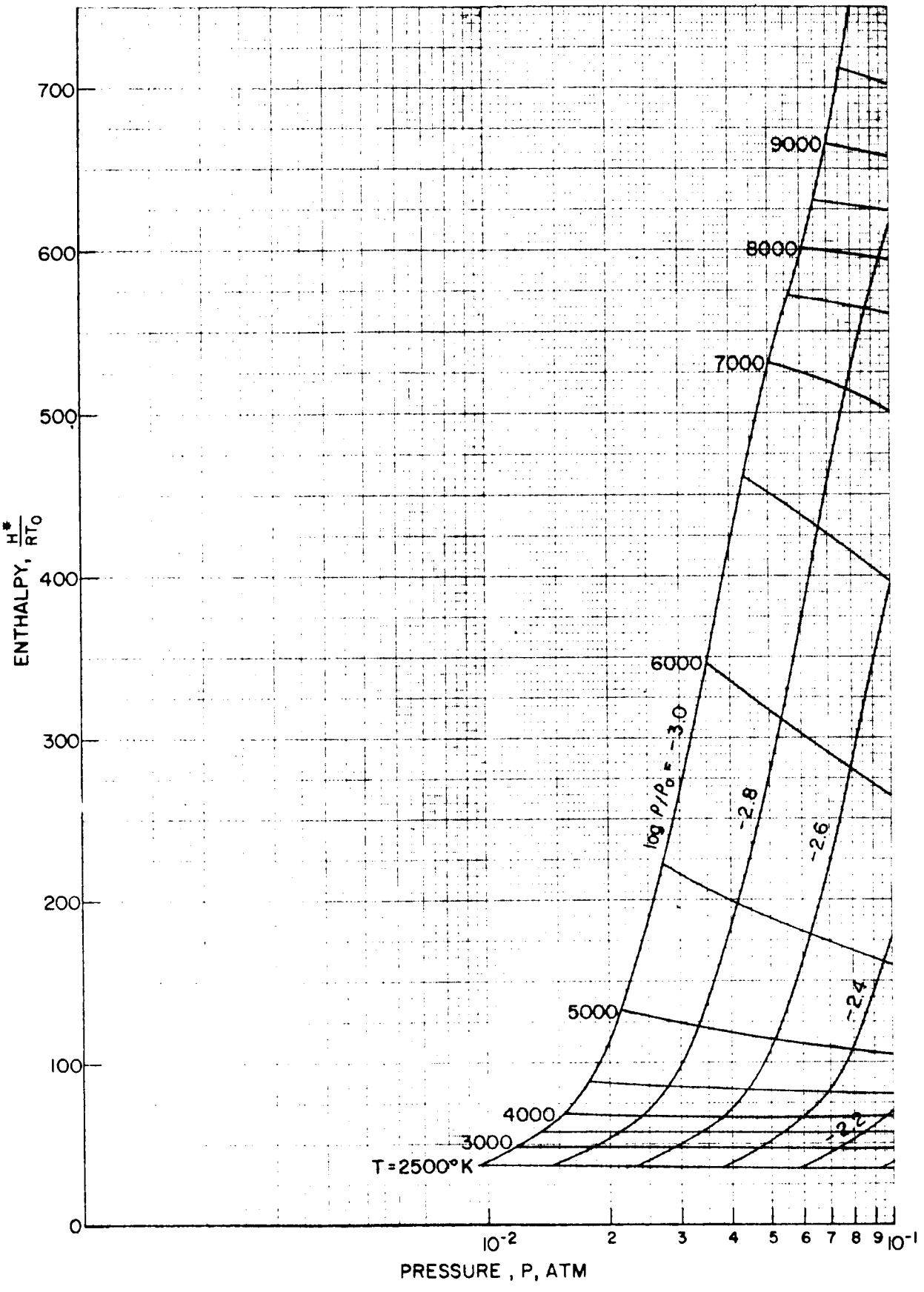

Figure 3.3 Chart 1 Thermodynamic Charts for 3% CO_2 - 97% N_2

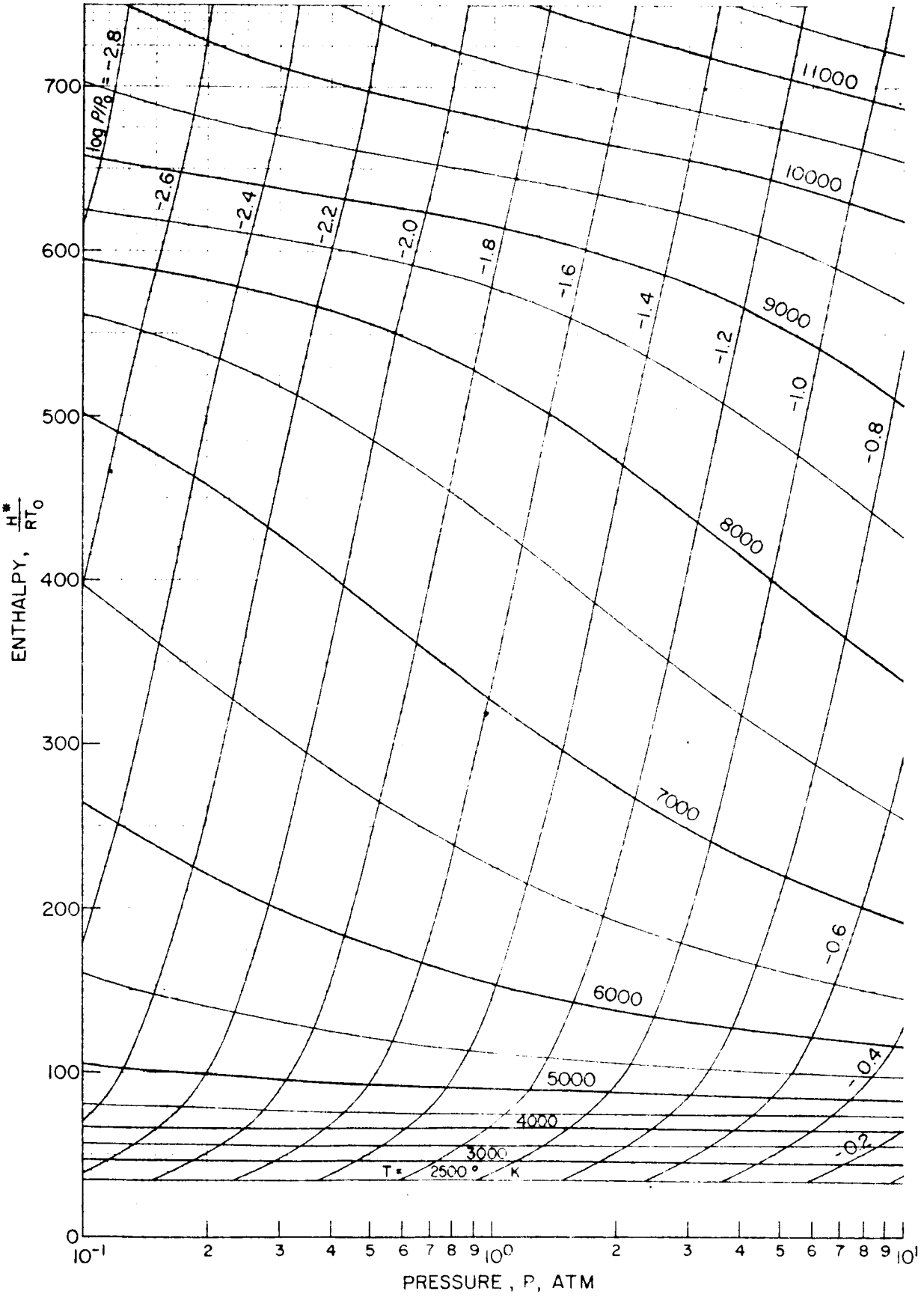

Figure 3.3 (Cont'd) Chart 2 Thermodynamic Charts for 3% CO_2 - 97% N_2

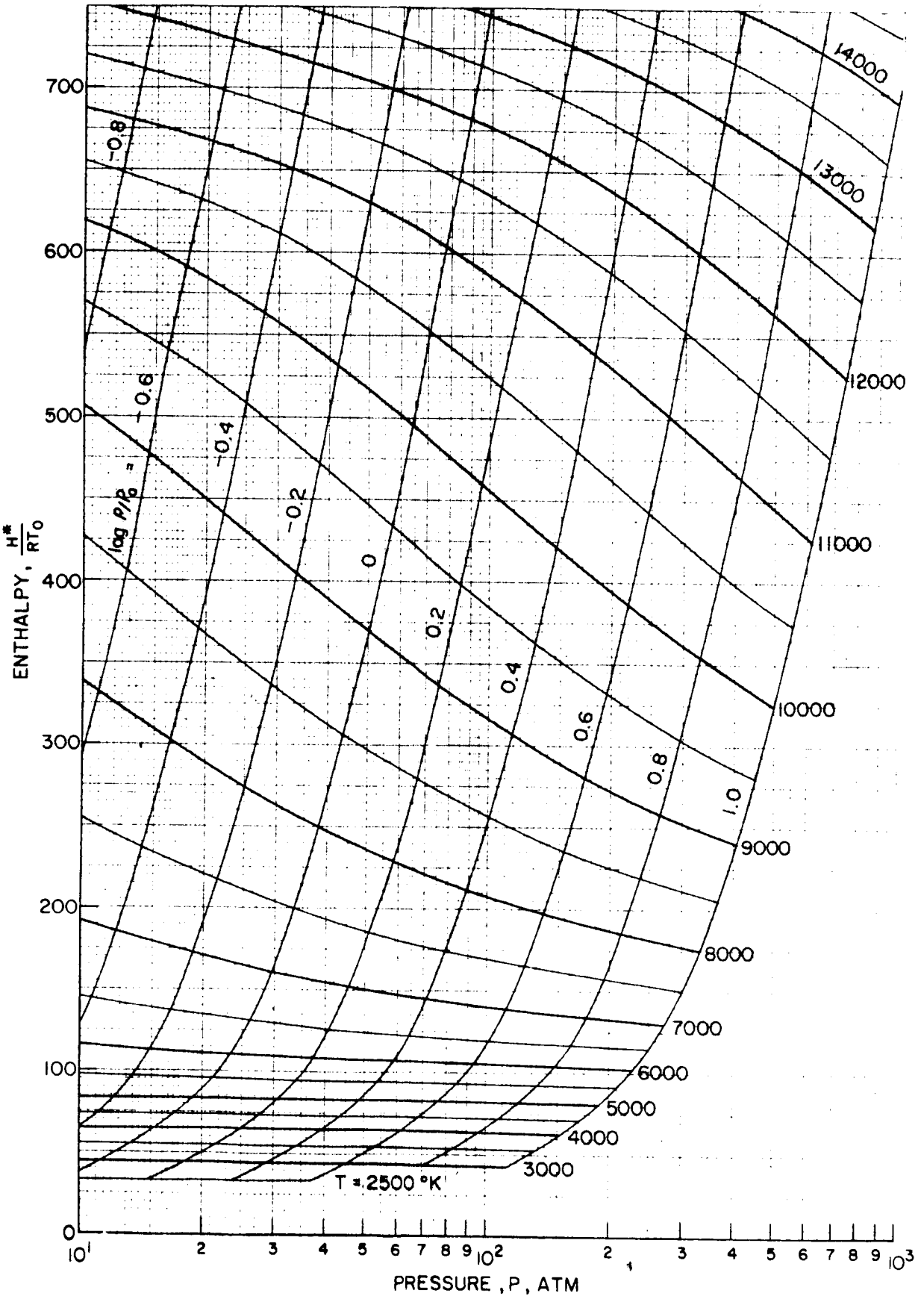

Figure 3.3 (Cont'd) Chart 3 Thermodynamic Charts for 3% CO_2 - 97% N_2

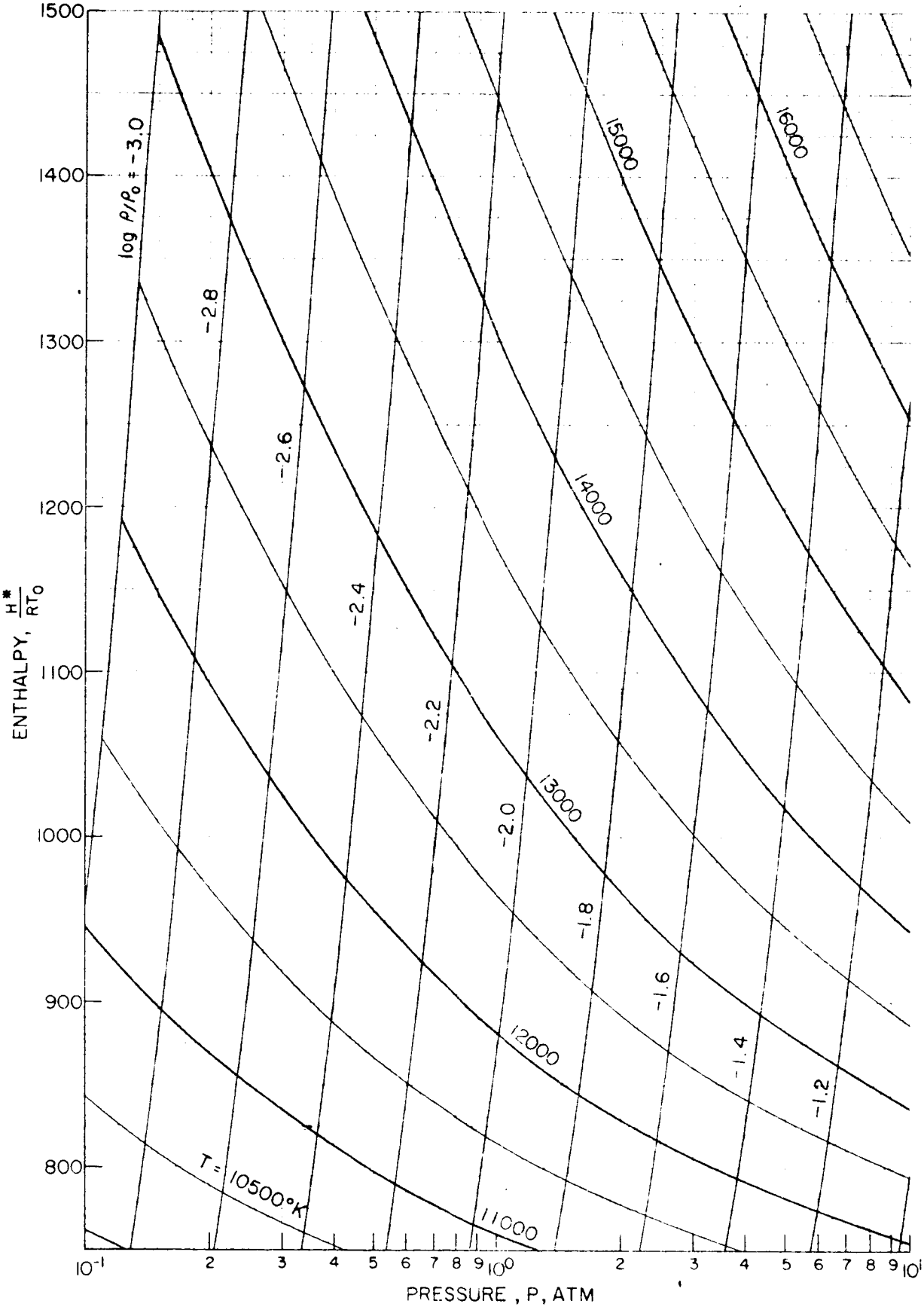

Figure 3. 3 (Cont'd) Chart 4 Thermodynamic Charts for 3% CO_2 - 97% N_2

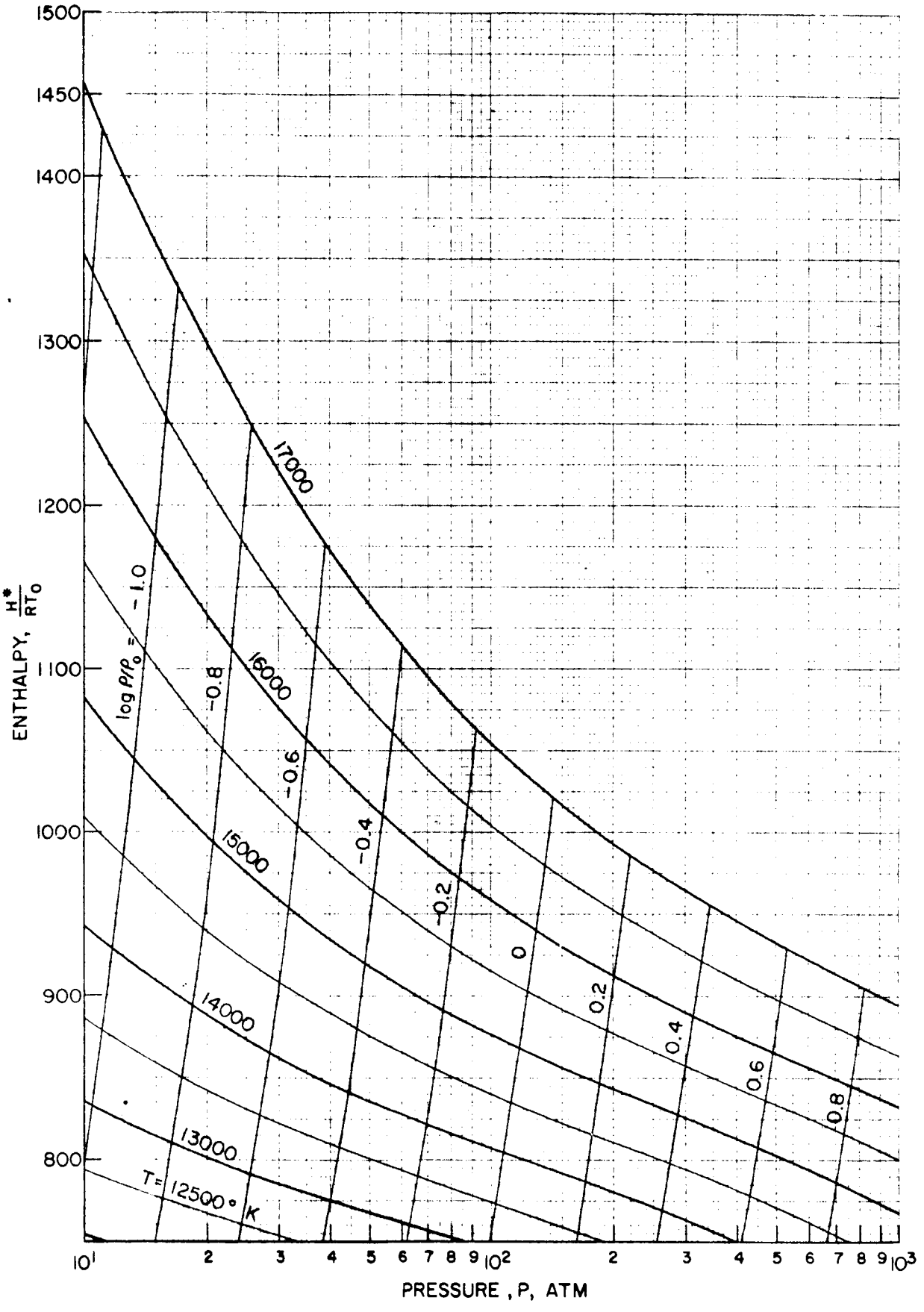

Figure 3.3 (Cont'd) Chart 5 Thermodynamic Charts for 3% CO_2 - 97% N_2

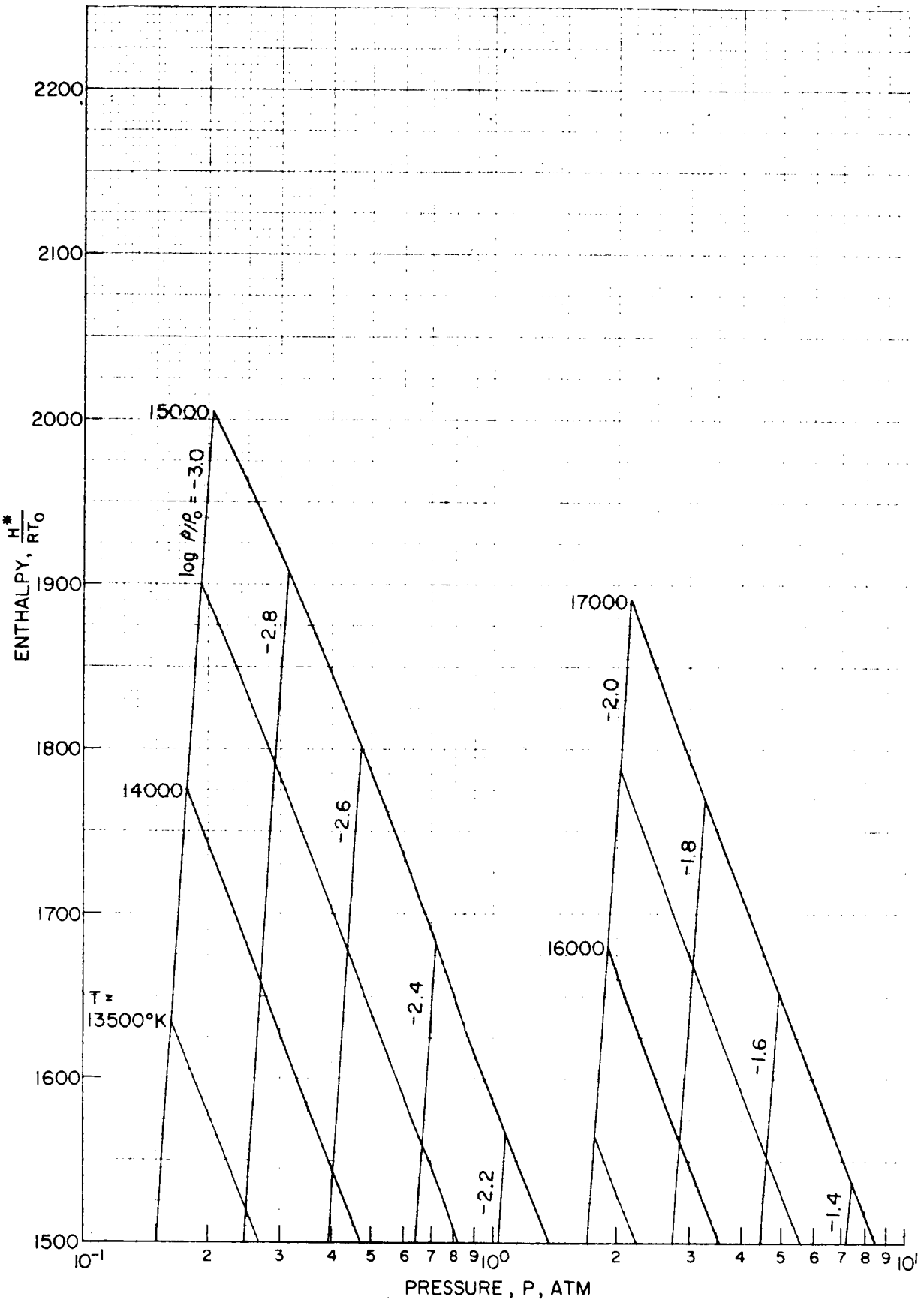

Figure 3.3 (Cont'd) Chart 6 Thermodynamic Charts for 3% CO_2 - 97% N_2

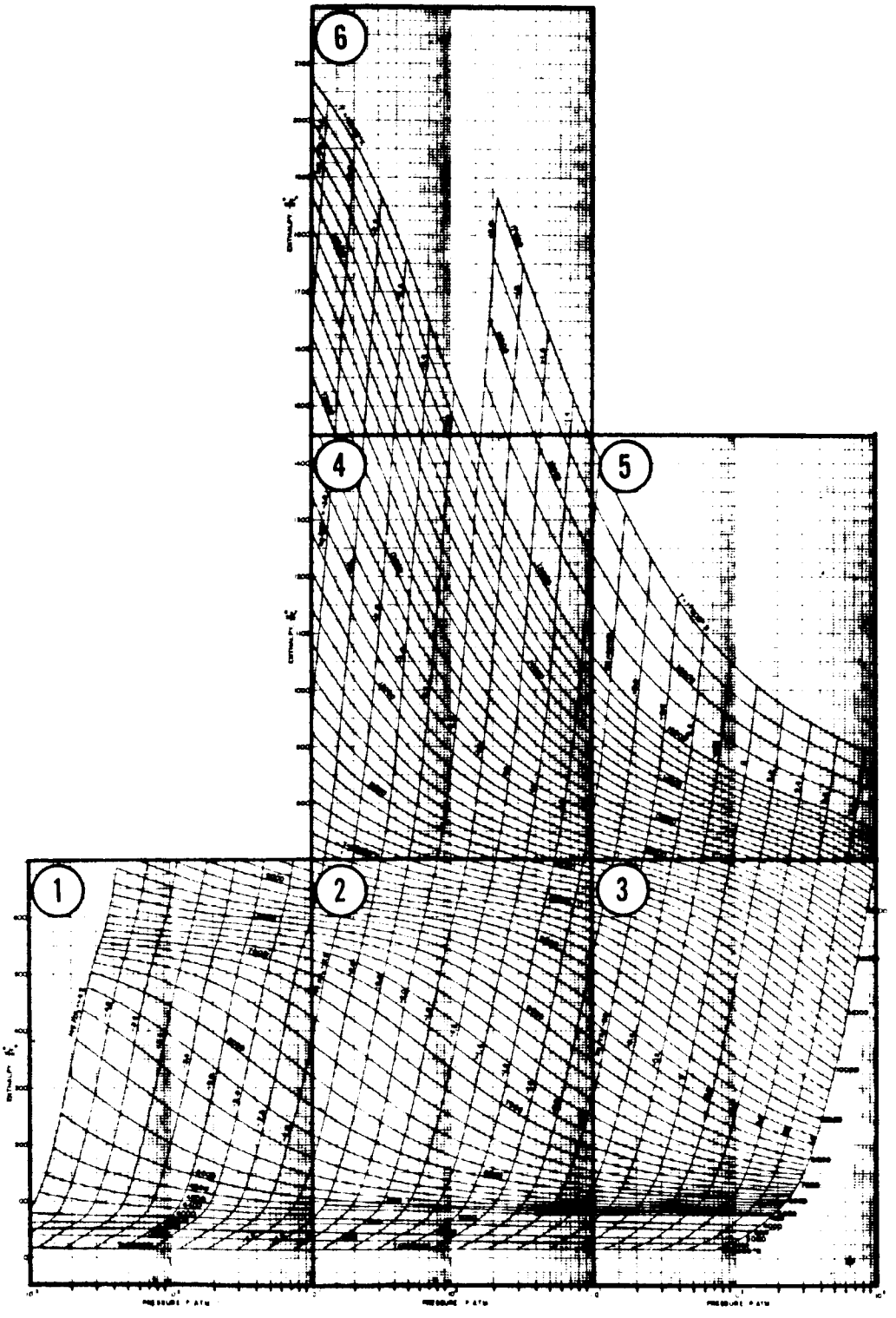

Figure 3.4 Key to Thermodynamic Charts for 9% CO_2 - 90% N_2 - 1% A

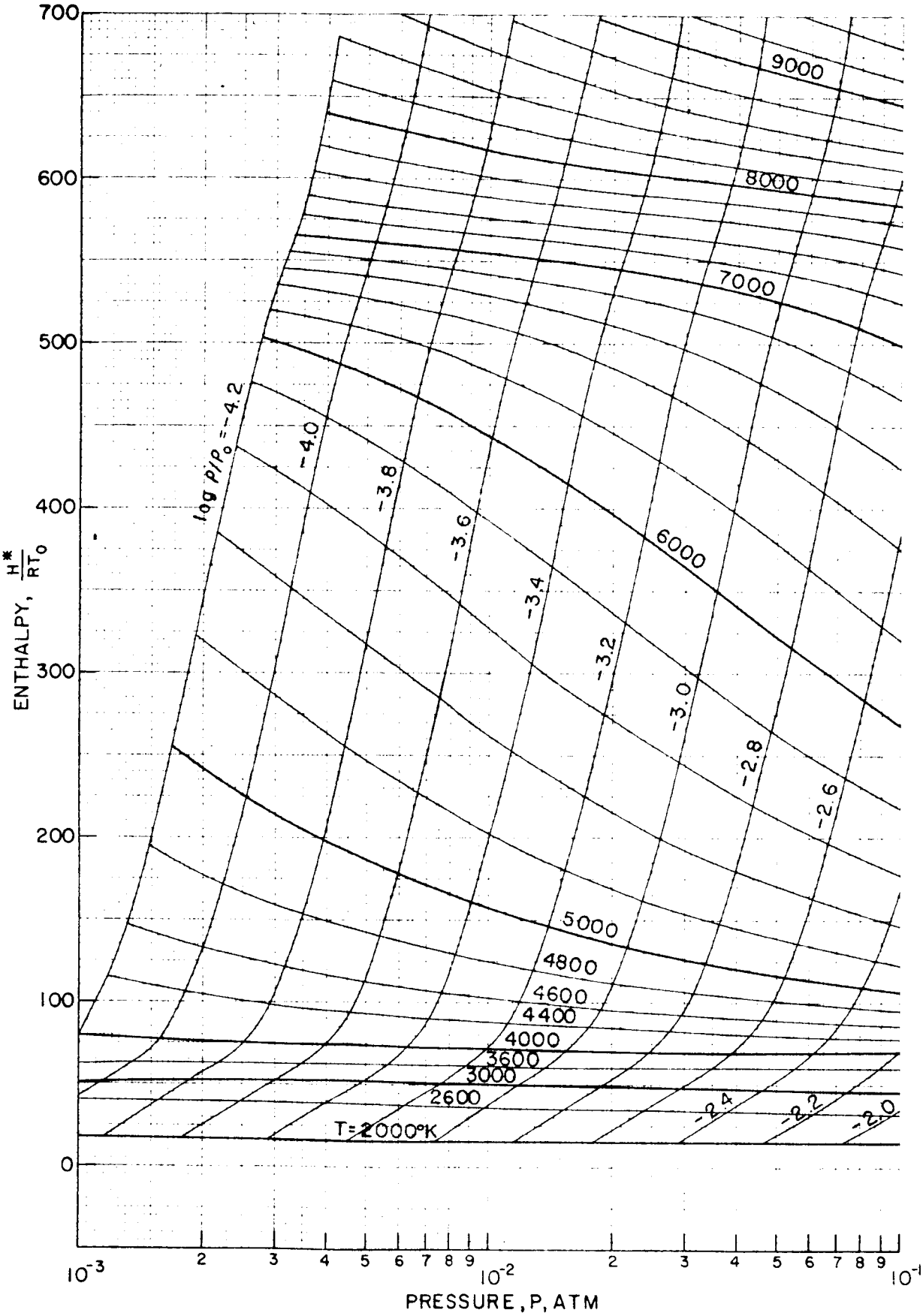

Figure 3.5 Chart 1 Thermodynamic Charts for 9% CO_2 - 90% N_2 - 1% A

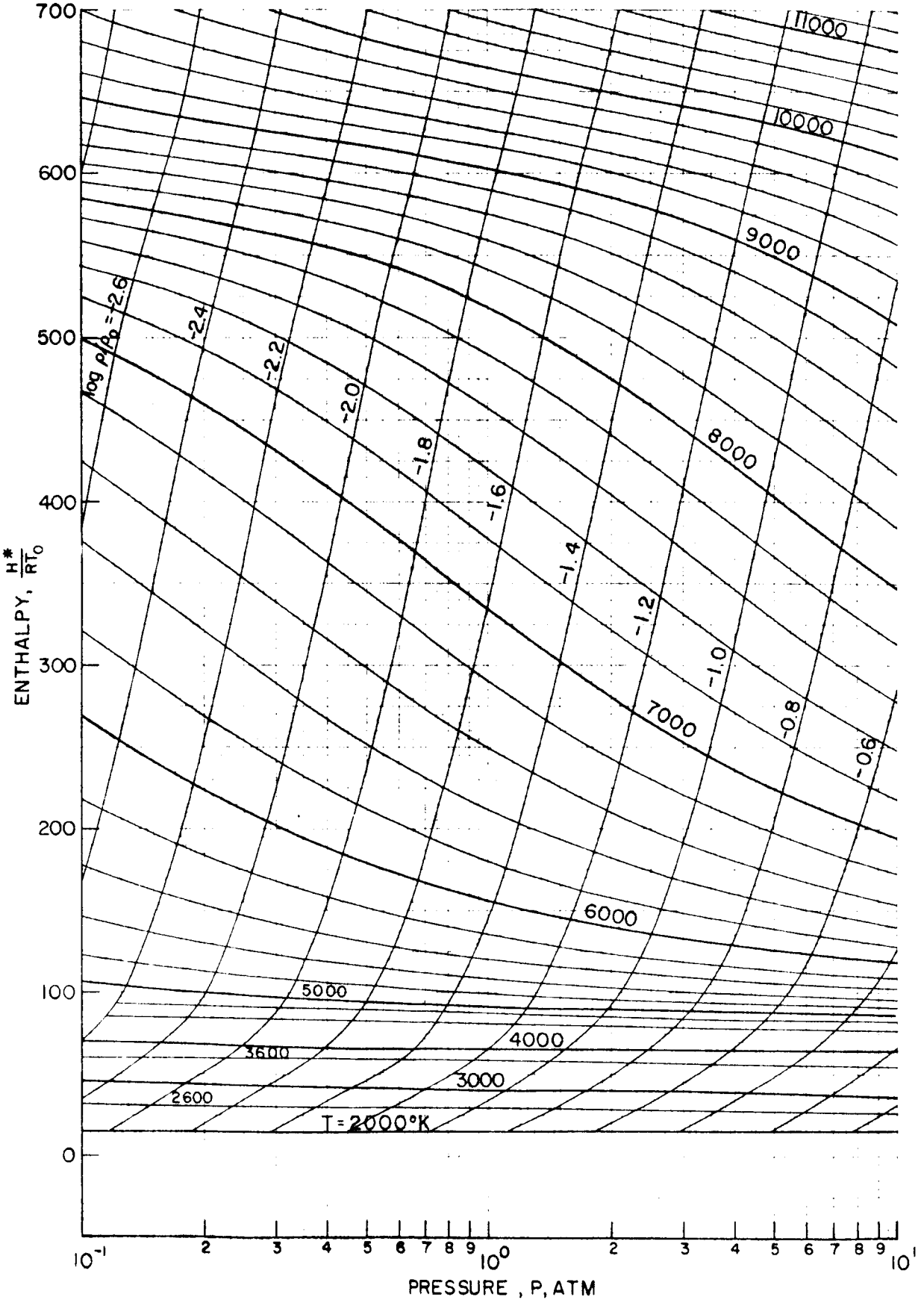

Figure 3.5 (Cont'd) Chart 2 Thermodynamic Charts for 9% CO_2 - 90% N_2 - 1% A

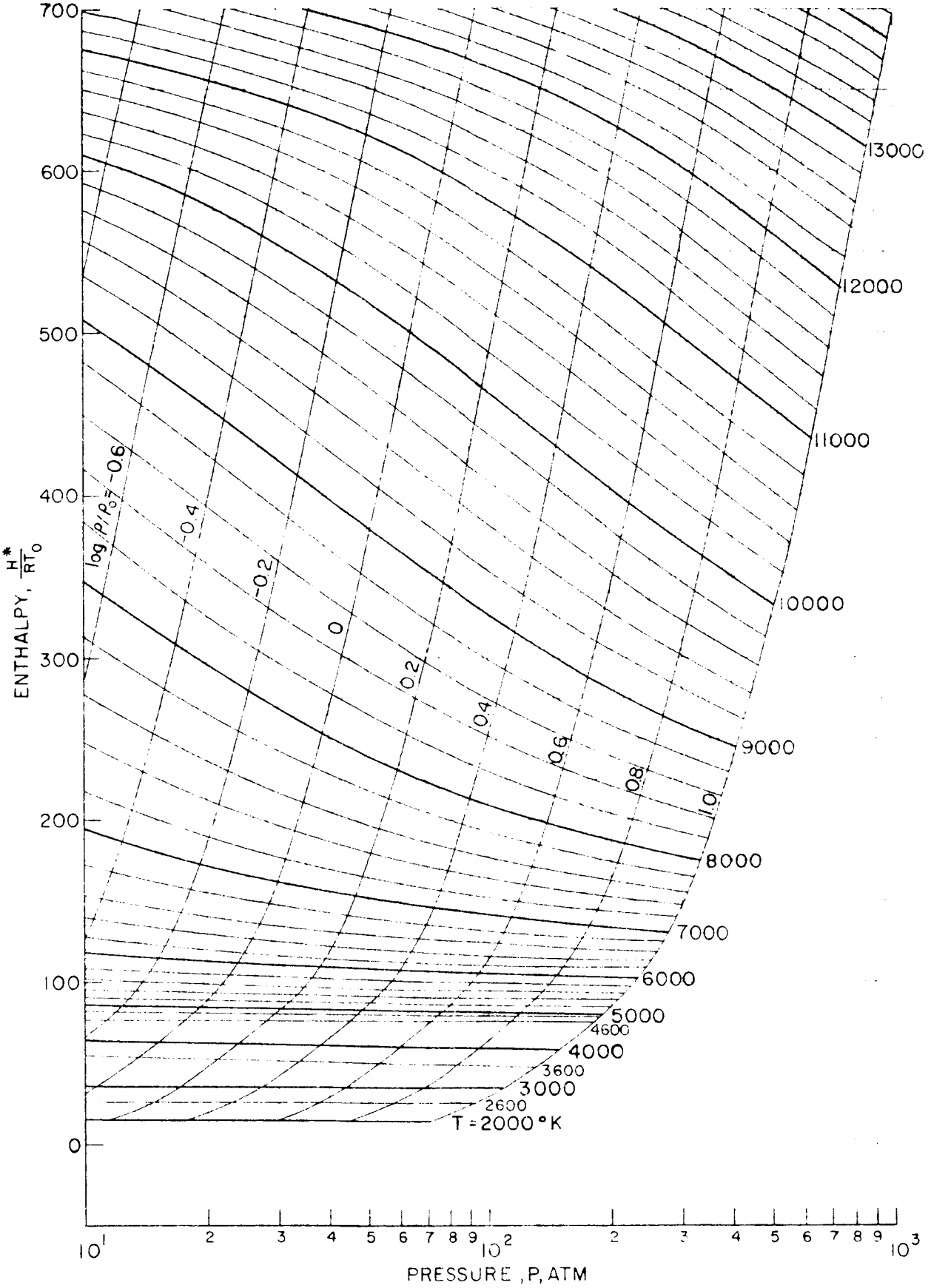

Figure 3.5 (Cont'd) Chart 3 Thermodynamic Charts for 4% CO_2 - 96% N_2 - 1% A

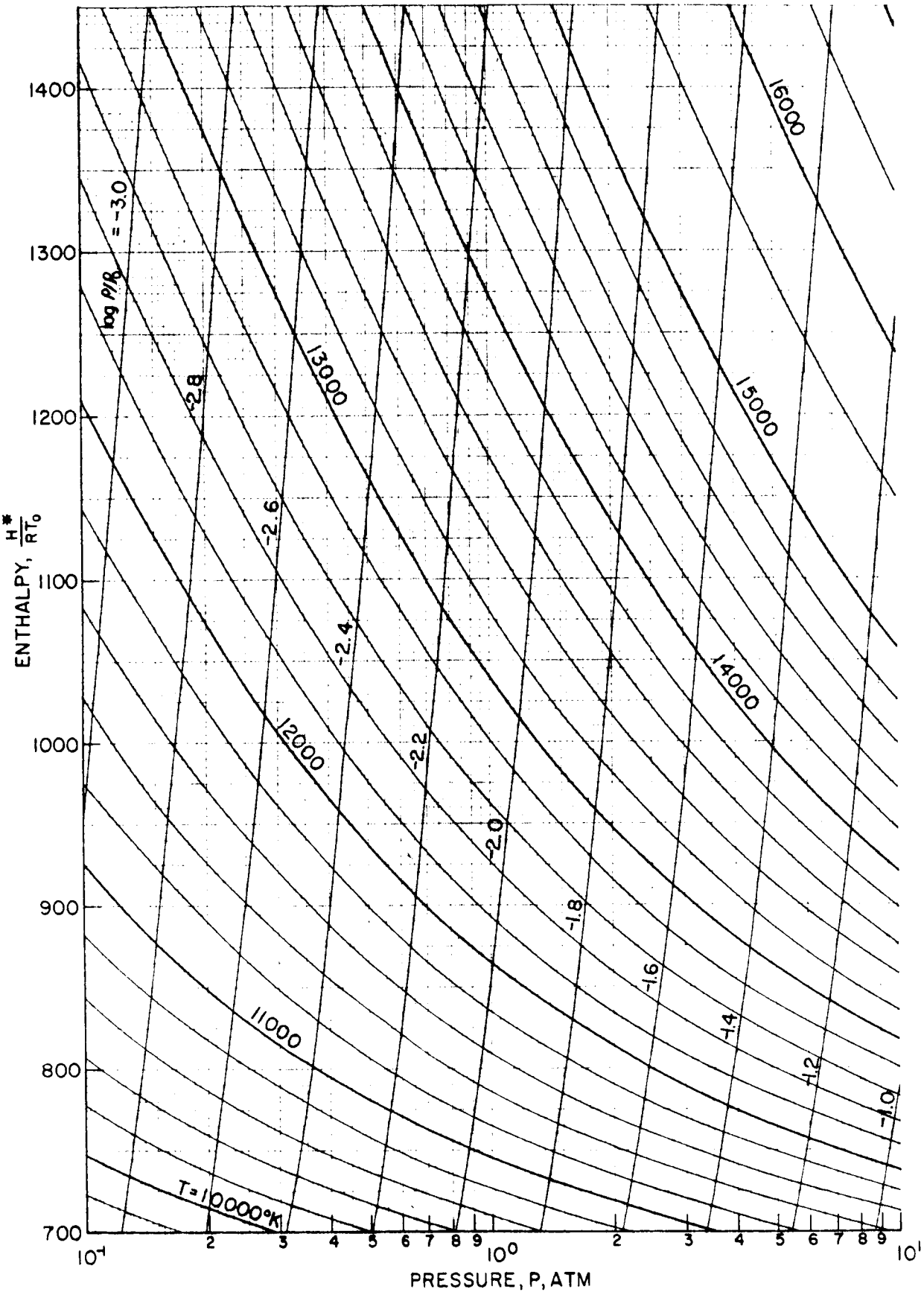

Figure 3.5 (Cont'd) Chart 4 Thermodynamic Charts for 9% CO_2 - 90% N_2 - 1% A

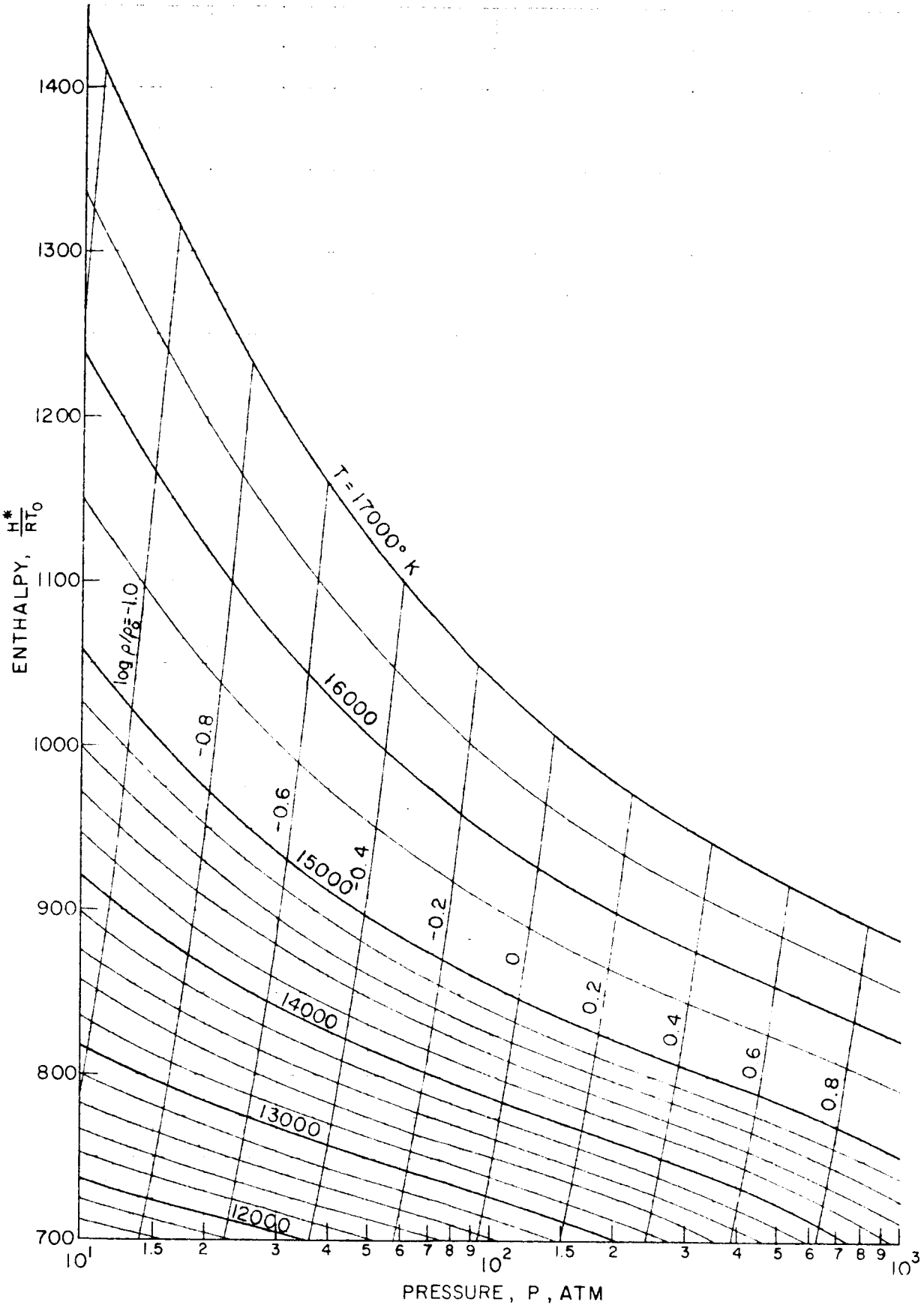

Figure 3.5 (Cont'd) Chart 5 Thermodynamic Charts for 9% CO_2 - 90% N_2 - 1% A

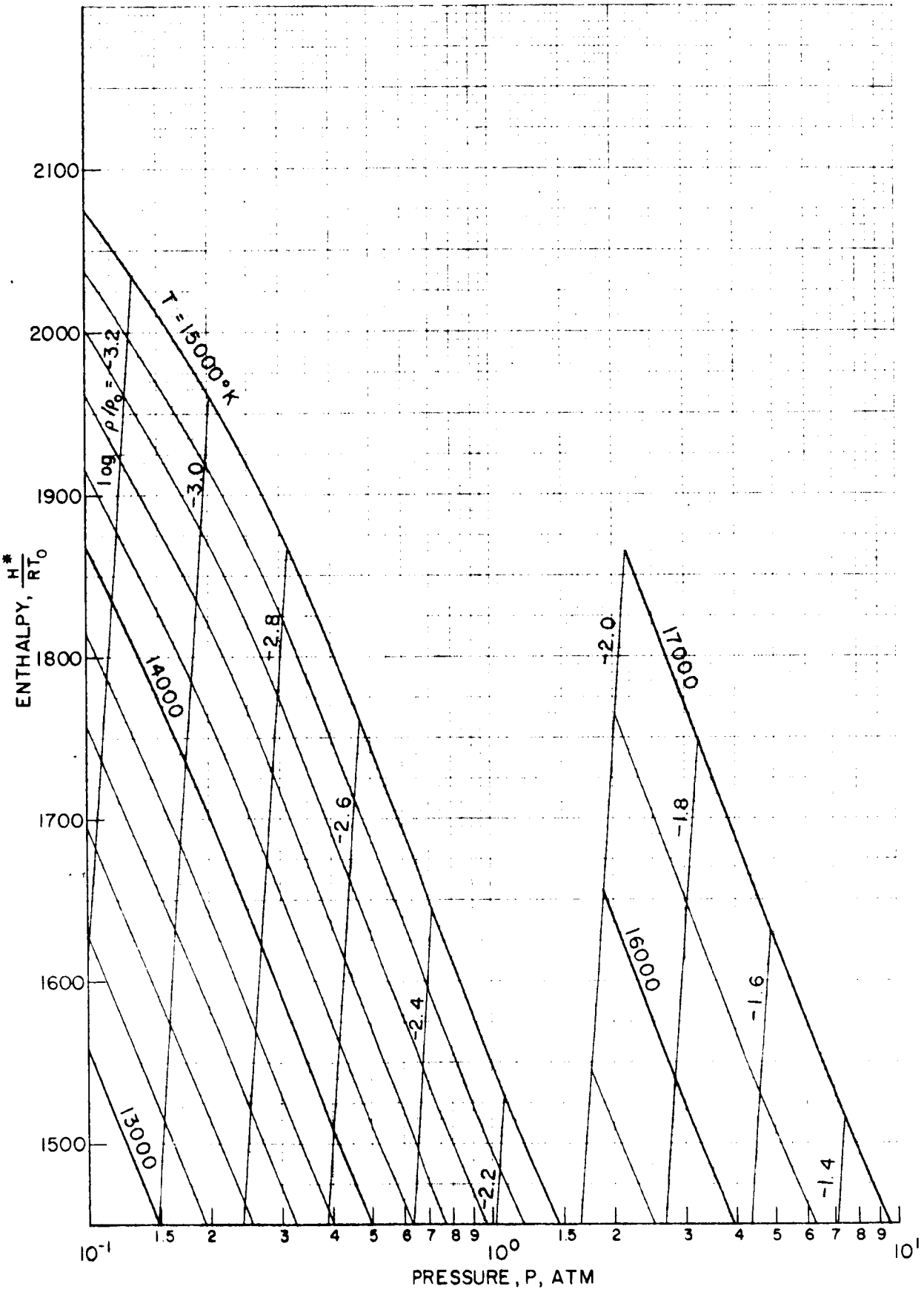

Figure 3.5 (Cont'd) Chart 6 Thermodynamic Charts for 9% CO_2 - 90% N_2 - 1% A

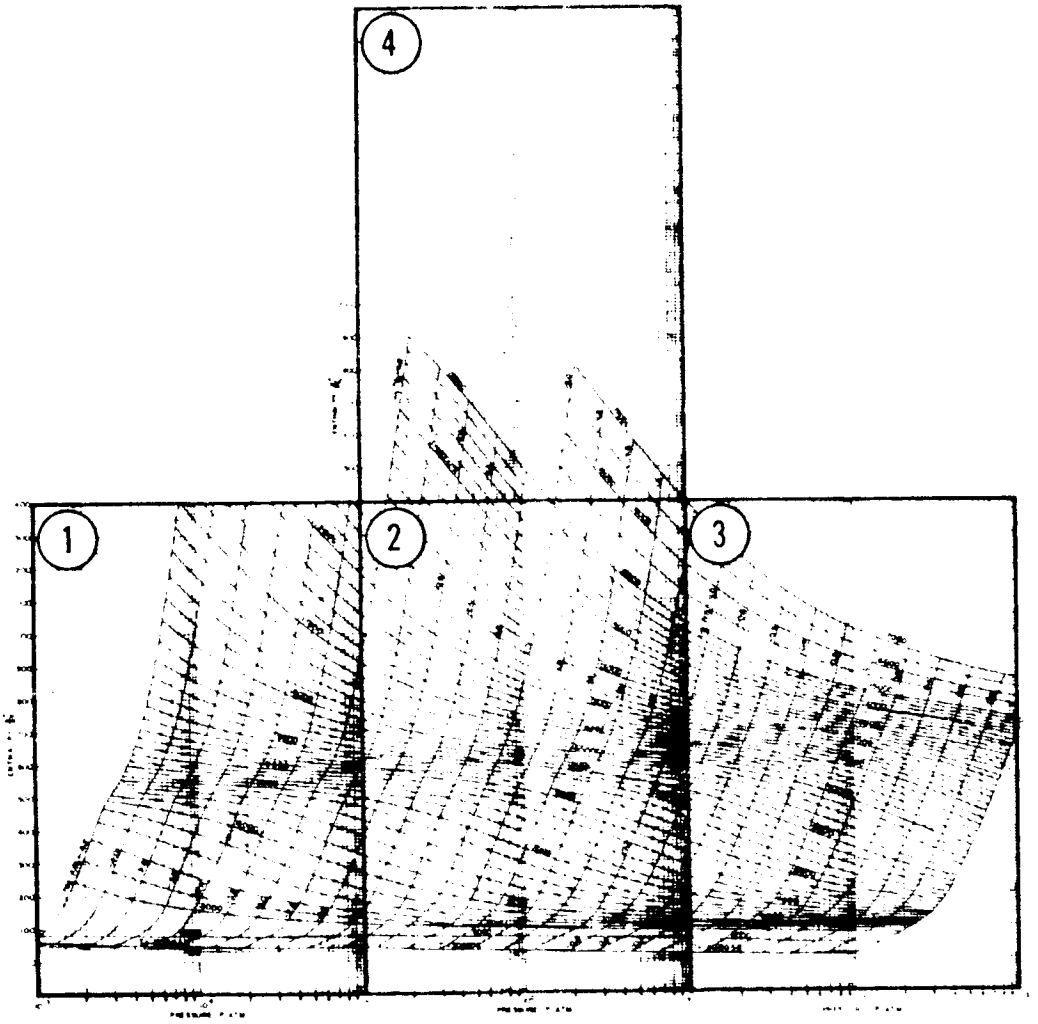

Figure 3.6 Key to Thermodynamic Properties 25% CO_2 - 74% N_2 - 1% A

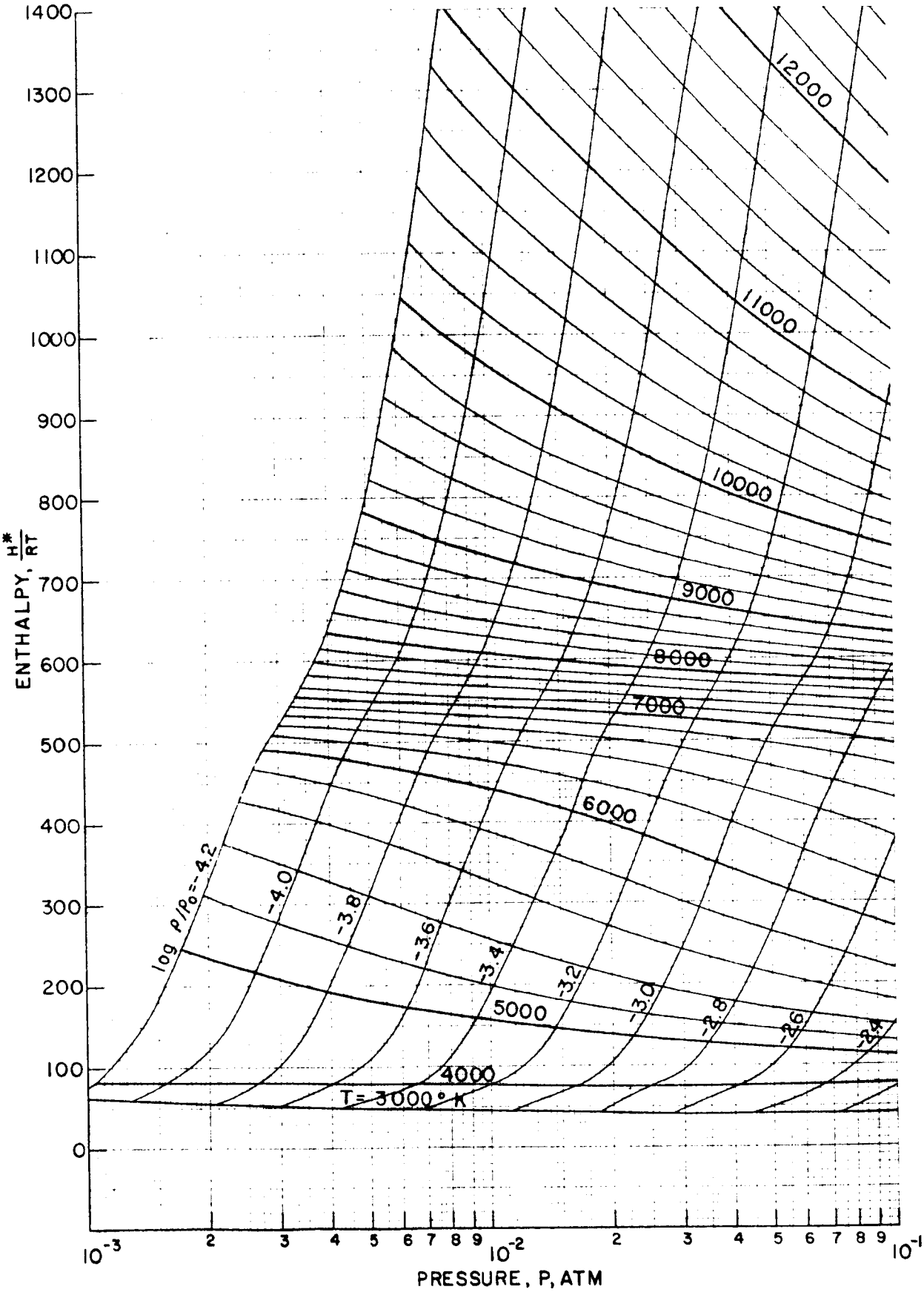

Figure 3.7 Chart 1 Thermodynamic Charts for 25% CO_2 - 74% N_2 1 1% A

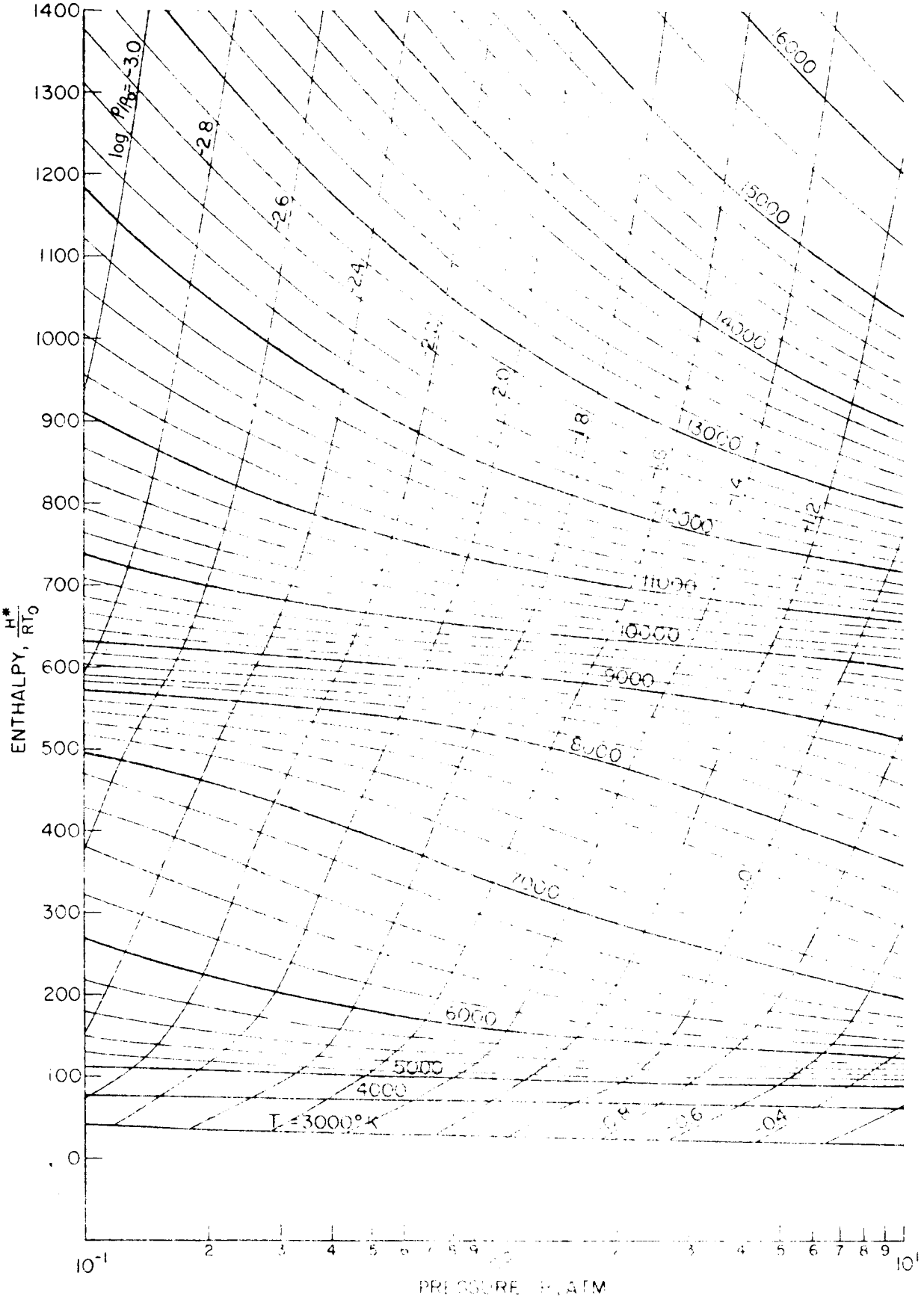

Figure 3.7 (Cont'd) Chart 2 Thermodynamic Charts for CO_2 - H_2O - N_2 at 10% CO_2

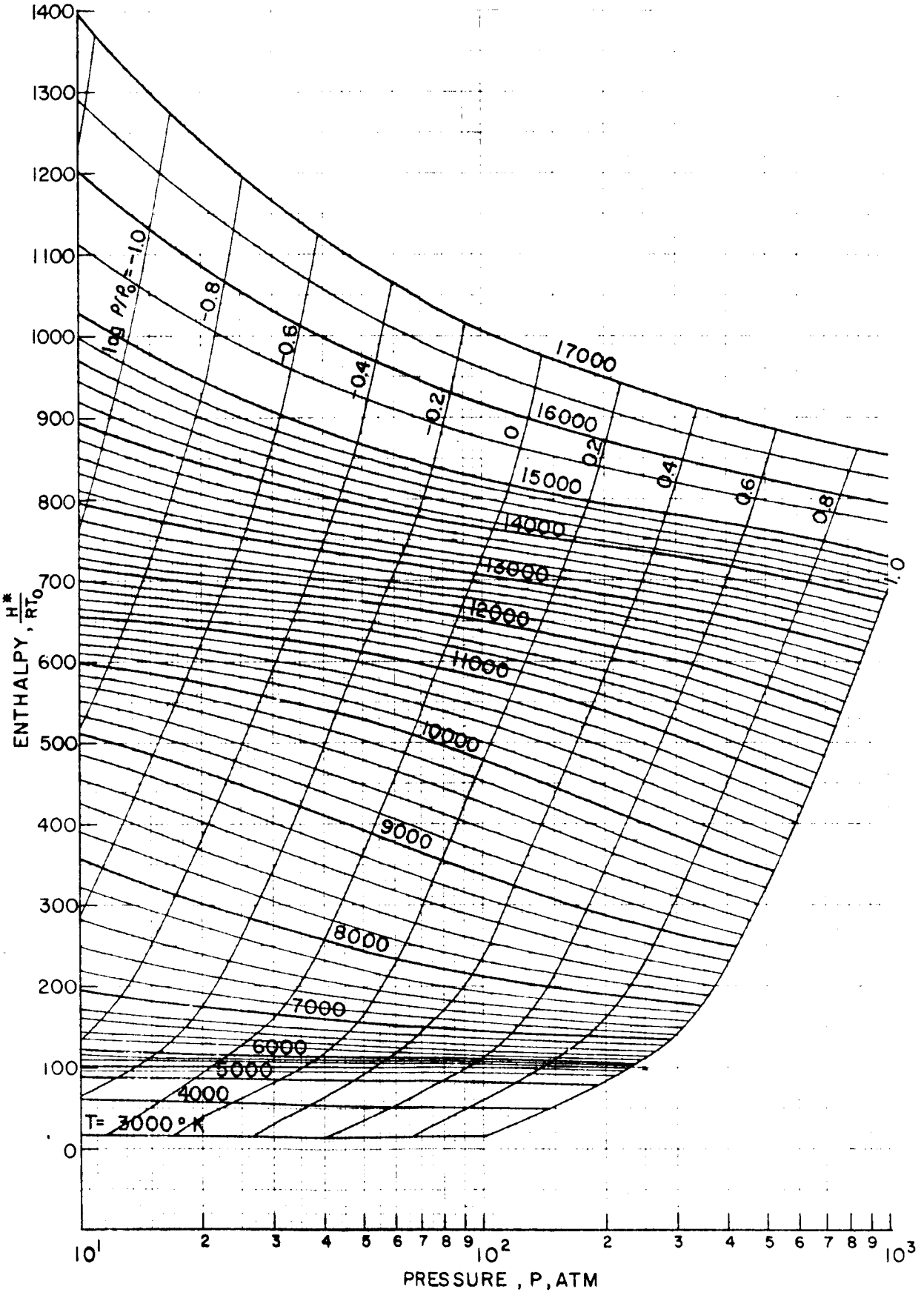

Figure 3.7 (Cont'd) Chart 3 Thermodynamic Charts for 25% CO_2 - 74% N_2 - 1% A

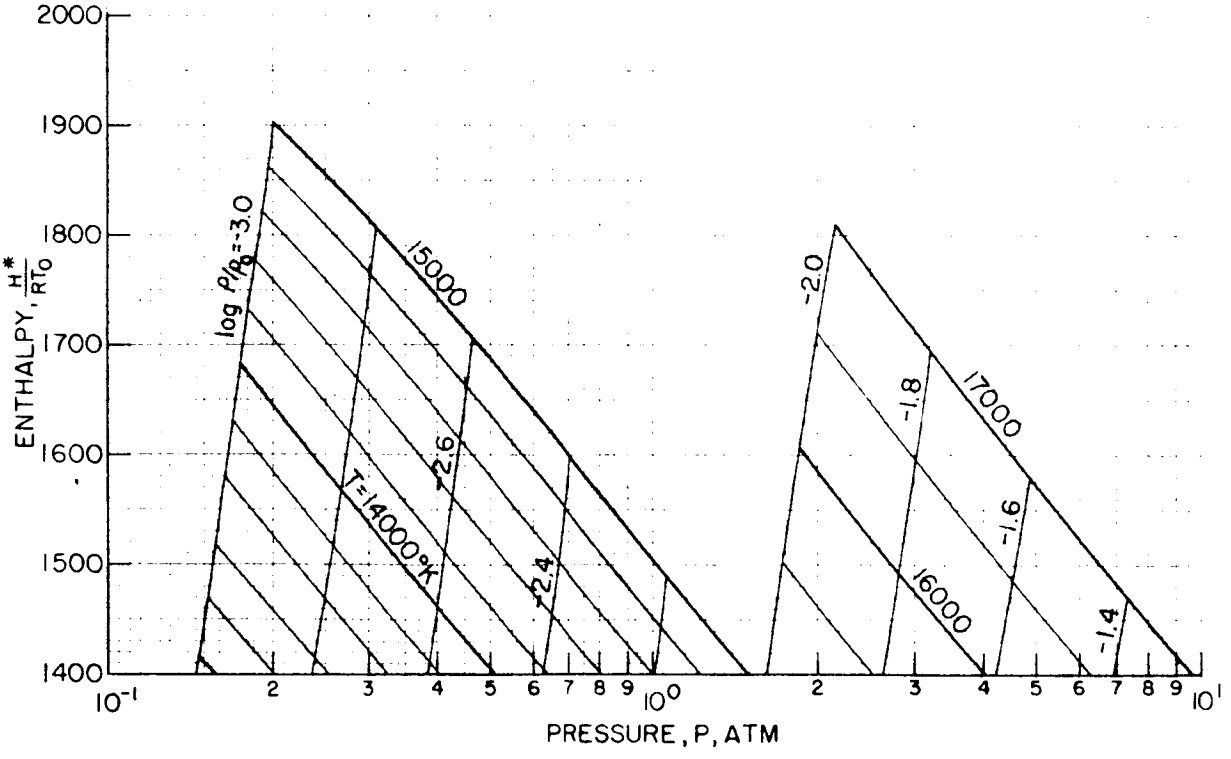

Figure 3.7 (Cont'd) Chart 4 Thermodynamic Charts for 25% CO_2 74% N_2 - 1% A

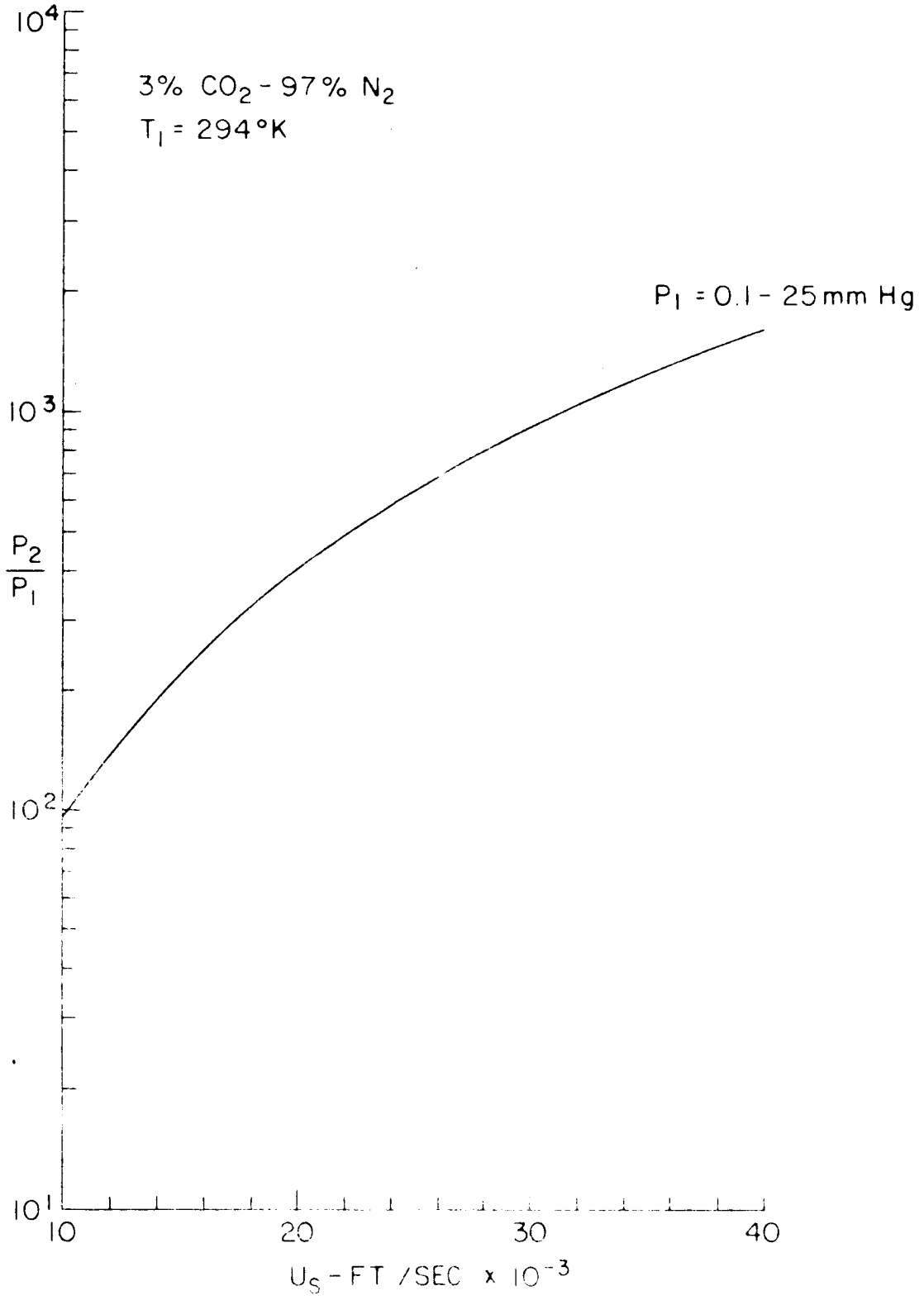

Figure 2.5 Pressure Ratio Across Incident Shock

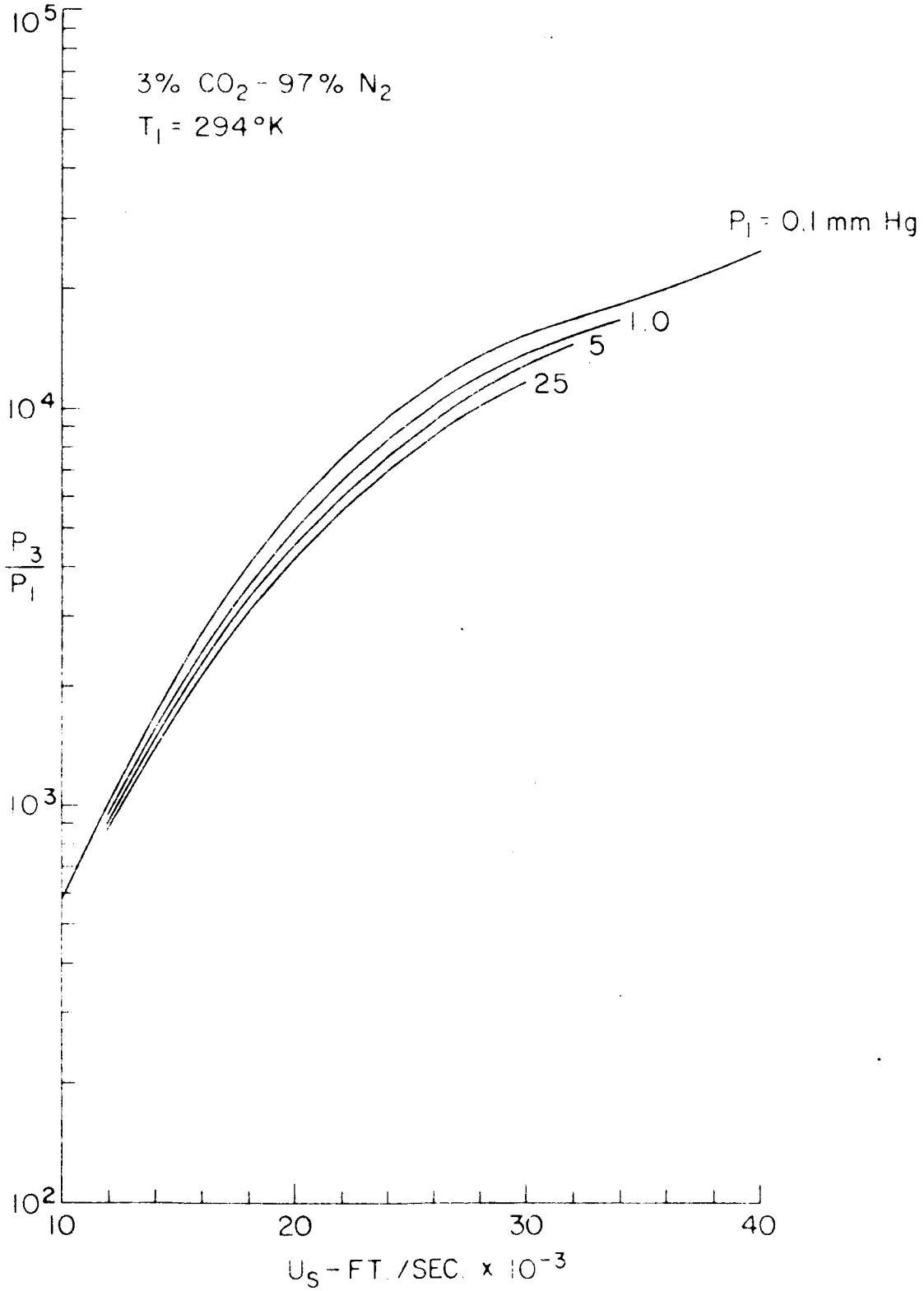

Figure 3. Pressure Behind Normal Shock

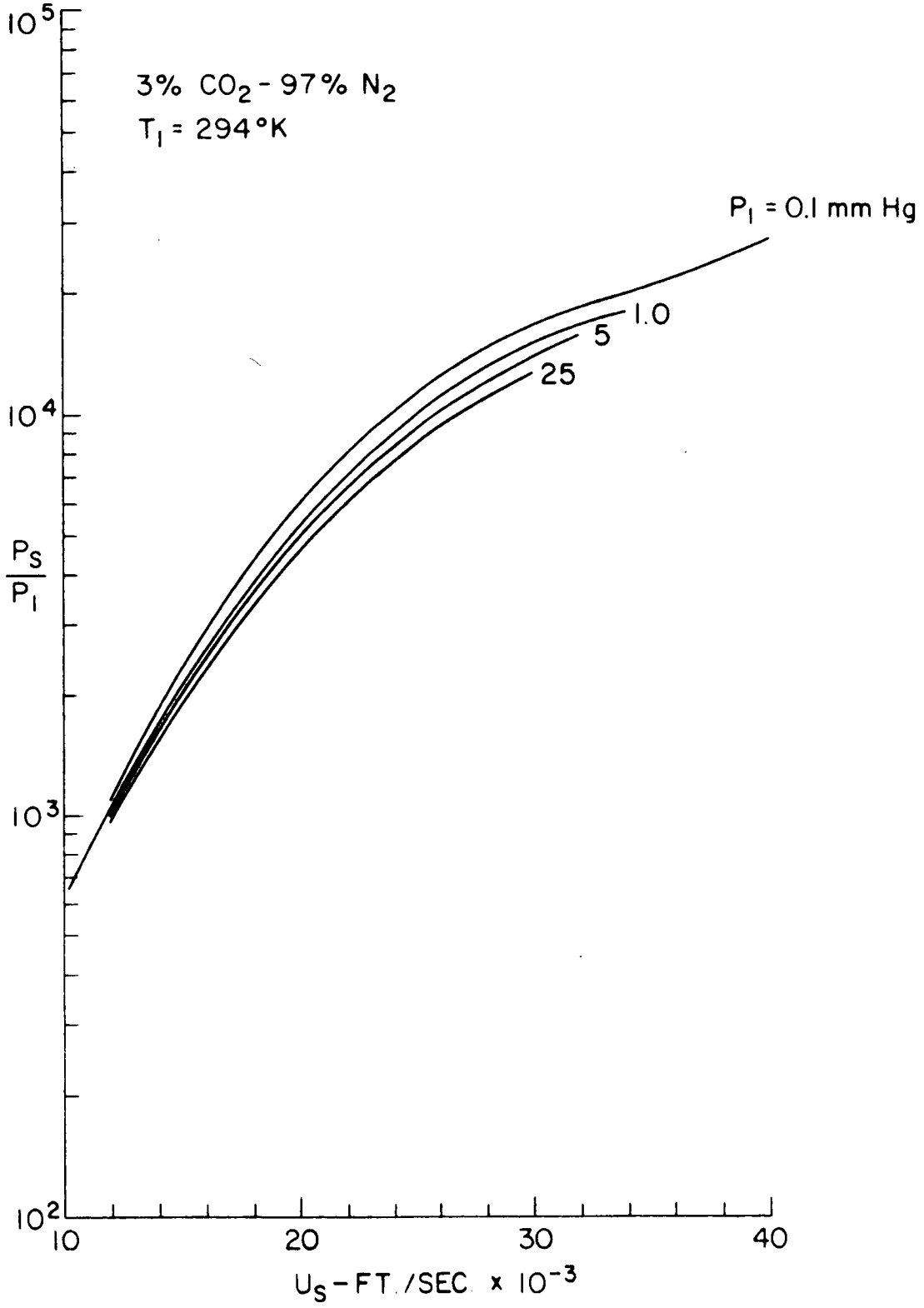

Figure 3.10 Stagnation Pressure

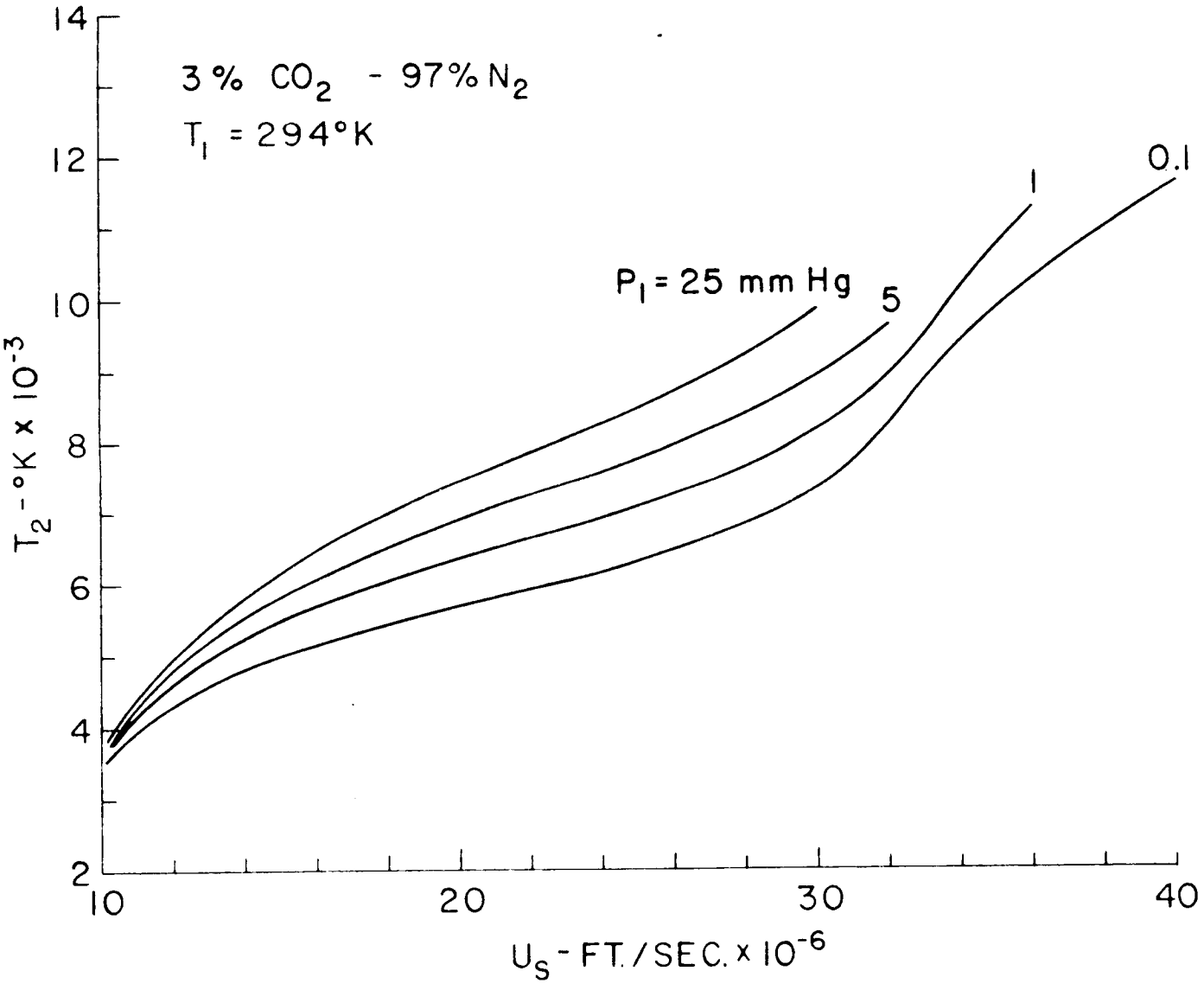

Figure 3.11 Temperature Behind Incident Shock

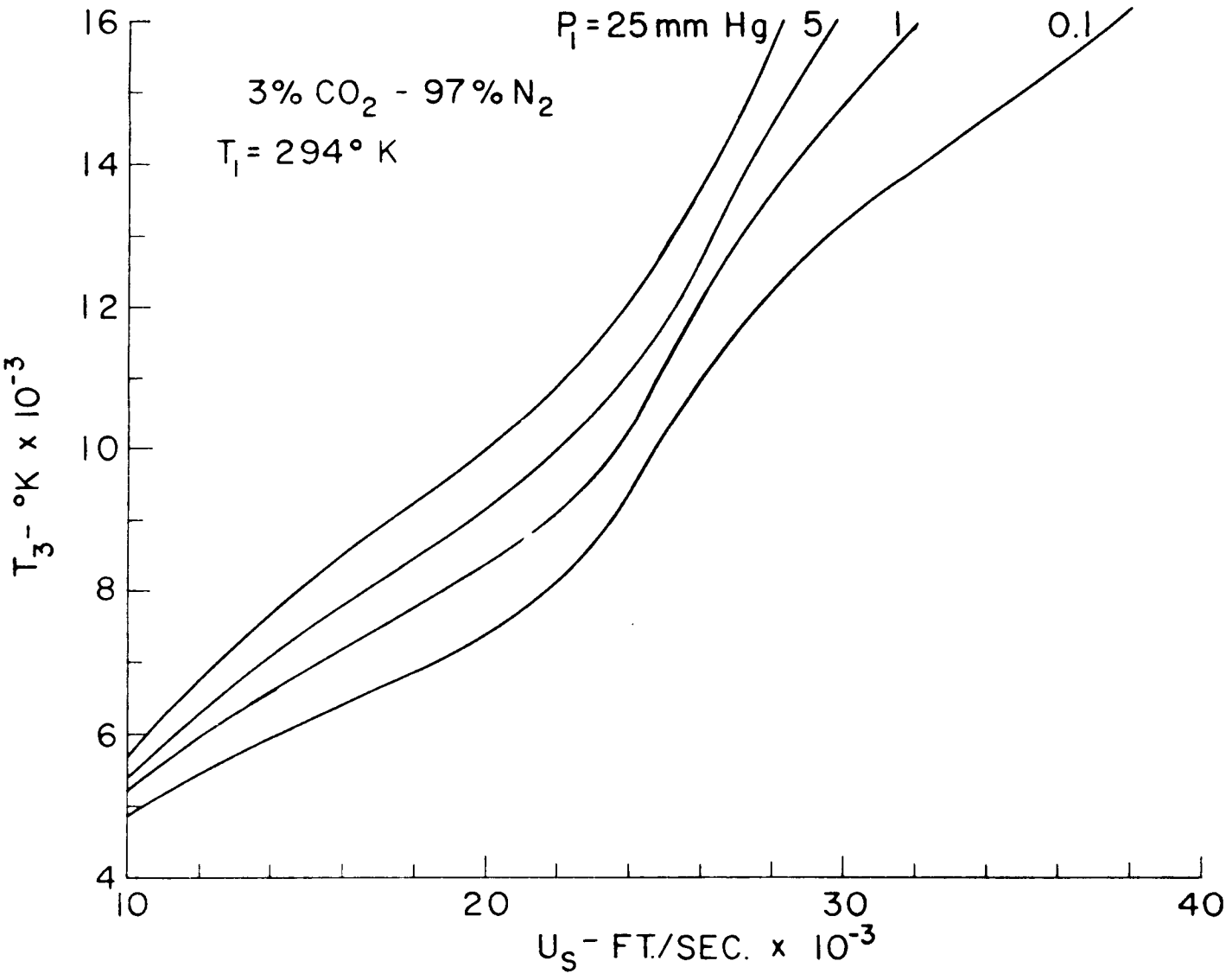

Figure 3.12 Temperature Behind Normal Shock

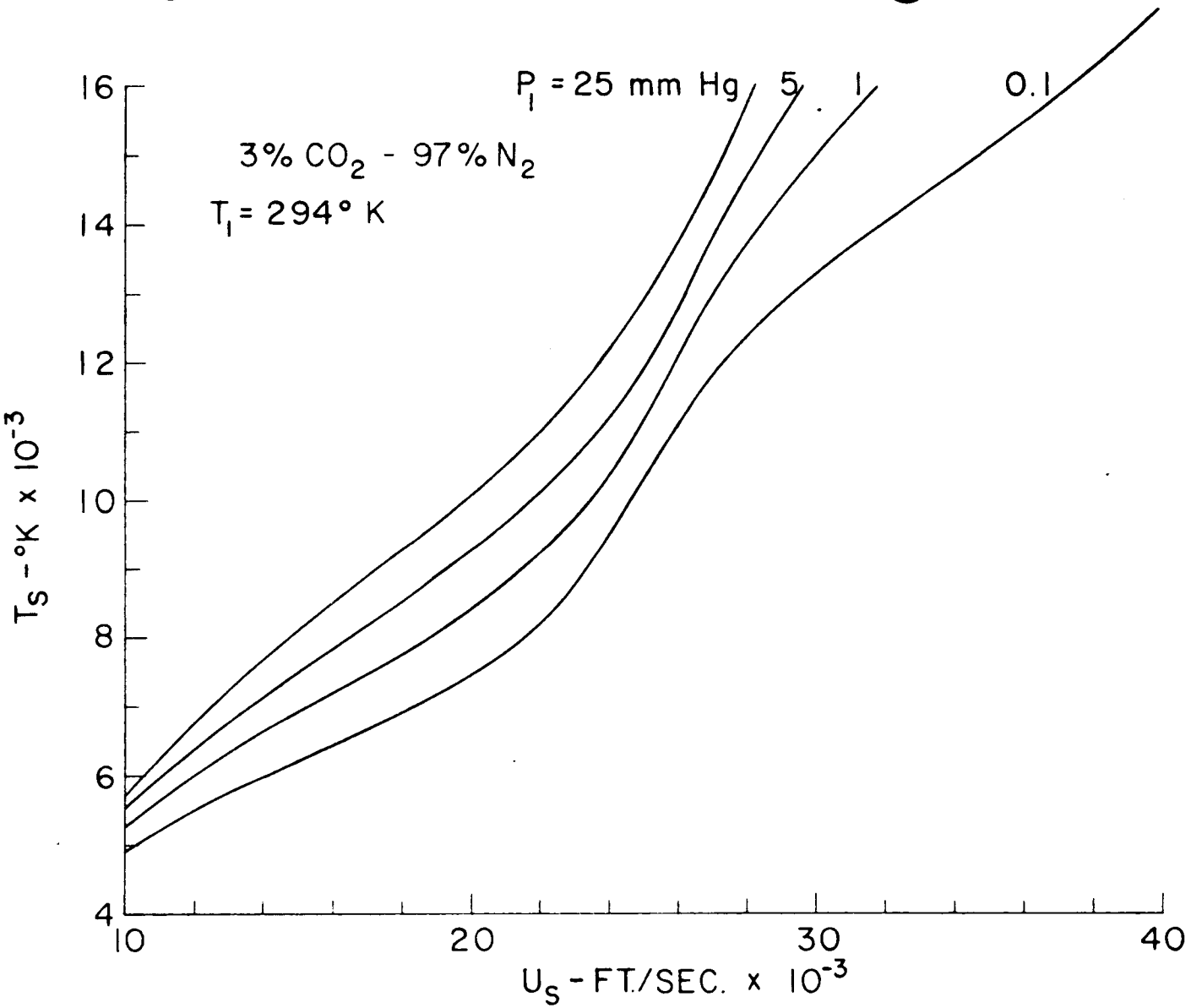

Figure 3.13 Stagnation Temperature

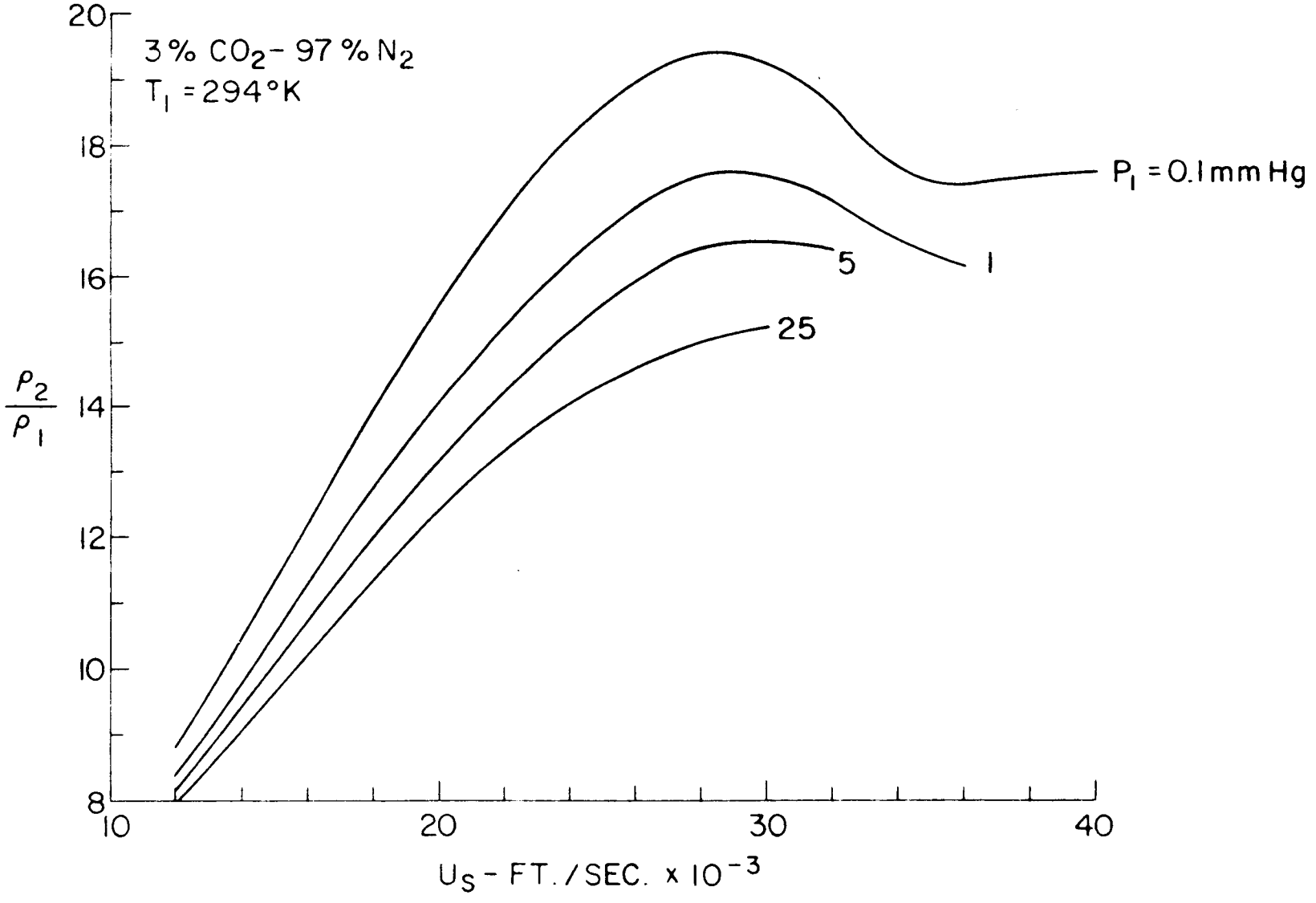

Figure 3.14 Density Behind Incident Shock

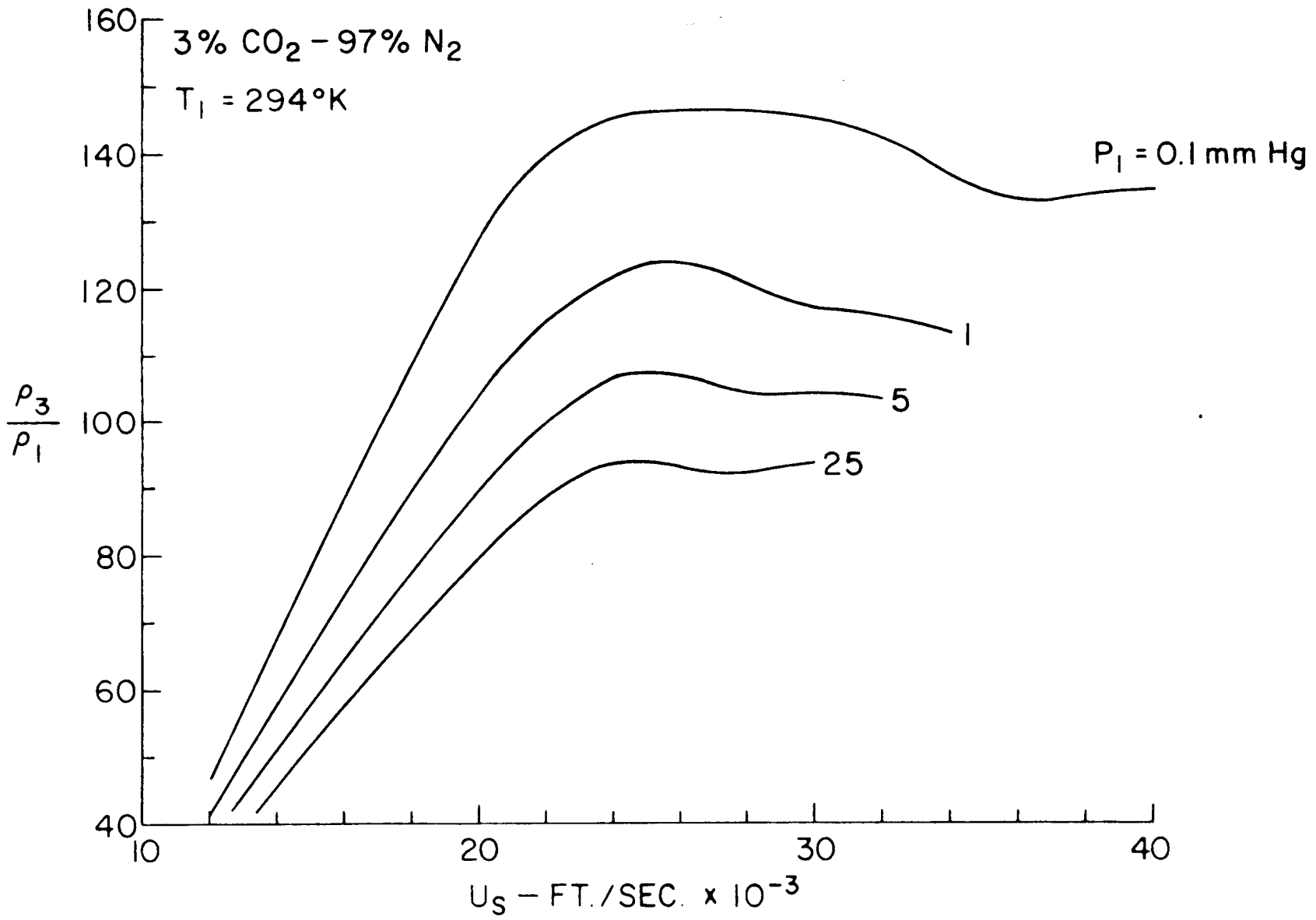

Figure 3.15 Density Behind Normal Shock

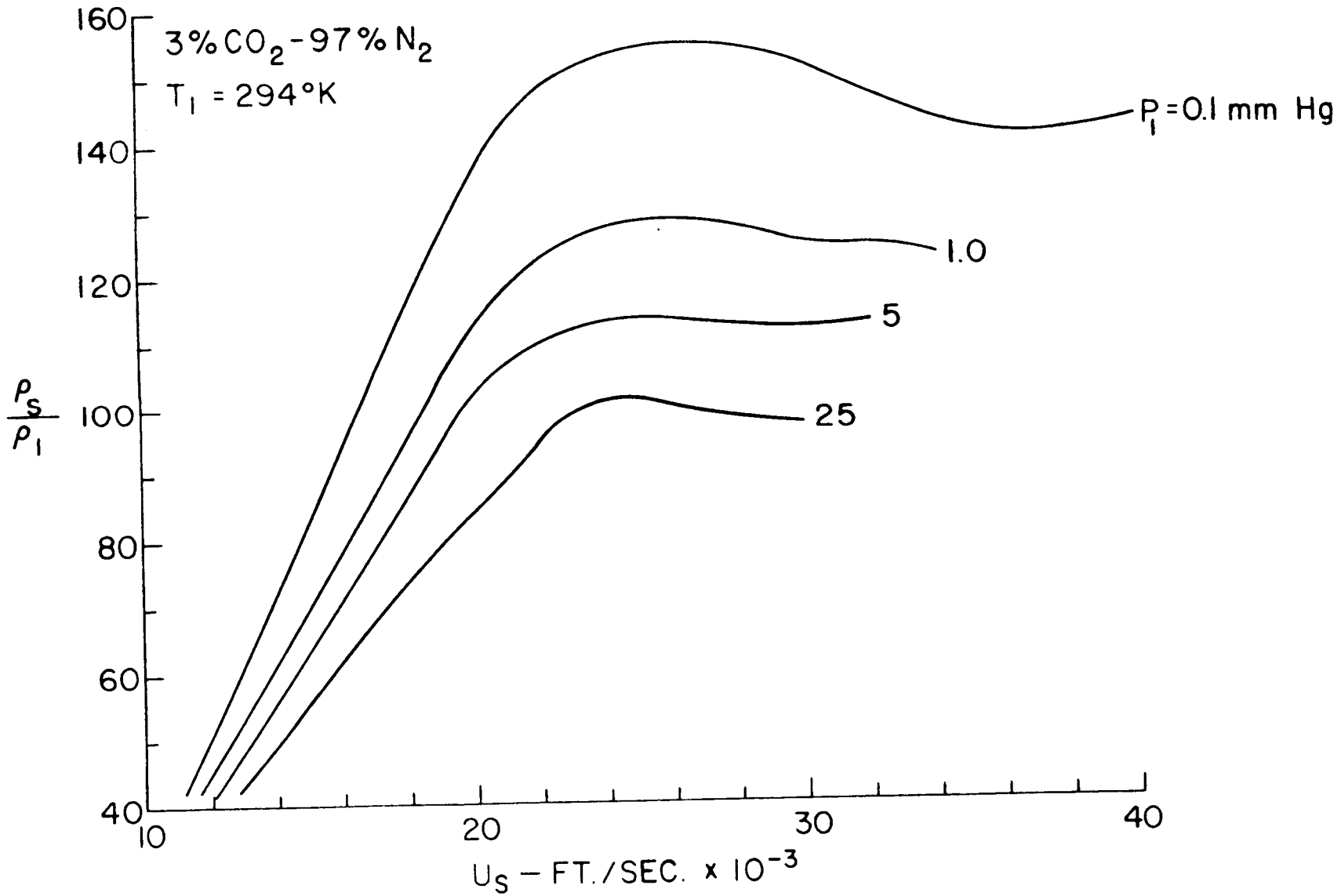

Figure 3.16 Stagnation Density

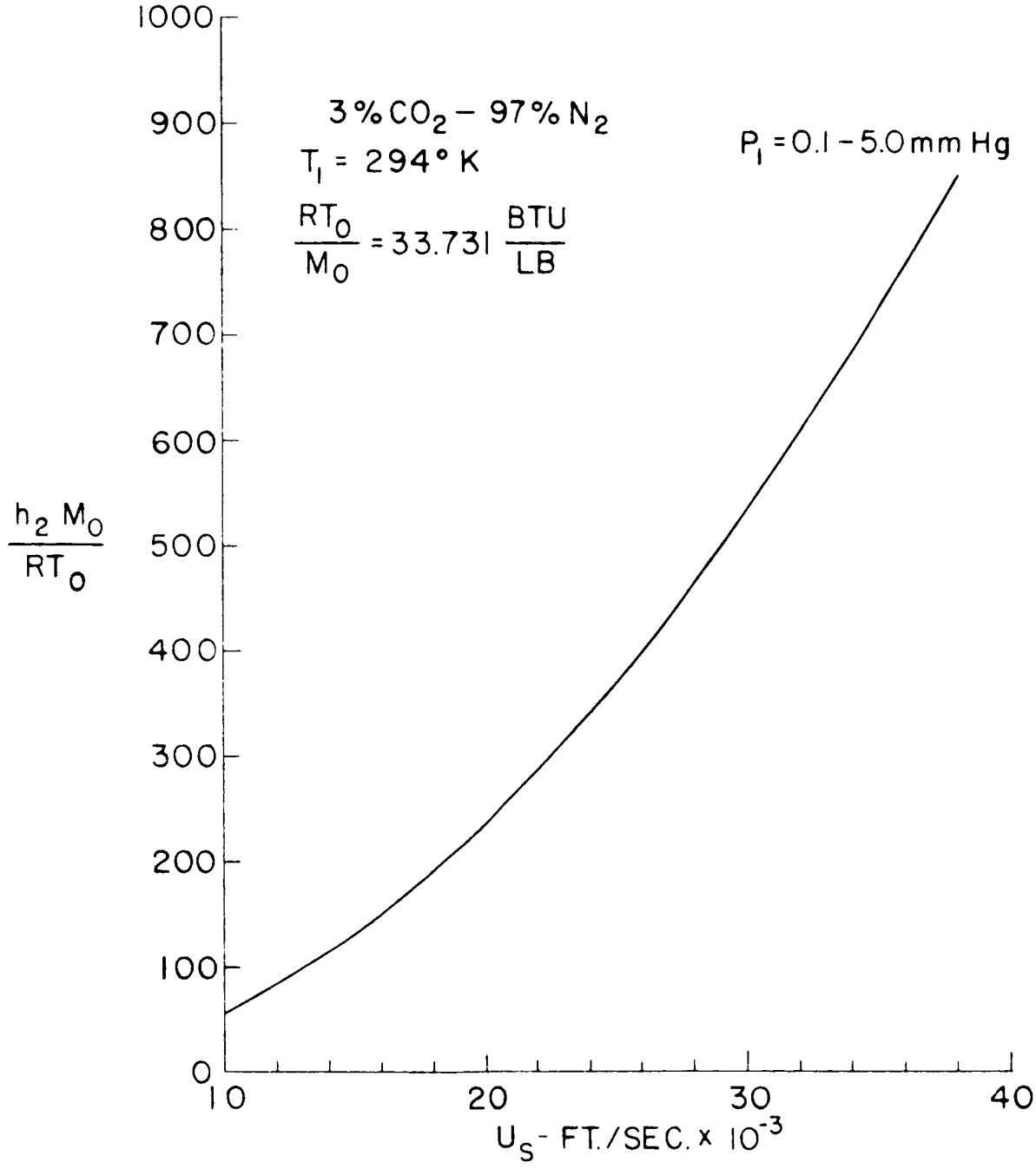

Figure 3.17 Enthalpy Behind Incident Shock

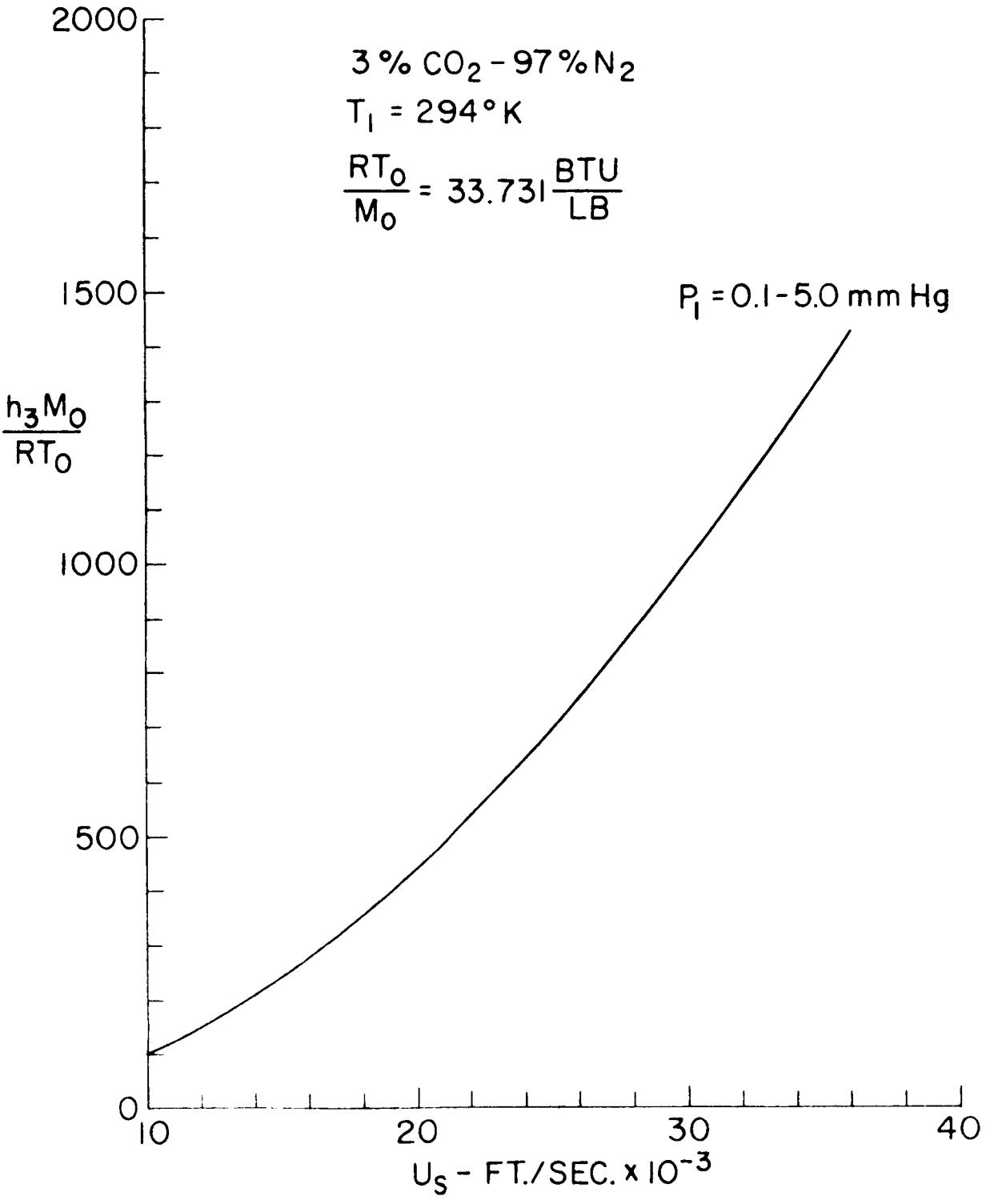

Figure 3.18 Enthalpy Behind Normal Shock

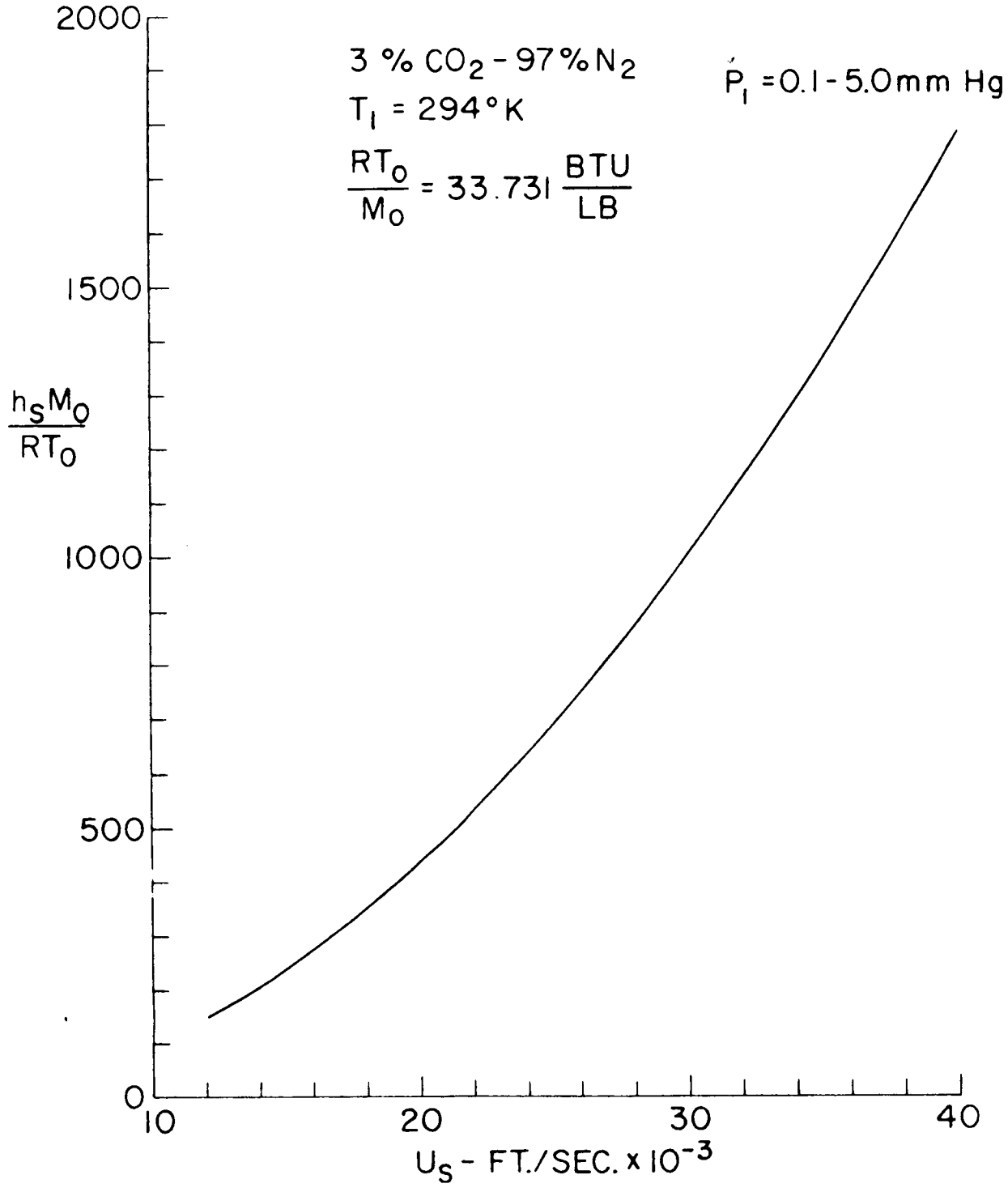

Figure 3.19 Stagnation Enthalpy

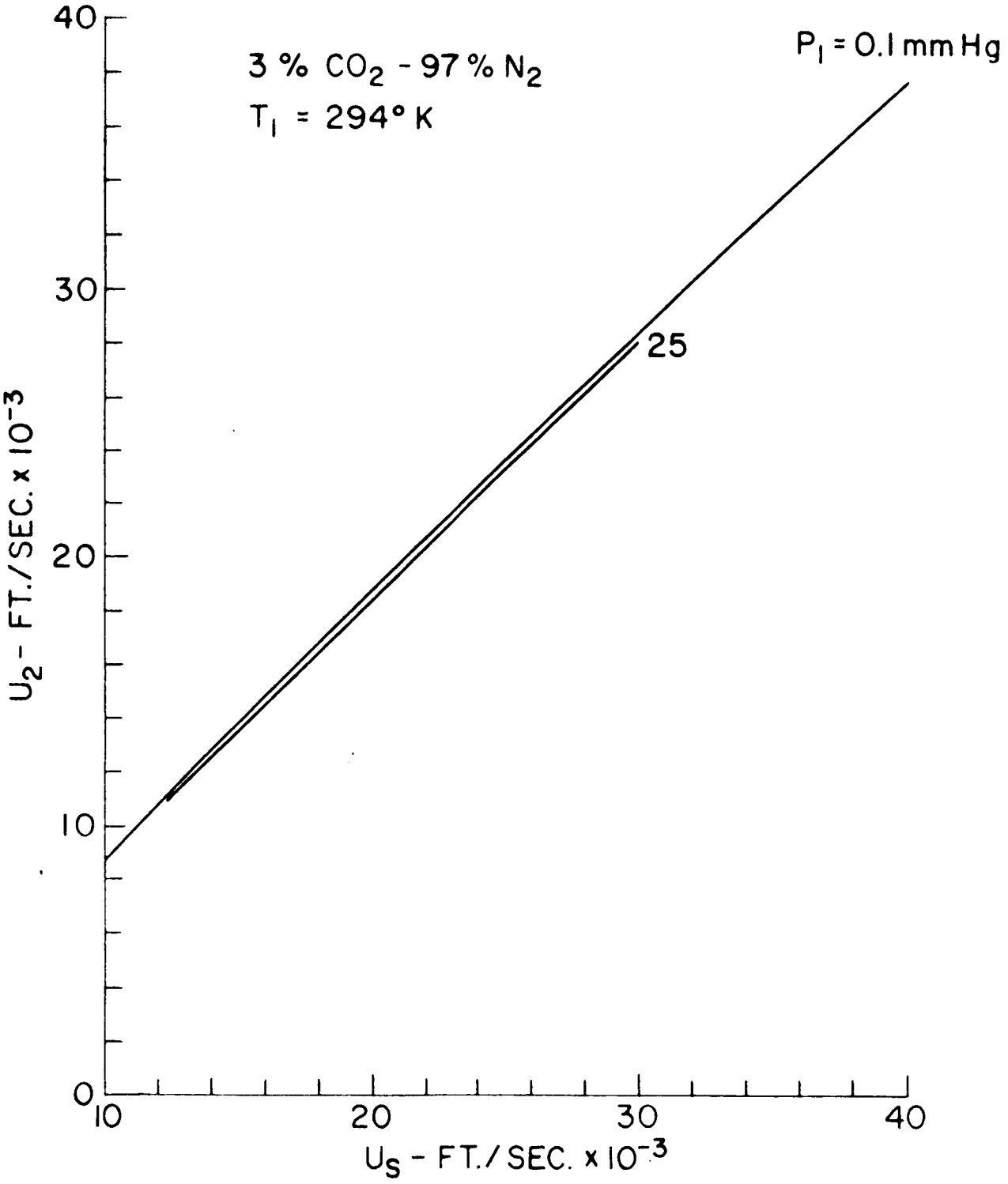

Figure 3.20 Velocity Behind Incident Shock

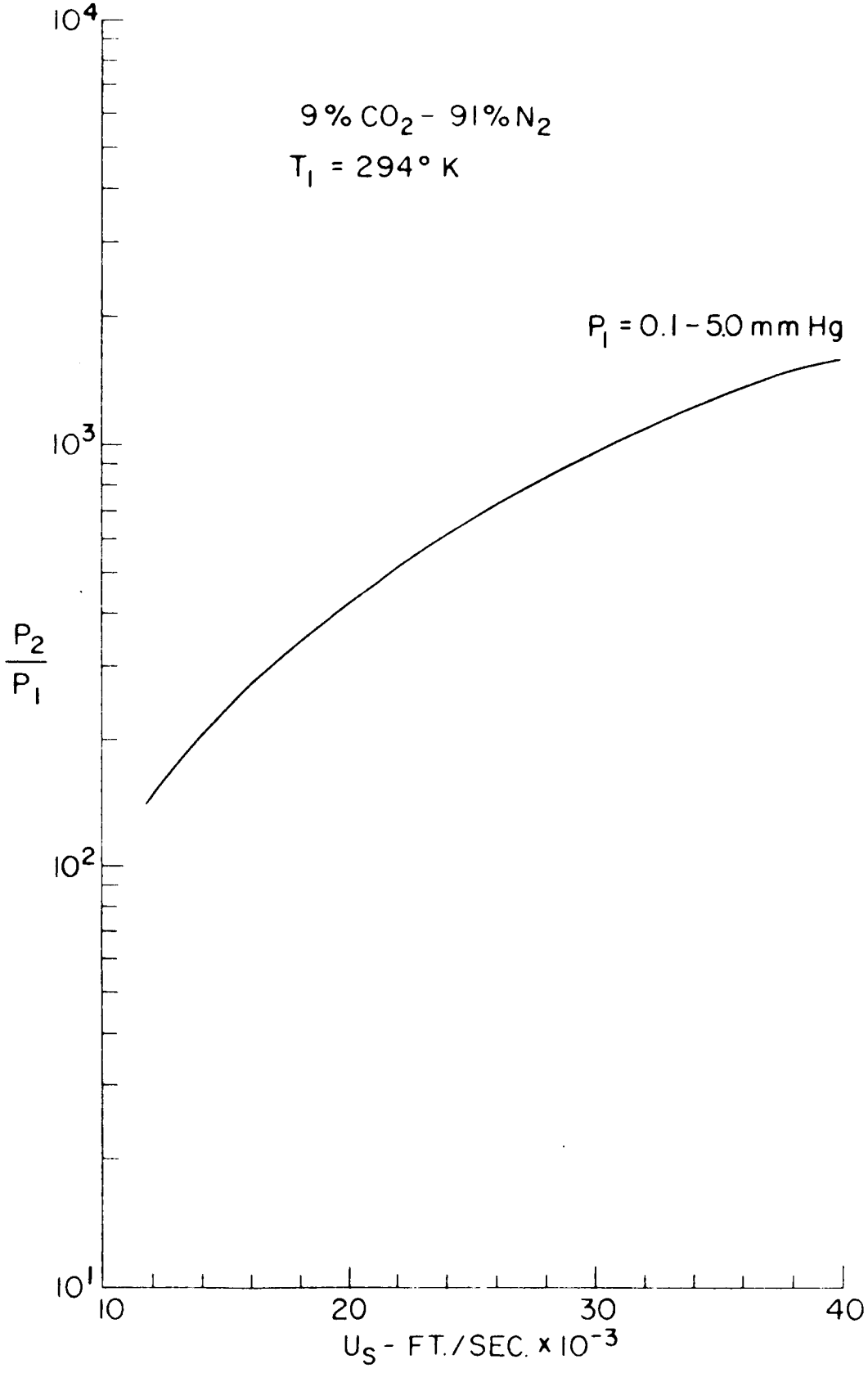

Figure 3.21 Pressure Behind Incident Shock

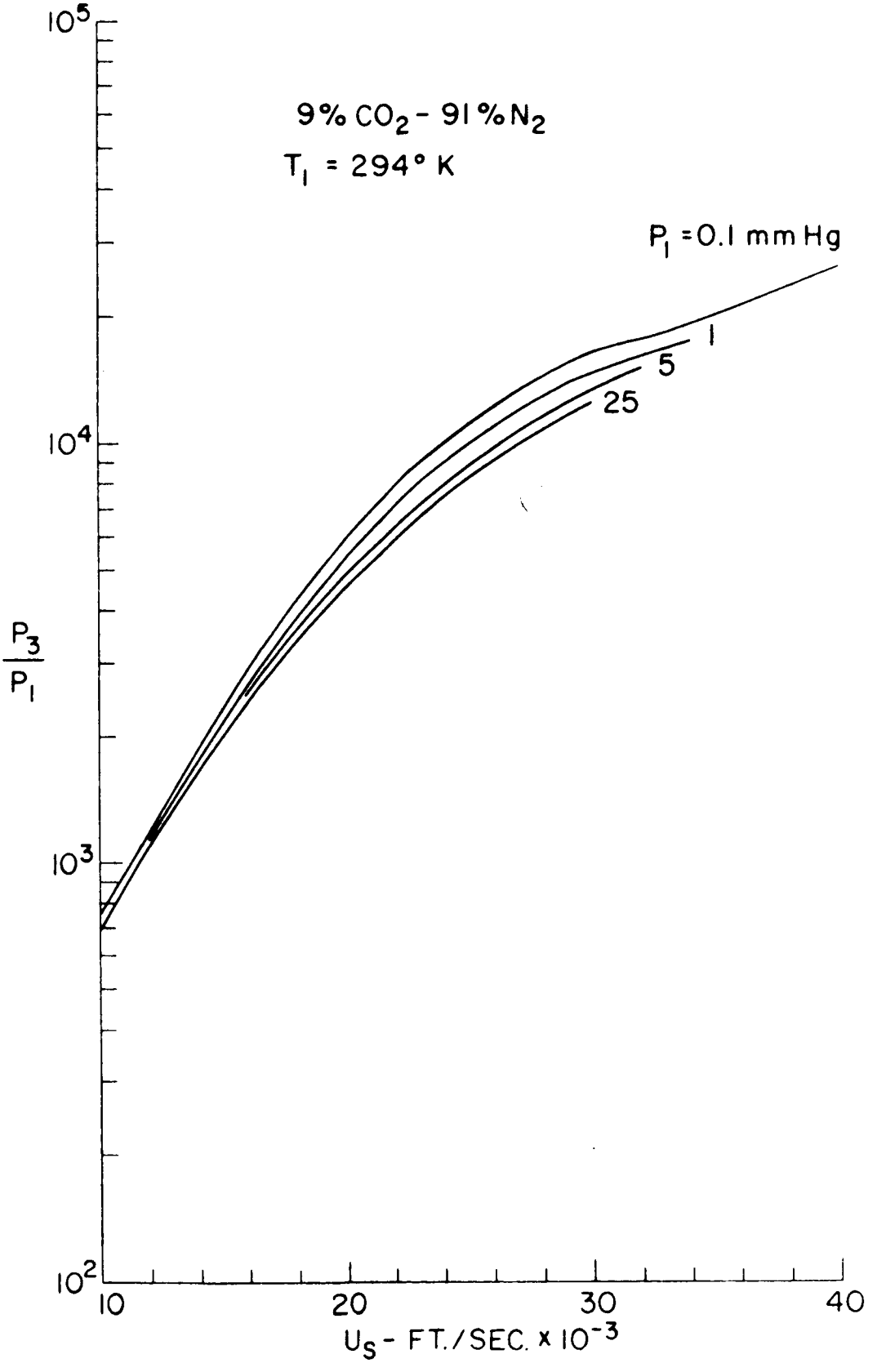

Figure 3.22 Pressure Behind Normal Shock

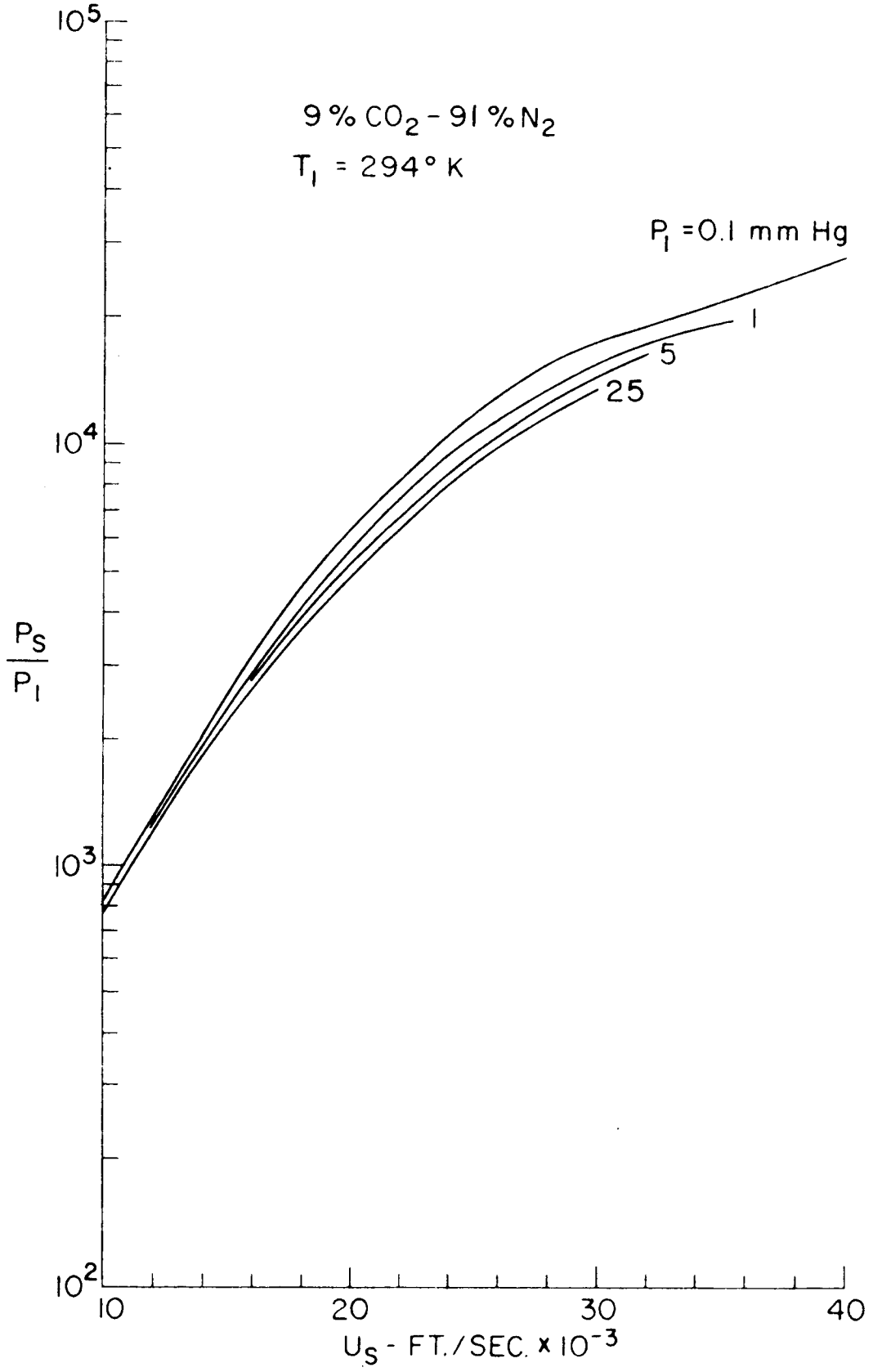

Figure 3.23 Stagnation Pressure

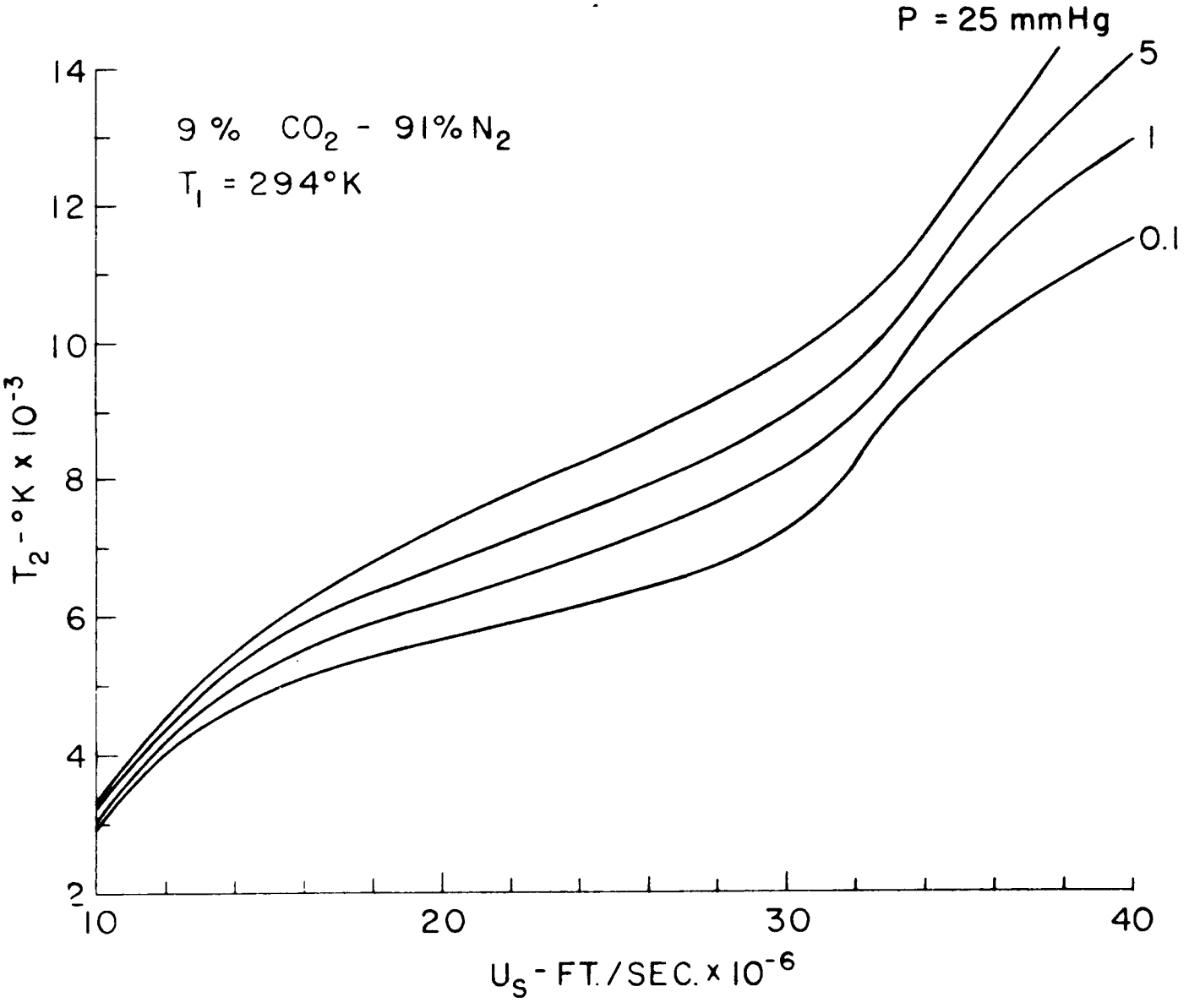

Figure 3.24 Temperature Behind Incident Shock

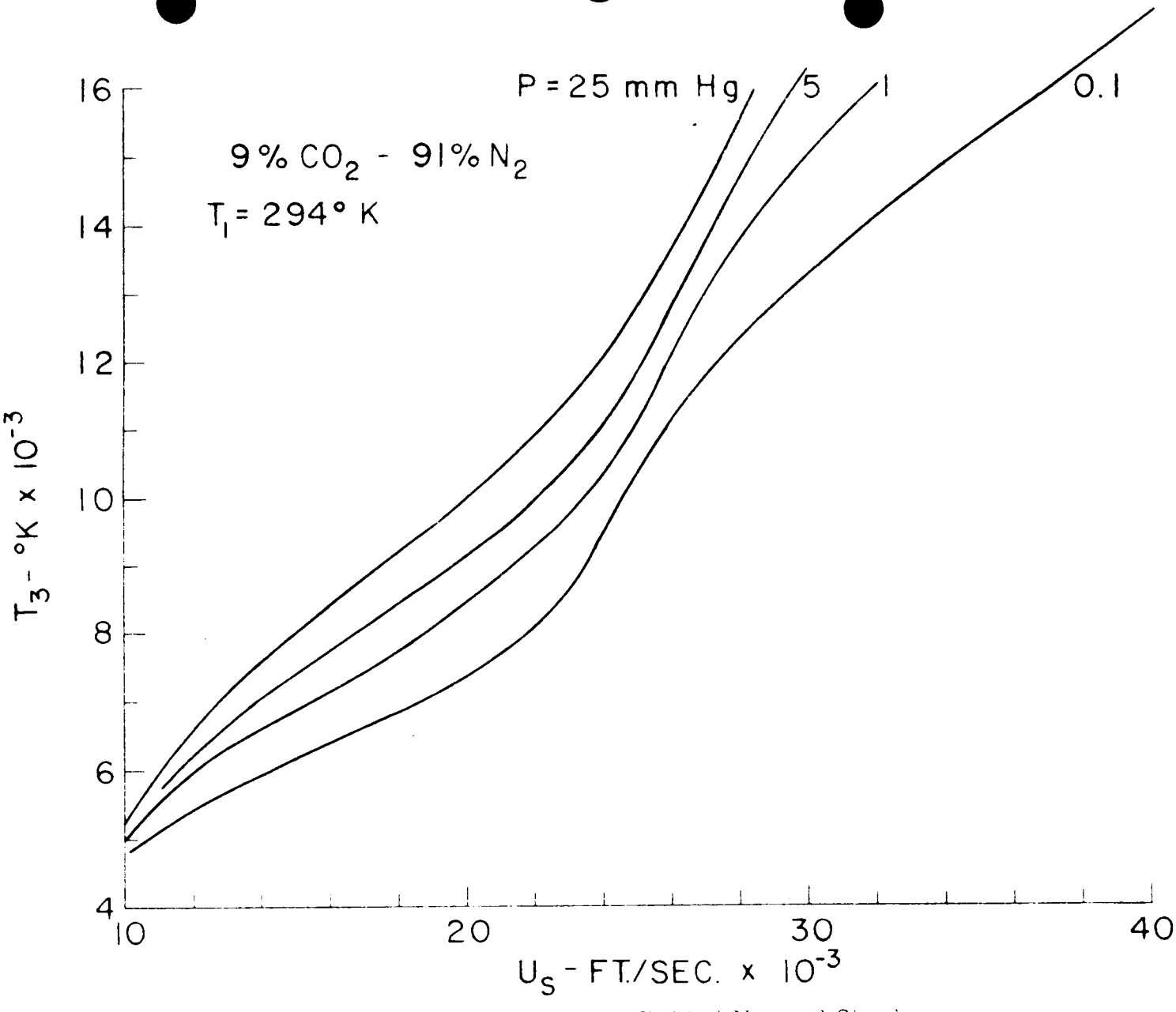

Figure 3.25 Temperature Behind Normal Shock

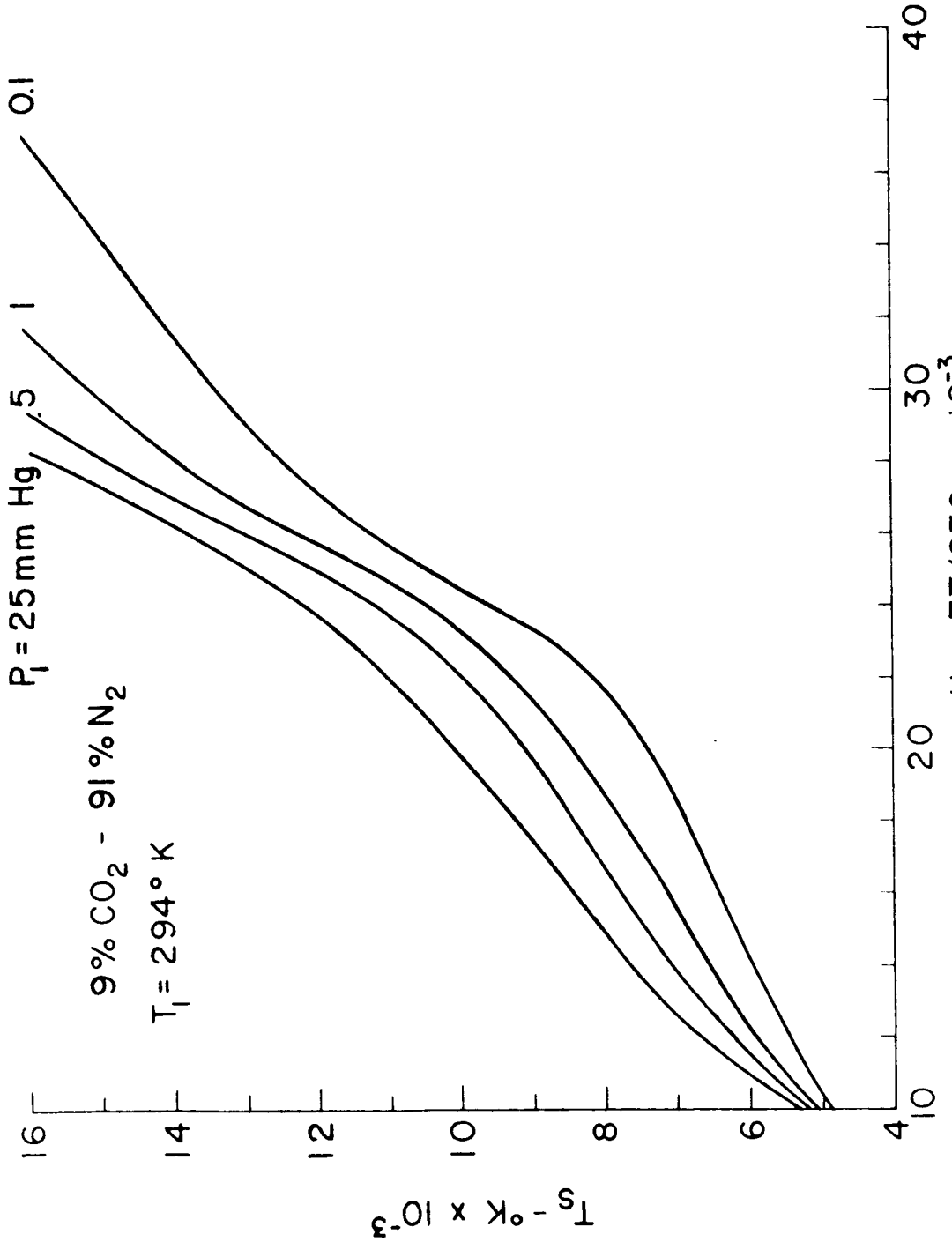

Figure 3.26 Stagnation Temperature

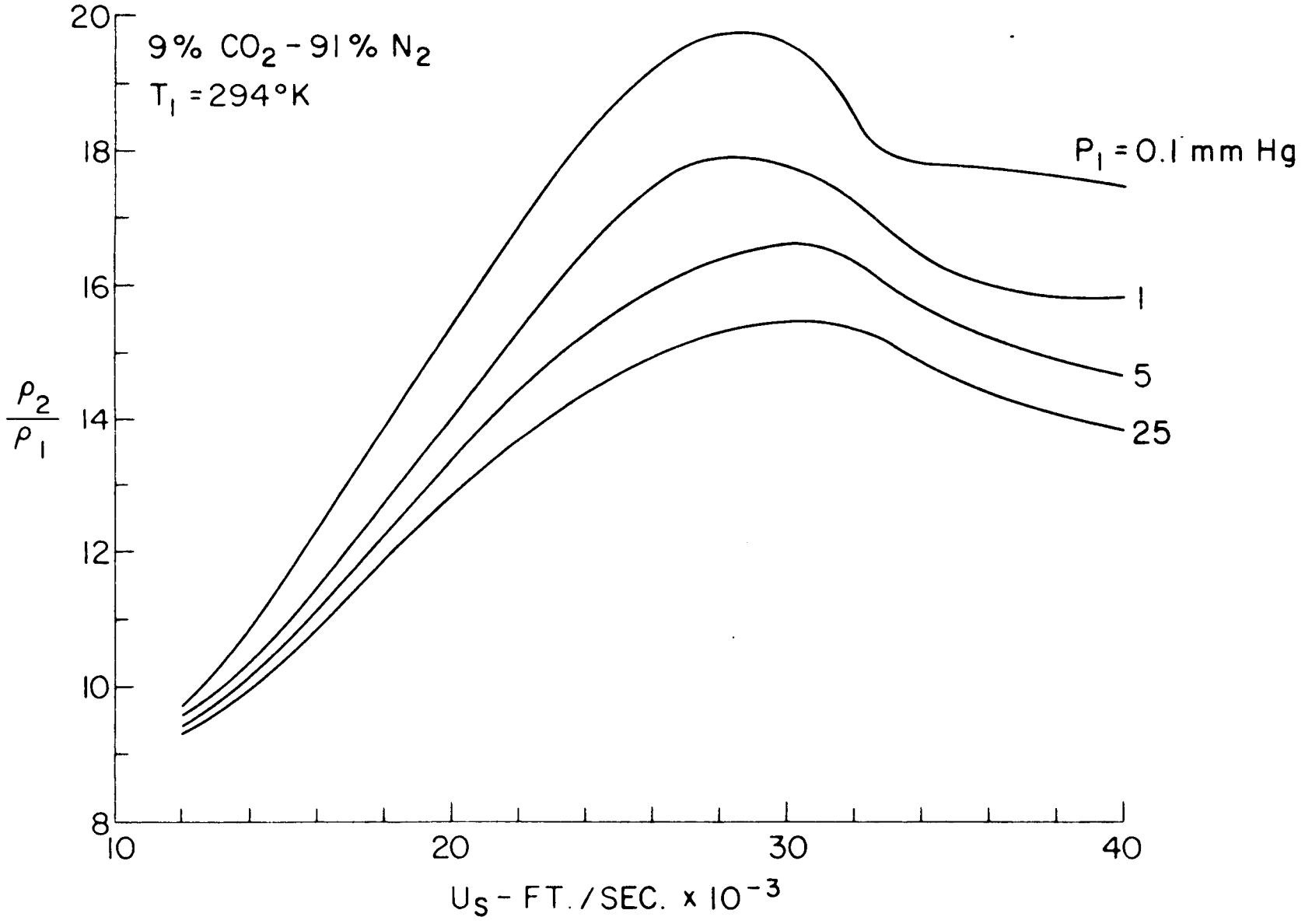

Figure 3.27 Density Behind Incident Shock

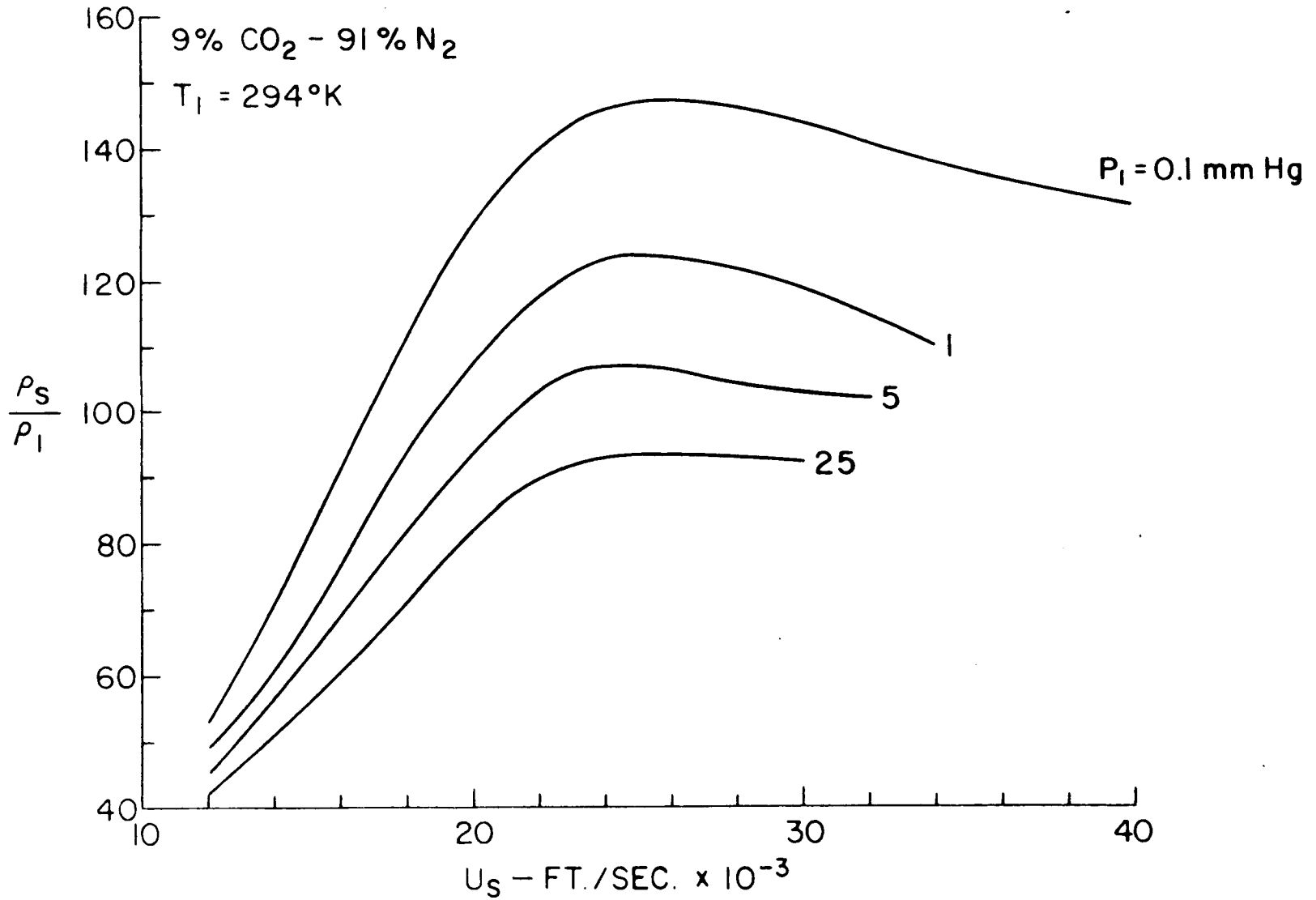

Figure 3.28 Stagnation Density

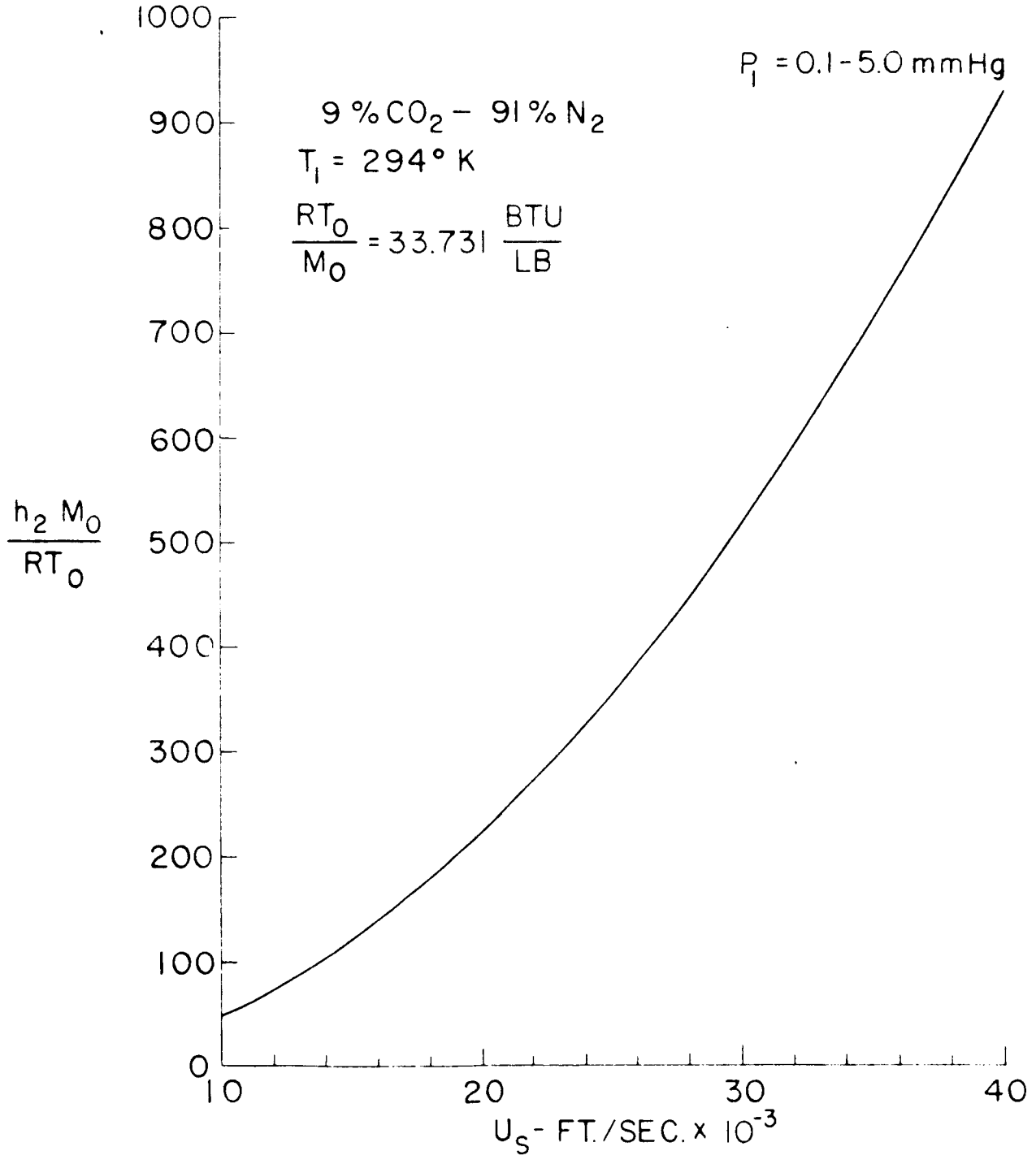

Figure 3.29 Enthalpy Behind Incident Shock

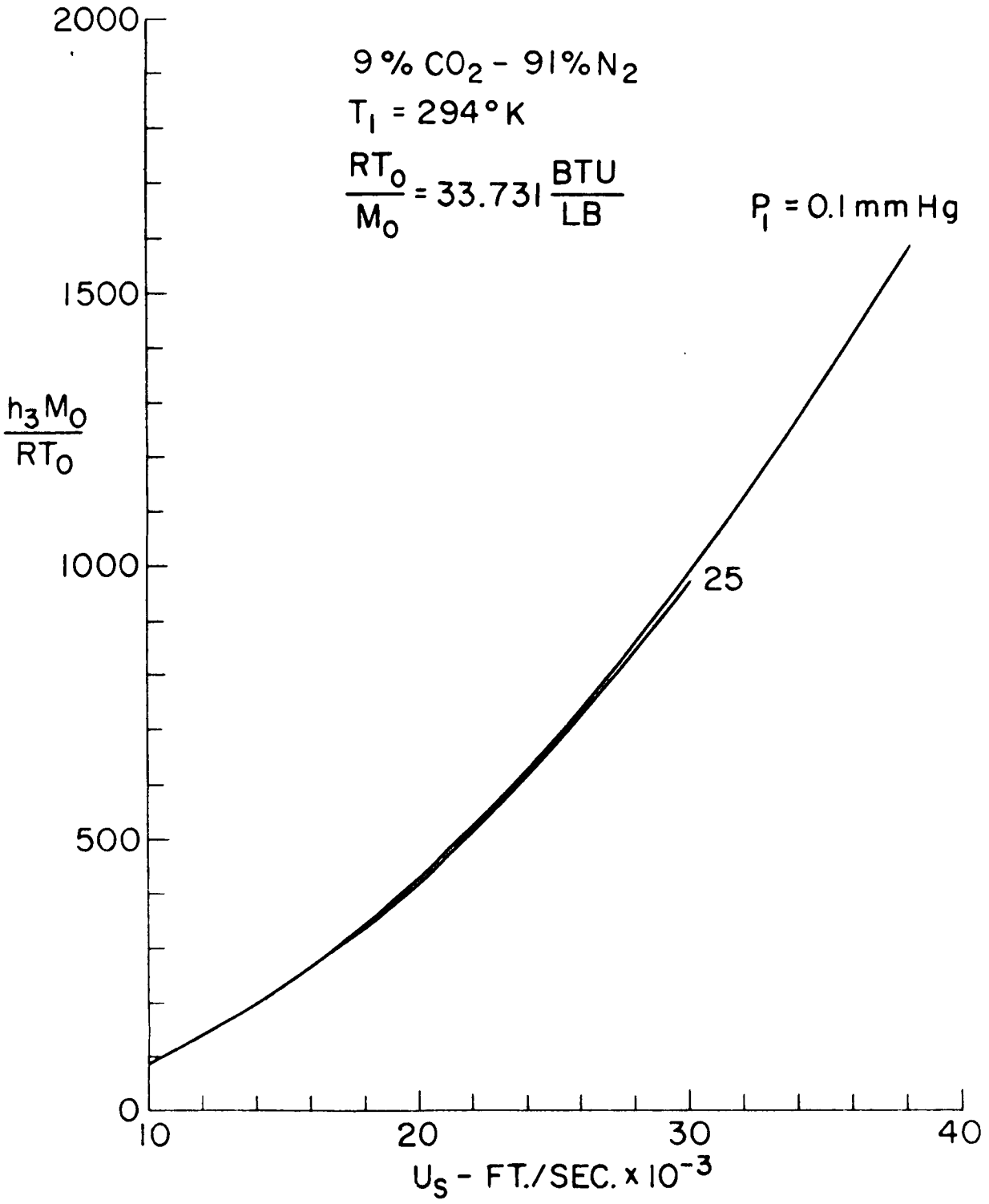

Figure 3.30 Enthalpy Behind Normal Shock

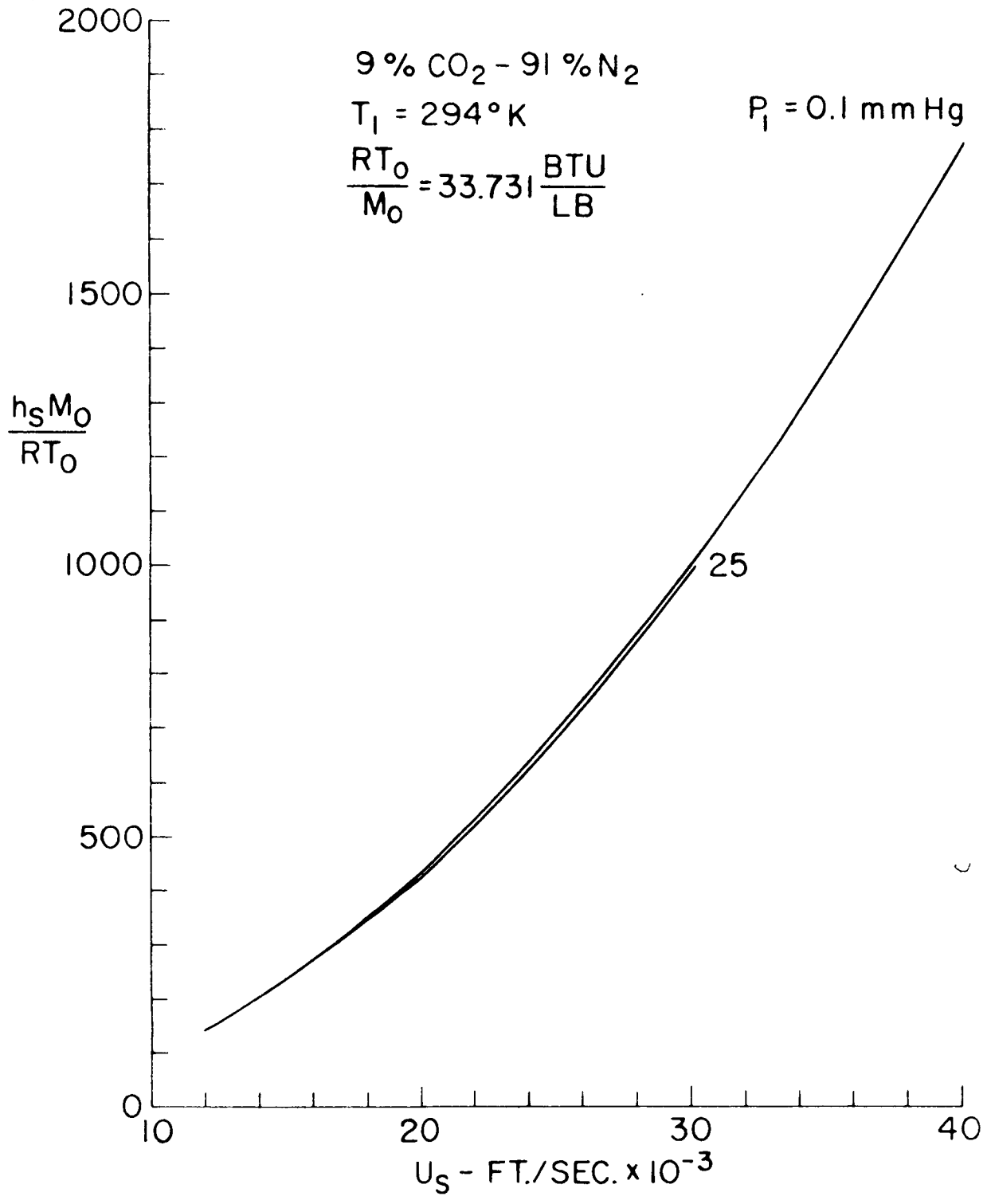

Figure 3.31 Stagnation Enthalpy

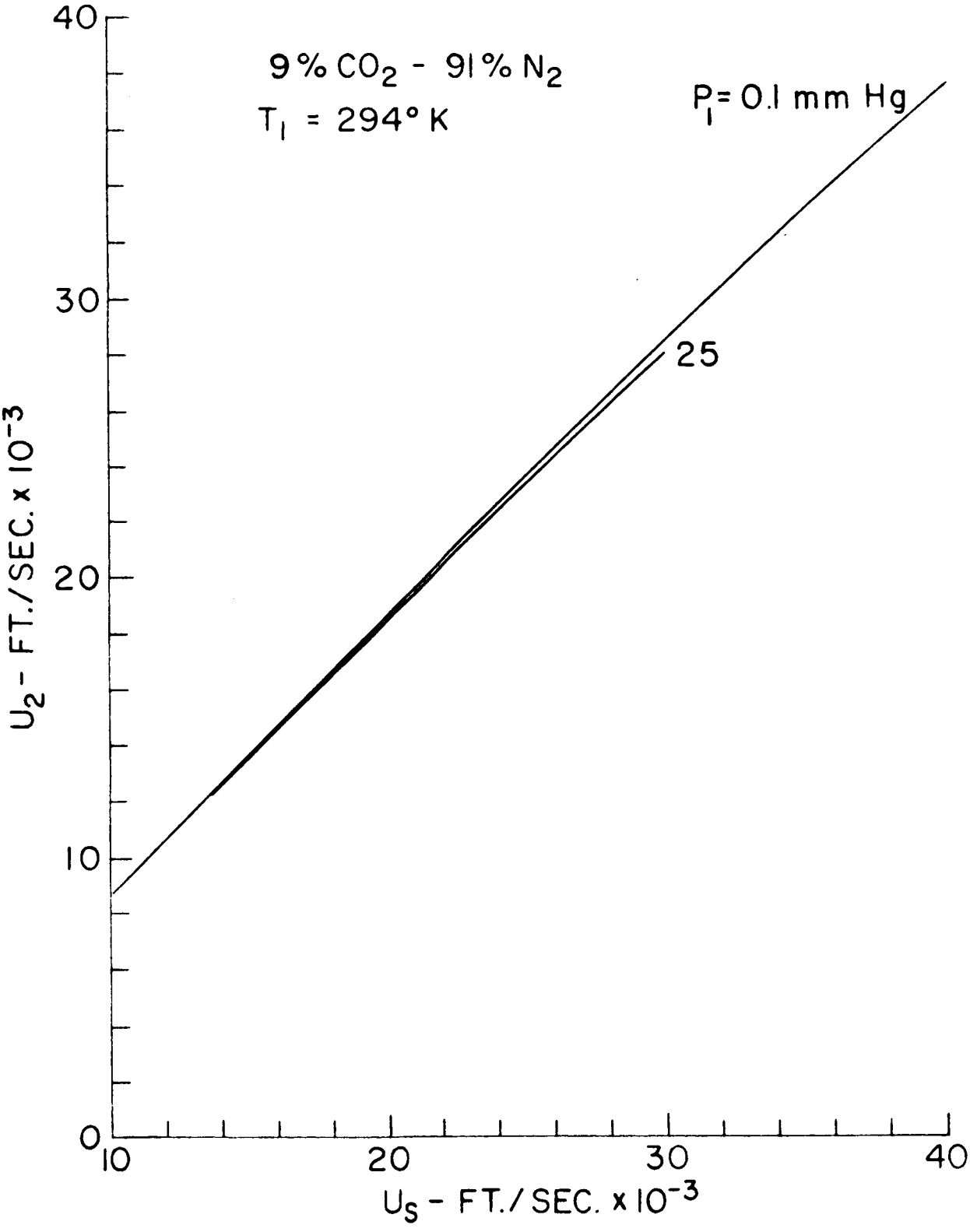

Figure 3.32 Velocity Behind Incident Shock

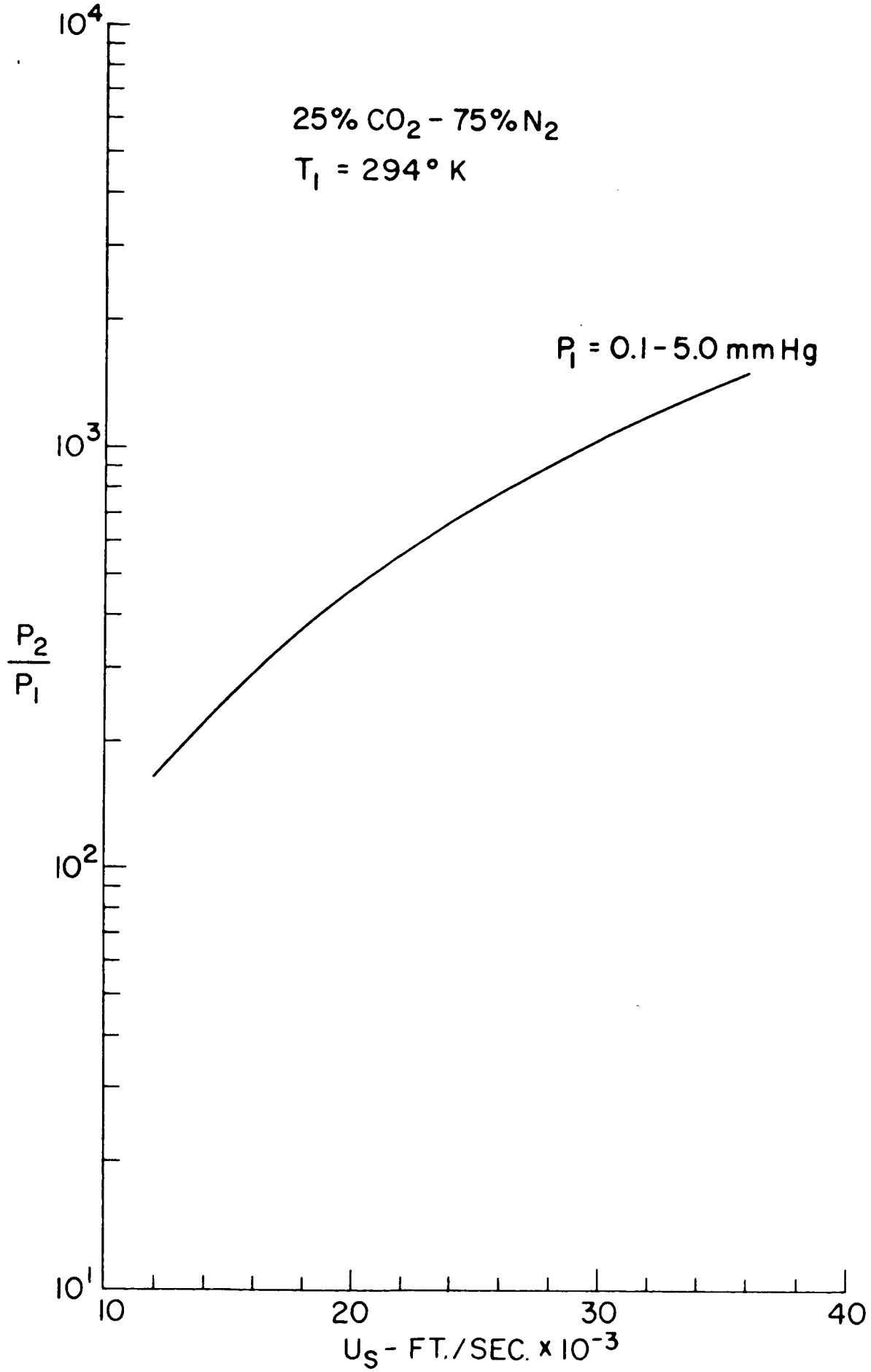

Figure 3.33 Pressure Behind Incident Shock

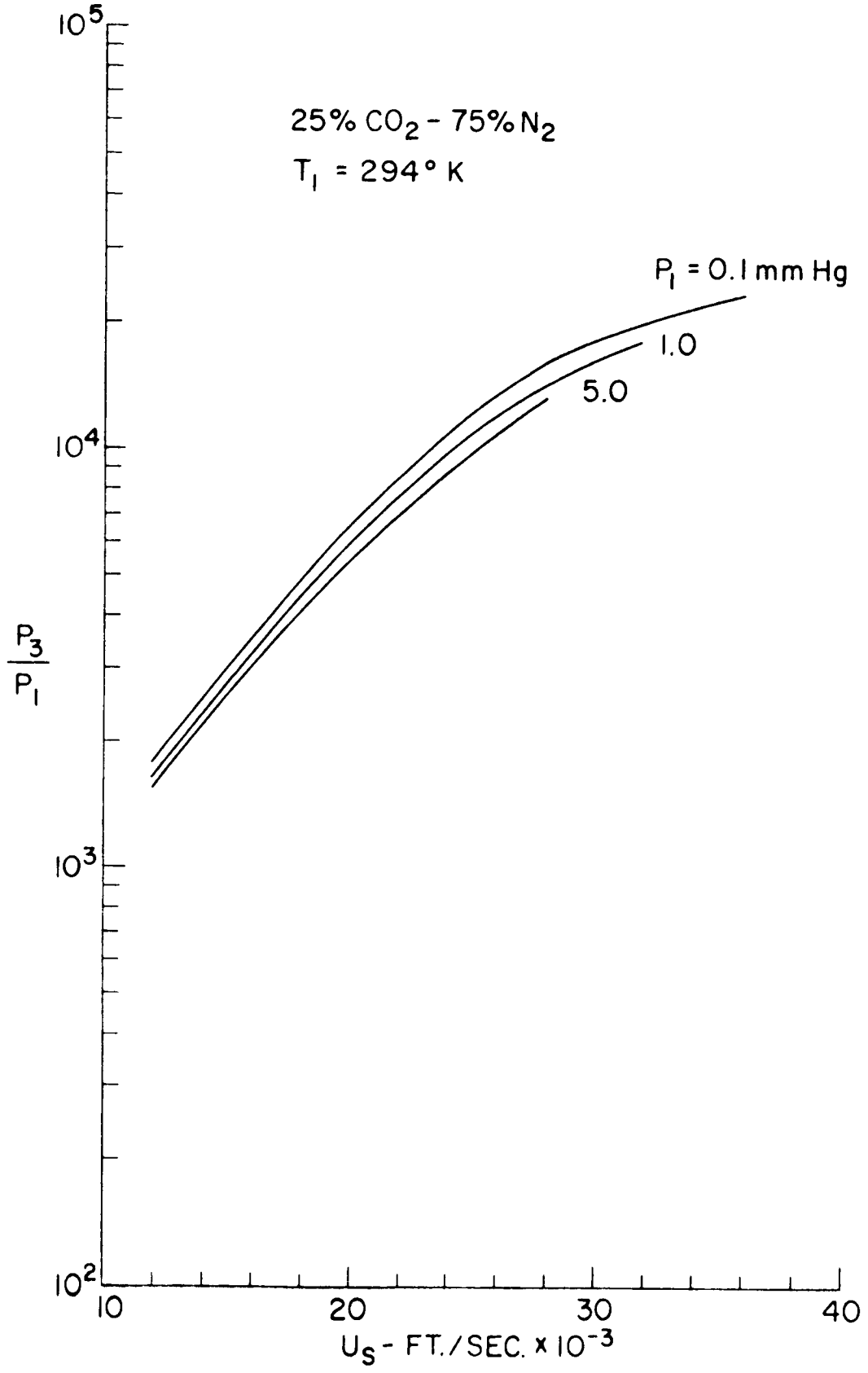

Figure 3.34 Pressure Behind Normal Shock

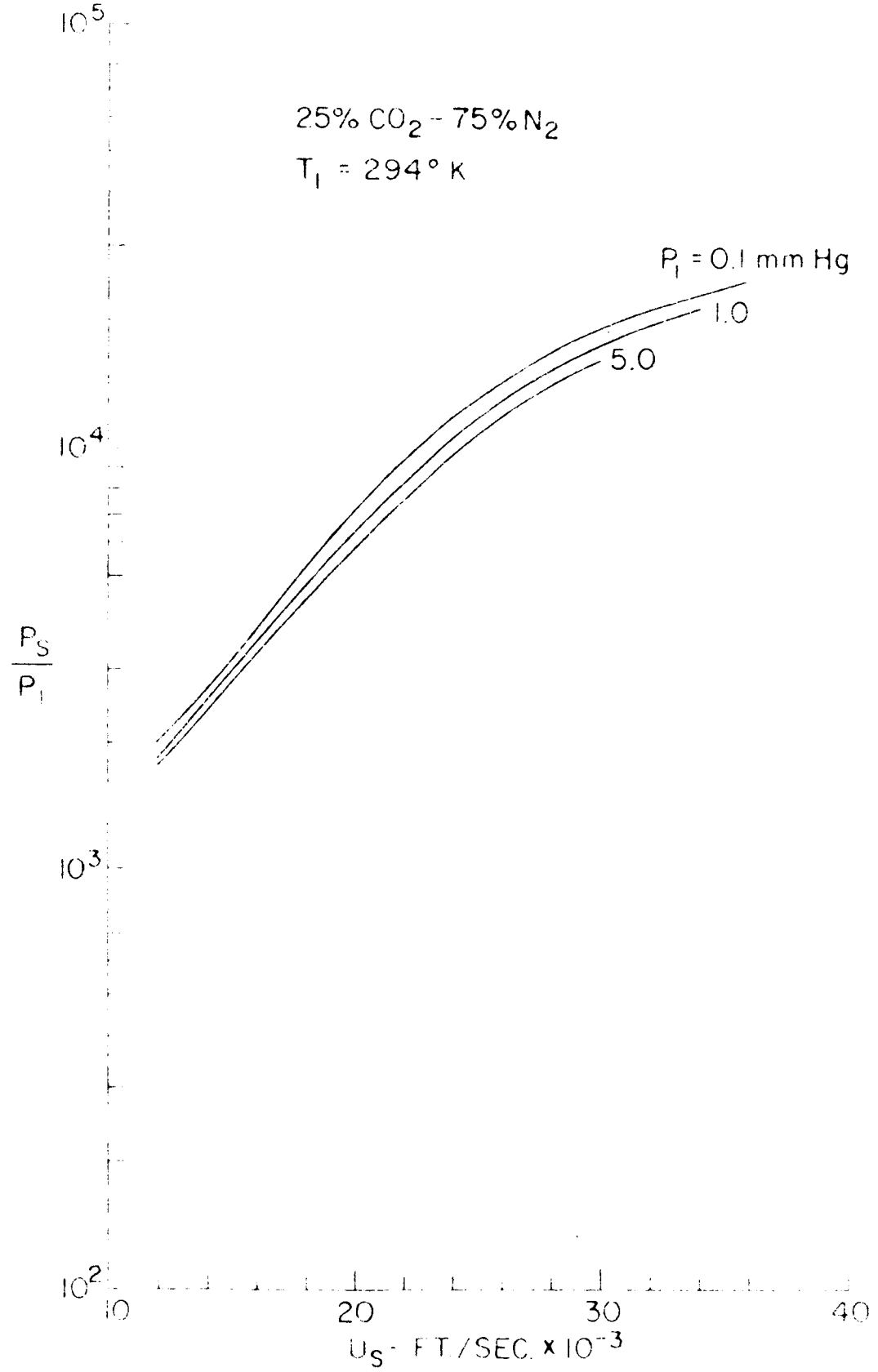

Figure 3. [illegible] Propagation Pressure

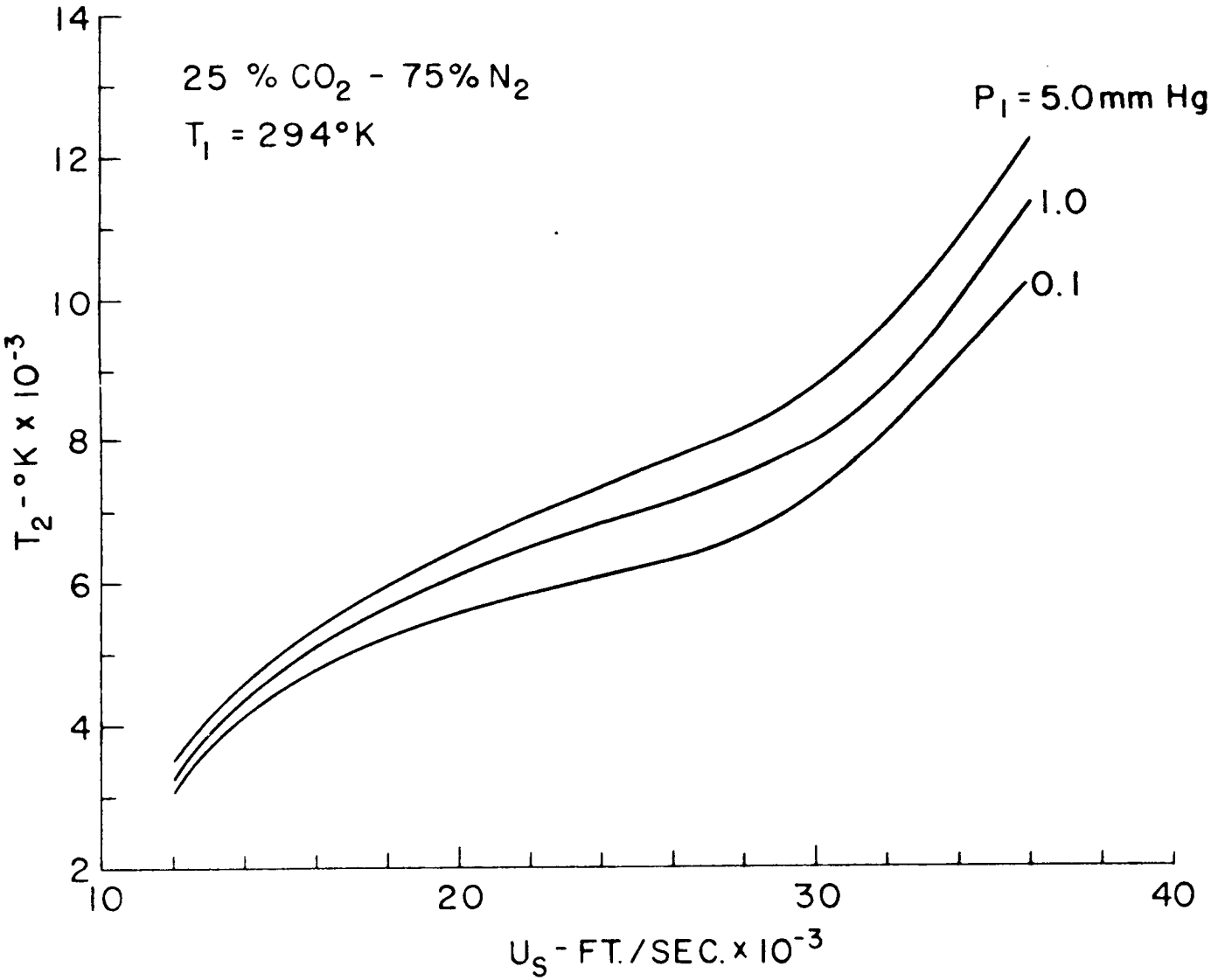

Figure 3.36 Temperature Behind Incident Shock

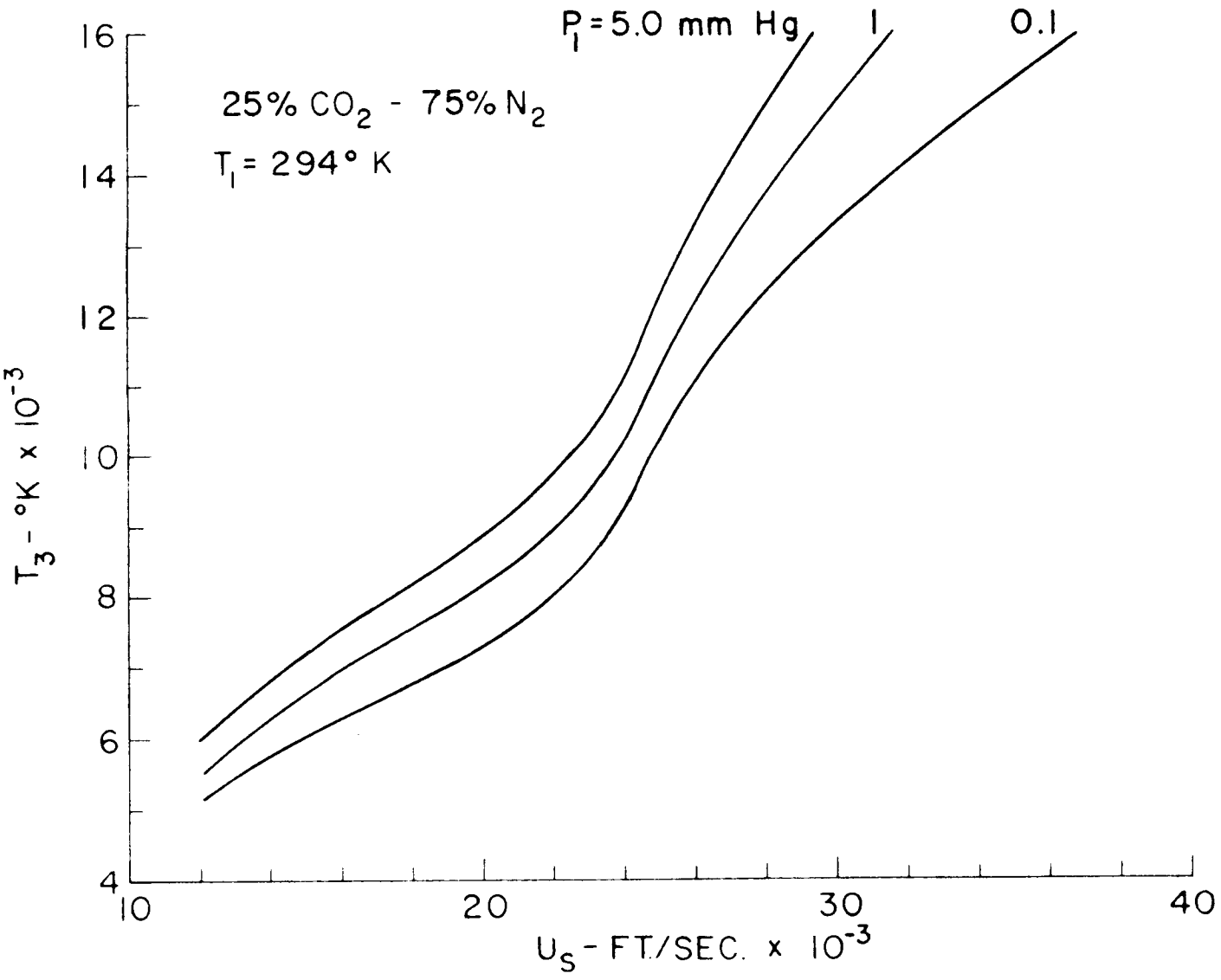

Figure 3.37 Temperature Behind Normal Shock

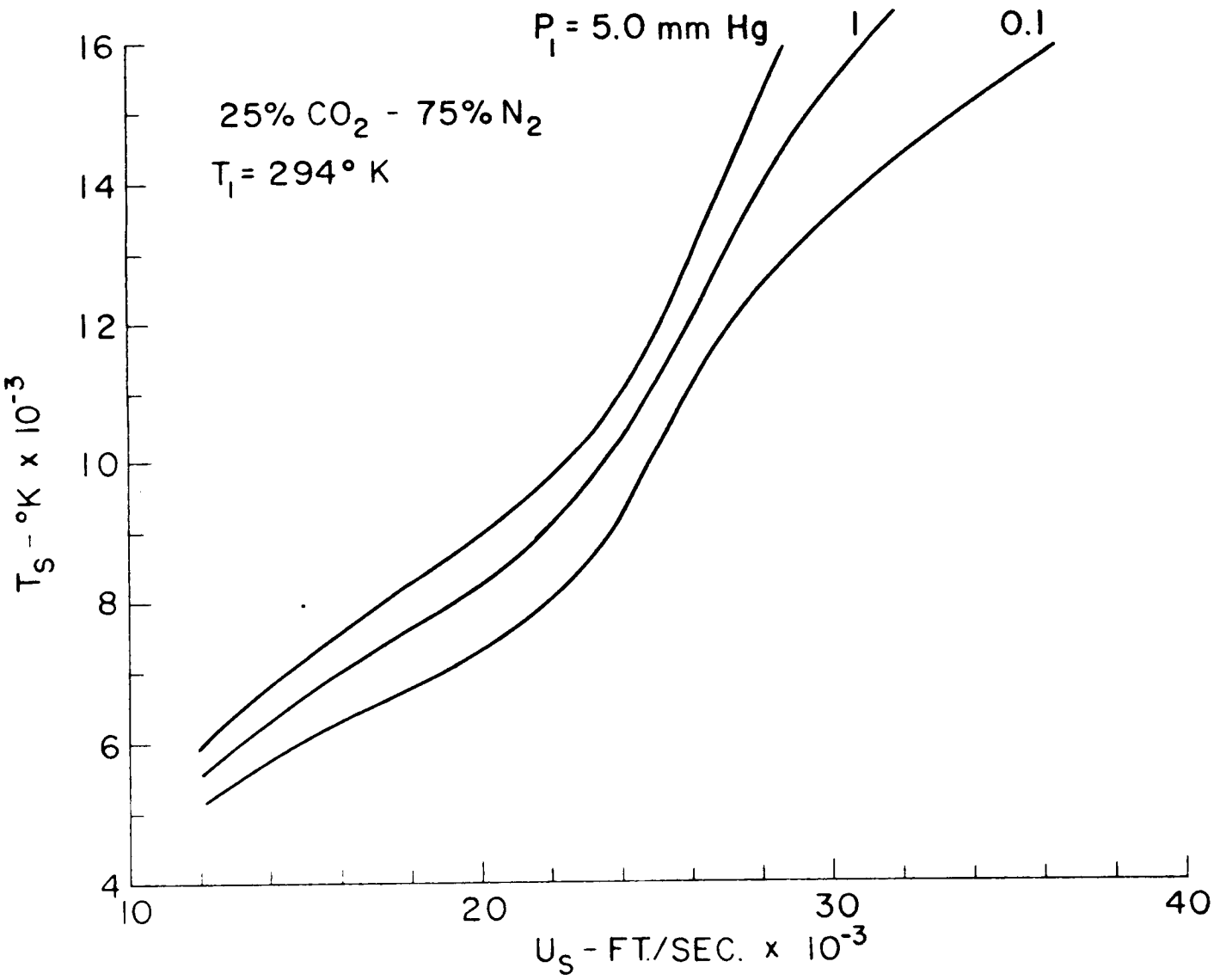

Figure 3.38 Stagnation Temperature

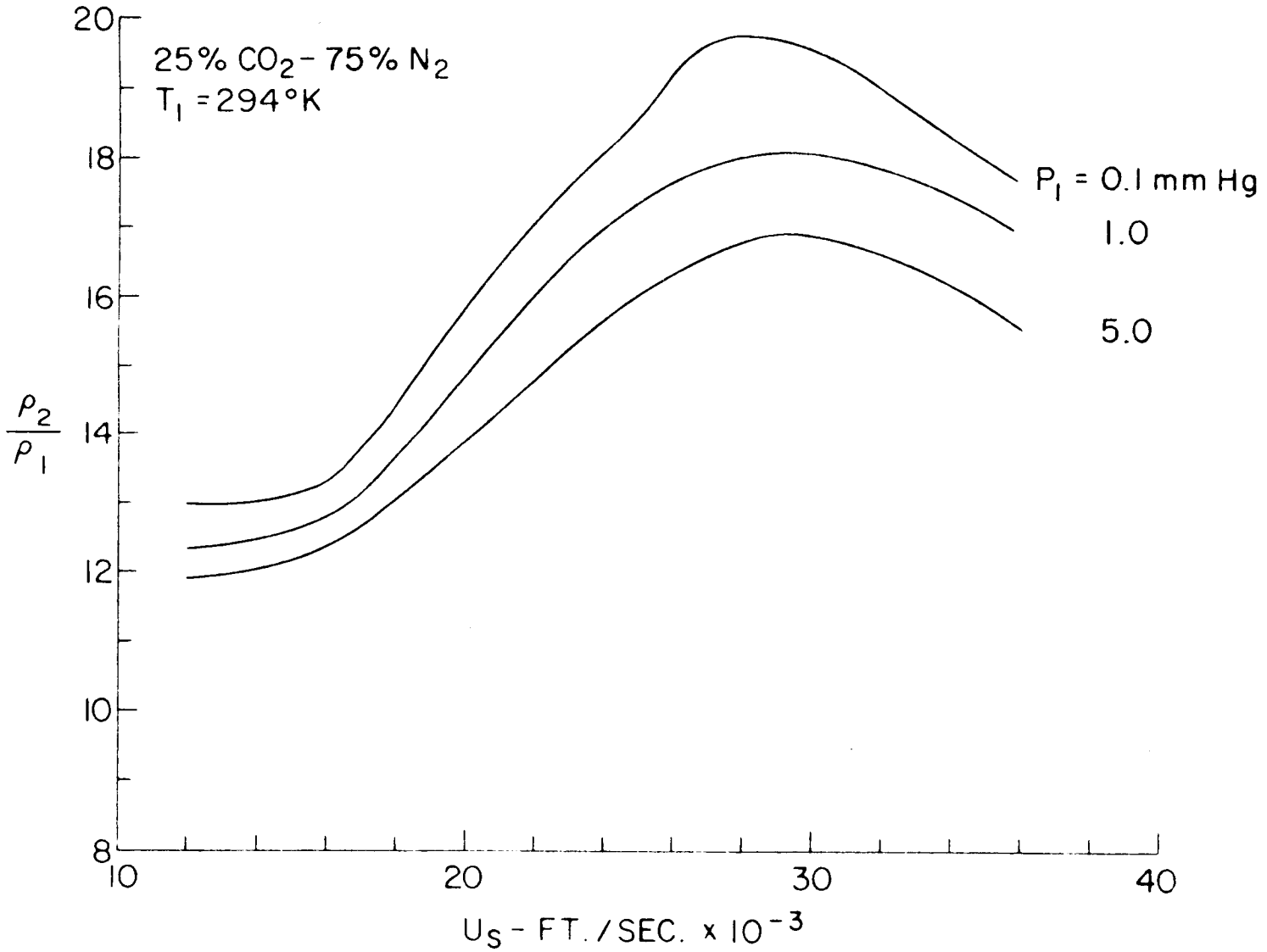

Figure 3.31 Density Behind Incident Shock

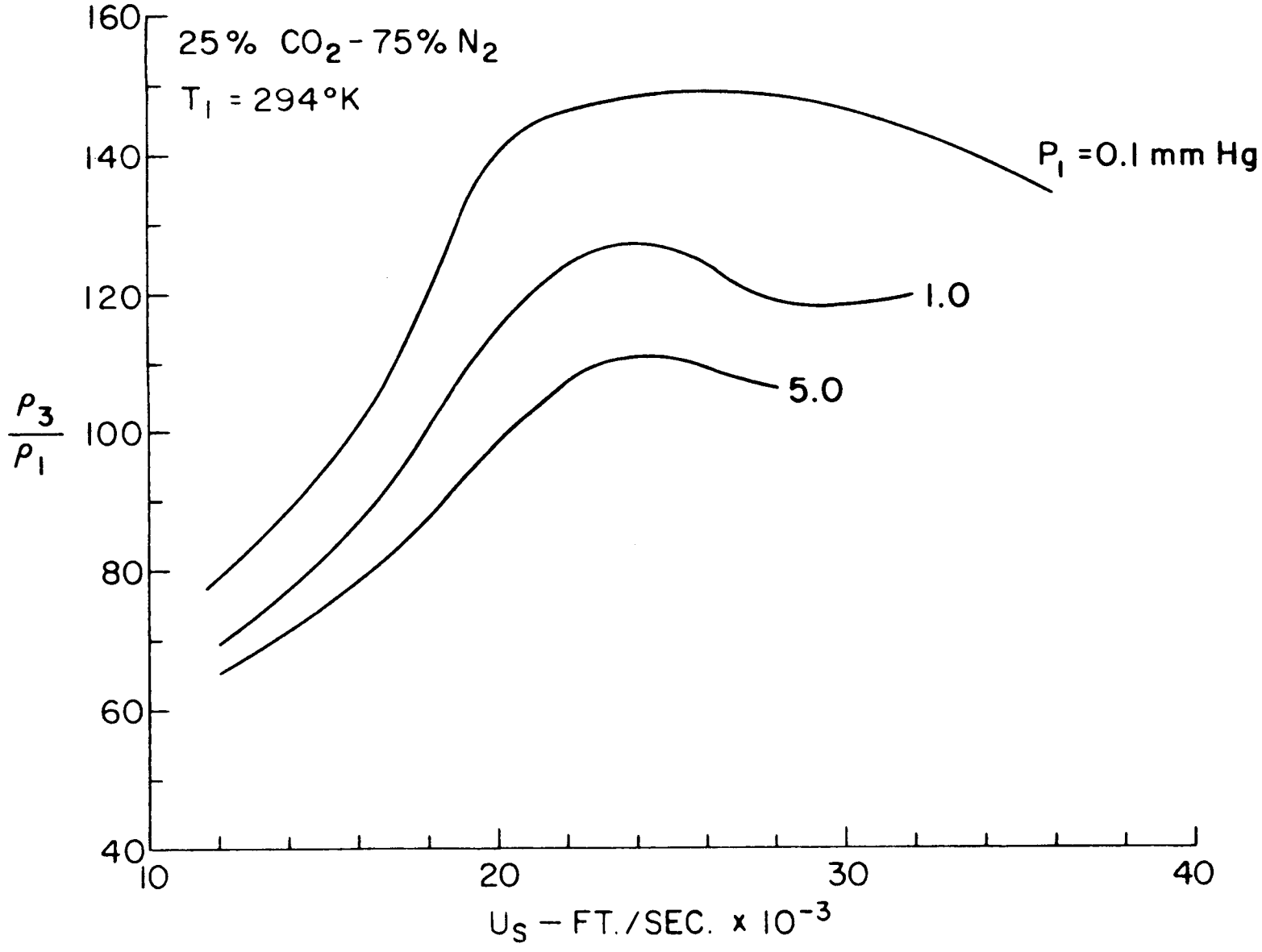

Figure 3.40 Density Behind Normal Shock

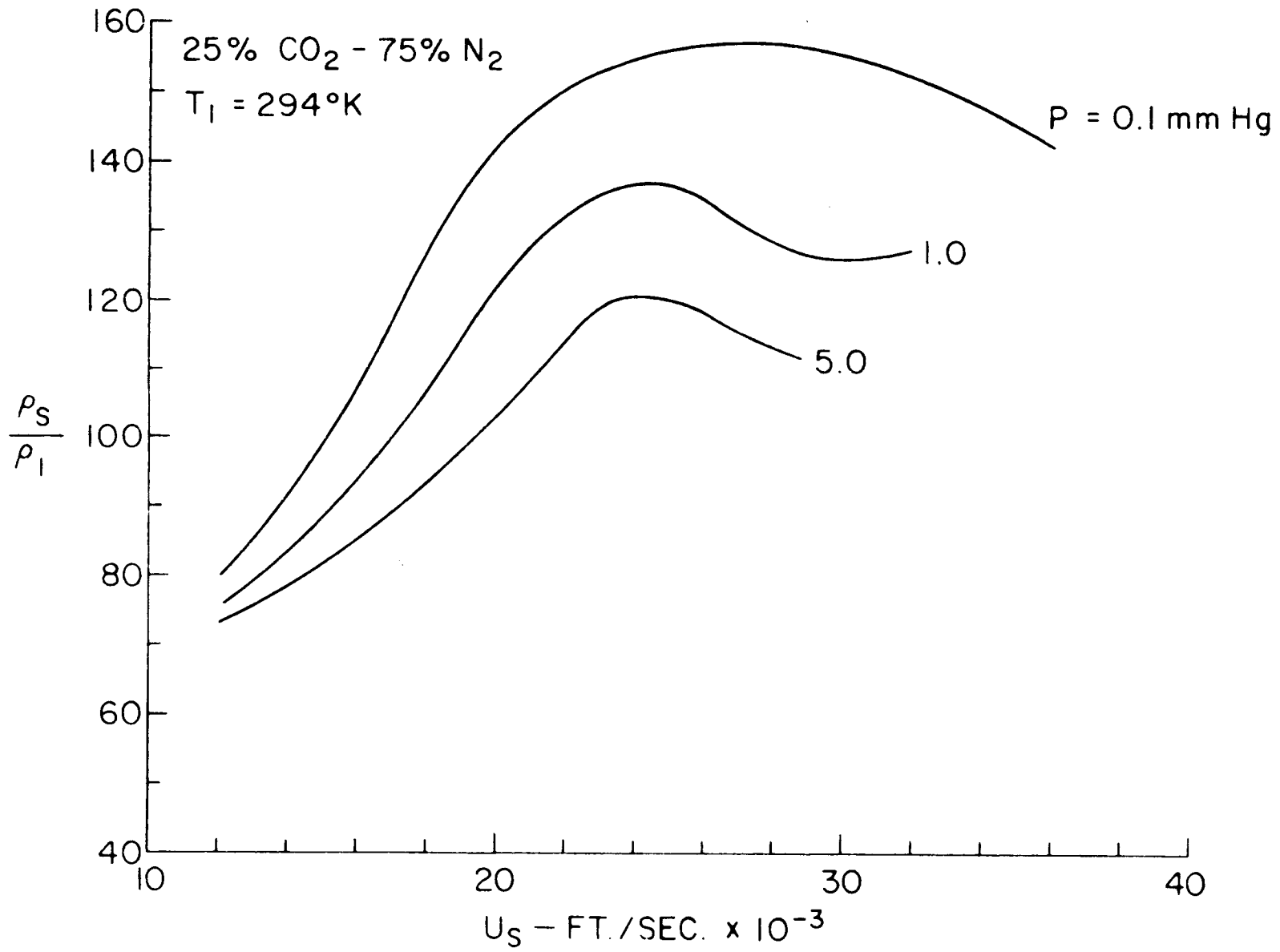

Figure 3.41 Stagnation Density

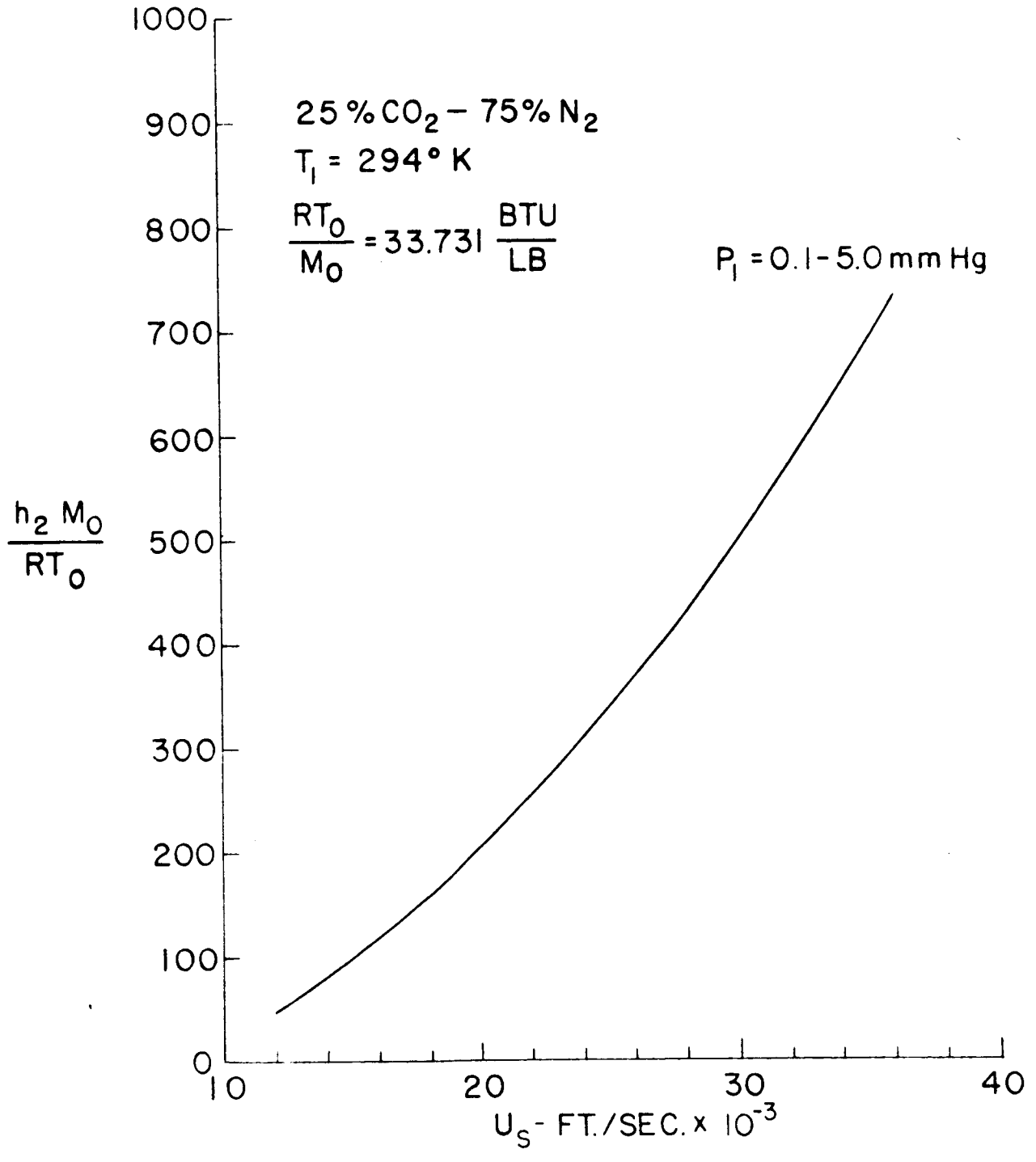

Figure 3.42 Enthalpy Behind Incident Shock

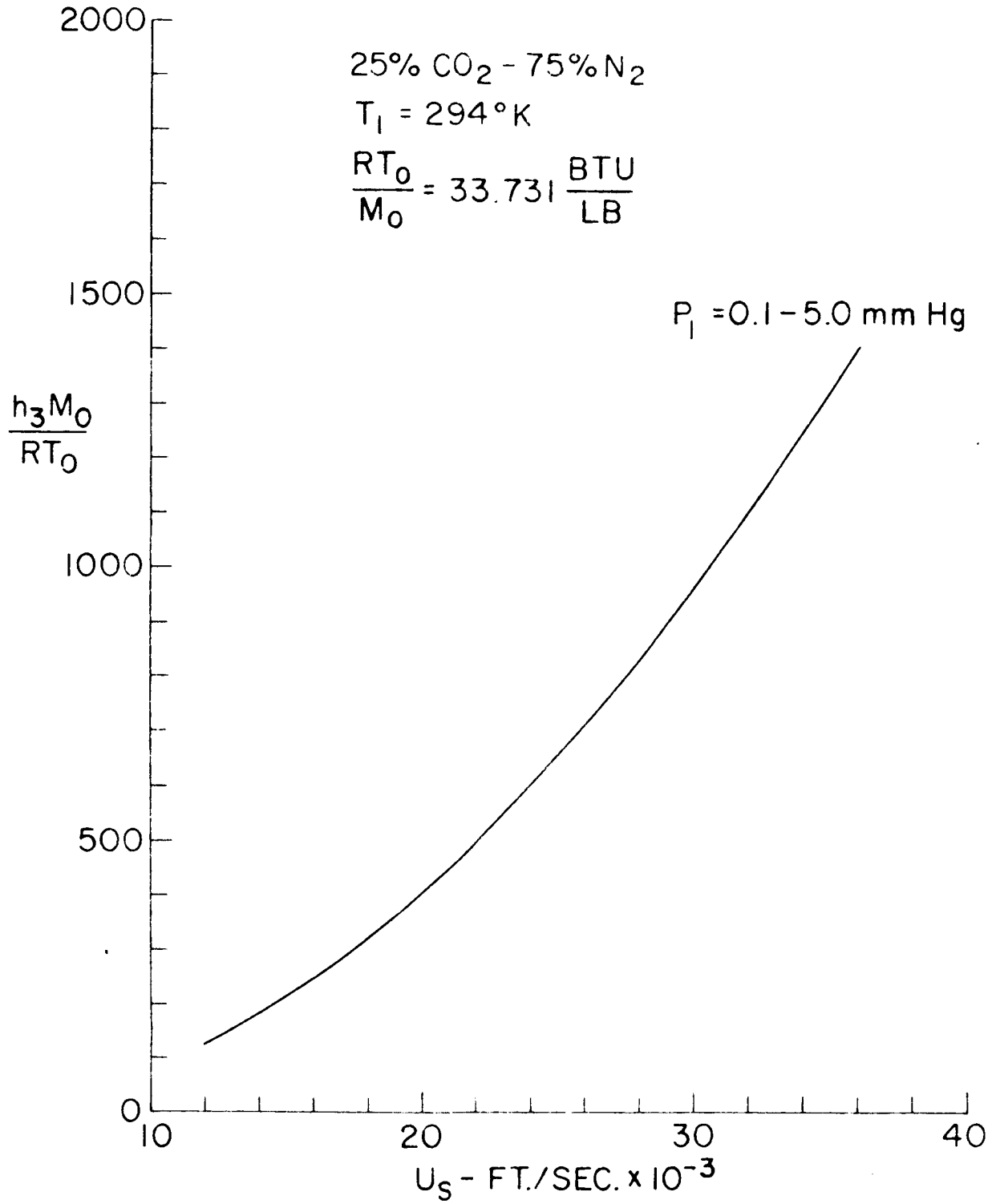

Figure 3.43 Enthalpy Behind Normal Shock

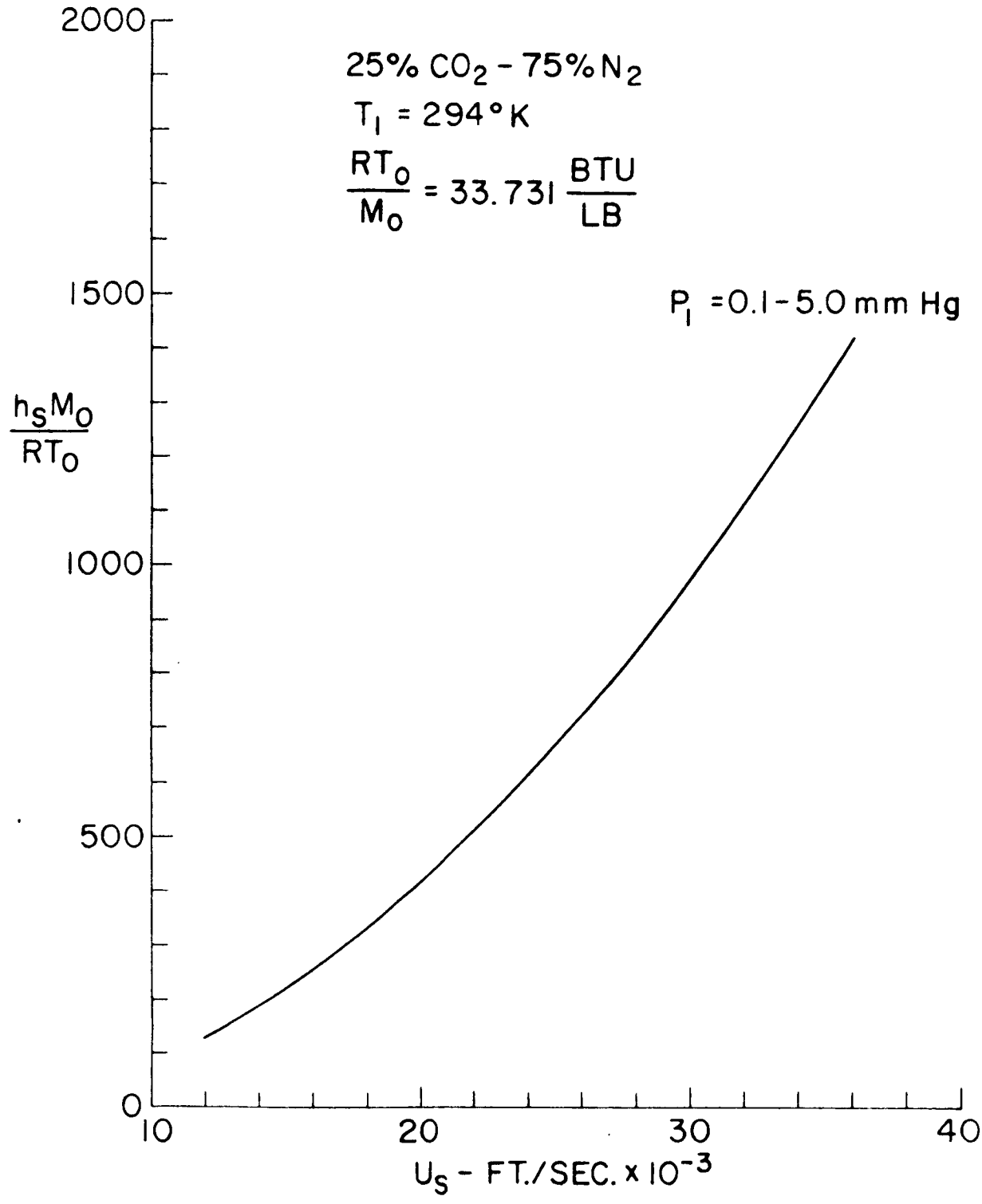

Figure 3.44 Stagnation Enthalpy

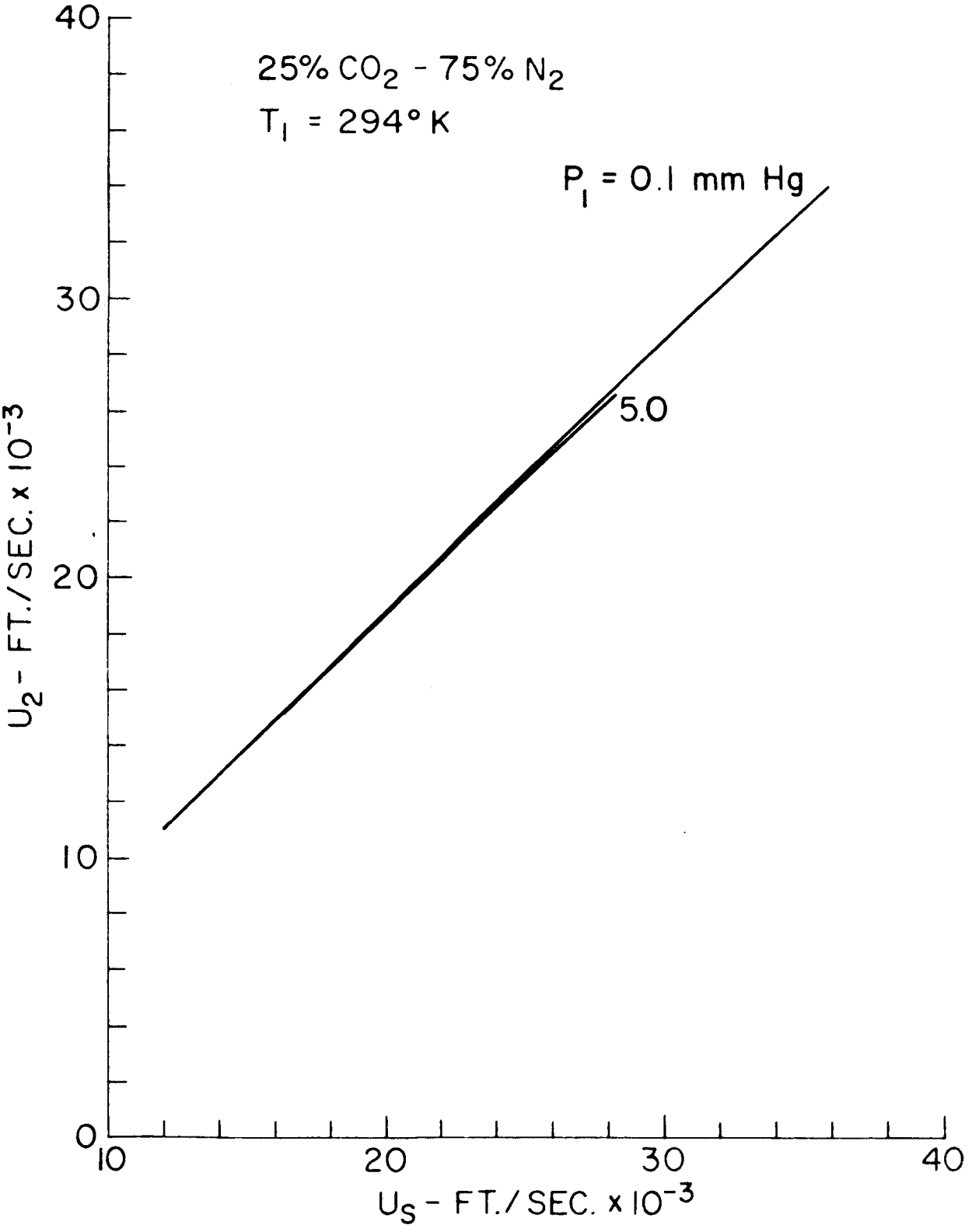

Figure 3.45 Velocity Behind Incident Shock Particle

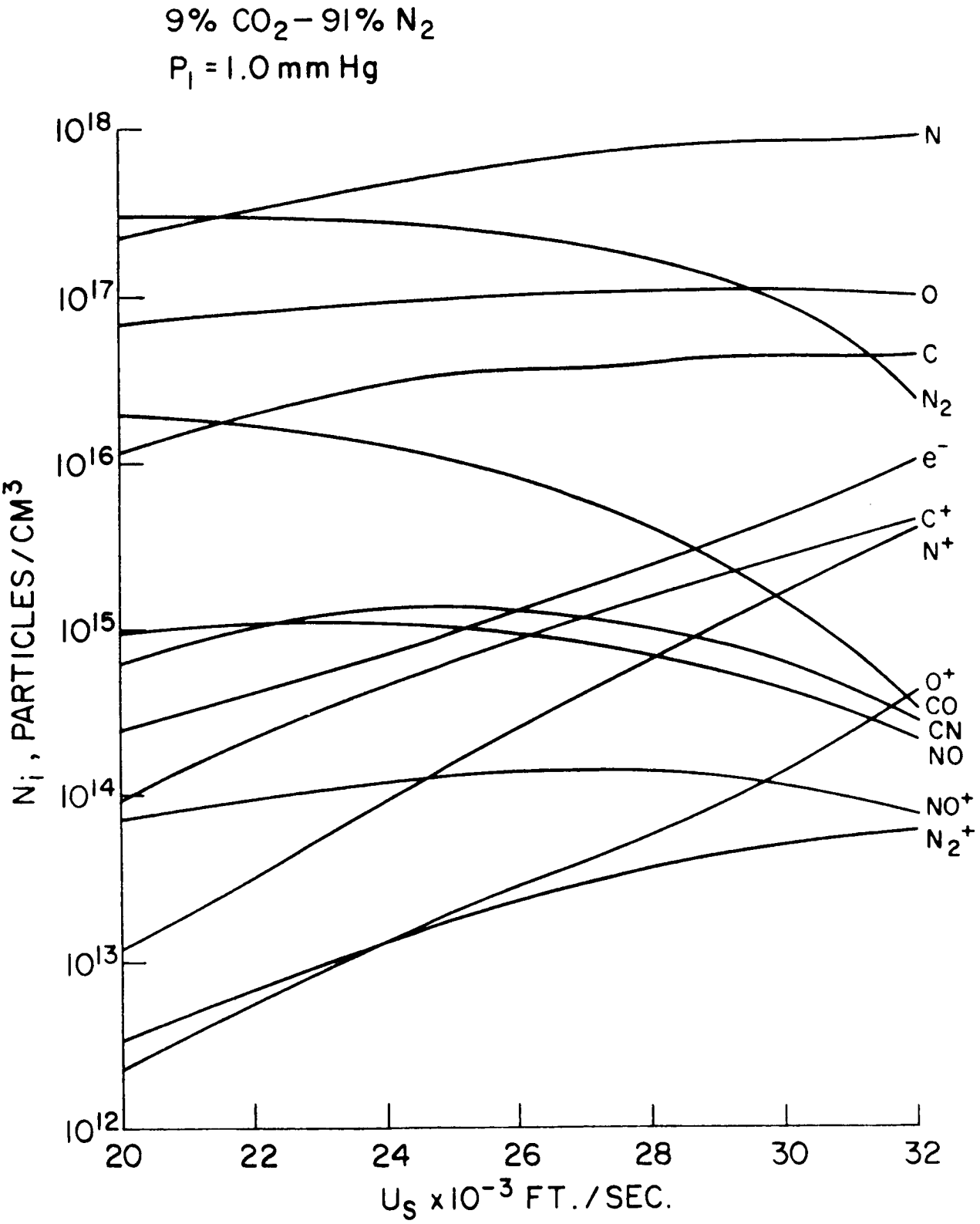

Figure 3.46 Species Density Behind Incident Shock Particle

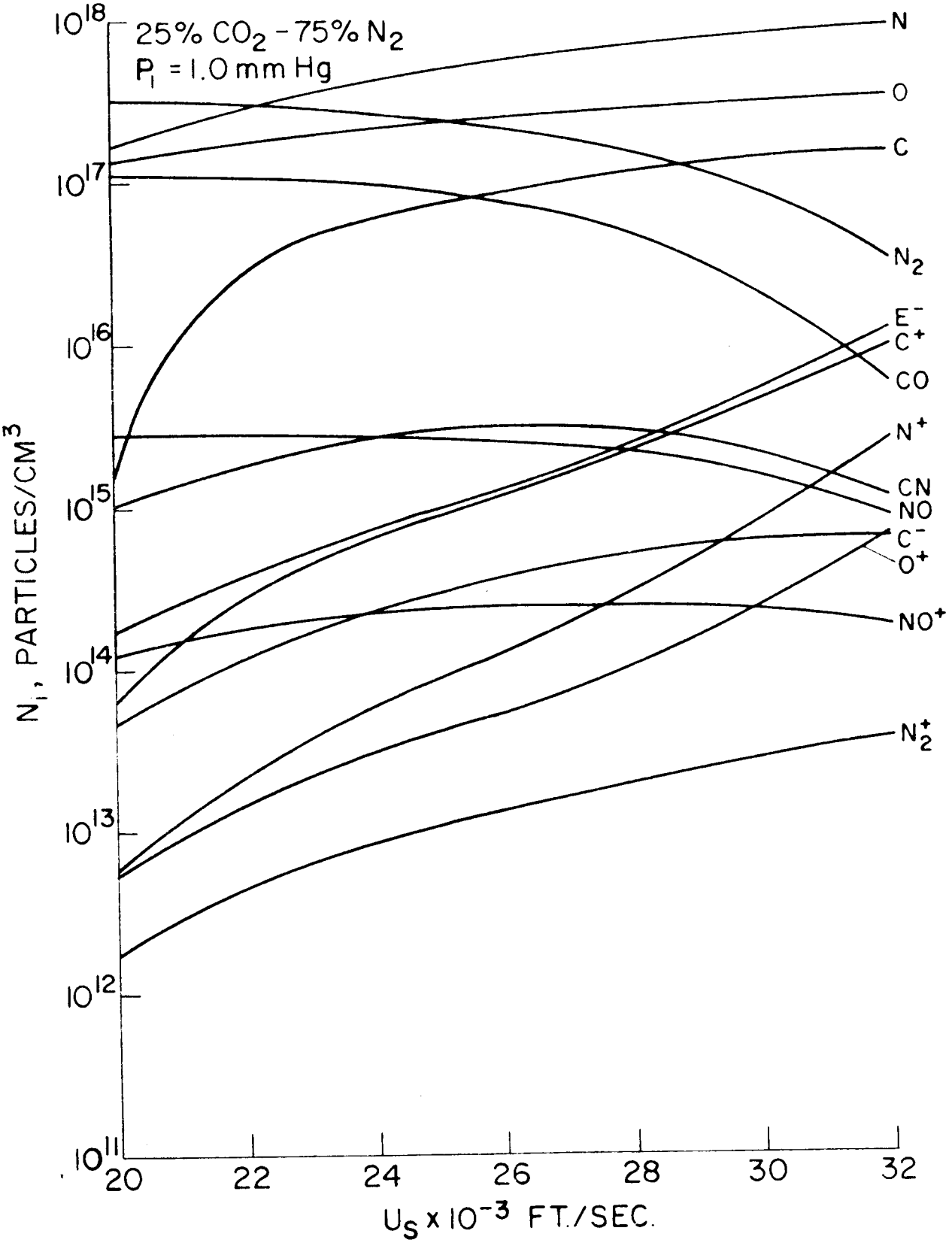

Figure 3.47 Species Density Behind Incident Shock

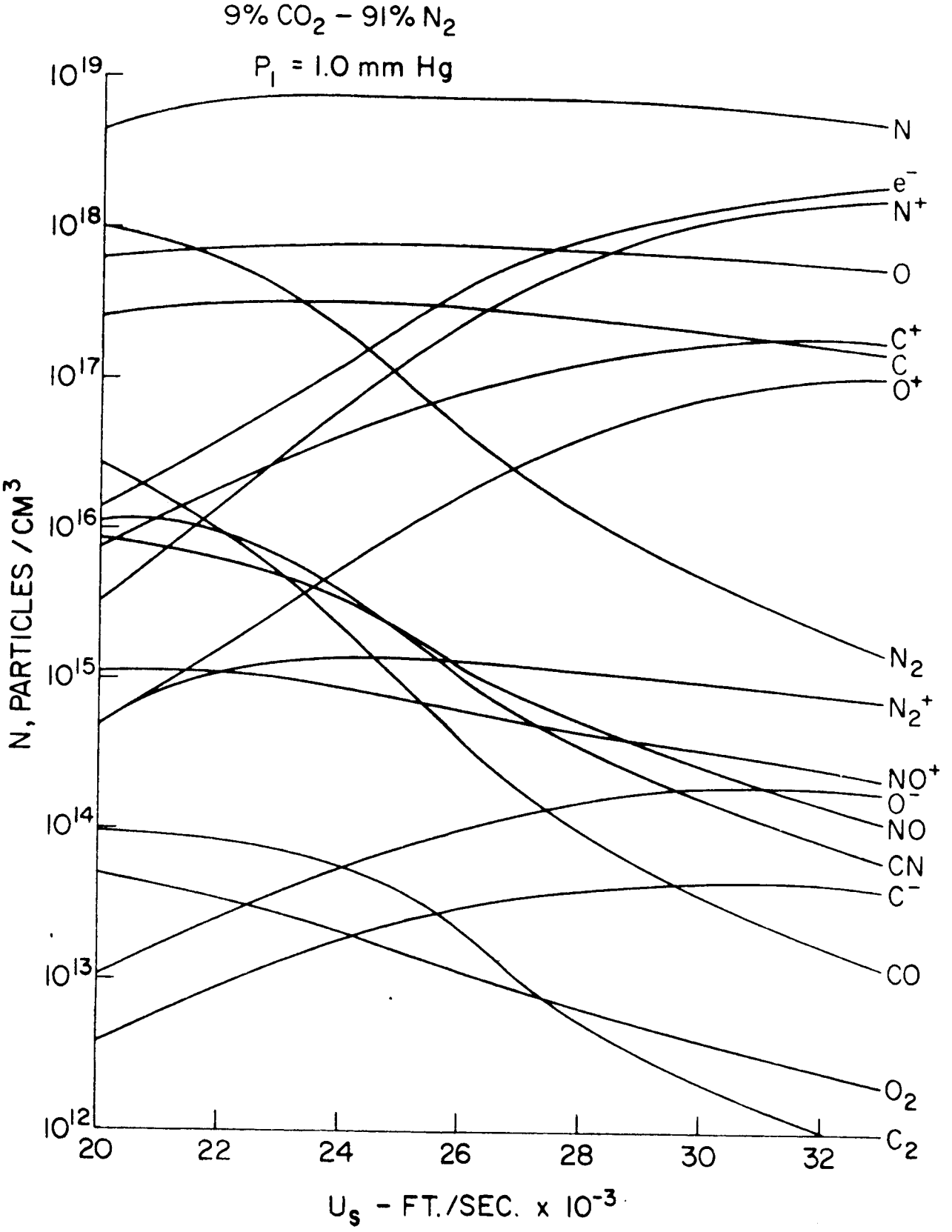

Figure 3.48 Stagnation Point Species Particle Density

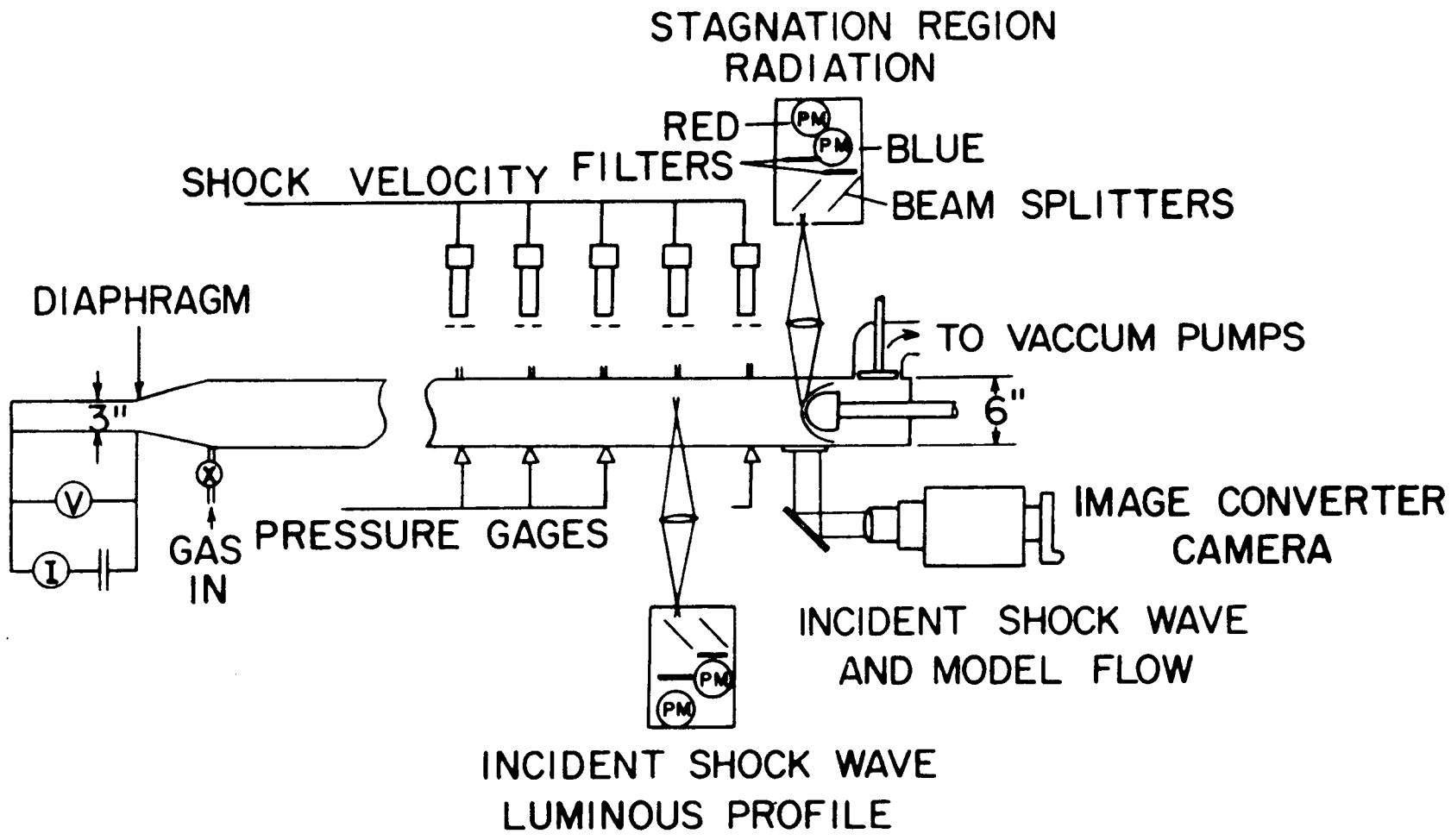

Figure 4.1 Schematic Diagram of Instrumentation for Shock Tube Performance Measurement

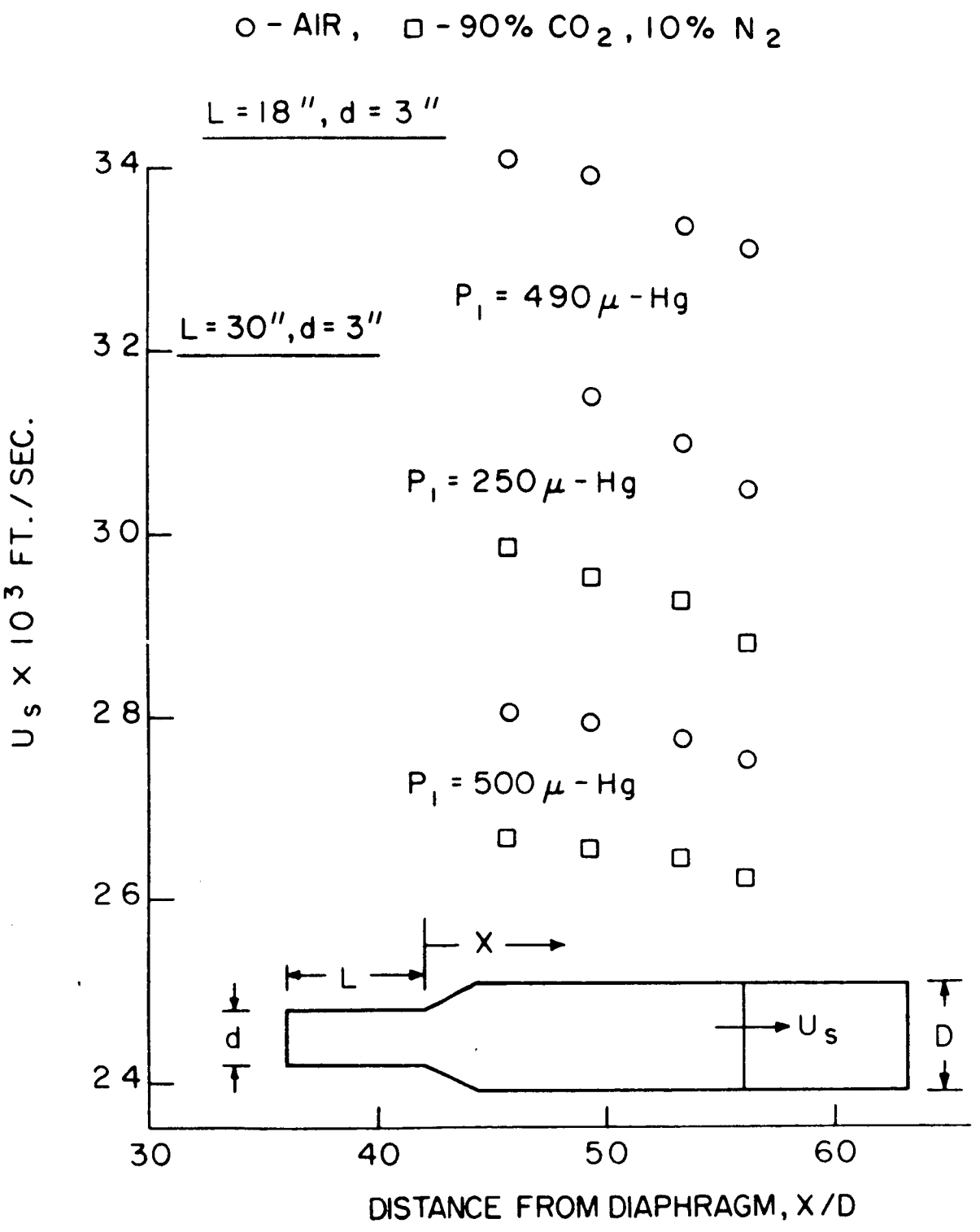

Figure 4.2 Variation of Shock Speed with Distance from the Diaphragm for Two Different Driver Lengths and Several Initial Driven Tube Pressures

9% CO_2 - 91% N_2

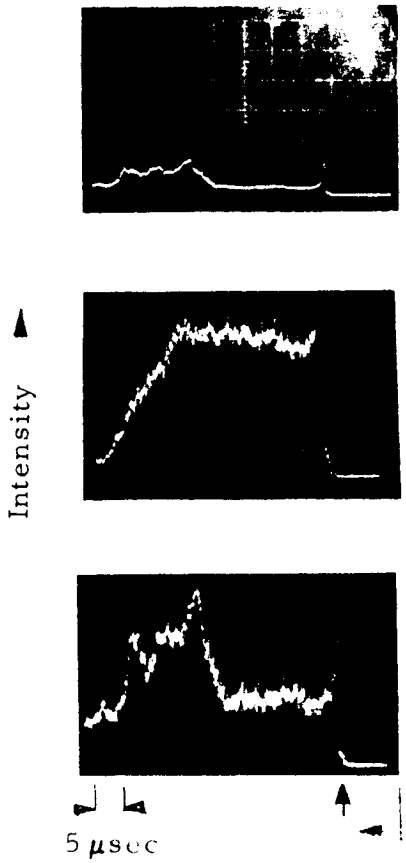

U_s = 27,950 ft/sec P_1 = 0.455 mm Hg

T_2 = 7400°K ρ_1/ρ_2 = 1.04 x 10^{-2}

Figure 4.3 Oscilloscope Traces of Radiation Behind Incident Shock Wave

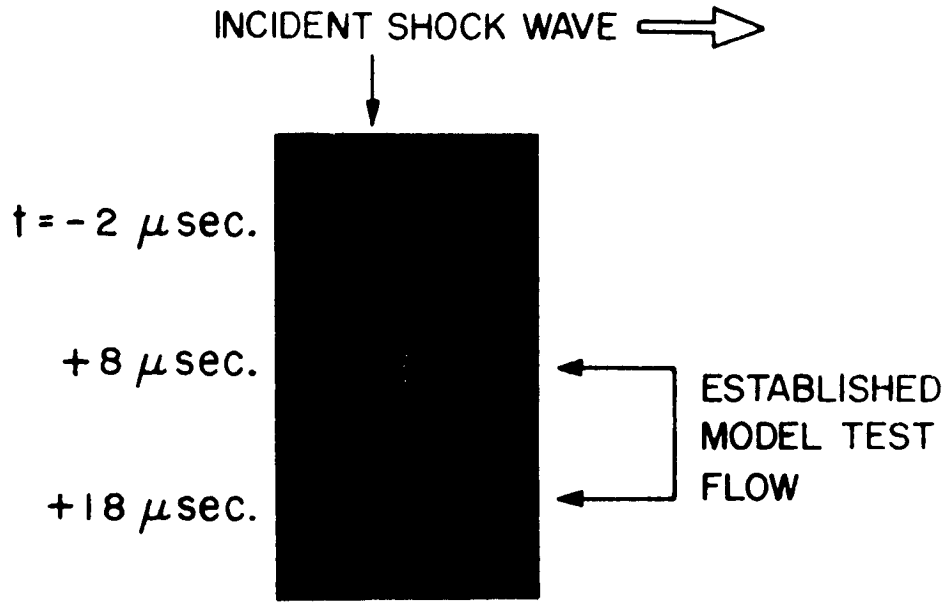

U_s = 28,000 FT./SEC. P_1 = 0.50 mm Hg

U_{fm} = 38,300 FT./SEC.

Δt EXPOSURE ≈ .05 μsec. R_N = 0.5 IN.

Figure 4.4a Image Converter Camera Photograph of Incident Shock Wave and Model Flow. The Three Frames are 10 sec Apart. Top Frame Shows Incident Shock Approach Model. Middle and Bottom Frames Show Established Flow Around a Hemispherical Model

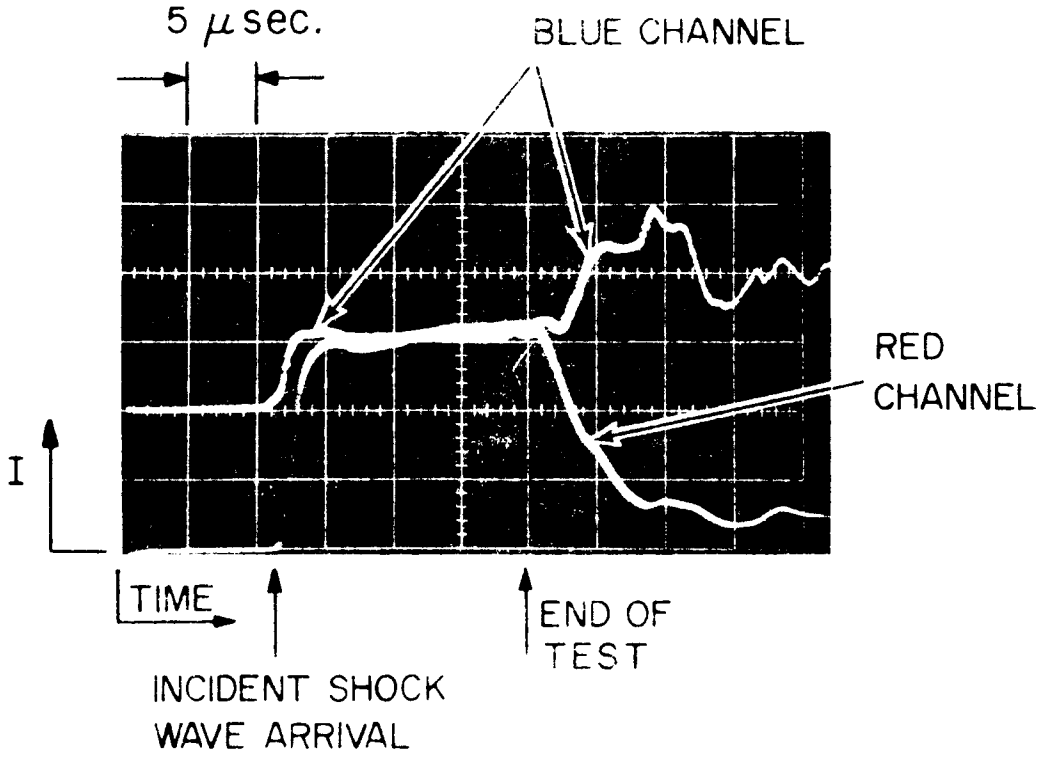

u_s = 28,000 FT./SEC. P_1 = 0.5 mm Hg

Figure 4.4b Oscilloscope Traces from Two-Color Photometer Viewing Stagnation Region of the Model. Top Trace Shows Blue Channel, (3500 - 4800 Å). Bottom Trace Red Channel (5800 - 12,000 Å)

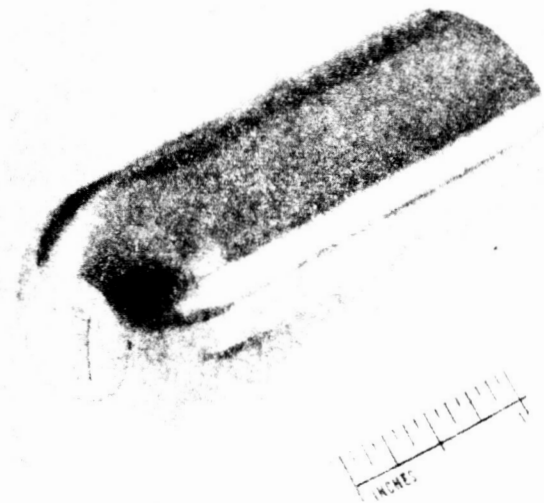

Figure 4.5a Photographs of Two Calorimeter Gage Model. Model R_n = 0.5 in.

Figure 4.5b Photograph of Thin Film Gage Model. Model R_n = 0.5 in.

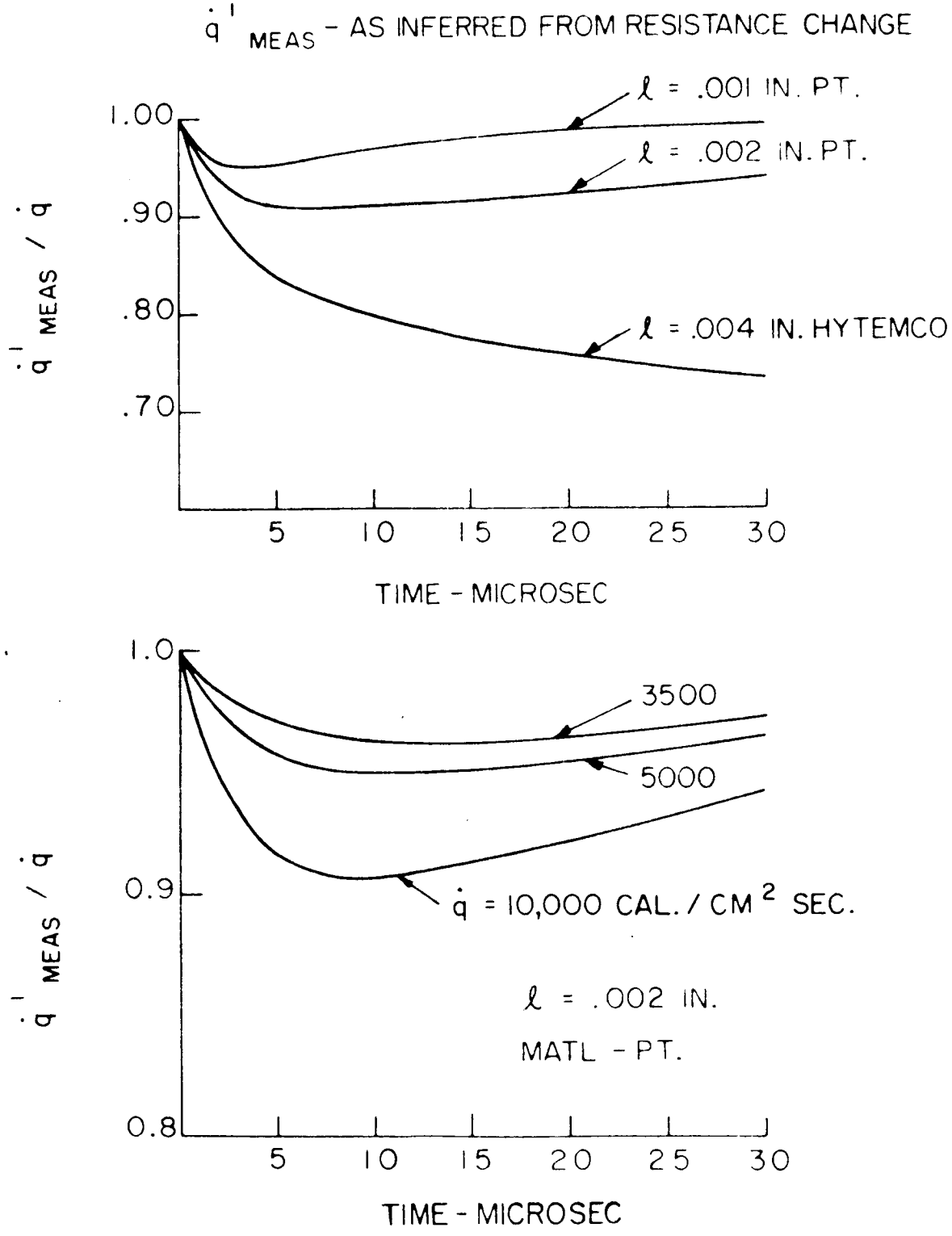

Figure 4.6 Theoretical Corrections for Platinum and Hytemco Calorimeter Heat Transfer Gages for Various Thickness and Heating Rates. Correction Only for Temperature Distribution Effect and not for Losses to Backing Material

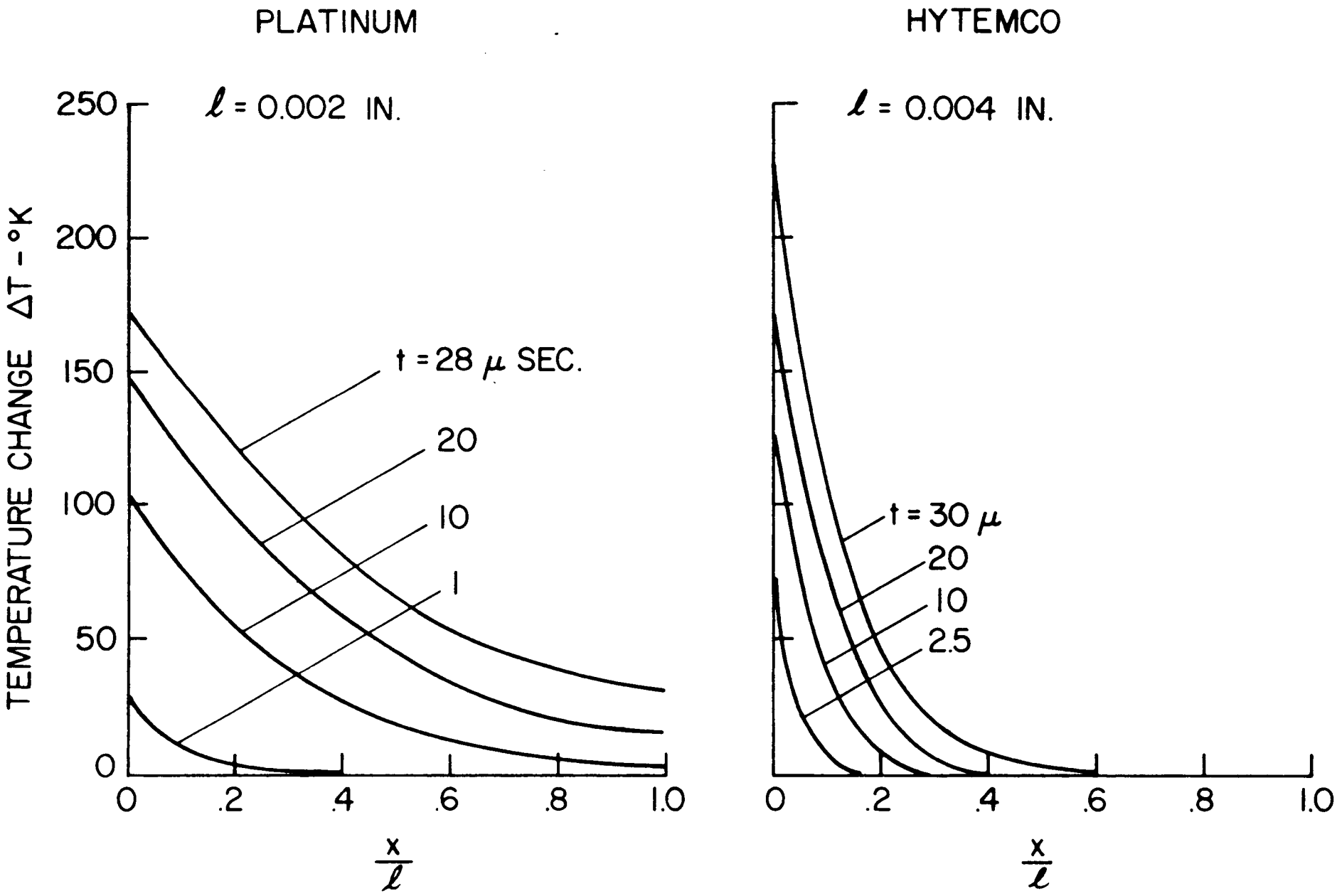

Figure 4.7 Temperature Distributions in Platinum and Hytemco Calorimeter Gages at Various Times from Application of Heat Pulse

Figure 4.8 Three Calorimeter Gage Model. R_n = 2.0 in.

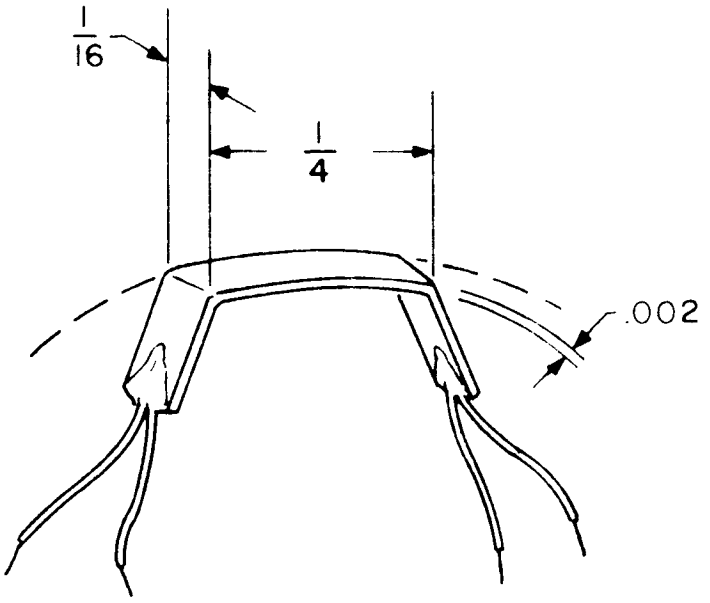

Figure 4.9a Geometry of Calorimeter Gage. Epoxy Plug Indicated by Dashed Line

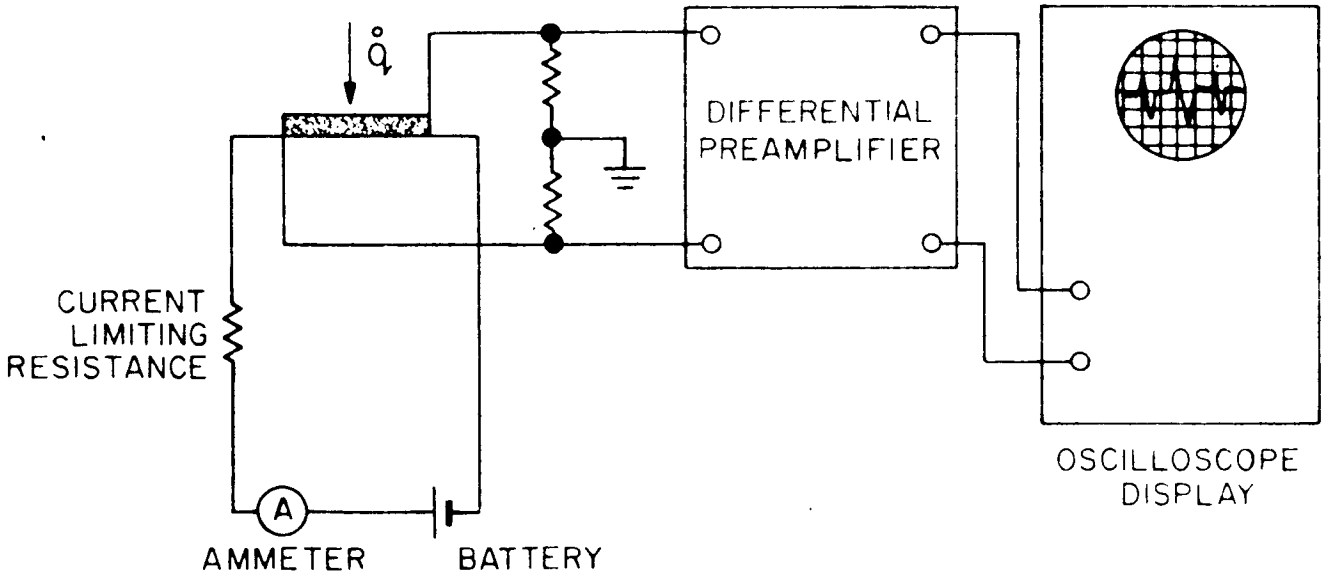

Figure 4.9b Schematic Diagram of Gage Electrical Circuit

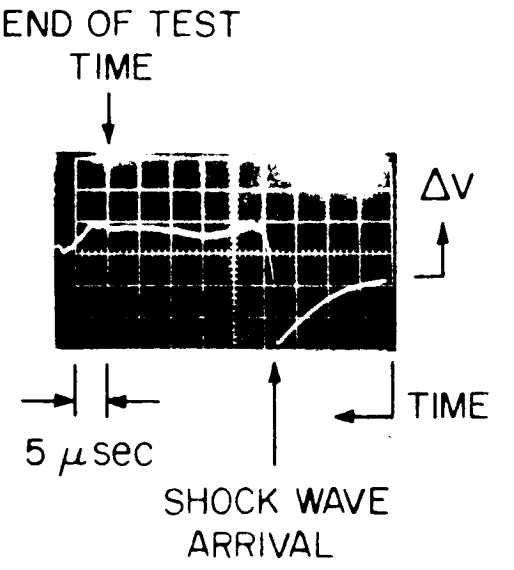

U_s = 29,700 FT./SEC. P_1 = 0.255 mm Hg

Figure 4.10a Potential Level with Respect to Ground of Calorimeter Gage

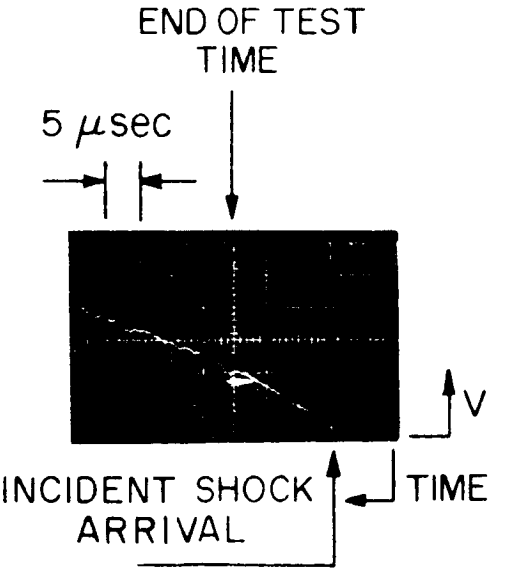

U_s = 27,900 FT./SEC. P_1 = 0.5 mm Hg

Figure 4.10b Oscilloscope Trace of Calorimeter Gage Signal. Careful Differential Preamplifier Balance Reduces Precursor at Instant of Incident Shock Arrival

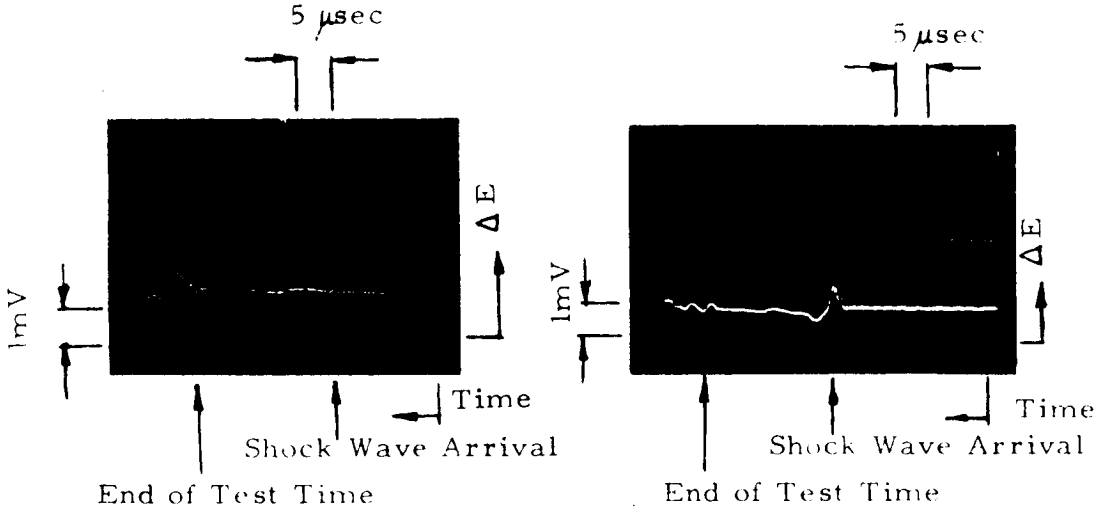

Gage Mtl. - Platinum

Gage Thickness - .002 in.

Gage Mtl. - Hytemco

Gage Thickness - .004 in.

U_s - 26,200 ft/sec

P_1 = .5 mm

Figure 4.11 Typical Calorimeter Gage Responses in Two Gage Model Test. Zero Gage Current Applied

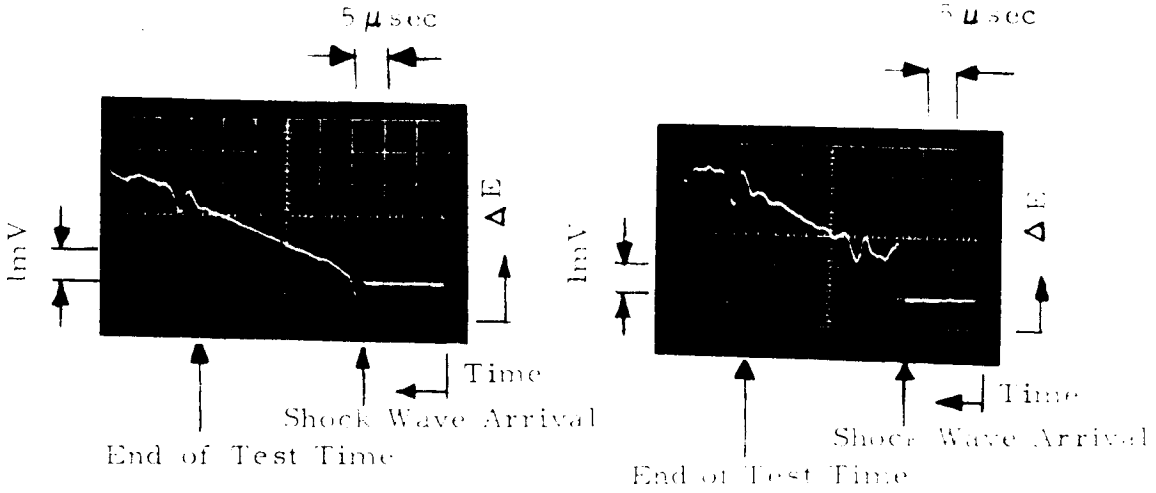

Gage Mtl - Platinum
Gage Thickness - .002 in.

Gage Mtl - Hytemco
Gage Thickness - .004 in

U_s = 28650 ft/sec
P_1 = .510 mm

Figure 4.12 Typical Calorimeter Gage Responses in Two Gage Model Test. Standard Gage Current Applied

9% CO_2 - 91% N_2

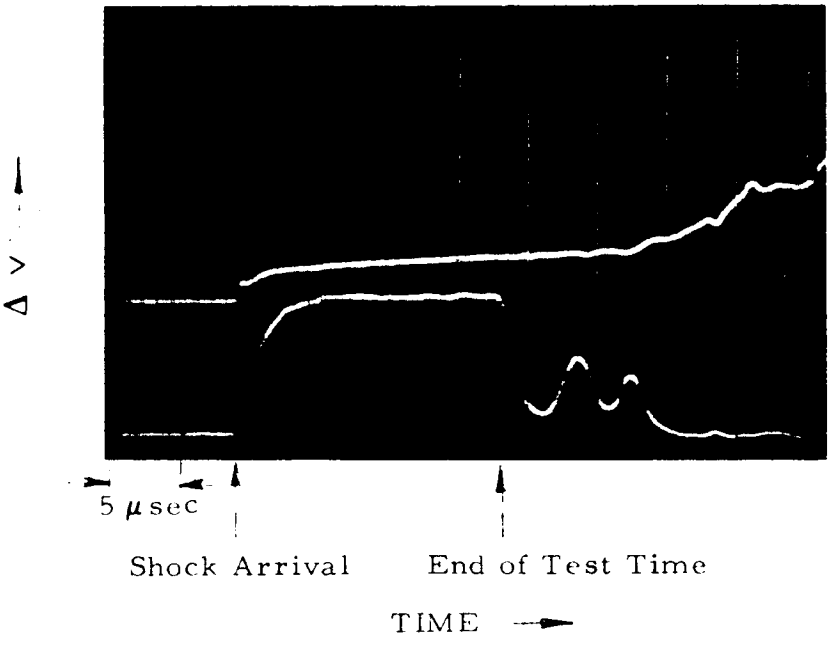

U_s = 29,700 ft/sec

P_1 = 0.475 mm Hg

R_N = 0.5 in.

Figure 4.13 Response of Stagnation Point Thin Film Heat Transfer Gage. Upper Trace - Heat Transfer Gage. Lower Trace - Side Wall Photomultiplier Viewing Shock Layer Ahead of the Stagnation Point

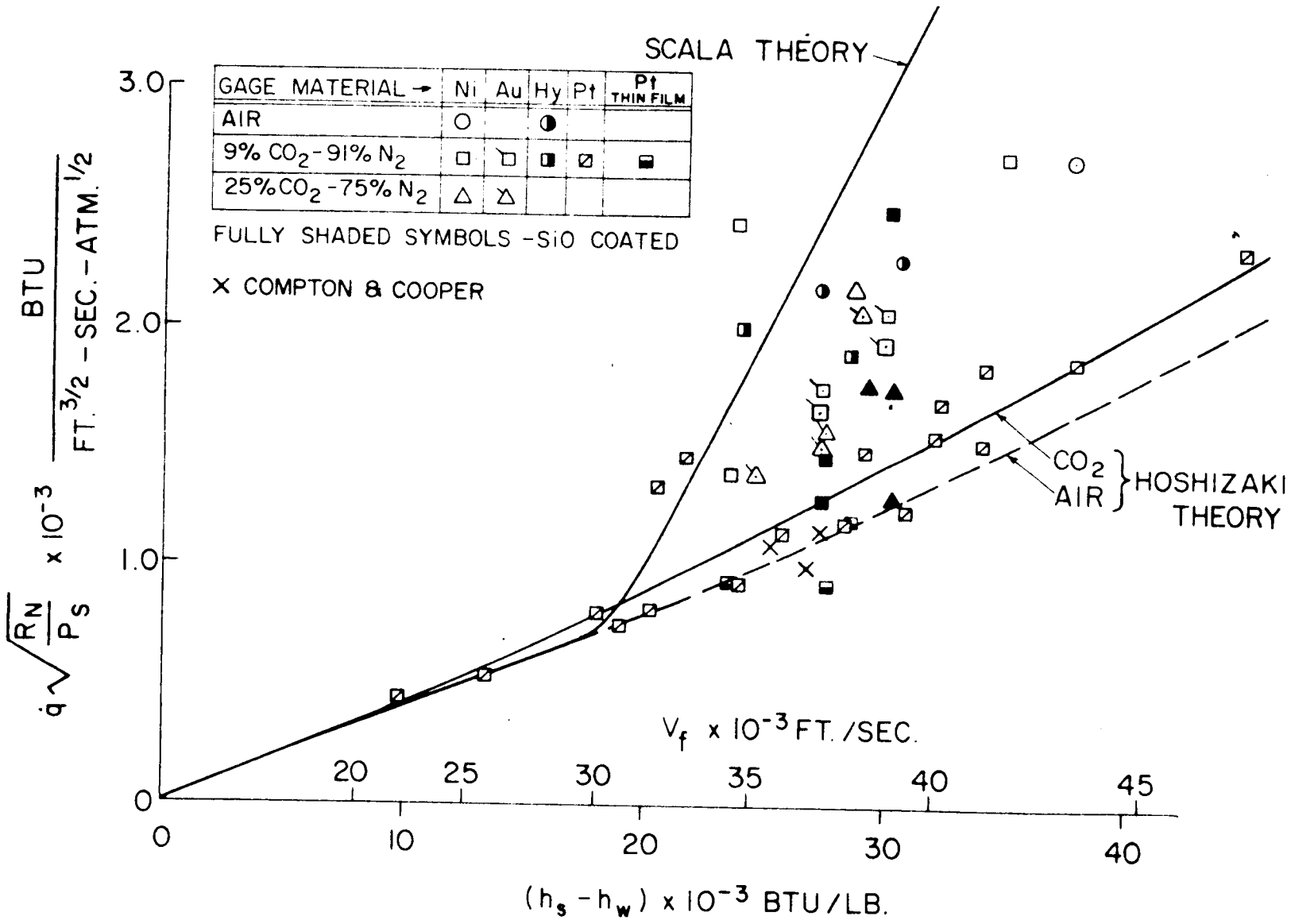

Figure 4.14 Comparison of Stagnation Point Heat Transfer Results Obtained with Different Material Gages

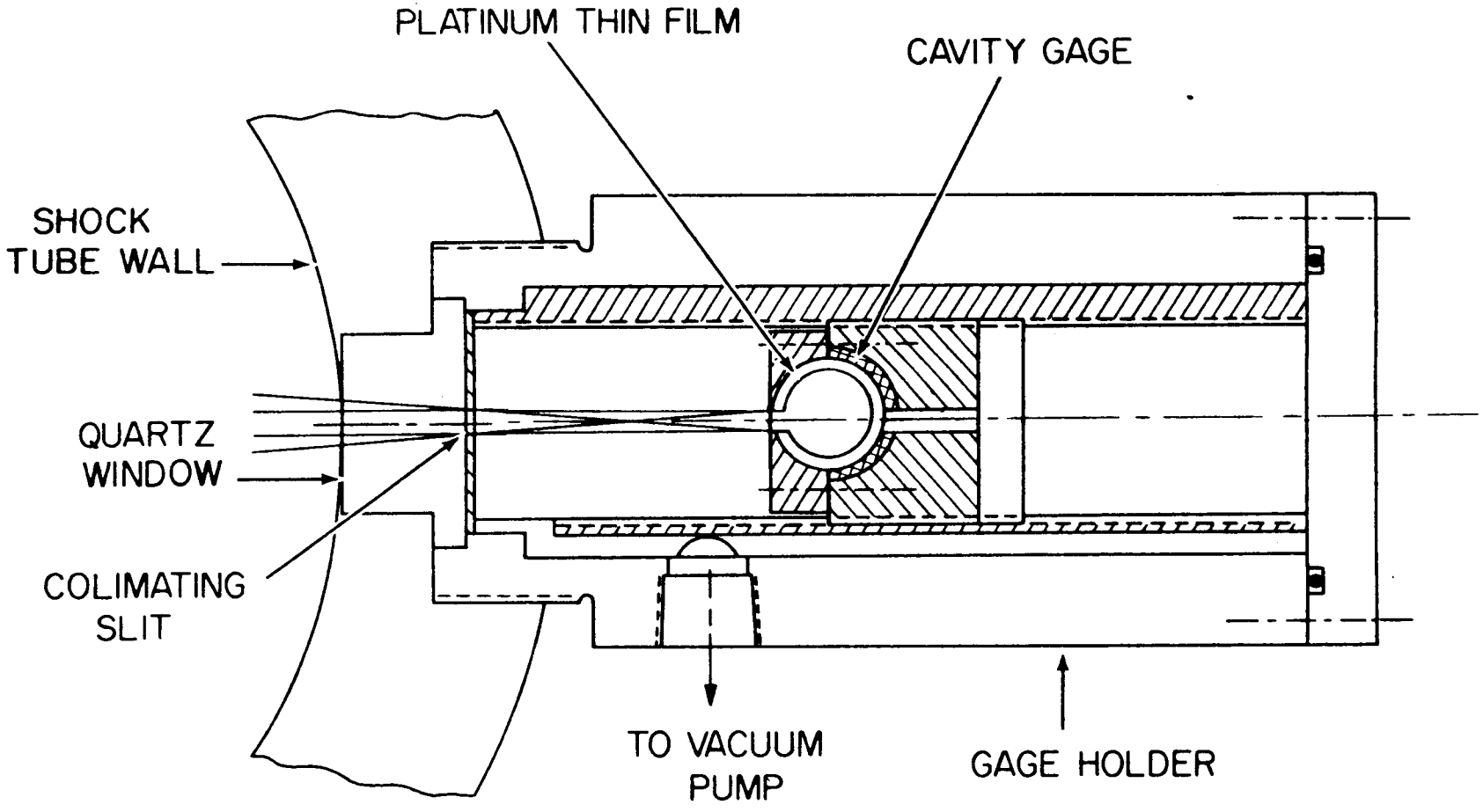

Figure 4.15 Schematic Diagram of Total Cavity Gave in Sidewall Configuration

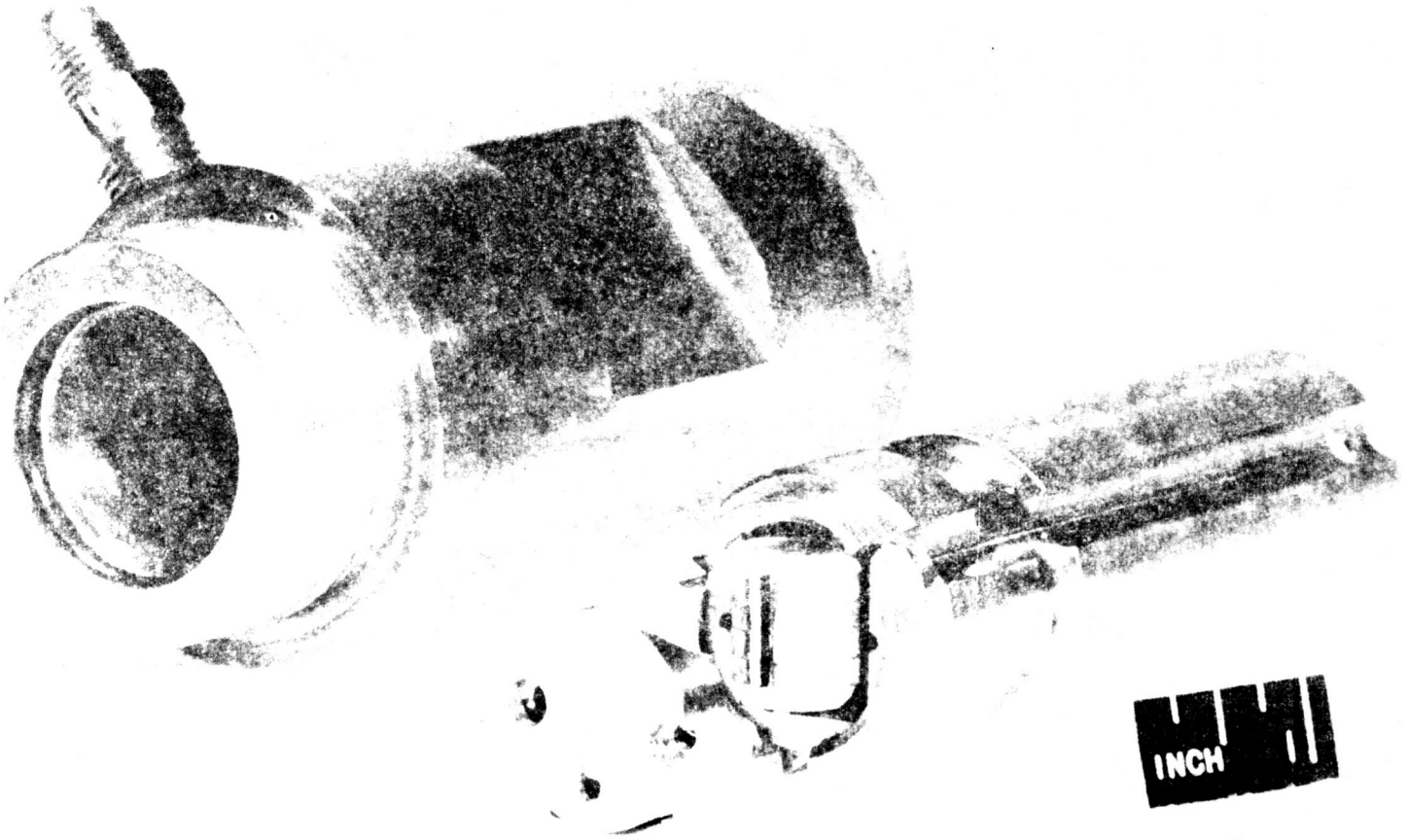

Figure 4.16 Photograph of Total Radiation Cavity Gage and Gage Holder

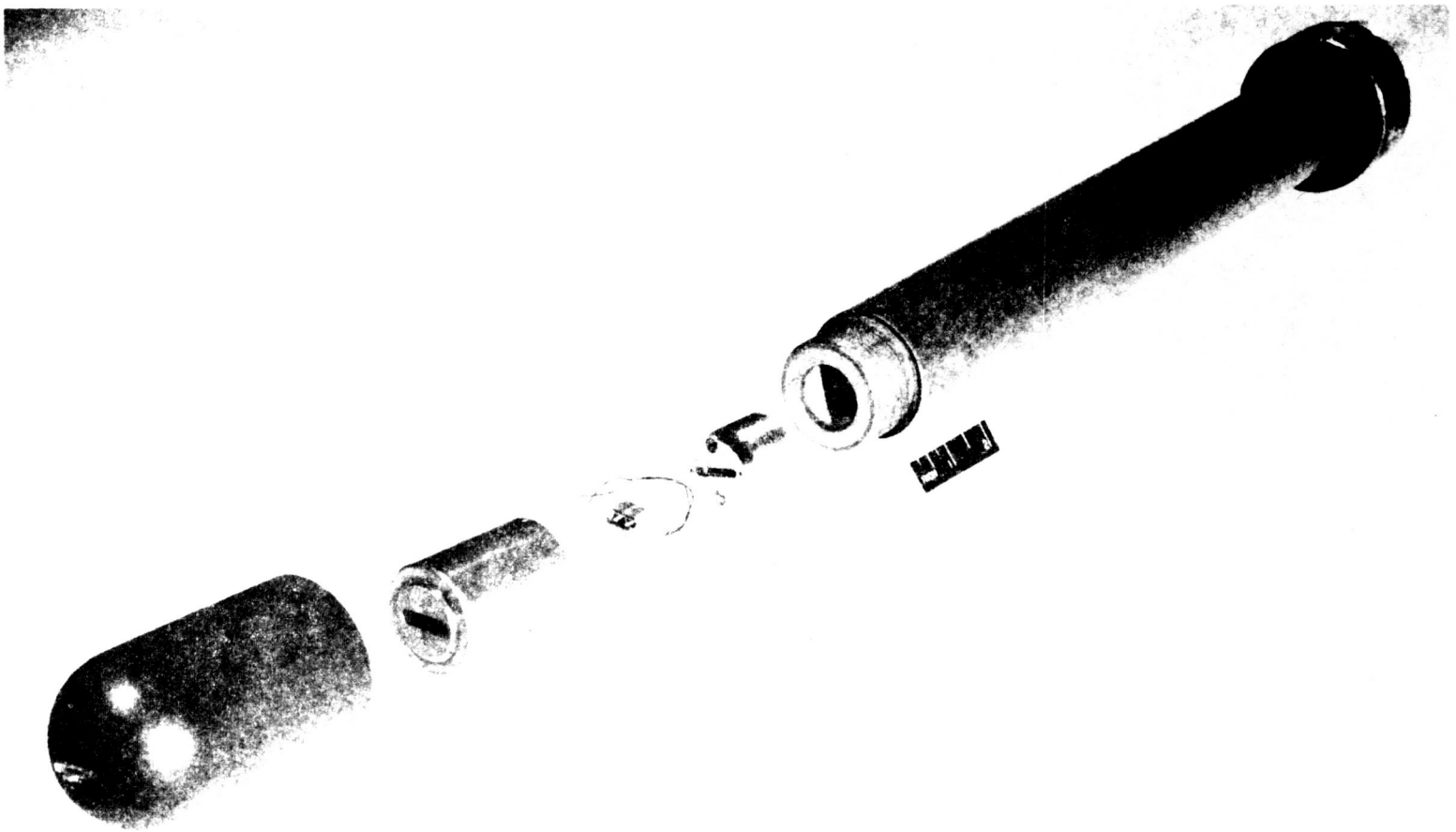

Figure 4.17 Stagnation Point Total Radiation Cavity Gage Model. Model R_n = 1 in.

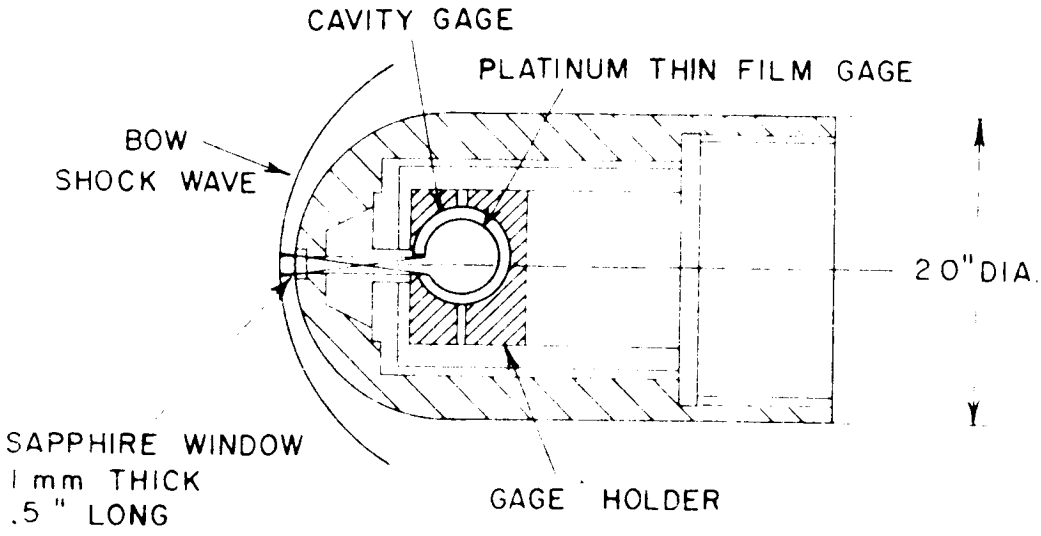

Figure 4.18 Internal Model Arrangement of Stagnation Point Total Radiation Cavity Gage

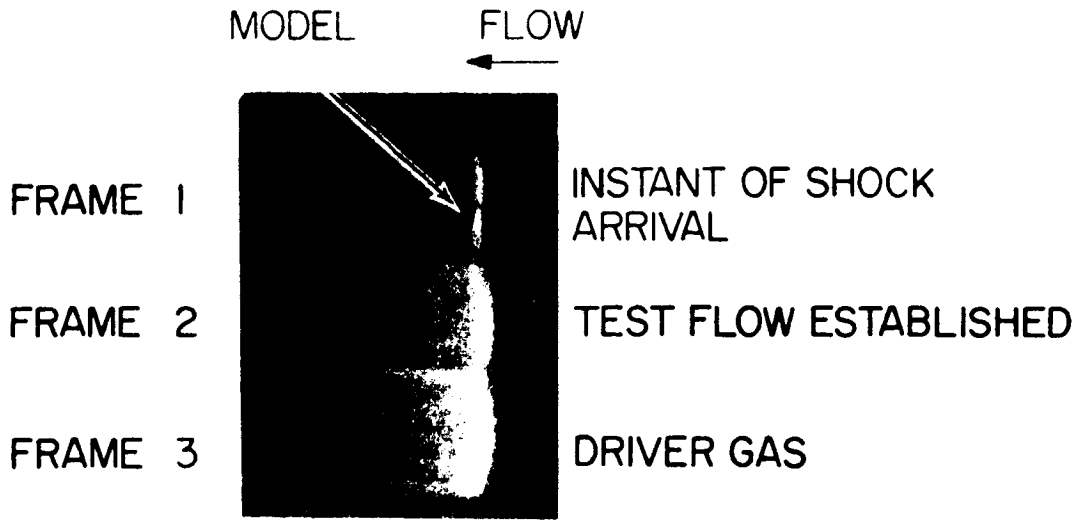

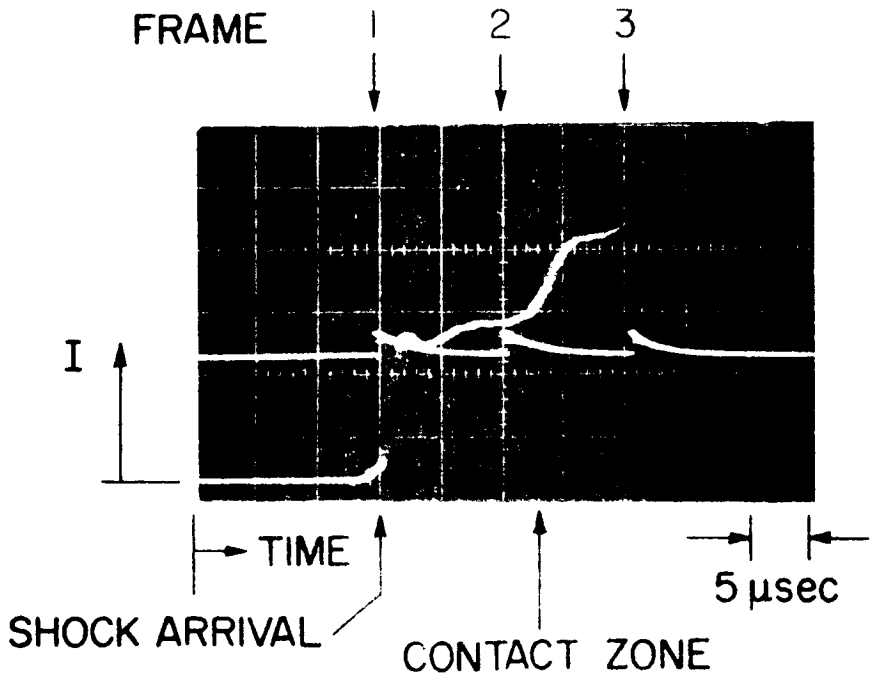

Figure 4.19 Image Converter Camera Photo of Shock Layer Ahead of 2.0 in. dia. Model and Oscillograph Traces of Camera Monitor and Blue Channel of Spectral Region Two-Color Photometer.

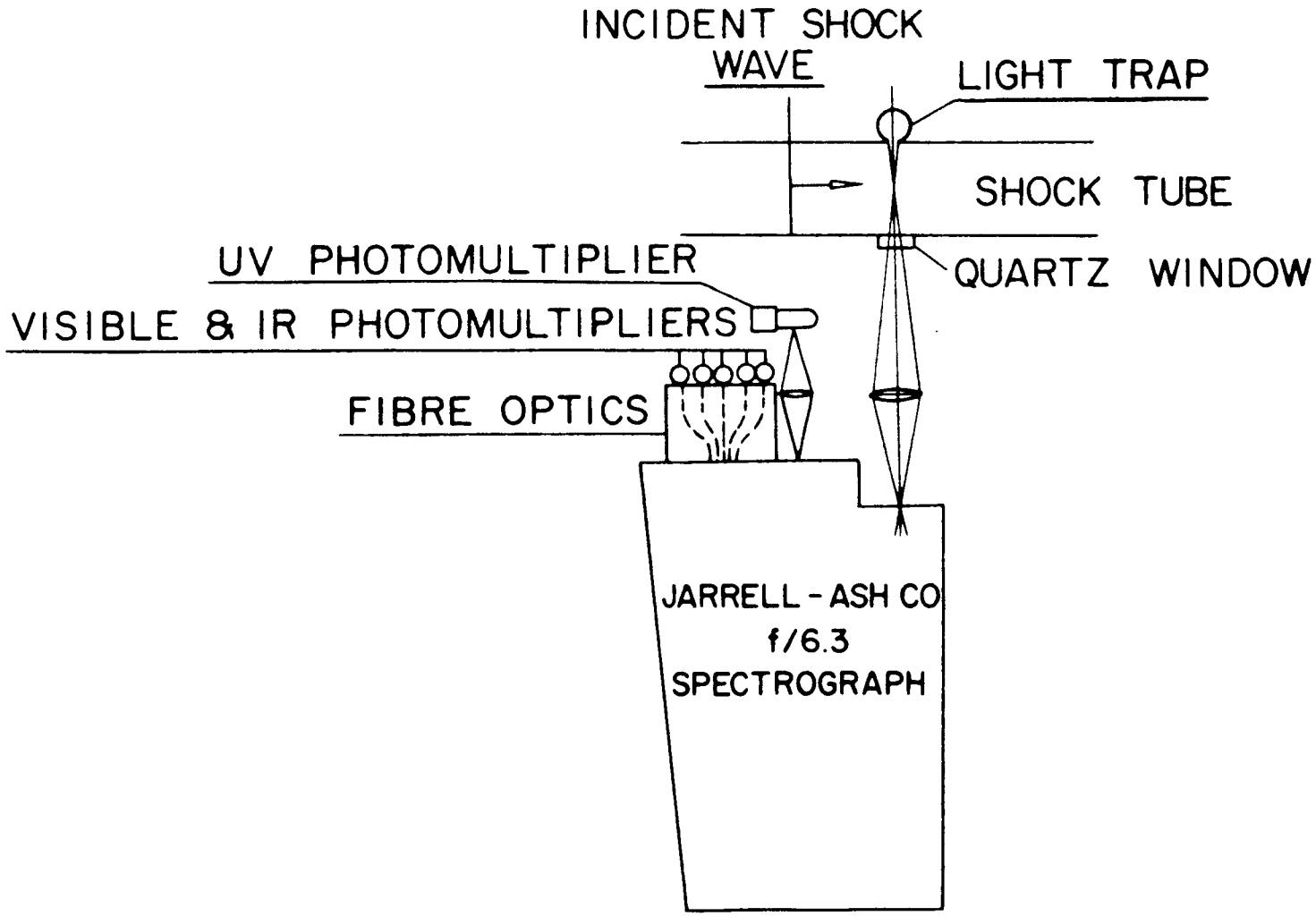

Figure 4.20 Schematic Diagram of Incident Shock Wave Radiation Instrumentation

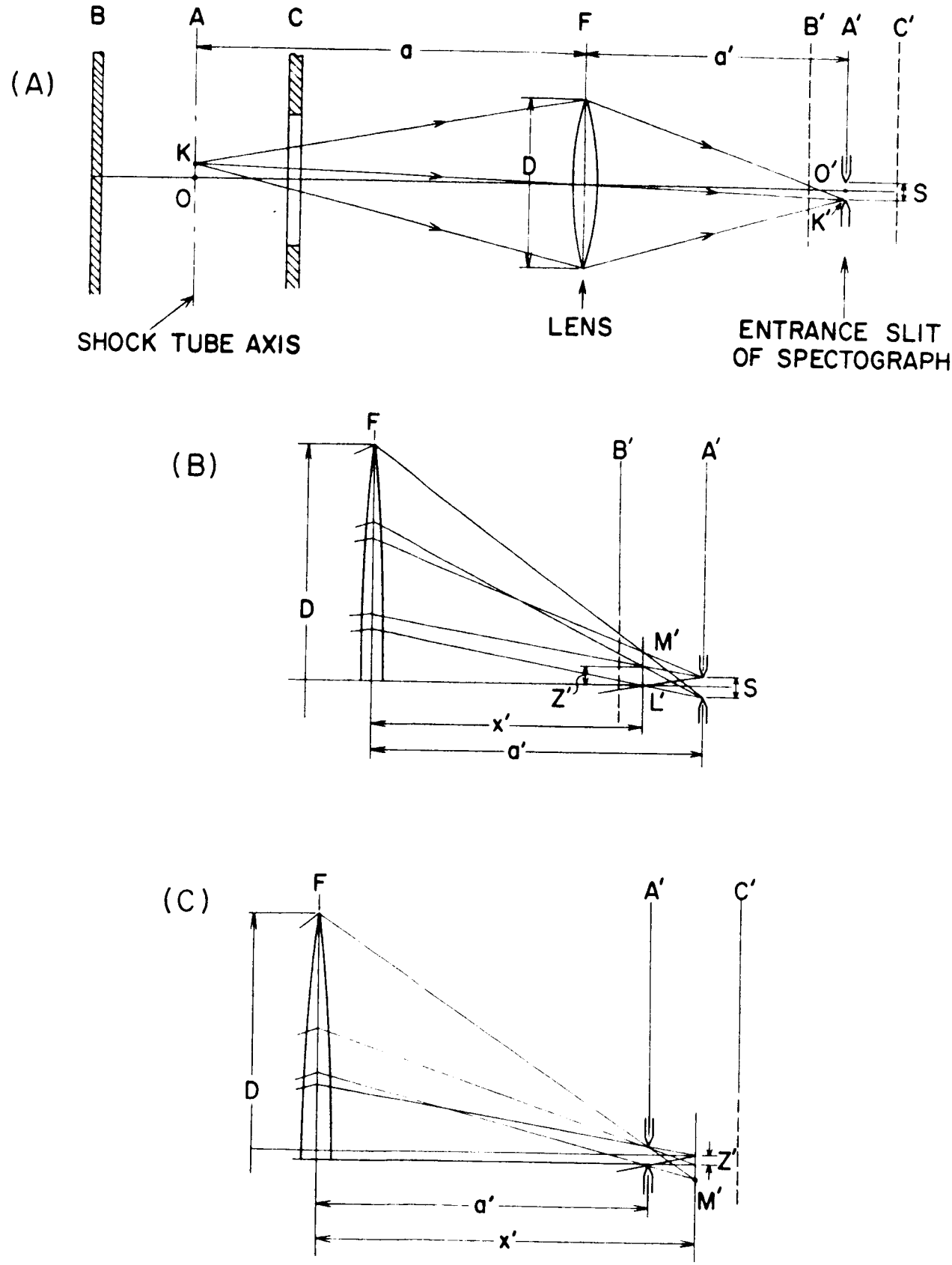

Figure 4.21a. Geometry of Optical System for Study of Incident Shock Radiation. Radiating Layer at Center of Shock Tube.
b. Geometry for Radiating Layer Between Planes A and B
c. Geometry for Radiating Layer Between Planes A and C.

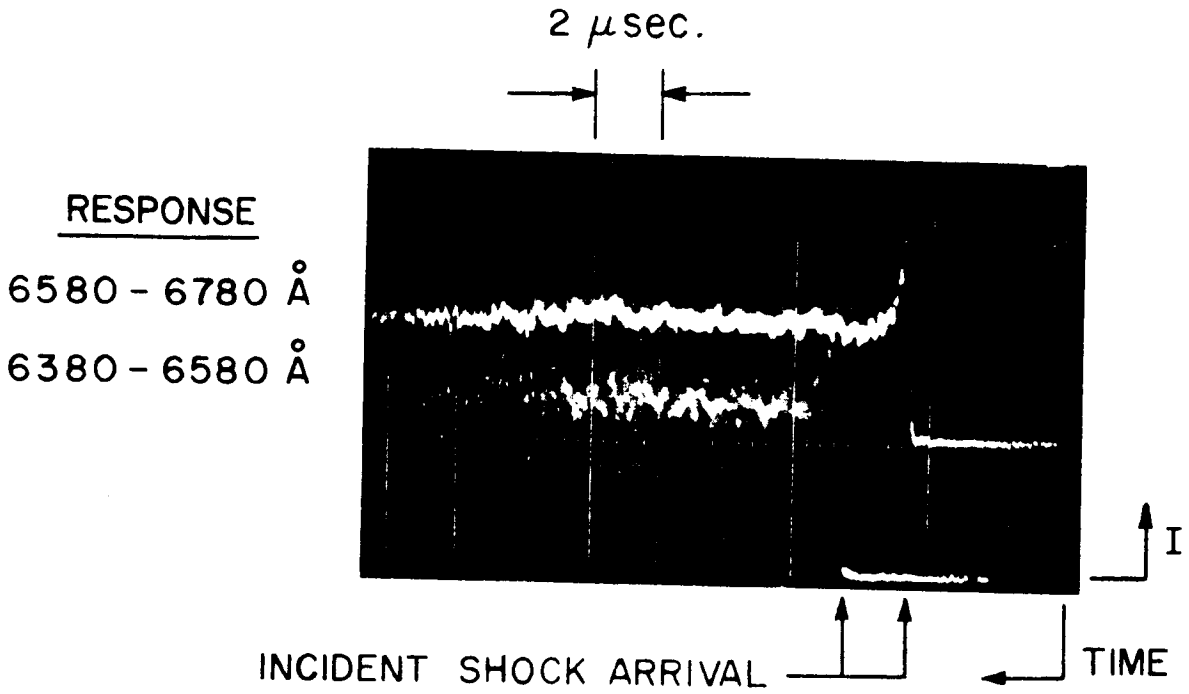

Figure 4.22 Typical Oscilloscope Traces from Two Channels of the Spectrophotometer

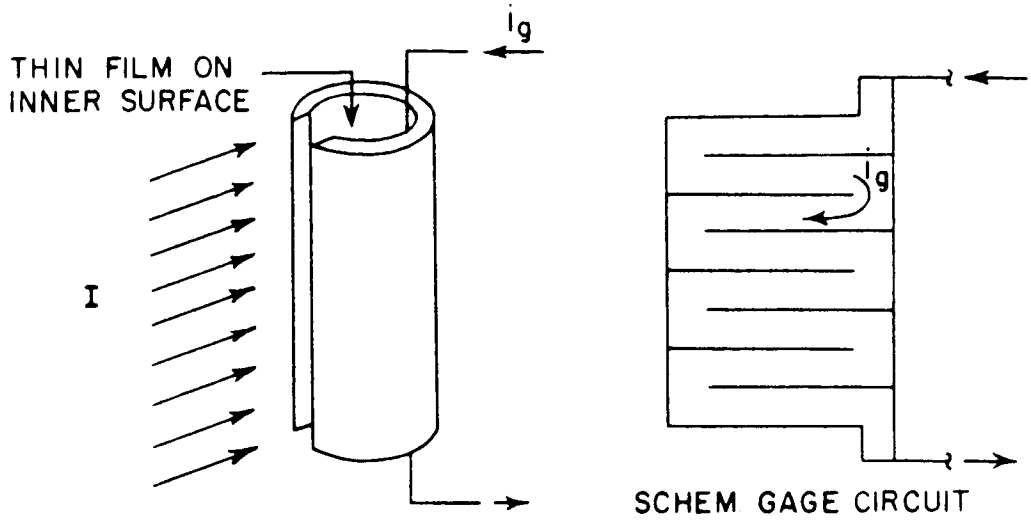

Figure 5.1a. Sketch of Cavity Gage Concept. Model Shown

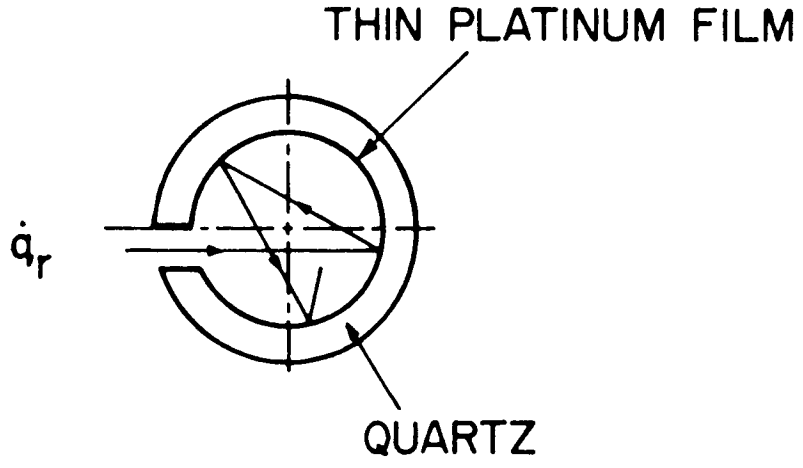

Figure 5.1b. Geometry of the Cylindrical Section of the Cavity Gage. The Entrance Slit is Set Off Axis. Path of a Parallel Ray in Multiple Specular Reflection is Shown

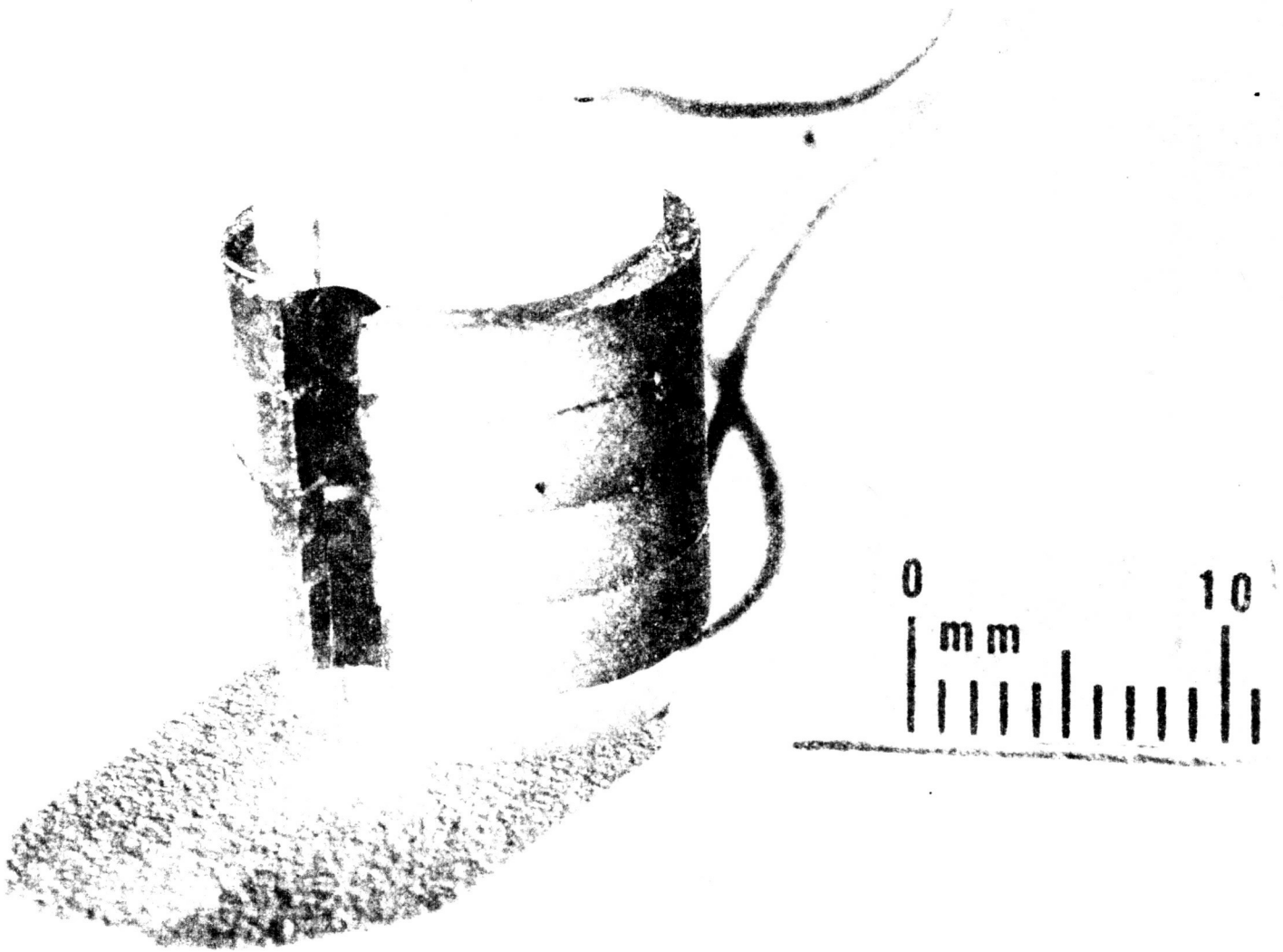

Figure 5.2. Total Radiation Cavity Gage. The Internal Diameter is 0.468 in., Thickness 0.065 in., and 0.125 in. High. The Entrance Opening is 0.10 in. Wide

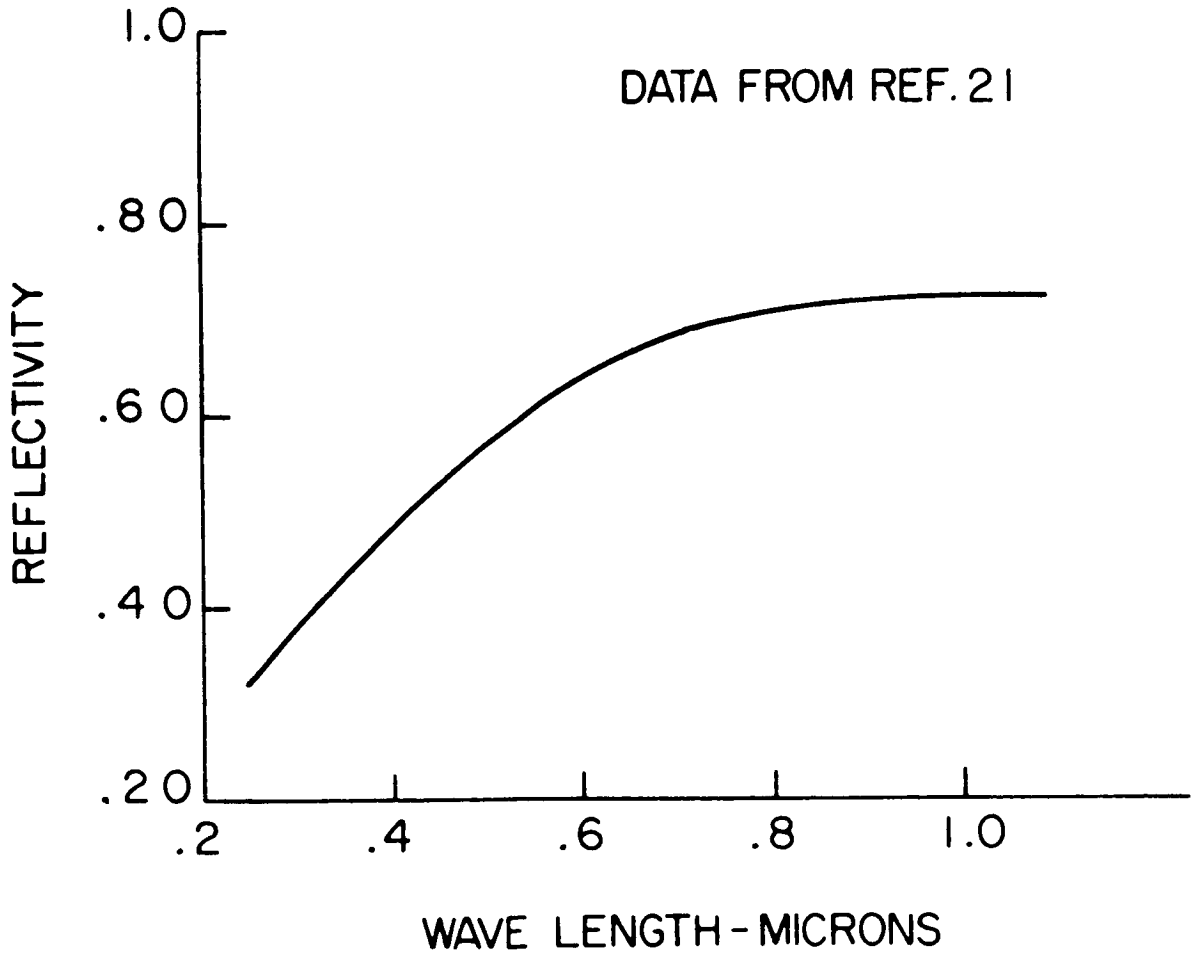

Figure 5.3. Reflectivity of Electrodeposited Platinum Thin Film

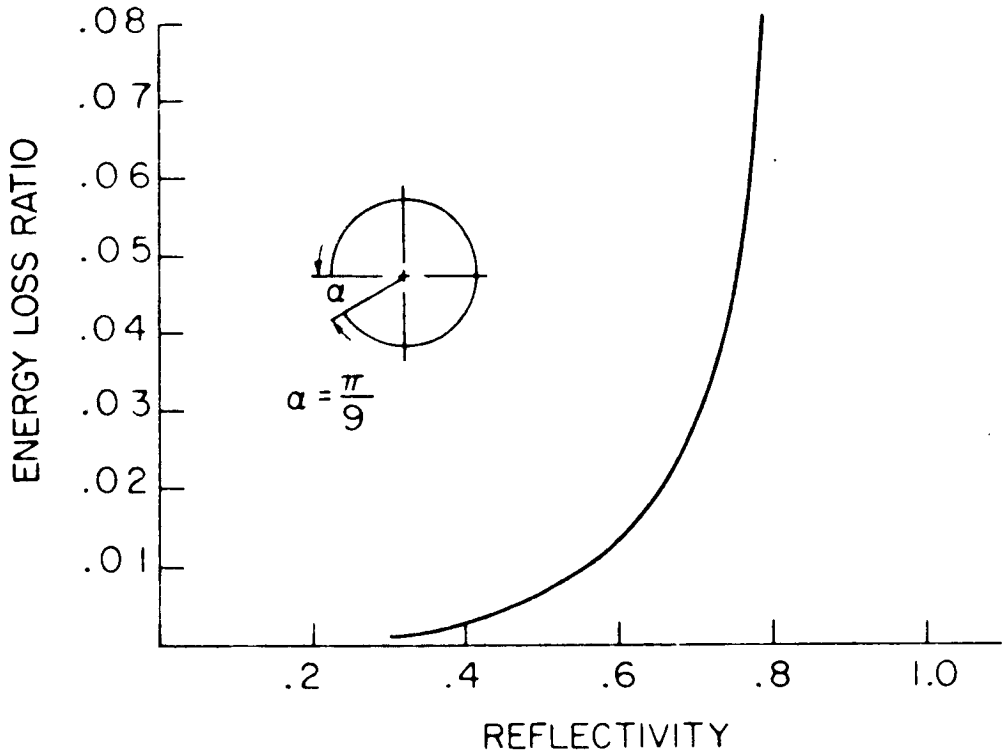

Figure 5.4. Energy Loss Ratio as Function of Platinum Film Reflectivity for Fixed Geometry of Collector

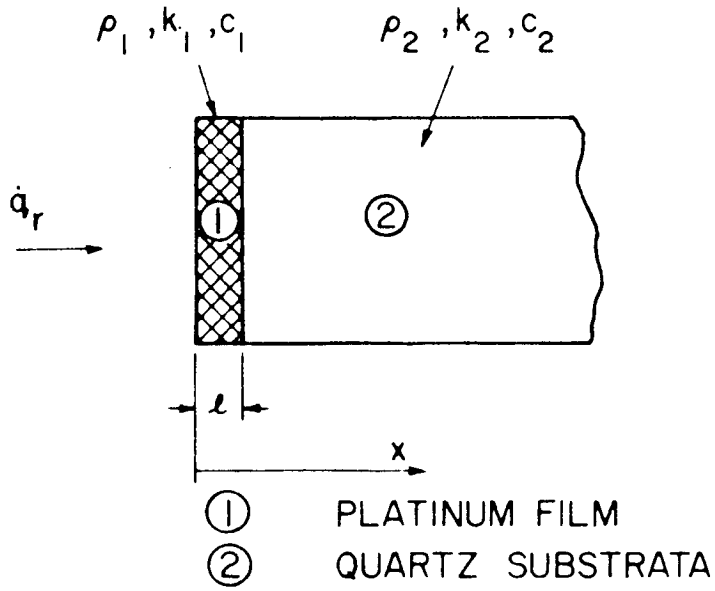

Figure 5.5. Configuration of the Analytical Model. The Quartz Substrate is Considered Semi-Infinite

9% CO_2 - 91% N_2
U_s 25,000 ft/sec
P_1 0.33 mm Hg

5 μsec Shock Arrival End of Test Time

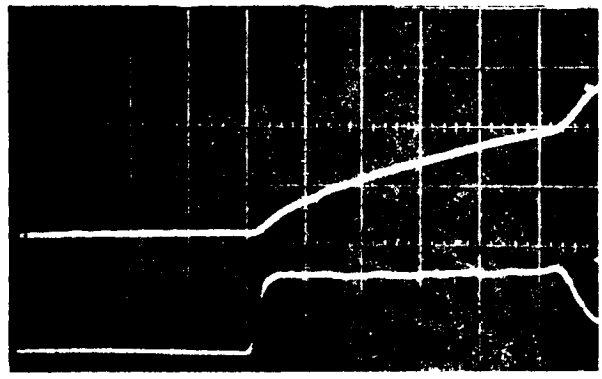

ΔV

2% CO_2 - 98% N_2
U_s = 29,500 ft/sec
P_1 0.33 mm Hg

5 μsec Shock Arrival End of Test Time

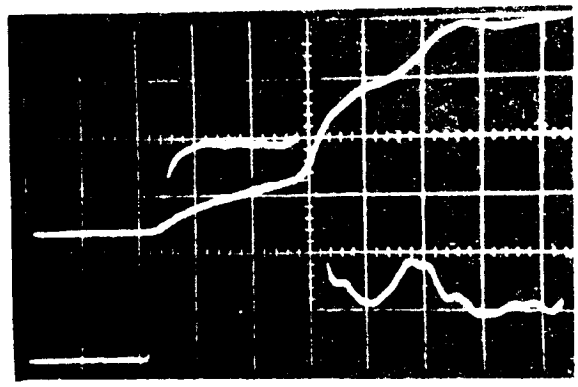

3% CO_2 - 97% N_2
U_s 33,000 ft/sec
P_1 = 0.34 mm Hg

5 μsec End of Test Time
Shock Arrival

TIME

Figure 5.6. Oscilloscope Traces Showing Thin Film Cavity Gage Response During Test Gas Flow. Upper Trace - Model Stagnation Region Cavity Gage. Lower Trace - Sidewall Photomultiplier Sensitive in the Red Viewing Stagnation Region Shock Layer

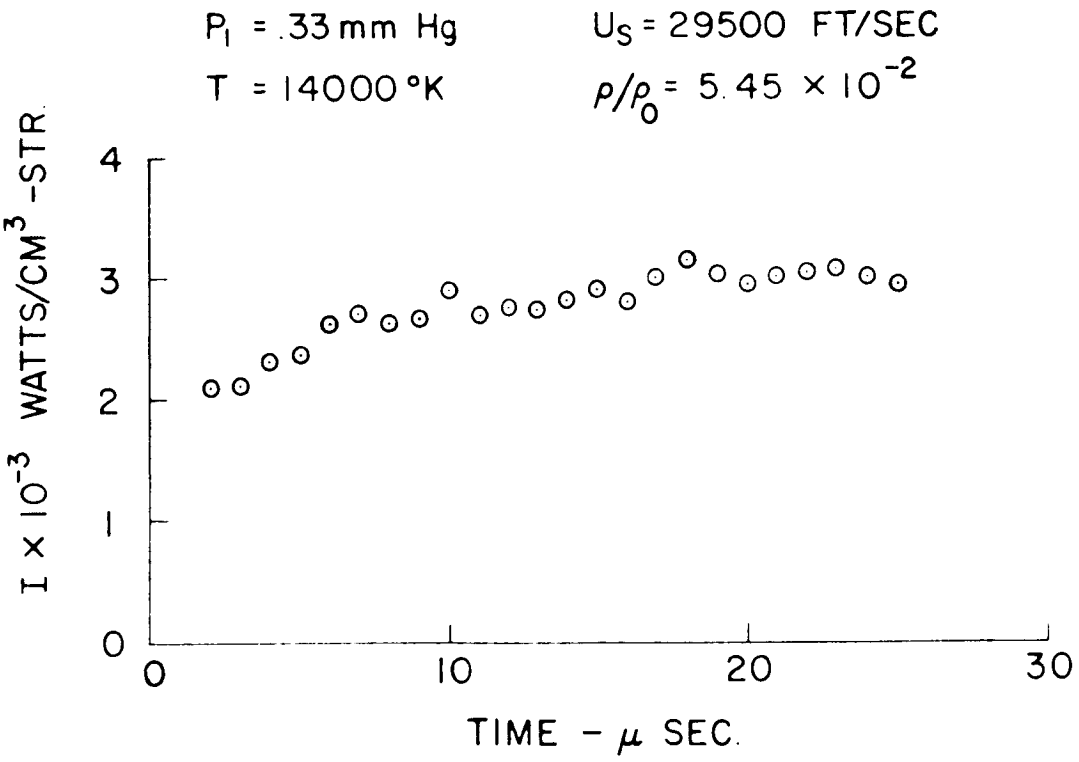

Figure 5.7. Radiance of Model Stagnation Region Gas as a Function of Time After Arrival of Incident Shock Wave at Model. Data Obtained From Analysis of Thin Film Cavity Gage Signal Shown in Fig. 5.6.

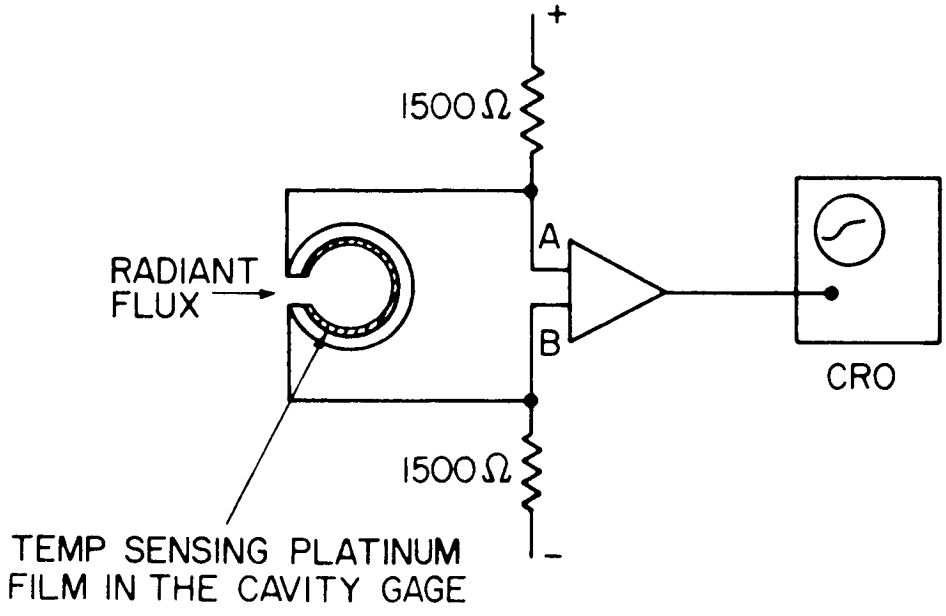

Figure 5.8. Schematic Diagram of Cavity Gage Electrical Circuit. The Potential Lead is Connected to Differential Preamplifier. Total Gage Resistance is 400Ω. Current is Kept Constant by Use of Large Resistance in Series with the Gage.

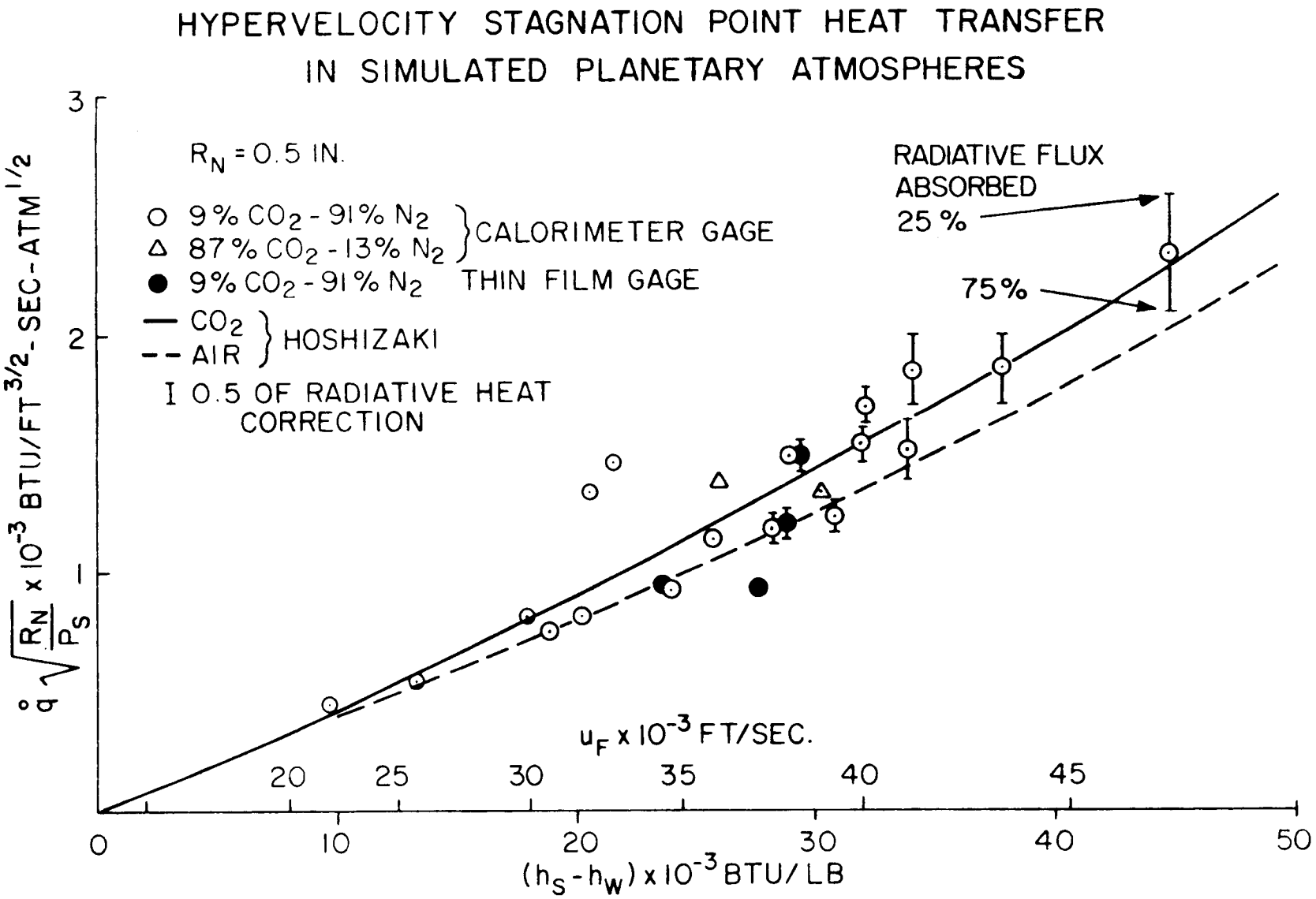

Figure 6.1. Hypervelocity Stagnation Point Heat Transfer in Simulated Planetary Atmospheres

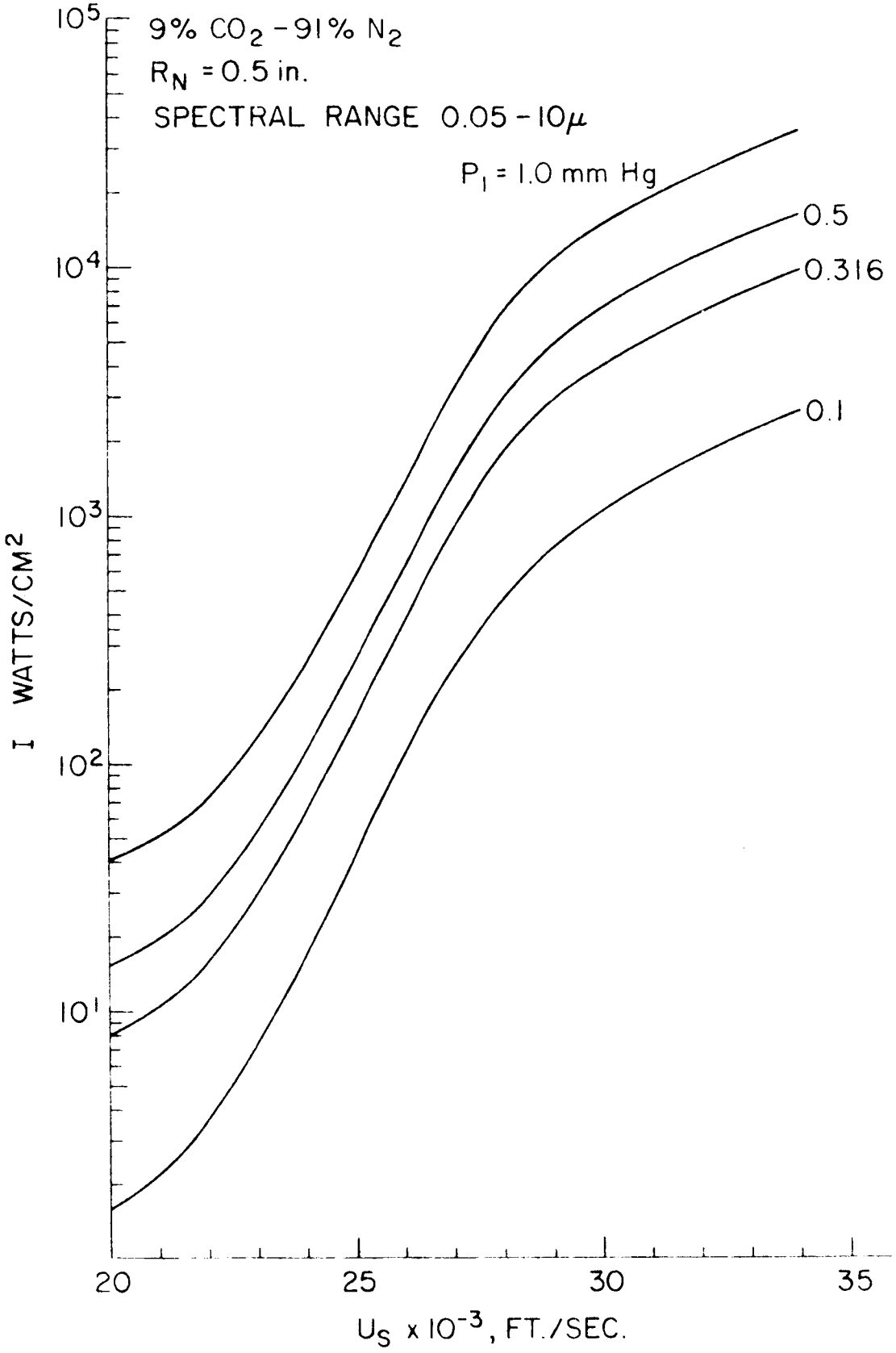

Figure 6.2. Radiative Heat Transfer to the Stagnation Point for Hemispherical Model with R_n = 0.5 in.

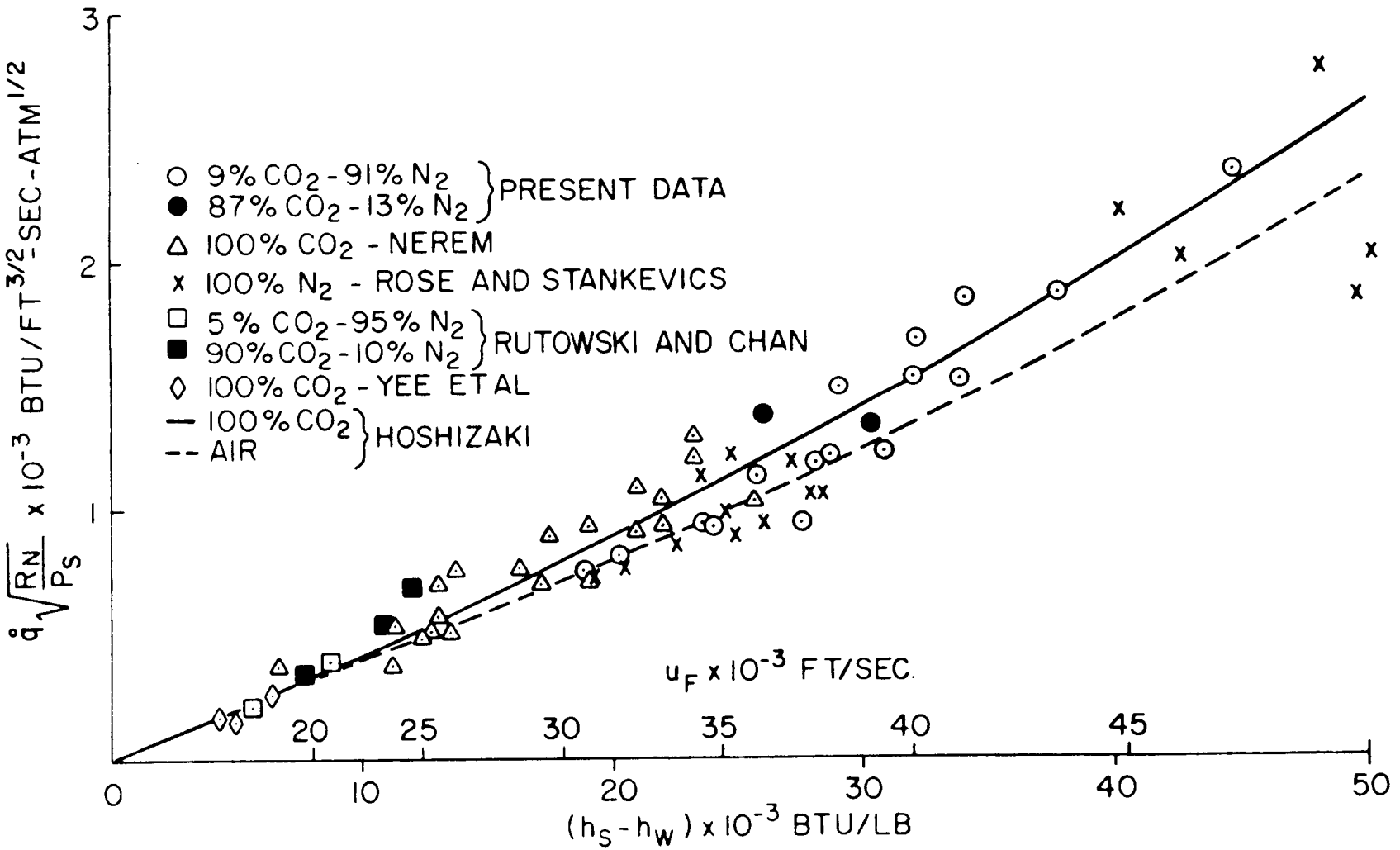

Figure 6.3. Comparison of Stagnation Point Heat Transfer Results in Carbon Dioxide, Carbon-Dioxide-Nitrogen Mixtures and Nitrogen

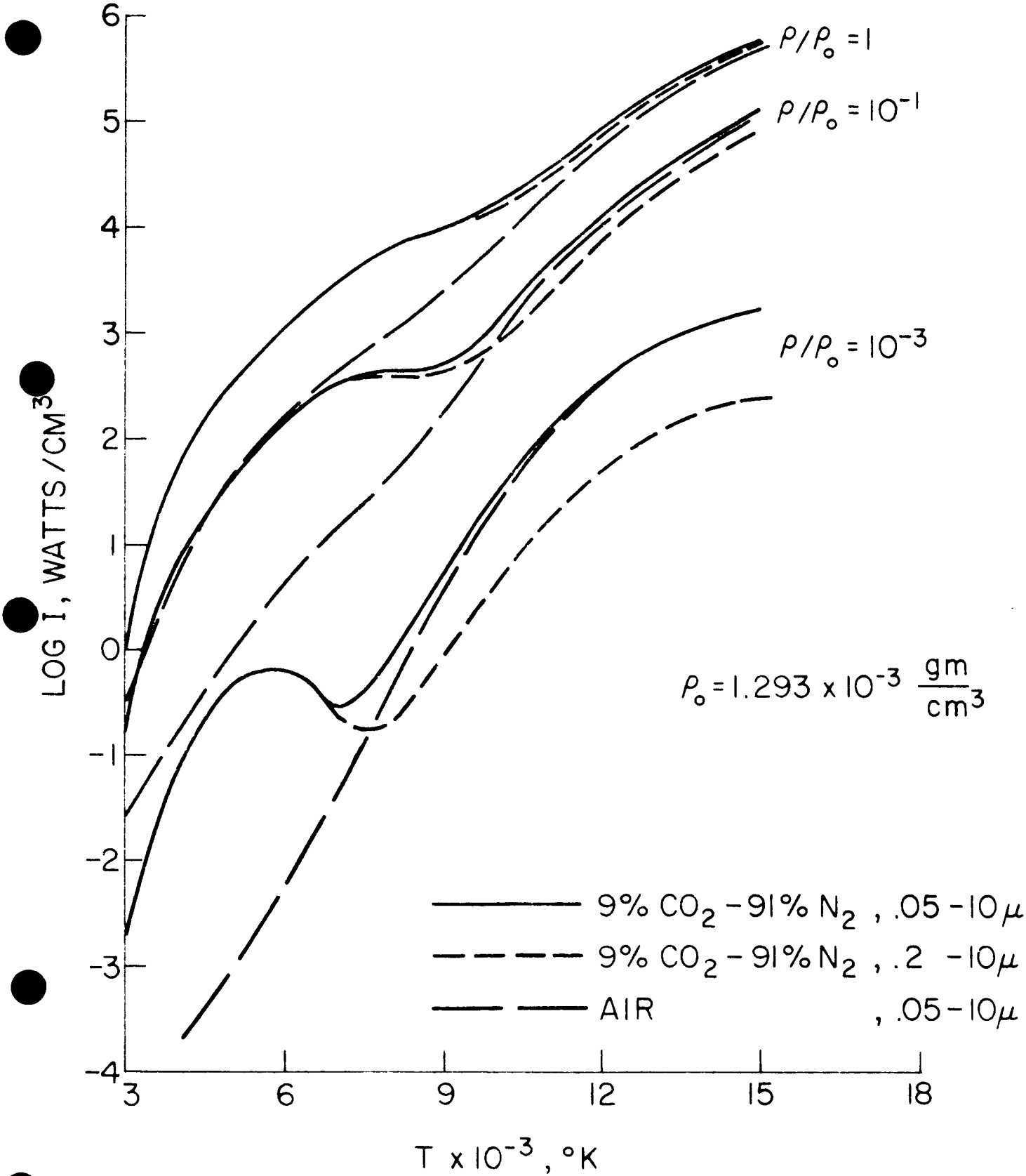

Figure 6.4. Theoretical Total Radiance of a 9% CO_2 - 91% N_2 Gas Mixture Compared for Two Wavelength Regions and Compared with Air. After Browne (4), Breene and Nardone (5), and Nardone, Breene, Zeldin, and Riethof (15).

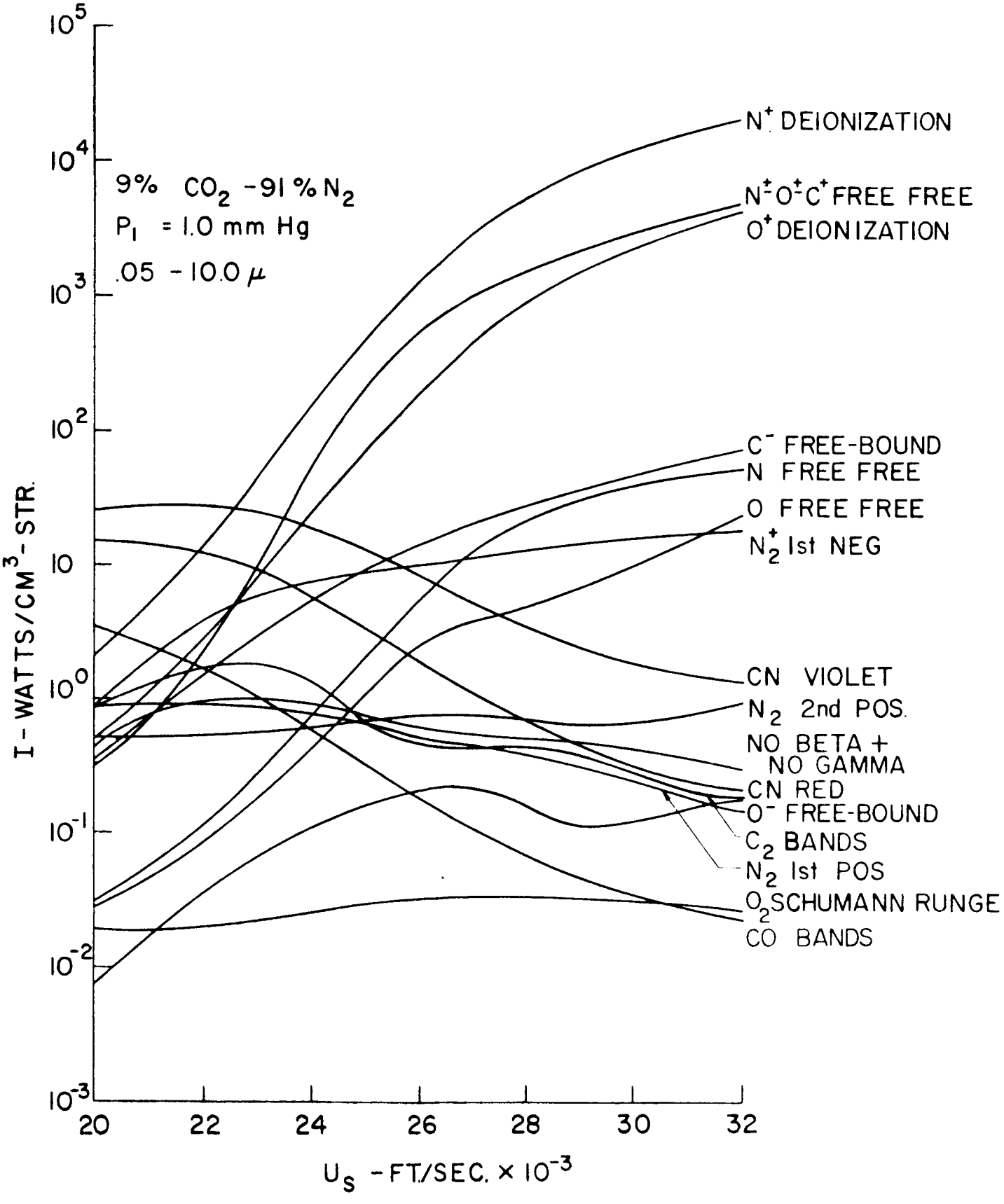

Figure 6.5 Species Radiation of Equilibrium Gas at Model Stagnation Point in the Shock Tube

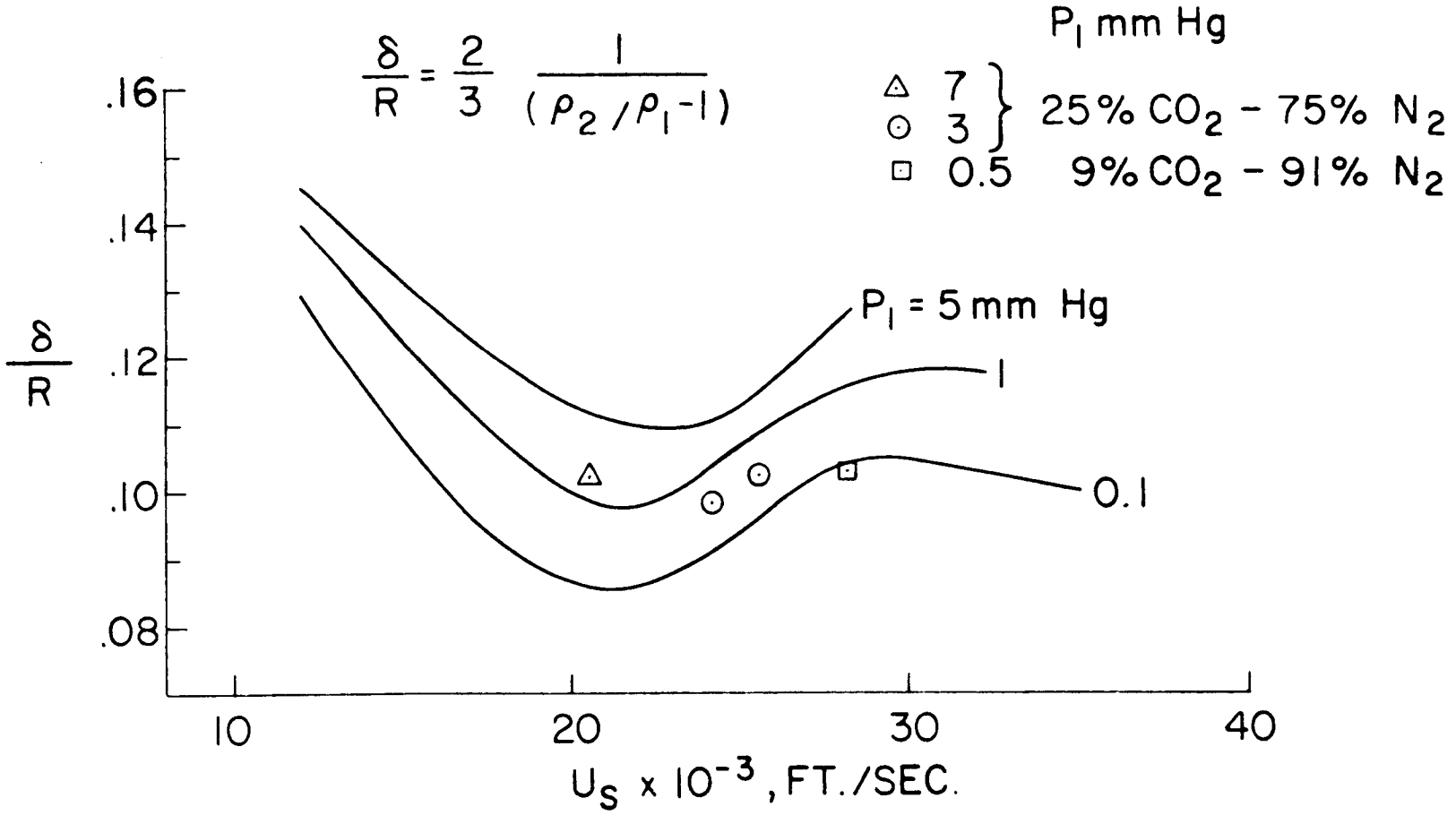

Figure 6.6 Stand-off Distance for Hypervelocity Shock Layer

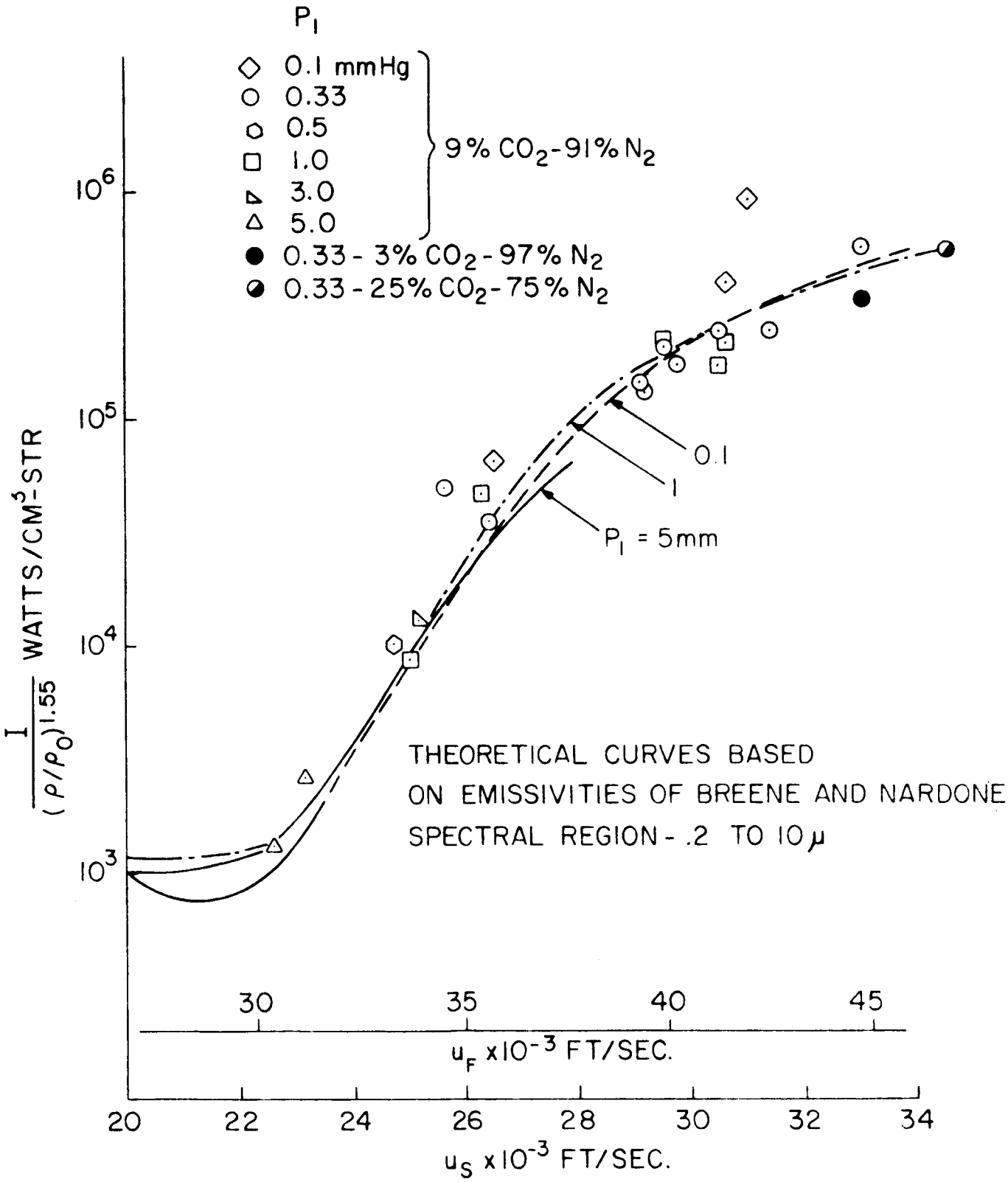

Figure 6.7. Stagnation Point Radiation in Simulated Venusian Atmosphere. Experimental Results Obtained with the Cavity Gage Compared to the Theoretical Predictions

9% CO_2 - 91% N_2

P_1 = 0.10 mm Hg U_s = 26,500 ft/sec

T = 11,600°K ρ/ρ_0 = 1.84 x 10^{-2}

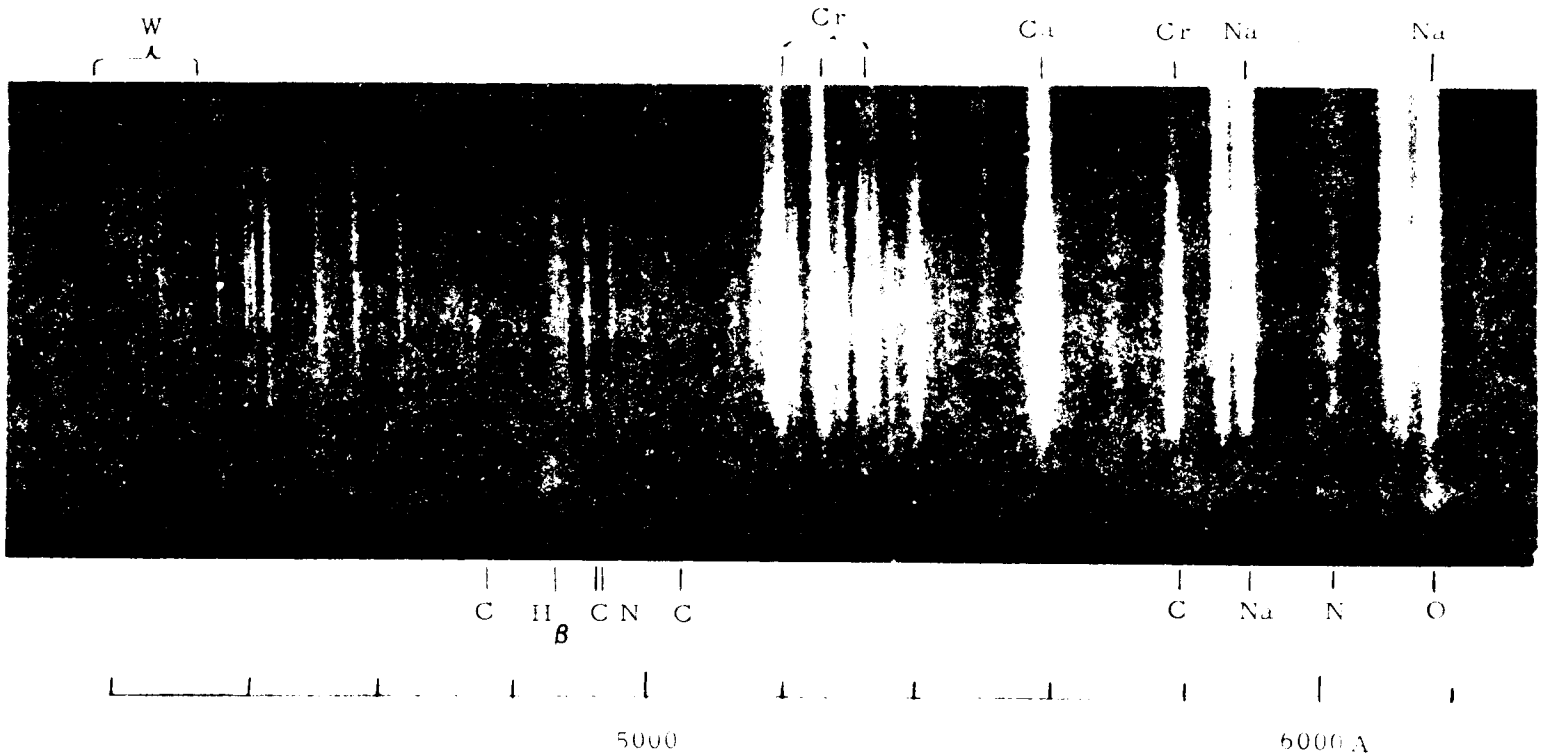

Figure 6.8 Time Resolved Spectrogram of Gas in the Stagnation Region to of Hemi-spherical Model. Instrument has f/3.5 Glass Optics and Time Resolution of 11 Microseconds.

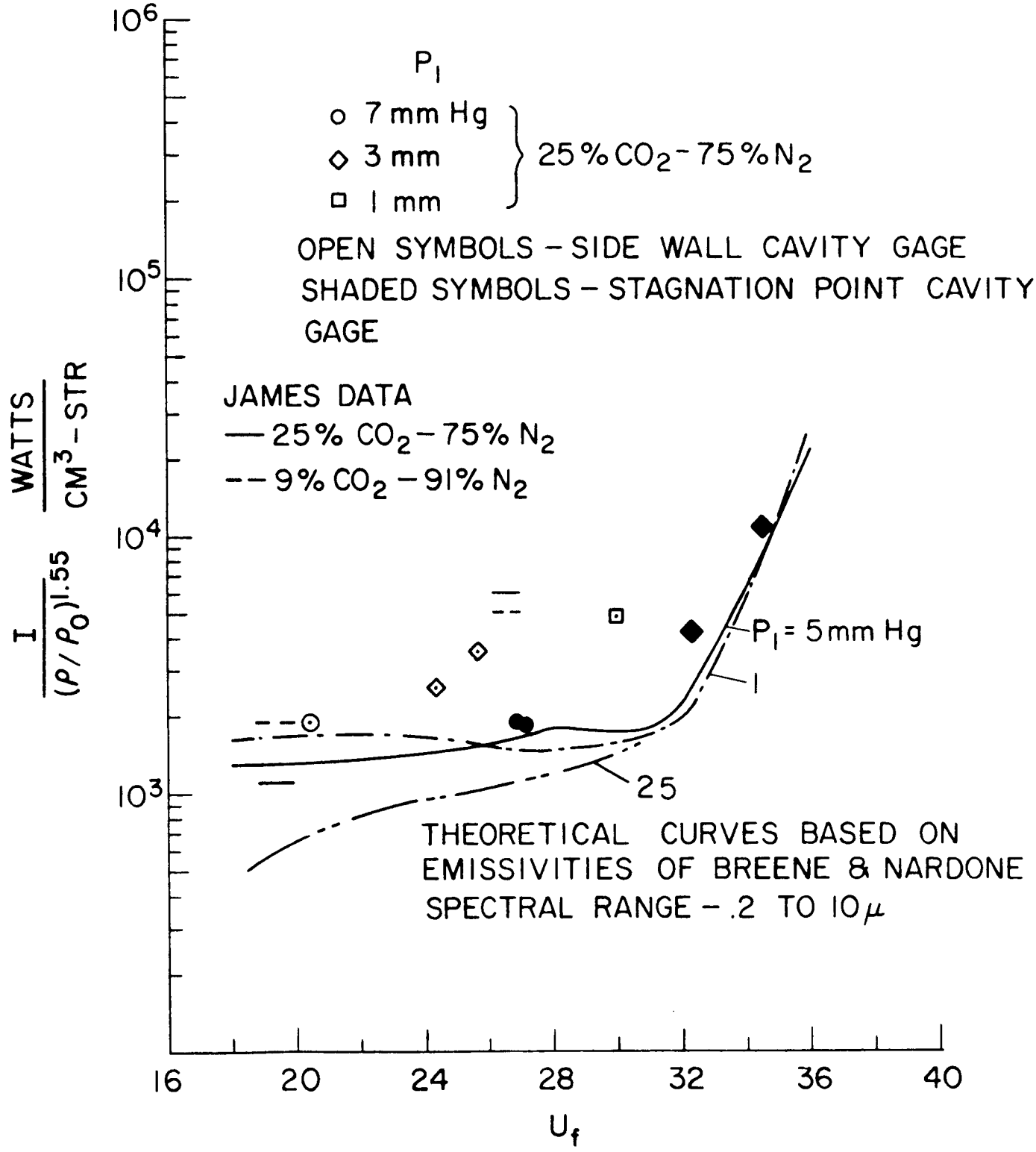

Figure 6.9. Equilibrium Radiation Behind Incident Shock in Simulated Venusian Atmosphere. Experimental Results Obtained with the Cavity Gage Compared to the Theoretical Predictions

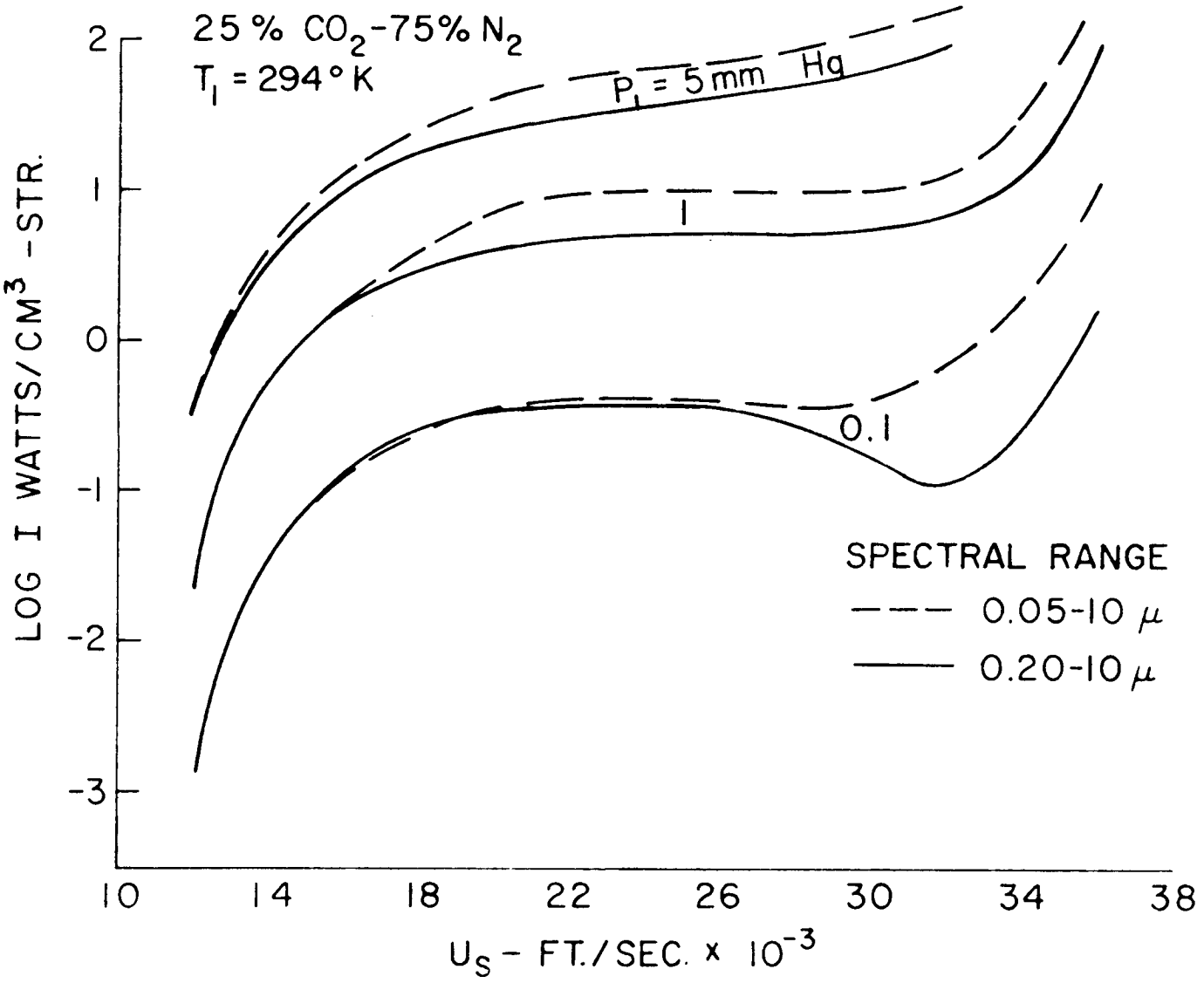

Figure 6.19. Equilibrium Radiance of Gas Behind Incident Schock Wave

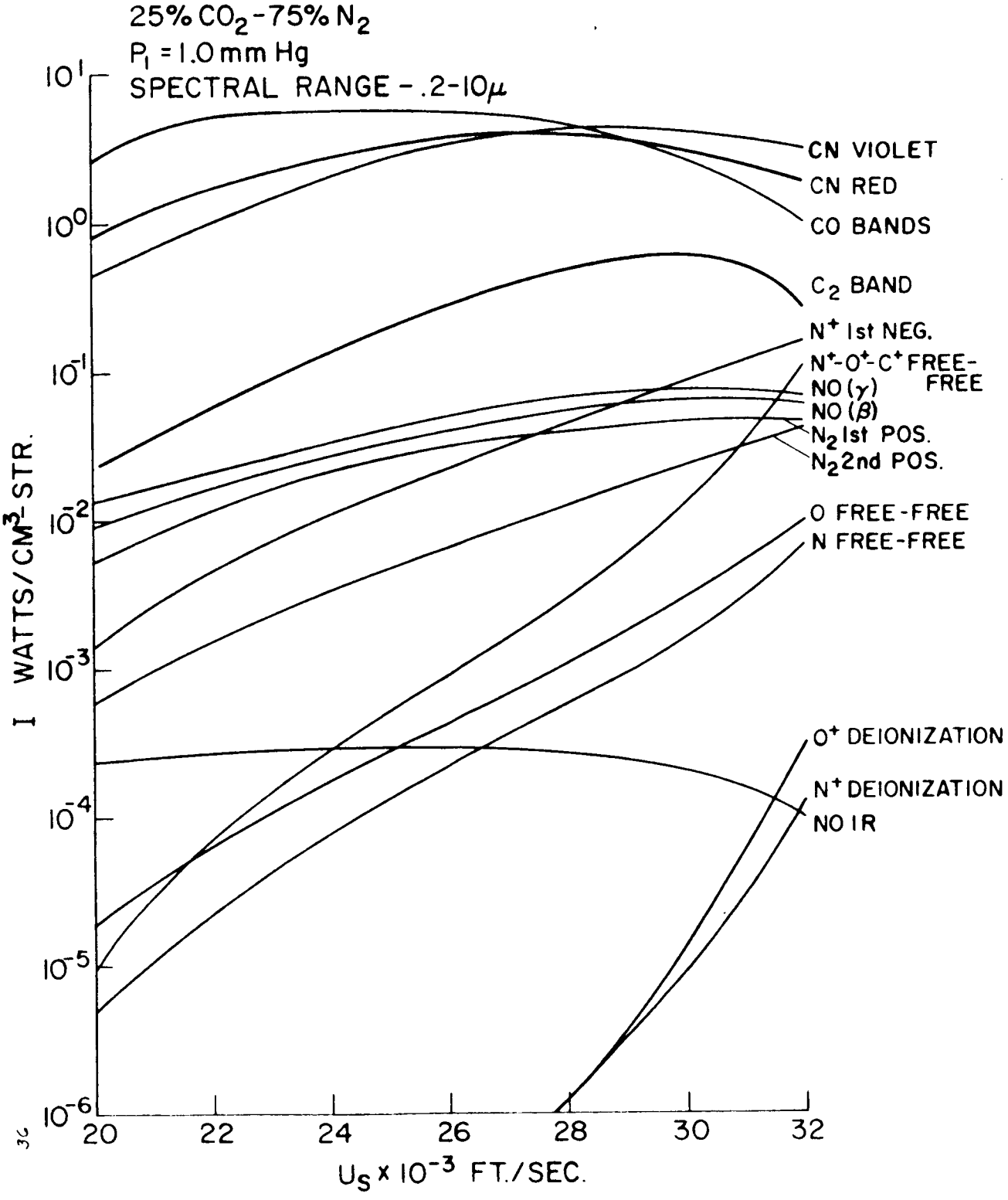

Figure 6.11. Species Radiation of Equilibrium Gas Behind Incident Shock Wave

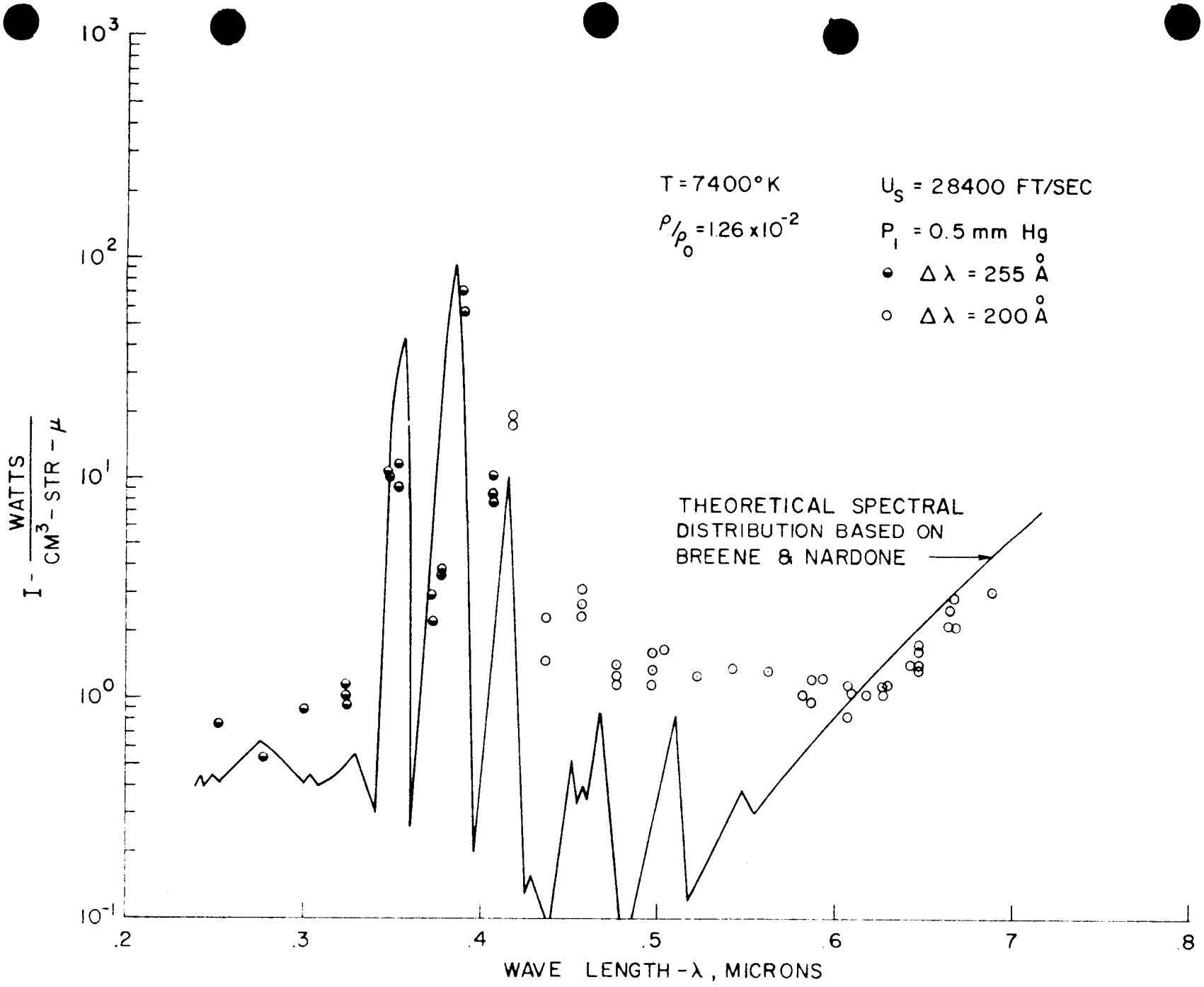

Figure 6.12. Spectral Distribution of Equilibrium Radiation Behind Incident Shock Wave, U_s = 28,400 ft/sec

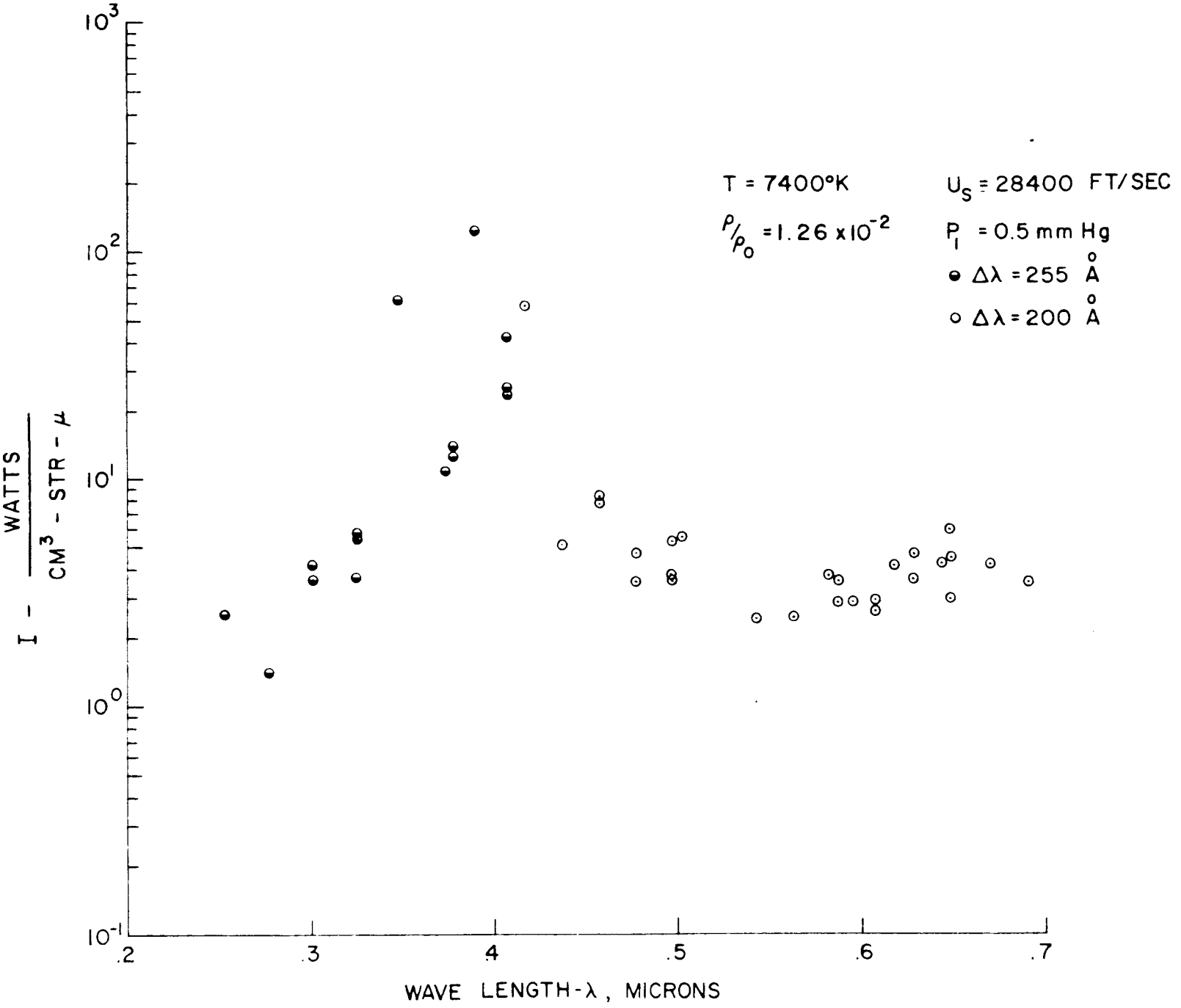

Figure 6.13. Spectral Distribution of Peak Nonequilibrium Radiation for U_s = 28,400 in Simulated Planetary Atmosphere

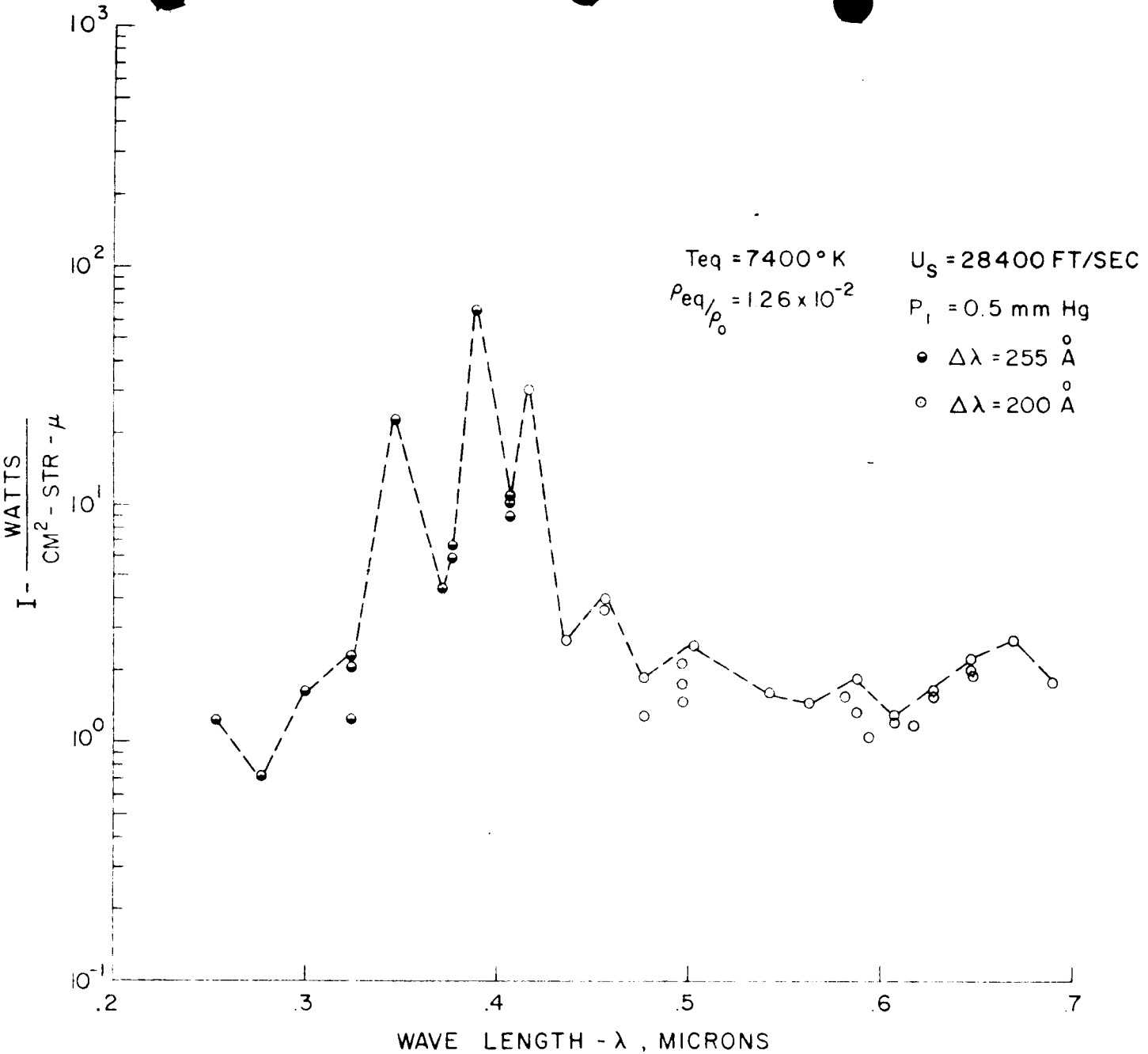

Figure 6.14. Spectral Distribution of Total Nonequilibrium Radiation from Shock Wave with U_s = 28400 ft/sec.